Dissertation

Submitted to the

Combined Faculty of Mathematics, Engineering and Natural
Sciences

of the Ruperto-Carola-University of Heidelberg, Germany

for the Degree of

Doctor of Natural Sciences (Dr. rer. nat.)

Presented by

M. Sc. Mohsen Ajdari

Born in Tehran, Iran

Oral examination: October 17th, 2023

Electronic Structure

and

Adsorption Geometry

of

Interfaces with N-Heteropolycycles

Referees:

Prof. Dr. Petra Tegeder

Prof. Dr. Milan Kivala

To my mother, Farahnaz.

Abstract

N-heteropolycycles are a class of aromatic compounds, in which C–H units of polycyclic aromatic hydrocarbons (PAHs) are substituted with N-atoms. These compounds are considered to be promising organic semiconductors with high potentials for the use as functional materials in (opto)electronic applications such as field-effect transistors and photovoltaic cells. For these applications, performance of a device is particularly dependent on the properties of the organic semiconductor at its interface with the metal electrodes. Therefore, gaining insights into the adsorption geometry and the electronic structure of N-heteropolycycles at the organic/metal interface and within their thin films are essential in improving and optimizing the device performance. In this thesis, this goal is achieved for various N-heteropolycyclic compounds by using two characterisation methods, high-resolution electron energy-loss spectroscopy (HREELS) and temperature-programmed desorption (TPD), in combination with density functional theory (DFT) calculations.

In the presented studies, all of the investigated molecules, at all coverages adopt a planar adsorption geometry relative to the substrate surface. By assigning the energies of the lowest excited singlet states (S) as well as the first triplet states (T_1), it is found that N-introduction can effect the electronic structure of N-heteropolycycles in three ways, namely narrowing the optical gap ($S_0 \rightarrow S_1$ transition), shifting the $S_0 \rightarrow T_1$ transition to a higher energy and inducing a pronounced rise in the intensity of the α - band ($S_0 \rightarrow S_2$ transition), in comparison to parent PAHs. Next, it is shown that the electronic structure of N-heteropolycycles can be fine-tuned by core substitution with halogens and aromatic groups, which results in a reduction of the transition energies of singlet and first triplet states. Subsequently, it is demonstrated that structural variation via connecting different moieties of N-heteropolycycles also leads to the narrowing the optical gap. Finally, it is determined that electron donating N-heteropolycycles in combination with well-known electron accepting molecules in donor/acceptor (D/A)-systems form charge transfer (CT)-complexes.

Kurzfassung

N-Heteropolyzyklen sind eine Klasse aromatischer Verbindungen, in denen CH-Einheiten polyzyklischer aromatischer Kohlenwasserstoffe (PAKs) durch N-Atome ersetzt sind. Diese Verbindungen gelten als vielversprechende organische Halbleiter mit hohem Potenzial für den Einsatz als Funktionsmaterialien in (opto)elektronischen Bauteilen wie Feldeffekttransistoren und Photovoltaikzellen. Bei diesen Bauteilen hängt die Leistung eines Geräts insbesondere von den Eigenschaften der Grenzfläche zwischen organischem Halbleiter und den Metallelektroden ab. Daher sind Kenntnisse der Adsorptionsgeometrie und der elektronischen Struktur von N-Heteropolyzyklen an der Organik/Metall-Grenzfläche und innerhalb ihrer dünnen Filme von wesentlicher Bedeutung für die Verbesserung und Optimierung der Geräteleistung. In dieser Arbeit wird dieses Ziel für verschiedene N-heteropolyzyklische Verbindungen durch den Einsatz von zwei Charakterisierungsmethoden, hochauflösender Elek -tronenenergieverlustspektroskopie (HREELS) und temperaturprogrammierter Desorption (TPD), in Kombination mit Berechnungen der Dichtefunktionaltheorie (DFT) erreicht.

In den vorgestellten Studien nehmen alle untersuchten Moleküle bei allen Bedeckungen eine planare Adsorptionsgeometrie relativ zur Substratoberfläche an. Durch Zuordnung der Energien der niedrigsten angeregten Singulett-Zustände (S) sowie der ersten Triplett-Zustände (T_1) wurde festgestellt, dass die N-Substitution drei verschiedene Effekte auf die elektronische Struktur der N-Heteropolyzyklen im Vergleich zu ihren Ausgangsverbindungen haben kann. Diese sind eine Verkleinerung der optischen Bandlücke ($S_0 \rightarrow S_1$ Übergang), eine Vergrößerung der Lücke zwischen S_0 und T_1 ($S_0 \rightarrow T_1$ Übergang) sowie ein deutlicher Anstieg der Intensität des α - Bandes ($S_0 \rightarrow S_2$ Übergang). Weiterhin wird gezeigt, dass die Übergangsenergien von Singulett- und ersten Triplettzuständen durch die Substitution von Wasserstoffatomen am aromatischen Kern durch Halogene oder aromatische Gruppen verringert werden kann. Anschließend wird gezeigt, dass strukturelle Variationen durch die Verbindung verschiedener Einheiten von N-Heteropolyzyklen auch zu einer

Verringerung der optischen Lücke führen. Schließlich wird festgestellt, dass elektronenspendende N-Heteropolyzyklen in Kombination mit bekannten elektronenakzeptierenden Molekülen in Donor/Akzeptor-Systemen (D/A) Ladungs -transferkomplexe (CT) bilden.

Contents

Contents

List of Tables

List of Figures

List of Acronyms

AES   Auger electron spectroscopy

BBT   Benzo[1,2-c;4,5-c']bis[1,2,5]thiadiazole

BBT-Ph   4,8-Diphenyl-benzo[1,2-c:4,5-c']bis[1,2,5]thiadiazole

BBT-Th   4,8-Dithiophene-benzo[1,2-c:4,5-c']bis[1,2,5]thiadiazole

BT   Benzothiadiazaole

BTD   Benzo[c][1,2,5]thiadiazole

CP   Compressed phase

CSP   Conventional surface plasmon

CT   Charge transfer

CW   Continuous wave

DCM   Dichloromethane

DAP   6,13-Diazapentacene

DBBA   10,10-Dibromo-9-9-bianthryl

DFT   Density functional theory

DMF   Dimethylformamide

DNP   Dynamic nuclear polarization

EELS   Electron energy-loss spectroscopy

EI-MS   Electron ionisation mass spectrometry

F$_4$TCNQ 2,3,5,6-Tetrafluoro-7,7,8,8-tetracyanoquinodimethane

fcc   Face-centred cubic

FWHM   Full width at half maximum

GNR   Graphene nanoribbon

hcp   Hexagonal close-packed

IP   Ionisation potential

HOMO   Highest occupied molecular orbital

HREELS   High-resolution electron energy-loss spectroscopy

LEED   Low-energy electron diffraction

LMOF   Luminescent metal-organic framework

LUMO   Lowest occupied molecular orbital

MASER   Microwave amplification by stimulated emission of radiation

ML   Monolayer

MO   Molecular orbital

MS   Mass spectrometry

N-HTA   N-heterotriangulene

N-HTA 550   Indolo[3,2,1-jk]carbazole

N-HTA 557   3a^2-Azabenzo[3,4]azuleno[2,1,8,7-jklm]fluorene

N-HTA 557SB   N-HTA 557 single bond

NTD   Naphto[2,3-c][1,2,5]thiadiazole

NTD-Br   Br-naphto[2,3-c][1,2,5]thiadiazole

NTD-Cl   Cl-naphto[2,3-c][1,2,5]thiadiazole

OFET   Organic field effect transistor

OLED   Organic light-emitting diode

OSC   Organic semiconductor

OTFT   Organic thin-film transistor

List of Acronyms

PAH   Polycyclic aromatic hydrocarbon

PEN   Pentacene

QMS   Quadrupole mass spectrometer

STM   Scanning tunneling microscope

TAP   6,7,12,13-Tetraazapentacene

TAPP-H   2,9-Bisperfluoropropyl-1,3,8,10-tetraazaperopyrene

TCNE   Tetracyanoethylene

TCNQ   7,7,8,8-Tetracyanoquinodimethane

TDS   Thermal desorption spectroscopy

THF   Tetrahydrofuran

TIPS   Triisopropylsilyl

TIPS-BAP   Triisopropylsilyl-dibenzodiazapentacene

TIPS-BP   Triisopropylsilyl-dibenzopentacene

TIPS-PEN   Triisopropylsilyl-pentacene

TPD   Temperature-programmed desorption

UHV   Ultra-high vacuum

UV/Vis   Ultraviolet/visible

XRD   X-ray diffraction

2PPE   Two-photon-photoemission

1. Introduction

In recent decades, special attention has been given to the development of organic semiconductors as an alternative to the legacy inorganic semiconductors, such as silicon[1] and germanium[2], for use as active materials in (opto)electronic devices[3–6]. This attention arises from unique properties of organic semiconductors such as ease of processing, transparency, flexibility, low weight and low costs that has made them attractive functional materials for use in a variety of applications including light-emitting diodes and field effect transistors[7–15]. The greatest advantage of organic semiconductors is the potential of tailoring their properties through chemical modification, which offers virtually endless possibilities for synthesizing molecules with desired properties[16]. A prime example of benefiting from this aspect is demonstrated with the synthesis of N-heteropolycyclic aromatic compounds by introducing nitrogen atoms into the π-conjugated molecular backbone of polycyclic aromatic hydrocarbons (PAHs)[17–21]. This leads to stabilization of frontier orbitals and increase of electron affinity that potentially changes the electronic properties of a molecule from a hole-transporting (p-channel) to an electron-transporting (n-channel) organic semiconductor[17–24]. Developing the n-channel organic semiconductors is of great interest for (opto)electronic applications, particularly field effect transistors. Therefore, N-heteropolycycles has become the subject of research in the scope of collaborative research center SFB 1249, which seeks to synthesize, characterize the properties, and investigate the device performance of this class aromatic compounds.

In (opto)electronic devices such as field effect transistors, adsorption geometry of organic molecules at the interface with a metallic electrode and within the molecular thin film plays a crucial role in determining the electronic properties of the organic molecule, namely charge transport characteristics or energy level alignment, and as such the performance of the device[25–32]. Therefore, as a member of SFB 1249, the studies presented in this thesis provides information on the adsorption and electronic properties of various N-heteropolycyclic compounds, which are adsorbed on a defined metallic substrate (Au(111) sin-

gle crystal), by using two characterisation method, high-resolution electron energy-loss spectroscopy (HREELS)[33] and temperature-programmed desorption (TPD)[34], in combination with density functional theory (DFT) calculations[35]. HREELS is a versatile tool, which utilizes low-energy electrons to characterize both adsorption geometries and electronic structures of adsorbates on (semi)conducting surfaces. In HREELS, by exciting molecular vibrations or electronic transitions, information about adsorbate orientation and its electronic properties such as energies of intramolecular electronic transitions (e.g. $S_0 \rightarrow S_1$)[36–40] and optically forbidden transition ($S_0 \rightarrow T_1$, triplet states)[41;42] can be gained. Furthermore, calculated intensities and frequencies of vibrational modes and their dynamic dipole moment via DFT, facilitates the determination of the adsorbate orientation. Additionally, though TPD measurements intact samples with defined coverage can be prepepared and potential on surface reactions can be monitored.

First goal of this work is to elucidate the influence of N-introduction on the adsorption and electronic properties of N-heteropolycyclic compounds in comparison to their parent PAHs. For this purpose, N-heteropentacene derivatives are investigated. Pentacene is a well known p-channel organic semiconductor, which is proven to be a promising active material for (opto)electronic applications such as field effect transistors[43]. Thus, there have been many efforts made in developing the n-channel counterpart of pentacene and its derivatives by substituting C-atoms with N-atoms in their aromatic molecular backbone[18–20;22–24;44]. Among the synthesized N-heteropentacenes, linear 6,13-diazapentacene (DAP) and 6,7,12,13-tetraazapentacene (TAP) derivatives are particularly suited for investigating the influence of N-introduction in general and the effect of the number and the position of the substituted N-atoms in particular. This is mainly due to their shared molecular structure with the parent pentacene (PEN), which its own adsorption and electronic properties on different metallic substrates is thoroughly studied and well understood[45–49]. Despite the promise of pentacene as an organic semiconductor, is lacks solubility and stability[50]. It has been shown that employing strategies such as introducing triisopropylsilylethynyl (TIPS) groups[50] or adding phenyl rings[51] to the acenes improves the stability and solubility of the molecule. A combination of these strategies results in synthesis of arrow-shaped silylethynylated pentacene derivatives[51], such as TIPS-dibenzodipentacene (TIPS-BP), which together with the corresponding N-substituted TIPS-dibenzodiazapentacene

(TIPS-BAP) are the subject of another study that seeks to gain insights into the effects of N-introduction on the properties of complex pentacene derivatives. Through these studies, it is found that N-introduction can effect the electronic structure of N-heteropolycycles in three ways, namely narrowing the optical gap ($S_0 \rightarrow S_1$ transition), shifting the $S_0 \rightarrow T_1$ transition to a higher energy and inducing a pronounced rise in the intensity of the α - band ($S_0 \rightarrow S_2$) in comparison to parent PAHs.

Substitution of small organic molecules with halogens[38;52] and aromatic groups[53;54] can be used as a strategy to alter their electronic properties. Therefore, in another set of studies, the influence of core substitution with Br and Cl atoms as well as phenyl and thiophene groups on the adsorption and electronic properties of thiadiazole derivatives is investigated. Similar to N-heteropolycycles, S-heteropolycyclic aromatic compounds are also of great interest for use in (opto)electronic applications, for instance small molecule organic solar cells[55–58]. This has led to comprehensive studies of the adsorption and electronic properties of these molecules, which are relevant for device applications, such as thiophene derivatives[58–67]. In contrast, similar properties of heteropolycycles containing both S and N atoms, such as naphto[2,3-c][1,2,5]thiadiazole (NTD) and benzo[1,2-c;4,5-c']bis[1,2,5]thiadiazole (BBT) and their derivatives have not yet been investigated. This is despite the fact that these molecules have shown to be promising electron accepting moieties[68–70] in donor/acceptor (D/A) -systems, which have wide-ranging applications in devices such as field effect transistors, solar cells, and light-emitting diodes[71–86]. In the presented studies, by investigating NTD and its halogenated derivatives (NTD-Br and NTD-Cl) as well as phenyl (BBT-Ph) and thiophene (BBT-Th) substituted BBT, it is shown that the core substitution via halogens and aromatic groups results in a reduction of the transition energies of singlet (s) and first triplet states (T_1) in the corresponding molecules.

Structural variation of molecules though connecting their moieties with suitable bridging units as demonstrated for N-heterotriangulenes (N-HTAs)[87;88] is a promising approach toward tailoring the electronic structure of these organic semiconductors. Therefore, in a presented study, the influence of connectivity via introduction of -C=C- bridge on the adsorption and electronic properties of N-HTAs is elucidated, by investigating two N-HTA derivatives, namely 3a²-azabenzo[3,4]azuleno[2,1,8,7-jklm]fluorene; 7-membered ring N-HTA 557 and indolo[3,2,1-jk]carbazole; 5-membered ring N-HTA 550. In

this study, it is demonstrated that the introduction of -C=C- bridge leads to the narrowing of the optical gap in the corresponding molecule. Additionally, it has been shown that N-HTA 557 can act as an electron donor and undergo D/A interaction with well-known electron acceptor molecules, such as tetracyanoquinodimethane (TCNQ) and 2,3,5,6-tetrafluoro-7,7,8,8- tetracyanoquinodimethane (F_4TCNQ)[88]. This interaction may lead to a potential charge transfer (CT) in the corresponding D/A-systems, which is desired in (opto)electronic applications[89–92], such as near-infrared photodetectors[93]. Therefore, in a subsequent study, the possibility of charge transfer in D/A systems of N-HTA 550 and N-HTA 557 with TCNQ and F_4TCNQ is investigated. The results from this study shows that the investigated D/A-systems form CT-complexes.

In the following, in the chapter, methods and experimental setup, the methods used in this thesis for characterization of the studied molecular systems as well as the experimental setup used for preparing the samples are introduced. Subsequently, the results from the conducted studies and the related findings are presented and thoroughly discussed in the results and discussion chapter, which consists of three sections and six subsections. Each section begins with an abstract, which highlights the most important findings of studies conducted under its scope and ends with a conclusion. At the beginning of each subsection, a short review of some of the reported properties of the given molecular systems is presented in order to provide the reader with the information, which maybe closely related to but not covered by the conducted studies. The presentation of the results, mostly, follows a similar approach, it begins with describing the obtained results from the TPD measurements and proceeds to analyse the results from vibrational and electronic HREELS measurements. The findings from each study are summarized at the end of each subsection.

2. Methods and Experimental Setup

2.1. Methods

2.1.1. Temperature-Programmed Desorption (TPD)

Temperature-programmed desorption (TPD)[34], also referred to as thermal desorption spectroscopy (TDS), is a desorption technique that can be used to great effect in surface science for studying adsorption processes and chemical reactions at surfaces as well as determining coverages and binding energies of adsorbates[94;95]. In a TPD measurement, an adsorbate-covered substrate is heated with a precise procedure[34] that is controlled by a computer program, to achieve a constant heating rate $\beta = dT/dt$ with high accuracy by changing the temperature of the substrate T_S from initial temperature T_0, linearly with time t : $T_S(t) = T_0 + \beta t$ [94]. Provided that the thermal energy received by the adsorbate be high enough to overcome the intermolecular forces and the binding energy of the adsorbate to the surface, the desorption occurs. Mass spectrometry (MS) allows the analysis of the desorbing species[34;94]. Under ultra-high vacuum (UHV) condition, mass of a parent molecular ion or its ionic fragments can be monitored by a quadrupole mass spectrometer (QMS)[34]. The desorption rate r_{des} is proportional to the net ion current signal output from QMS[96]. r_{des} is described by the Polanyi-Wigner equation[97] as

$$r_{des} = -\frac{d\theta}{dt} = \nu_0 \theta^n \exp(-\frac{E_{des}}{k_B T}) = k_{des} \theta^n, \qquad (2.1)$$

where θ is the coverage, ν_0 the pre-exponential factor, n the desorption order, E_{des} the desorption energy and k_{des} the rate constant. By inserting the expression for β in the equation 2.1, it assumes the form of

$$-\frac{d\theta}{dT_S} = \frac{\nu_0}{\beta} \theta^n \exp(-\frac{E_{des}}{k_B T_S}). \qquad (2.2)$$

A TPD spectrum is plotted with the the recorded QMS signal for a given mass-to-charge ratio (m/z) as a function of the substrate temperature (see

Figure 2.1 top). In a substrate, covered with multiple layers of an adsorbate, the TPD spectrum includes a pronounced desorption feature associated with molecules desorbing from higher layers followed by another desorption feature at higher temperatures. The later feature originates from the molecules in direct contact to the substrate, adding up to a monolayer, which require higher thermal energy to overcome the strong adsorbate/substrate interactions, before the desorption takes place. By measuring the TPD spectrum of the desorbing molecule with the same m/z value for different initial coverages, a coverage dependent TPD spectra can be plotted. Shape of the desorption spectra in the resulting plot is an indicator of the desorption order n and the correlation between desorption rate and the adsorbate coverage[98].
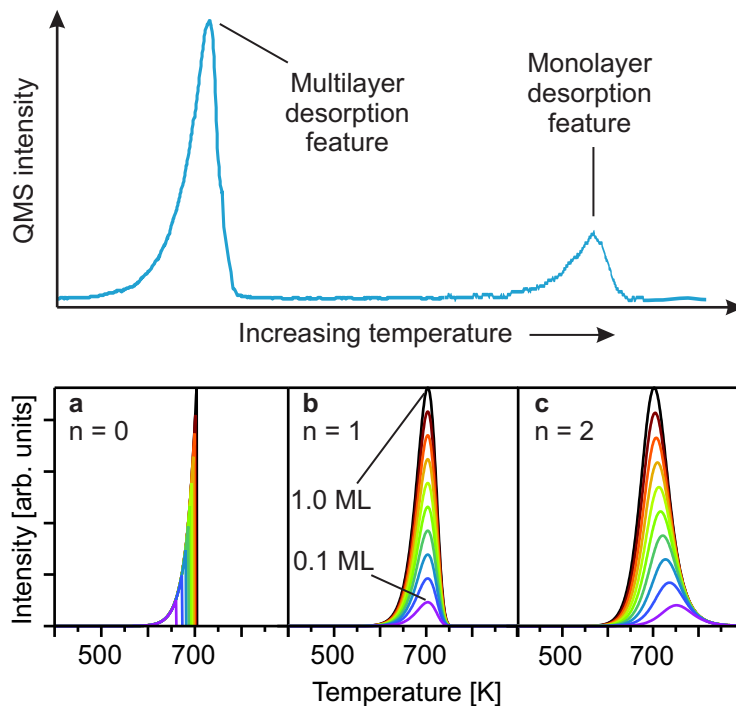
Figure 2.1.: Top: TPD spectrum of an adsorbate covered substrate. Bottom: Simulated desorption spectra of zero- (a), first- (b) and second-order (c) (detailed descriptions in Ref.[95]) with constant heating rate $\beta = 1 \text{ Ks}^{-1}$ and pre-exponential factor $\nu_0 = 10^{-13}$ for coverages increasing with 0.1 steps from 0 to 1 ML. Adapted from Ref.[95].

At a multilayer coverage, by increasing the temperature, layers of the molecu -le desorb in succession. Thus, for higher initial coverages, desorption picks with common rising edges shift to higher temperatures until the peak maximum suddenly drops to zero at a certain temperature, upon desorption of the last

adsorbate (see Figure 2.1 bottom (a)). This leads to a zero-order desorption, i.e. the desorption rate is independent of the coverage[95]. In a desorption process of first-order, with increasing the temperature, the desorption peak maximum remains at the same temperature for higher initial coverages, provided that lateral interactions of molecules are not considered (see Figure 2.1 bottom (b)). The monomolecular[94] (non-associative) desorption exhibit this desorption kinetic. The lateral interactions lead to the coverage dependency of the desorption peak maximum. Depending on the involved interactions, the first-order desorption spectra evolves with increasing temperature to the so-called pseudo-zero-order (attractive interaction) or pseudo-second-order (repulsive interaction) desorptions by the shift of the desorption peak maximum for different initial coverages to higher or lower temperatures, respectively[95]. In case of bimolecular or recombinative (associative) desorption, by increasing the initial coverage, the desorption peak maximum shifts to lower temperatures[94], leading to a desorption process of second-order (see Figure 2.1 bottom (c)). In this thesis, TPD measurement is used primarily for preparing intact samples with defined coverages and additionally gaining insights into potential on surface reactions. A more detailed description of TPD can be found in Ref.[95].

2.1.2. High-Resolution Electron Energy-Loss Spectroscopy (HREELS)

High-resolution electron energy-loss spectroscopy (HREELS) is a unique spectroscopy technique that utilizes low-energy electrons ($E_0 < 20$ eV)[94] in surface inelastic-scattering experiments to provide information on the adsorbate geometry and electronic properties. The name HREELS derives from the high-energy resolutions of up to 0.5 meV[33] that can be achieved in this technique, which sets HREELS apart from electron energy-loss spectroscopy (EELS) that uses electrons with higher primary energies at the cost of lower energy resolutions. In HREELS, a cathode produces the low-energy electrons that are monochromatized before being accelerated toward a sample with a pre-set primary electron energy E_0 (trajectory of electrons are illustrated with red curves in Figure 2.2 (a)). After interacting with the sample, the scattered electrons can be detected with a channeltron by changing the analyzer potentials (energy-resolved) or position (angle-resolved).
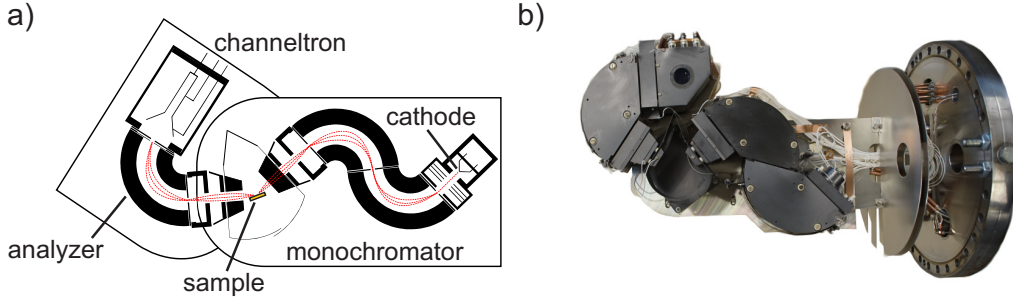
Figure 2.2.: Sketch of the used high-resolution electron energy-loss spectrometer (SPECS Delta 0.5) in this thesis (a) and a picture of the spectrometer (b). Adapted from Ref.[95].

The inelastic-scattering from a surface involves the transfer of the energy $\hbar\omega$ and the momentum transfer parallel to the surface $\vec{q}_{||}$, for excitation of vibrations or electronic transitions. Considering the energy E conservation during this process on a crystalline surface, the transferred energy is

$$E_s - E_i = \hbar\omega, \tag{2.3}$$

with E_i and E_s being the energy of the incident and scattered electrons. On a perfect crystalline surface with $\vec{G}_{||}$ as an arbitrary 2D reciprocal lattice vector[94], the wave vector parallel with the surface $\vec{k}^{||}$ is also conserved:

$$\vec{k}_s^{||} - \vec{k}_i^{||} = \vec{q}_{||} + \vec{G}_{||}, \tag{2.4}$$

where $\vec{k}_i^{||}$ and $\vec{k}_s^{||}$ are the parallel wave vectors of the incident and scattered electron. In scattering from non-perfect surfaces (e.g. with defects and adsorbed atoms), conservation of wave vector is not valid[94] and $\vec{q}_{||}$ equals to the difference of the parallel wave vectors of the incident and scattered electron.
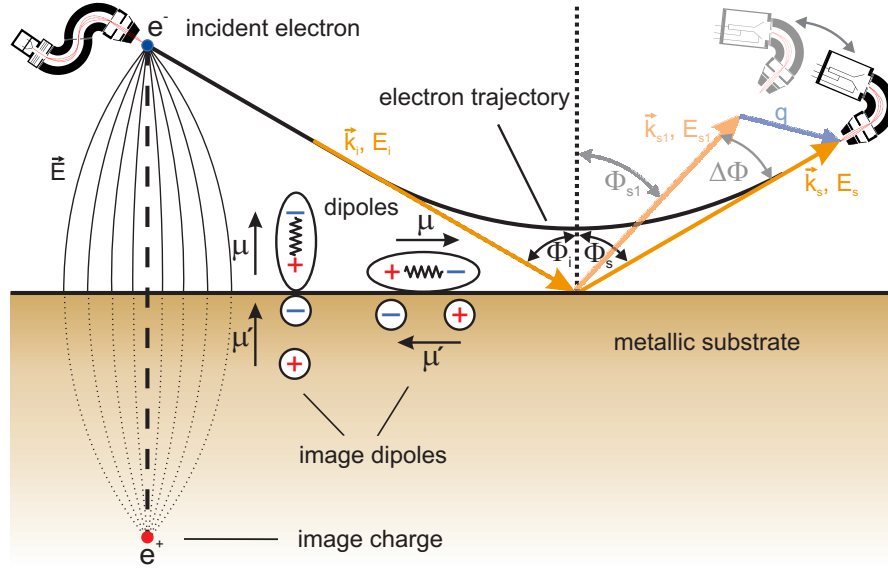
Figure 2.3.: Upper left: Emitted incident electron e^- from the monochromator forms an electric field $\vec{E}$ with its image charge e^+ in the metal as it approaches the metallic substrate under the incident angle Φ_i with the wave vector of $\vec{k}_i$ and the kinetic energy of E_i. Middle: Dynamic dipole moments μ of molecular vibrations and their image dipoles μ' in the metal, oriented normal to and parallel with the substrate surface. The incident electron is scattered with the angle of Φ_s after interacting with the dipoles according to the surface selection rule (detailed description in text). Upper right: The dipole scattered electron ($\vec{k}_s \neq \vec{k}_i$, $E_s \neq E_i$ in inelastic scattering) is detected by the analyzer in specular direction ($\Phi_s = \Phi_i$). The analyzer can be rotated to an off-specular angle (Φ_{s1}), to only detect the impact scattered electrons ($\vec{k}_{s1}$, E_{s1}). Adapted from Ref. [95].

Depending on the used primary energy for electrons, HREELS measurements can be divided into vibrational and electronic regimes. In the vibrational measurement regime, by choosing electron energies of lower than 5 eV, molecular vibrations can be resolved, while using higher electron energies in the electronic measurement regime leads to excitation of electronic transitions. In the vibrational measurement regime, electrons can be scattered inelastically with three mechanism: dipole scattering, impact scattering and resonance scattering[34;94]. In an adsorbate-covered substrate, oscillating dipole fields generated by dynamic dipole moments μ of vibrations originating from the adsorbed molecules give rise to long-range scattering potentials known as dipole scattering[94]. When an incident electron e^- approaches the surface of a metallic substrate, it forms an electric field $\vec{E}$ with its image charge of an opposite sign (e^+) in the metal (see Figure 2.3 upper left). Direction of field lines in the

generated electric field are normal to the substrate surface. Thus, only the dynamic dipole moment of a molecular vibration with an orientation normal to the substrate surface can couple with the electric field according to the surface selection rule[94]. The dipole moments induce image dipoles μ' in the metallic substrate, which are oriented in opposite direction of a dipole parallel with the substrate surface and in the same direction of a dipole normal to the substrate surface (see Figure 2.3 middle). Consequently, the contribution of parallel dipole moment diminishes, while the effect of normal oriented dipole moment is amplified, leading to a large electron scattering cross section at small angles around the specular direction ($\Phi_s = \Phi_i$, see Figure2.3 upper right), which produces a pronounced loss feature in a measured spectrum[94].

Other than long-range scattering potentials of dipole fields, local atomic potentials of the substrate or adsorbate atoms can scatter electrons through the so-called impact scattering[94]. In this mechanism, an incident electron virtually excites an electronic state of an atom. A vibrational quantum (e.g. an adsorbate vibration) then releases the electron shortly after occupying the excited state, inelastically[94]. This scattering potential is short ranged (at the atomic scale) with a large value for the momentum transfer parallel to the surface $\vec{q}_{||}$[94]. This leads to a small electron scattering cross section at large angles around the specular direction[94]. Thus, the main mechanism involved in the scattering of electrons can experimentally be identified by moving the analyzer and measuring the scattered electrons in an off-specular angle ($\Phi_s \neq \Phi_i$, see Figure2.3 upper right), where the impact scattered electrons can be distinguished from dipole scatter electrons that are constrained to small angles around the specular angle.

Depending on the primary energy of an incident electron, it can temporarily become trapped in a molecular orbital and forms a short-lived negative ion. The decay of the negative ion with a Frank-Condon transition[34] into the ground state leads to a re-emission of the electron in the so-called negative ion resonance scattering mechanism. Previous primary electron energy-resolved measurements[95] did not show any indication of negative ion resonance for the used primary electron energies in this thesis and as such this scattering mechanism will not be discussed any further. A detailed description of HREELS can be found in literature[99;100] and other theses[95;101;102].

2.1.3. Density Functional Theory (DFT)

In this thesis, the detected vibrations in the measured HREELS spectrum of an adsorbate are assigned by carrying out density functional theory (DFT) calculations on the relaxed geometry of a single molecule in the gas phase and subsequently obtaining the corresponding vibrational modes with the associated dynamic dipole moments μ from the simulated and visualized frequencies of the vibrations. DFT is based on the Hohenberg and Kohn findings[103], which states that ground-state energy E of a system is determined solely by its electron density ρ. In DFT, E can be estimated as a function of ρ by

$$E(\rho) = T(\rho) + E_{ne}(\rho) + J(\rho), \tag{2.5}$$

where T is the kinetic energy of the electrons, E_{ne} the attractive electron-nuclear interaction, and J the Coulomb-term, which describes the electron-electron interaction. The accuracy of this estimation is improved by considering orbitals in the form of one-electron Kohn-Sham equations[104]:

$$(-\frac{1}{2}\nabla^2 + \upsilon_{eff}(\vec{r}) - \epsilon_j)\varphi_i(\vec{r}) = 0, \tag{2.6}$$

in which ϵ_j is the energy, φ_i the Kohn-Sham function, and υ_{eff} the effective potential. Equation 2.6 can be re-written as

$$\upsilon_{eff}(\vec{r}) = \upsilon(\vec{r}) + \int \frac{n(\vec{r'})}{|\vec{r} - \vec{r'}|}\mathrm{d}^3r' + \upsilon_{XC}(\vec{r}), \tag{2.7}$$

where υ is the external (electron-nuclear) potential, n the electron density, and υ_{XC} the exchange-correlation potential, which itself can be approximated by different functionals that includes hybrid methods, where υ_{XC} is derived by a combination of DFT and ab-initio Hartree-Fock method. To achieve satisfactory results in the DFT calculations using suitable functionals and associated basis sets is essential. In order to describe complex systems like small molecules, B3LYP[105] is an adequate hybrid functional. In this thesis, all of the DFT calculations are carried out with B3LYP functional by Becke[106] and Lee *et al.*[107] and 6-311G basis set (detailed description in Ref.[95]) . The programme package Gaussian09[108] is used for conducting the calculations. A more detailed description of DFT can be found in literature[35] and another thesis[95].

2.2. Experimental Setup

The experimental setup used for conducting the studies presented in this thesis is previously described in details in other theses[101;109;110]. Even though, over time, some alteration has been made to the setup, its principal functions, i.e. sample preparation and characterization, remained unchanged. Therefore, in this section only a brief overview of the setup is provided, in order to introduce its main components and their functions. This is followed by the description of the Au(111) single crystal as the used substrate and standard procedures for preparing and characterizing a sample.

2.2.1. Ultra-High Vacuum (UHV) System

In this thesis, samples of investigated molecular systems are prepared and characterized under UHV condition ($p \approx 10^{-10}$ mbar) in an integrated UHV system, which consist of a preparation (see Figure 2.4 (a) top) and a spectrometer (containing SPECS Delta 0.5 HREEL spectrometer, see Figures 2.4 (a) bottom and 2.2 (b)) chamber, that are separated with a gate valve in order to isolate the spectrometer chamber during sample preparation. Conducting the experiments under UHV conditions serves two purpose: one is to ensure a contamination free and well-defined surface can be achieved and kept as such for the total course of its characterization[110], and second to be able to detect electrons with low energies. In the corresponding setup, the base pressure of approximately 2×10^{-10} mbar is realized by pumping each chamber separately and with two different methods. The preparation chamber is pumped in three stages, starting with a membrane pump, which provides a pre-vacuum condition, followed by two turbo-molecular pump with pumping speeds of 60 l s^{-1} and 520 l s^{-1} that are used in sequence to achieve final UHV condition. In the spectrometer chamber the desired vacuum is reached by using a single ion getter pump backed by a membrane pump.

In this setup, molecules are deposited *in situ* on a substrate at regulated temperatures using a Knudsen effusion cell evaporator or doser (see Figure 2.4 (b) 14). The doser is separated from the preparation chamber with a gate valve and is kept independently under UHV condition by using a two stage pumping sequence (a membrane pump in combination with a 60 l s^{-1} turbo-molecular pump). A QMS (see Figure 2.4 (b) 13) provides the ability of monitoring the mass of the parent molecular ion or its ionic fragments up to 200 amu

(detection limit of the used QMS device) upon molecule deposition onto or desorption from the substrate.

The substrate, an Au(111) single crystal is fixed on a molybdenum made sample holder with two tantalum wire, which are used for resistive heating of the crystal (see Figure 2.4 (c)). A thermocouple wire attached to the side of the crystal provides an accurate reading of its temperature. The sample holder is mounted on a liquid nitrogen-cooled cryostat, capable of cooling the sample down to 95 K (see Figure 2.4 (b) 9). The cryostat is placed on a x,y,z,β-manipulator (see Figure 2.4 (b) 10), which can be moved in x-, y- and z- directions and rotated around the z-axis (β). This allows the sample holder to be moved into a required position, e.g. facing the sputter gun (see Figure 2.4 (b) 11) for substrate surface cleaning. Additionally, the setup includes a combined low-energy electron diffraction (LEED) and auger electron spectroscopy (AES) system (see Figure 2.4 (b) 12), which is not used in the presented studies in this thesis. Other components of the setup are the control units (see Figure 2.4 (b) 2 - 4 and 6) and power supplies (see Figure 2.4 (b) 1, 5 - 8) of the mentioned devices as well as the cooling unit of the doser (see Figure 2.4 (b) 17) and a transport rod (see Figure 2.4 (b) 15), which can be used to remove the sample holder from the inside of the preparation chamber through a load-lock (located beneath the QMS) without breaking the vacuum.
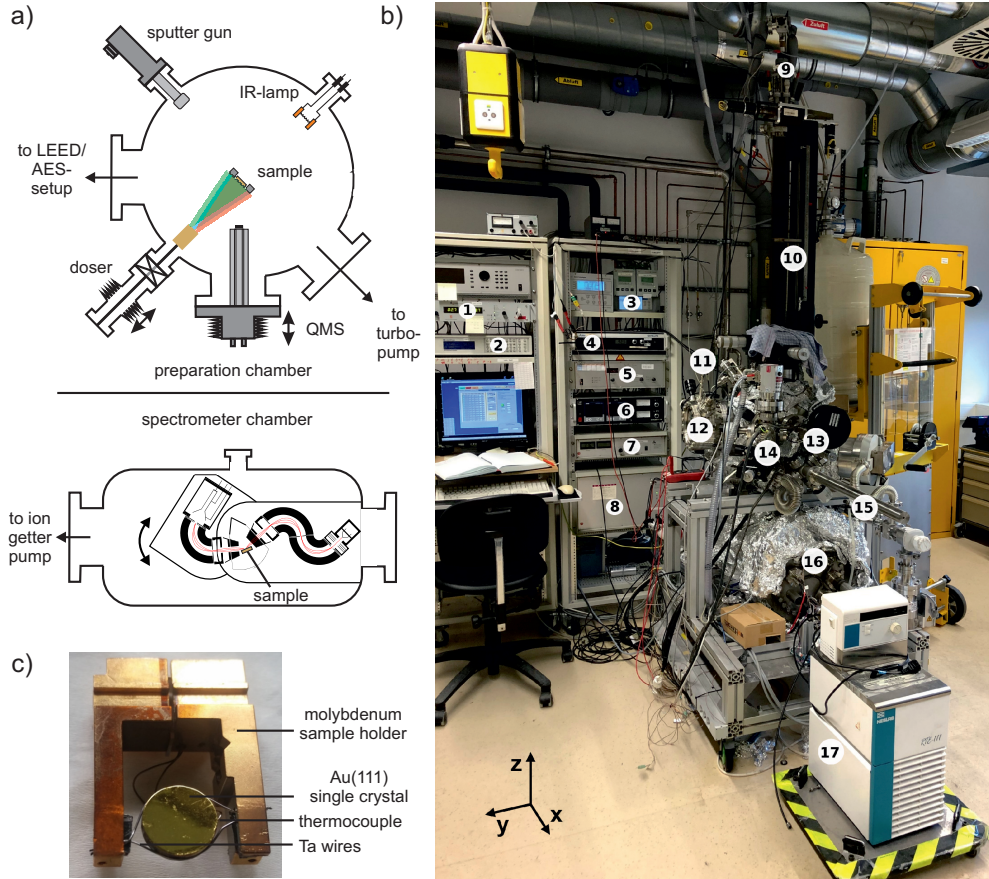
Figure 2.4.: Experimental setup: (a) Sketch of the UHV preparation (top) and spectrometer (bottom) chambers. (b) Main components of the setup as pictured; power supplies for substrate resistive heating (1), sputter gun (5), doser (6), channeltron (7), and HREELS (8). Control units of substrate temperature regulator (2), ion getter and turbo-molecular pumps (3), QMS (4), and doser (6). Cryostat (9), x,y,z,β-manipulator (10), sputter gun (11), LEED/AES setup (12), QMS (13), doser (14), transfer rod (15), HREEL spectrometer (16), and doser cooling unit (17). (c) Sample holder. Adapted from Ref. [95].

2.2.2. Au(111) Substrate

Owing to its high conductivity and resistivity toward corrosion, gold is widely used as a contact material in microelectronics[111]. Gold is chemically inert (filled d-orbital), which results in its weak reactivity with adsorbates. Thereby, it is a suitable substrate material for investigating adsorbed organic molecules. All of the studies presented in this thesis are conducted on samples, which are prepared on a Au(111) single crystal. The Au(111) surface is achieved by cutting the face-centred cubic (fcc) structure of gold single crystal along 111 plane (see Figure 2.5 (a)). The resulting pristine surface, then reconstructs into a more energetically favourable herringbone pattern[112] (see Figure 2.5 (b)) with $22 \times \sqrt{3}$ stripes of alternating fcc and hexagonal close-packed (hcp) domains (see Figure 2.5 (c)). The herringbone reconstruction can always be restored by Ar^+ sputtering and annealing cycles.
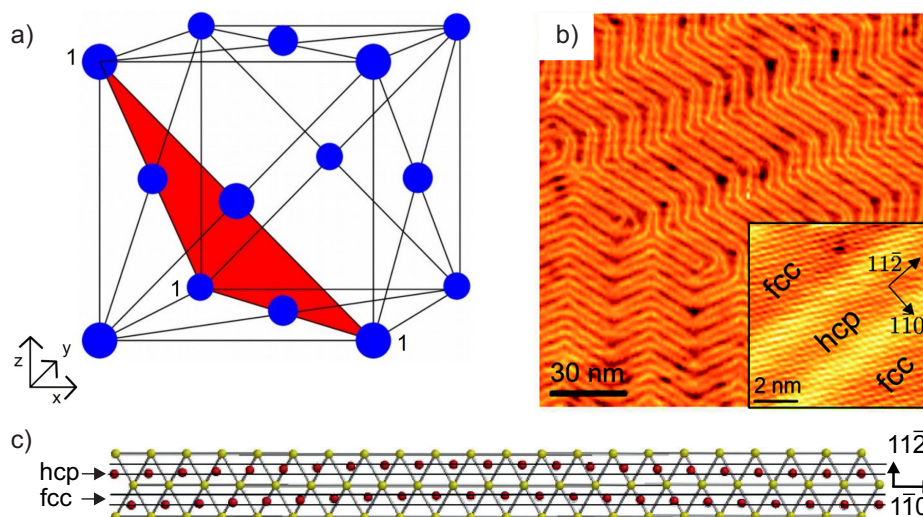
Figure 2.5.: (a) Face-centred cubic (fcc) unit cell and 111 plane (in red), adapted from Ref.[113]. (b) Scanning tunneling microscope STM image of herringbone reconstruction of the Au(111) surface (inset: magnified fcc and hcp domains), adapted from Ref.[114]. (c) Calculated positions of fcc and hcp domains, adapted from Ref.[115].

2.2.3. Sample Preparation and Characterization Procedures

In order to prepare a standard sample (adsorbate/Au(111)), first the substrate surface is cleaned by p $\approx 10^{-6}$ mbar Ar^+ sputtering at 1 keV kinetic energy for 15 min, followed by 20 min annealing at 750 K. Next, the cleaned sub-

strate, which is held at a constant temperature (T_S) is exposed to the flux of a molecule, that is being evaporated (dosed) at a regulated temperature by opening the gate valve separating the preparation chamber and the doser. At the same time, mass of the parent molecular ion or its ionic fragments are monitored by time-resolved QMS measurement (see Figure 2.6 (a)). Depending on the dosing time (t_D), different adsorbate coverages ranging from sub-monolayer to multilayer can be achieved with a constant dosing temperature (T_D). The coverage (Θ) of the adsorbate can be determined through the TPD measurement (see Figure 2.6 (b)), by heating the sample (from T_S up to 750 K) with a heating rate of $\beta = 1$ Ks^{-1}, integrating the obtained spectrum and comparing the area of the total integral with the area of the monolayer desorption region[110].
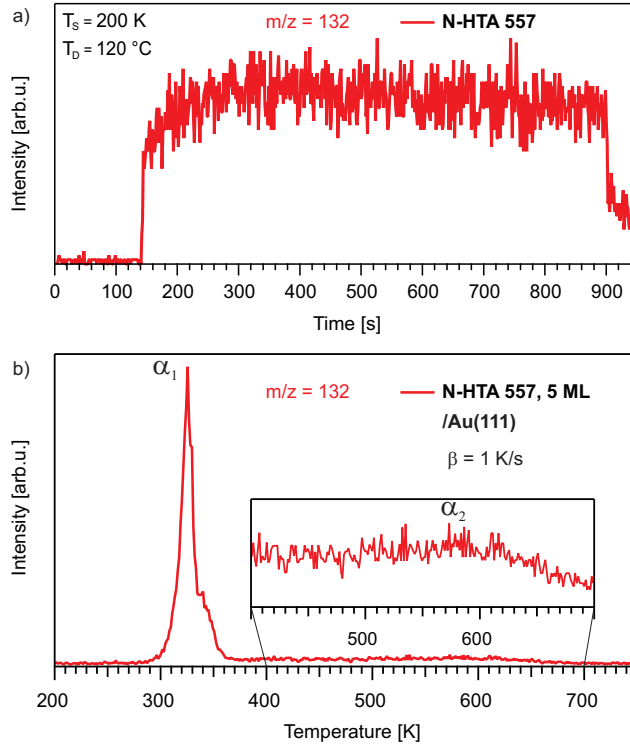
Figure 2.6.: (a) Dosing spectrum of an exemplary molecule (N-HTA 557) on Au(111) substrate, held at 200 K with dosing temperature of 120°c (393 K), that is monitored with QMS for m/z=132. The sudden rise and then fall of the intensity of the measured spectrum are the result of opening and closing of the gate valve, that is separating the doser from the preparation chamber. (b) Corresponding TPD spectrum of the adsorbed molecule at a coverage of 5 monolayer (ML) on Au(111) substrate, measured with m/z=132 (α_1 and α_2 are assigned to the desorption features from multi- and monolayer coverage).

By determining the desorption temperatures of different coverages with TPD analysis, it is possible to prepare monolayer or sub-monolayer of an adsorbate by dosing larger amounts of the corresponding molecule, adding up to a multi - or 2nd - layer coverage and subsequently heating the sample up to or beyond the desorption temperatures of the corresponding coverage in order to desorb the higher layers, thus preserving the monolayer or sub-monolayer. As for non-standard samples (adsorbate(B)/adsorbate(A)/Au(111)), which involve two different molecules, the substrate is first covered with a certain coverage of molecule A and subsequently molecule B is dosed on top of the underlying coverage.

After dosing at elevated temperatures ($T_D > 300$ K), the heated molecules are examined for a possible degradation by electron ionisation mass spectrometry (EI-MS) measurement, which is conducted by Mass Spectrometry Facility of the Organisch-Chemisches Institut at the Universität Heidelberg. In case of an intact molecule, the obtained EI-MS spectrum after dosing should agree with the one of the pristine molecule, measured before dosing. Additionally, the EI-MS spectrum of the pristine molecule can be used to select masses of different ionic fragments to be used as reference in QMS, in order to monitor the dosing and measure the TPD spectrum. Exemplary EI-MS spectra is provided in appendix F.1 (see Figure F.1).

After preparing a sample, the adsorbate geometry and its electronic properties are investigated via vibrational and electronic HREELS measurements, respectively. In the vibrational measurement regime, by setting the primary electron energy (E_0) of the incident electrons to 3.5 eV, a resolution lower than 4 meV (as determined from the full width at half maximum (FWHM) of the elastic peak) can be achieved, which is suitable for resolving the molecular vibrations. This measurement is done in specular ($\Phi_s = \Phi_i$) and off-specular ($\Phi_s \neq \Phi_i$) scattering geometry. By comparing the obtained spectra from the two measurements, the dipole-active vibrations can be distinguished from the non-dipole-active vibrations based on the reduced intensity of the corresponding vibrations, going from specular to off-specular scattering geometry. The detected vibrations of an adsorbate are assigned to the vibrational modes of the corresponding molecule by conducting DFT calculations. By comparing the dipole-active vibrations with the vibrational modes possessing a dynamic dipole moment perpendicular to the molecular backbone, the adsorbate orientation with respect to the substrate surface can be determined.

In the electronic measurement regime, with $E_0 = 15$ eV, the electronic transitions are excited and can be detected in the obtained spectrum as electron energy loss features. These features are fitted with the Gaussian function for an accurate determination of their energetic position (peak position). By comparing these energies, principally with values obtained from quantum chemical calculation (conducted at the Prof. Dr. Andreas Dreuw group of the Interdisziplinäres Zentrum für Wissenschaftliches Rechnen at the Universität Heidelberg), the detected loss features are assigned to different electronic transitions.

3. Results and Discussion

3.1. Influence of N-introduction on the Adsorption and Electronic Properties of Pentacene Derivatives

In this section, the influence of N-introduction on the adsorption and electronic properties of pentacene and its derivatives adsorbed on Au(111) is studied by using TPD, vibrational and electronic HREELS. The investigated molecular systems include linear 6,13-diazapentacene (DAP, Figure 3.1 (a.2)) and 6,7,12,13-tetraazapentacene (TAP, Figure 3.1 (a.3)) as well as arrow-shaped triisopropylsilyl-dibenzodiazapentacene (TIPS-BAP, Figure 3.1 (b.2)) and the corresponding (PAH) TIPS-dibenzodipentacene (TIPS-BP, Figure 3.1 (b.1)).

a)

1. X = Y = CH ; pentacene (PEN)
2. X = N , Y = CH ; 6,13-diazapentacene (DAP)
3. X = Y = N ; 6,7,12,13-tetraazapentacene (TAP)

b)

1. X = CH ; TIPS-dibenzopentacene   (TIPS-BP)
2. X = N ; TIPS-dibenzodiazapentacene (TIPS-BAP)
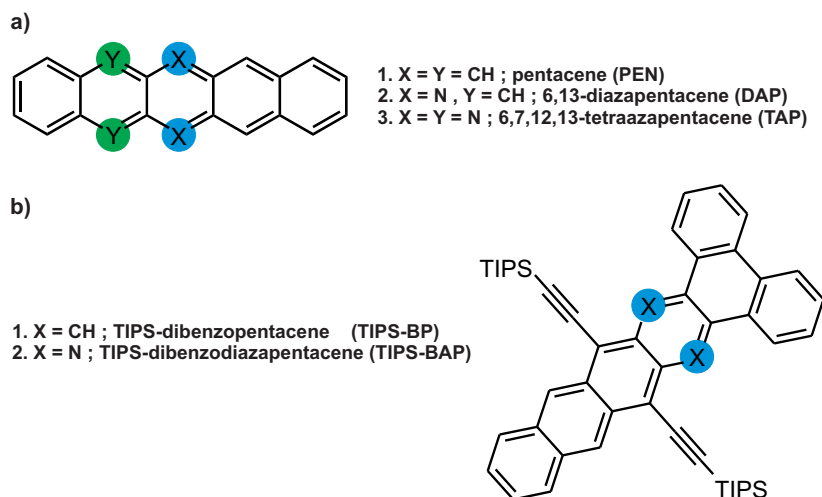
Figure 3.1.: Investigated molecular systems:(a) Pentacene (PEN, (1)), 6,13-diazapentacene (DAP, (2)) and 6,7,12,13-tetraazapentacene (TAP, (3)) as well as (b) TIPS-dibenzopentacene (TIPS-BP, (1)) and TIPS-dibenzodiazapentacene (TIPS-BAP, (2)).

The results from these investigations are presented in two subsections. In the first subsection, by comparing the obtained results for DAP and TAP with the

Results and Discussion

results from the previously studied parent pentacene (PEN, Figure 3.1 (a.1)), effect of N-introduction as well as number and position of the introduced nitrogen atoms on the properties of the given linear pentacenes are studied. In the second subsection, by comparing the obtained results for TIPS-BAP and TIPS-BP, influence of N-introduction on an arrow-shaped derivative of the silylethynylated pentacenes is investigated. Through these studies, it is determined that intact thin films of each molecule can be prepared via deposition at elevated temperatures into the ultra-high vacuum chamber and onto Au(111) substrate. All of the investigated molecules adopt a planar adsorption geometry in which the molecular backbone is oriented parallel with respect to the Au(111) surface. The assigned energies of the lowest excited electronic singlet states (S) as well as the first triplet states (T_1) indicate that N-introduction has three major effects on the electronic structure of the corresponding molecules. First, it results in a narrowing of the optical gap that can be summarized to a narrowing of 100 meV from 2.1 eV for PEN to 2 eV for DAP and by 500 meV to 1.6 eV for TAP, as well as a narrowing of 200 eV from 2.1 eV for TIPS-BP to 1.9 eV for TIPS-BAP. Second, a pronounced rise in the intensity of the α - band ($S_0 \rightarrow S_2$) for TIPS-BAP in comparison to TIPS-BP and going form PEN to DAP and then TAP, while at the same time the intensity of β - band ($S_0 \rightarrow S_9$ for DAP and $S_0 \rightarrow S_8$ for TAP) is reduced by going in the reverse order. Third, shift of the assigned $S_0 \rightarrow T_1$ transition to a higher energy by 300 meV from 0.9 eV for DAP and PEN to 1.2 eV for TAP.

3.1.1. Linear N-Heteropentacene Derivatives

The simple geometry of unsubstituted linear pentacenes makes this class of compounds a prime candidate for investigating the influence of N-introduction on the adsorption and electronic properties of OSC on metallic substrates. Therefore, in this study it was chosen to investigate the properties of adsorbed DAP and TAP on Au(111) surface.

DAP was first synthesized by VanAllan *et al.* in 1962[116]. Since then, the properties of this molecule have been investigated by a variety of theoretical and experimental methods[18;76;116–126]. According to Kummer *et al.*[125], DAP is not soluble in alcohol. Therefore, the electronic spectrum of the molecule was measured in chloroform ($CHCl_3$). The obtained optical gap for DAP from this measurement was reported to be 16000 cm^{-1} ($\approx$ 1.98 eV). Later UV/Vis measurements on DAP delivered a value of about 1.9 eV in dimethylformamide (DMF, $(CH_3)_2NC(O)H$)[126] and tetrahydrofuran (THF, $(CH_2)_4O$)[123] solutions as well as 1.8 eV (calculated from the absorption maxima) for a 40 nm-thick thin film of the molecule deposited on a quartz wafer[126] and about 2 eV for the molecule in *p*-terphenyl[120]. Considering that the optical gap of the parent pentacene is measured to be about 2.16 eV in the THF[123] and 2.1 eV in *p*-terphenyl[120], it can be estimated that N-introduction in DAP results in a narrowing of the optical gap up to 200 meV. The calculated energies of the frontier molecular orbitals of DAP indicates that upon N-introduction in the molecule in form of a pyrazine ring, the energy levels of HOMO and LUMO decreases in comparison to pentacene, while the HOMO-LUMO gap remains unchanged[118] (see Figure 3.2 (a)). As for TAP, the reported optical gap of the molecule in chloroform is 14800 cm^{-1} ($\approx$ 1.83 eV)[125]. Therefore, according to the obtained values from literature, introduction of four nitrogen atoms into the backbone of TAP, leads to a further narrowing of the optical gap by approximately 150 meV from 1.98 eV for DAP to 1.83 eV for TAP as measured in chloroform solution.

The packing motifs of both DAP and TAP are also affected by N-introduction[18;121]. It has been reported that both molecules adopt a geometry, in which π-planes of the molecules are stacked with an offset relative to each other and are shifted laterally relative to the neighbouring molecule[18] (see Figure 3.2 (c)). A computational study on the crystalline packing of pentacene and its derivatives, suggests that in case of DAP, the molecular geometry exhibits a "criss cross" packing motif, in which parallel stacks of the molecule are

Results and Discussion

twisted relative to each other[121]. The difference in the packing motif of DAP from the characteristic herringbone packing of pentacene (see Figure 3.2 (b)) is attributed to formation of strong and localized electrostatic interactions or in some cases hydrogen bonds in heteropentacenes, due to high electronegativity of the introduced heteroatoms such as nitrogen in the backbone of the molecule, which interferes with the uniform electrostatic potential at the periphery of pentacene[121]. Measured X-ray diffraction (XRD) of DAP from its crystalline powder indicates that molecules in the crystal adopt a face-to-face stacking geometry, in which the π-planes of the molecule are shifted across the long molecular axis[126]. Contrary to DAP, the crystallographic analysis of TAP revealed that its single crystal is formed from one-dimensional columns of the molecules, that are arranged in a slip-stacking geometry[127] (see Figure 3.2 (d)).
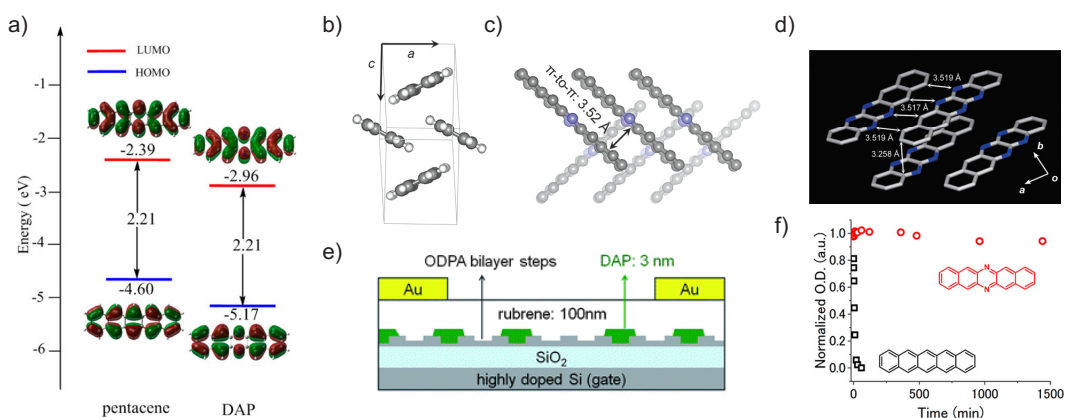
Figure 3.2.: (a) Calculated energy levels of HOMO and LUMO (at the B3LYP/6-31G(d) level) of pentacene (PEN) and DAP, adapted from Ref.[118]. Different packing motifs; (b) Herringbone (PEN), (c) Stacked π-planes with an offset (DAP), adapted from Ref.[18] and (d) Stacked slipped π-planes with an offset (TAP), adapted from Ref.[127]. (e) Schematic of rubrene based OTFTs with DAP as a template on octadecylphosphonic acid (ODPA)-treated SiO_2, adapted from Ref.[126]. (f) Stability of PEN and DAP under ambient conditions obtained from time dependent optical density measurements on THF suspensions of the molecules at their absorption peaks, adapted from Ref.[123].

Liu *et al.*[126] were first to report on the performance of DAP as an active material in organic thin film transistors (OTFTs). The results from their research indicate that DAP act as a p-type semiconductor, with an ambient air field effect mobility in the range of $10^{-5}\text{cm}^2\text{V}^{-1}\text{s}^{-1}$. The low hole mobility of DAP is attributed to the low-energy level of HOMO, that is estimated to

be -5.56 eV as well as the instability of the cation. As for TAP, it has been reported that thin film of the molecule behaves as n-type semiconductor with a field-effect mobility of $3.8 \times 10^{-5} cm^2V^{-1}s^{-1}$ [127]. Additionally, N-introduction also improves the stability of the molecule[128]. The stability measurements carried out on THF suspensions of pentacene and DAP indicate that under ambient light and air conditions, half life time of DAP is much longer (>1500 min) than of pentacene (<5 min)[123] (see Figure 3.2 (f)).

Even though, DAP is not a suitable organic semiconductor for use as an active material in OFETs, due to its low field-effect mobility, other properties of this molecule has made it a promising candidate for use in a variety of applications. It is reported that in rubrene based OTFTs, using DAP as a template for rubrene in the active channel, results in increased crystallization of the rubrene, which otherwise suffers from low crystallinity (see Figure 3.2 (e)). Thus, fabricating an OTFT with polycrystalline rubrene thin film that exhibits an increased field-effect mobility up to 0.68 $cm^2V^{-1}s^{-1}$. Interestingly, for this application, the low charge carrier mobility of DAP is desired, since a template should not contribute to the conductivity of the active channel[126]. A computational research by Bogatko *et al.*[120] suggests that DAP can be used as a target for continuous wave (CW) room-temperature MASER, potentially replacing pentacene, due to comparable $S_1 \rightarrow T_n$ intermolecular crossing rates of DAP and pentacene. Additionally, Kouno *et al.*[123] demonstrated that the superior air stability and polarizability of DAP in comparison to air-sensitive pentacene, makes DAP a favourable triplet polarizing agent for use in triplet dynamic nuclear polarization (triplet-DNP) method under ambient condition.

Overall, this short review of some of the reported properties for DAP and TAP suggests that N-introduction strongly affects the electronic structure, packing motifs and charge carrier mobility of the corresponding molecules. In this subsection, the results from the carried out TPD, vibrational and electronic HREELS measurements on DAP and TAP provide comprehensive insight into the adsorption and electronic properties of the molecules on Au(111), which adds to the cumulative knowledge of N-heteropentacenes. Some of the results presented in this subsection are published in Ref.[129;130]. The presented results for PEN are reproduced from the conducted measurements by Dr. Friedrich Maaß.

The molecules were synthesized by Dr. Hilmar Reiss (DAP) and Olena Tverskoy (TAP) of the Prof. Dr. Uwe H. F. Bunz group of the Organisch-

Results and Discussion

Chemisches Institut at the Universität Heidelberg.

For this study, DAP and TAP samples were prepared *in situ* by deposition of the corresponding molecules at 460 K (DAP) and 490 K (TAP) into the UHV chamber and onto Au(111) substrate, held at room temperature (300 K). First, through coverage dependent and fragment-mass-resolved TPD measurements, the possibility of preparing thin films and well-defined monolayers of the molecules on Au(111) surface is investigated and second, the influence of N-introduction on the adsorption properties of the molecules within the thin film and at the interface with Au(111) is explored.

Figure 3.3 (a) shows the coverage dependent TPD spectra of DAP with different initial coverages ranging from 1.5 ML to 5 ML for the selected mass-to-charge ratio of 140 m/z (the structure formula is depicted in Figure 3.3 (a)), which corresponds to the half of the mass of the parent molecular ion (m=280 amu). The spectra consist of two desorption regions. The first region includes a desorption peak at approximately 380 K (α_1), which exhibits a zero-order desorption kinetic and does not saturate with increasing coverage. Therefore, α_1 is assigned to the desorption of a multilayer coverage[129]. The second region includes a desorption peak at approximately 440 K (α_2), which is followed by a broad desorption feature (α_3) extending from 470 K to 700 K. The α_2 peak can be assigned to the desorption of a more densely packed compressed phase[129] as previously reported for benzene[110;131] and other aromatic organic molecules adsorbed on coinage metal surfaces[132–138]. Consequently, α_3 is attributed to the desorption of a sub-monolayer coverage[129]. Thus, the desorption spectrum of monolayer coverage can be defined as a spectrum, in which both α_2 and α_3 are saturated. The inset shows the enlarged monolayer desorption region of the measured spectrum with the coverage of 5 ML, extending from 410 K to 700 K. In this study, the coverage of the adsorbed molecules on the substrate is determined by integrating a measured TPD spectrum and comparing the area of the monolayer desorption region (α_2 and α_3) with the total integral[110].

The spectrum of DAP resembles the one obtained for the adsorbed PEN on Au(111)[49]. However, upon a closer comparison of the overlaid spectra of DAP (3 ML) and PEN (2.7 ML) (see Figure 3.3 (c)), it becomes evident that N-introduction in DAP results in a shift of the desorption feature associated with the compressed phase (α_2) to a higher temperature by 40 K from 396 K for PEN to 436 K for DAP. Additionally, the sub-monolayer desorption feature (α_3) of DAP extend beyond the desorption temperature of the same
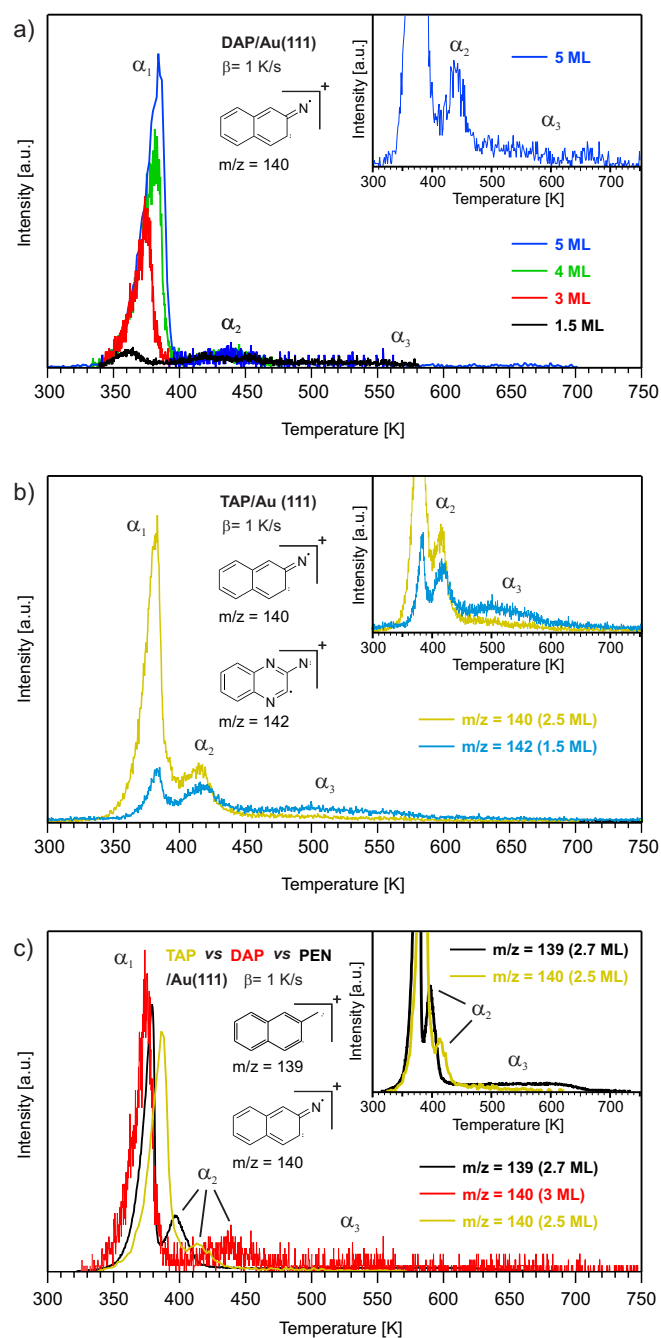
Figure 3.3.: TPD spectra of (a) DAP for the selected mass-to-charge ratio (m/z) of 140 with different initial coverages (adapted from Ref.[129]) and (b) TAP for the selected m/z of 140 and 142 adsorbed on Au(111), measured with a heating rate of $\beta = 1\ K/s$. (c) Shows an overlay of the TPD spectra of PEN, DAP and TAP. The desorption features are labelled with α_1, α_2 and α_3. The insets show the compressed phase (α_2) and the sub-monolayer desorption tail (α_3). The structural formulas of the selected ionic fragments from each molecule are depicted in their corresponding figures.

coverage for PEN by approximately 30 K and ends at 700 K. These observations clearly indicate that introduction of nitrogen atoms into the backbone of DAP leads to an increase in adsorbate/substrate-interactions, which in turn result in an increased desorption temperature of the monolayer coverage. In contrast, the multilayer coverages of both molecules desorb at approximately similar temperatures (α_1) and exhibit similar zero-order desorption kinetic. Therefore, it can be concluded that the influence of N-introduction on the adsorbate/adsorbate-interactions of the molecules in the thin film of DAP, in comparison to the same coverage of PEN is negligible.

In case of TAP (m=282 *amu*), the measured TPD spectra for selected ionic fragments of the molecule (m/z = 140 and m/z = 142, the structure formulas are depicted in Figure 3.3 (b)) with coverages of 2.5 ML and 1.5 ML also include three desorption features, labelled with α_1, α_2 and α_3 as shown in figure 3.3 (b). Overall, the spectrum of TAP follows a similar trend as the spectrum of DAP, in which the desorption from the multilayer coverage (α_1) is followed by the desorption from the compressed phase (α_2) and subsequently, the sub-monolayer coverage (α_3). However, the overlay of the desorption spectra of DAP (3 ML) and TAP (2.5 ML) reveals that for TAP, the α_2 peak is shifted by about 23 K to a lower temperature at 413 K, when compared to DAP as shown in figure 3.3 (c). Moreover, the DAP sub-monolayer desorption feature (α_3) is broader and extend up to 700 K, whereas for TAP, the desorption of sub-monolayer coverage ends at 600 K. This indicates that introduction of two additional nitrogen atoms into the backbone of TAP at the 7 - and 12 - positions does not directly translate into stronger adsorbate/substrate-interaction.

The fragment-mass-resolved TPD spectra of DAP and TAP provides further insight into the adsorption properties of the molecules on Au(111) (see Figure B.1). For both molecules, the desorption features of the multilayer coverage (α_1), the compressed phase (α_2) and the sub-monolayer coverage (α_3) coincide at the same temperature for all of the selected fragments. This suggests that the molecules do not degrade during the TPD measurements. However, the determined coverages of both molecules from each of their fragments differs from the reference coverage of 9.5 ML (DAP) and 5 ML (TAP) as measured for 140 *m/z*. This suggests that by increasing the substrate temperature up to 750 K, DAP and TAP molecules may have not been desorbed completely from the Au(111) surface. Indeed, a subsequent vibrational HREELS measurements

on DAP and TAP revealed, that even after heating the prepared samples up to 750 K, vibrational peaks associated with the adsorbates can still be detected in the measured vibrational spectra of both molecules (see Figure B.2 (a) and (c)). In case of a complete and intact desorption of any adsorbates from the Au(111) substrate, the post desorption HREELS spectra of the sample should, ideally, resembles the spectra of a pristine Au(111) substrate (see Figure A.1). Given that this is not the case for the DAP and TAP samples, it can be concluded that the molecules does not desorb completely. Therefore, the determined coverages of either molecule are only an estimation ($\pm$ 0.5 ML). Whether the remaining adsorbates on the substrate surface are intact molecules, consists of their fragments or a combination of both, can not be determined, since the observed vibrations can not be assigned to any vibrational modes associated with either molecules with high level of certainty. It should also be noted that PEN undergoes a complete desorption from the substrate[49].

According to the results obtained from the conducted TPD measurements on the adsorbed molecules, it was chosen to prepare the monolayer coverage of the DAP and TAP samples by depositing a large amount of molecules adding up to a multilayer coverage and subsequently heating the samples up to 400 K (DAP) and 404 K (TAP) in order to desorb the higher laying layers, while preserving the monolayer coverage. The used parameters for preparing the samples are given in table H.1.

In the following, angle-resolved vibrational HREELS is utilized to further investigate the influence of N-introduction in DAP and TAP on the adsorption geometry of the molecules on Au(111). Figure 3.4 shows the vibrational spectra of DAP (left) and TAP (right), for mono - (a and d) and multilayer (b and e) coverages, measured in specular (black spectra) and off-specular (red spectra) electron scattering geometry along with the calculated intensities and frequencies of vibrational modes possessing a dynamic dipole moment perpendicular to the molecular backbone (c and f).

The spectra of DAP at the mono - and multilayer coverage include four pronounced vibrations with high intensity ratio between the specular and off-specular scattered electrons (see Figure 3.4 (a) and (b)), which is in consistent with dipole-active vibrations. By comparing the results from the vibrational spectra with the calculated intensities and frequencies of B_{3u} vibrational modes of the corresponding D_{2h} molecular point group in the gas phase (see Figure 3.4 (c)), the identified dipole-active vibrations are assigned to the out-of-plane

Results and Discussion

γ(C-N-C) and γ(C-C-C) (at 369 and 482 cm^{-1}) as well as γ(C-H) modes (at 731 and 863 cm^{-1})[129]. Additionally, the spectra also include vibrations at around 3000 cm^{-1} with only a small difference between the intensities of the specular and off-specular scattered electrons. This indicates that the main excitation mechanism of these vibrations is impact scattering and as such they correspond to the non-dipole-active vibrations and are assigned to the in-plane ν(C-H) stretching mode[129]. The results from DFT calculations also indicate that the assigned dipole-active vibrations posses a dynamic dipole moment perpendicular to the molecular plane (x-direction)(see Figure 3.5), while the dynamic dipole moment of the assigned non-dipole-active vibrations is parallel with the molecular plane along the long axis (z-direction)[129] (see Figure B.3). Table 3.1 provides more details on the assignment of the identified vibrations of DAP.

By comparing the measured mono - and multilayer spectra of DAP, it becomes evident that with increasing the coverage to 4 ML, thus decoupling the molecules at higher layers from the metallic substrate, the overall intensity of the γ(C-N-C), γ(C-C-C) vibrations slightly increases relative to the rest of the spectrum. Considering that the spectra of DAP at mono - and multilayer coverage consists of predominantly dipole-active vibrations with large components of their dipole moment perpendicular to the Au(111) surface, it can be concluded that at mono- and multilayer, DAP molecules adopt a planar adsorption geometry on Au(111), in which the molecular backbone of the adsorbates are oriented parallel with the substrate surface[129]. Given that PEN also adopts a similar adsorption geometry on the Au(111) surface[95], it can be concluded that N-introduction in 6 - and 13 - positions of DAP backbone does not result in a change in the adsorption geometry of the molecule.

As for TAP, the spectrum of the monolayer coverage (see Figure 3.4 (d)) is dominated by a high intensity dipole-active vibration assigned to the out-of-plane γ_ω(C-H) wagging mode (at 753 cm^{-1}), which is accompanied by other dipole-active vibrations, assigned to the out-of-plane γ_τ(N-C-N) twisting and γ_ω(C-H) wagging modes (at 472 and 844 cm^{-1}) as well as four non-dipole-active vibrations assigned to the in-plane δ(C-H) scissoring, ν(C-C), ν(C-N) and ν(C-N) stretching modes (at 1131, 1283, 1470 and 3056 cm^{-1})[130].
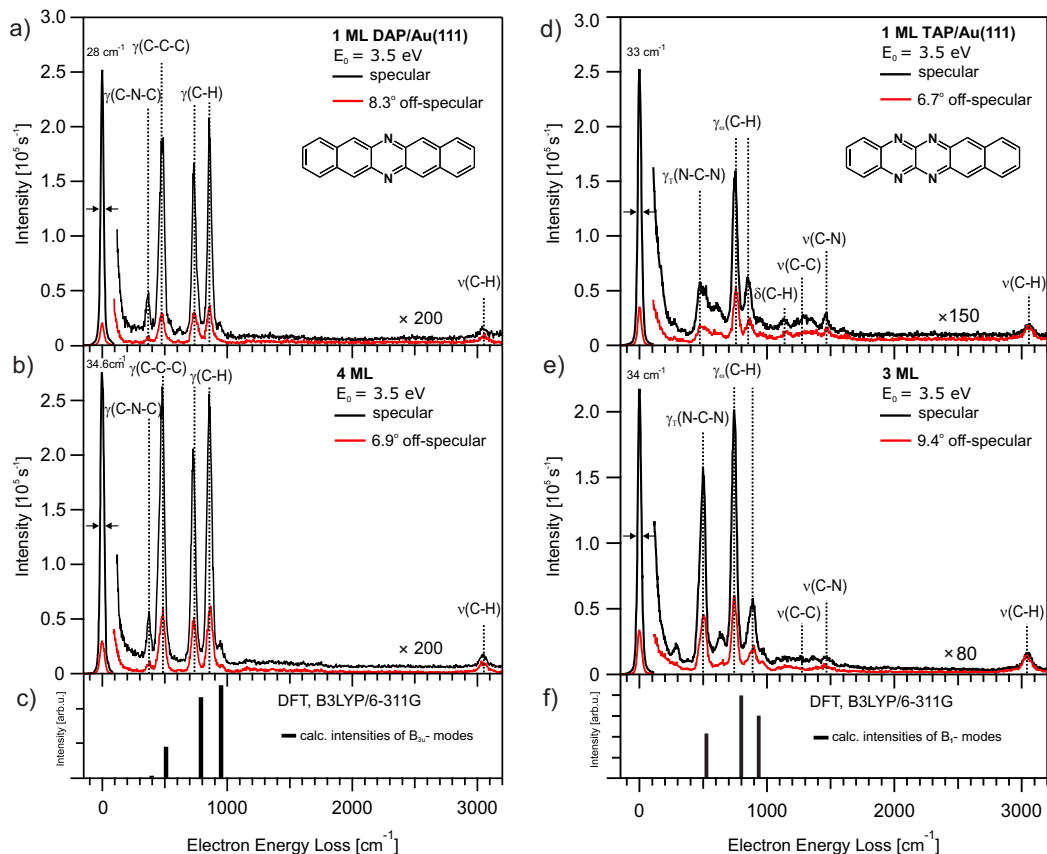
Figure 3.4.: Vibrational HREELS spectra of DAP (Left) and TAP (right) measured in specular (black spectra) and off-specular (red spectra) scattering geometry for mono - (a and d) and multilayer (b and e) coverages adsorbed on Au(111) with the associated DFT-calculations (B3LYP/6-311G) for intensities and frequencies of B_{3u} and B_1 symmetric vibrational modes with a dynamic dipole moment perpendicular to the molecular plane (c and f). E_0 is the primary energy of the incident electrons. The energy resolution of the specular spectra is measured as the full width at half maximum (FWHM) of the elastic peak (zero energy loss peak) and is given in wavenumbers (cm^{-1}). The assigned vibrations are listed in table 3.1. Adapted from Ref. [129;130].

By increasing the coverage of TAP to 3 ML, the overall intensity of the dipole-active vibrations, particularly the one assigned to γ_τ(N-C-N) twisting mode (at 498 cm^{-1}) are increased relative to the rest of the spectrum (see Figure 3.4 (e)). In contrast, aside from ν(C-H) stretching mode (at 3049 cm^{-1}), the intensity of other non-dipole-active vibrations, ν(C-C) and ν(C-N) stretching modes (at 1263 and 1453 cm^{-1}) are reduced. Additionally, the vibration, previously assigned to δ(C-H) scissoring mode can not be detected in the multilayer spectrum. The out-of-plane γ_τ(N-C-N) vibration originates from the

Results and Discussion

N-C-N bonds. Therefore, it can be assumed that at the monolayer coverage, due to strong interactions between the nitrogen atoms in the backbone of TAP and the Au(111) substrate, the intensity of this particular vibration is suppressed[130]. At the multilayer coverage, higher layers are decoupled from the substrate, thus the N-C-N bonds can vibrate freely, which results in an intensity rise of γ_τ(N-C-N) vibration. This assumption is supported by the blue-shift of this mode from 472 cm^{-1} (for 1 ML) to a higher vibrational frequency at 498 cm^{-1} (for 3 ML)[130]. A similar shift is also observed for the γ_ω(C-H) wagging mode (at 844 cm^{-1} in 1 ML) by 44 cm^{-1} to 888 cm^{-1} in 3 ML. The assigned vibrations of TAP belong to the irreducible representation, B$_1$ of the C$_{2v}$ molecular point group symmetry, in which the dipole-active vibrations posses a dynamic dipole moment perpendicular to the molecular plane (x-direction)(see Figure 3.5), while the dynamic dipole moment of the non-dipole-active vibration is parallel with the molecular plane along the long axis (z-direction)[130] (see Figure B.3). Table 3.1 provides more details on the assignment of the the identified vibrations of TAP.

Considering that the dominant vibrations, as detected in the spectra of TAP at mono - and multilayer coverages are dipole-active with large components of their dipole moment perpendicular to the Au(111) surface, it can be concluded that at mono- and multilayer coverage, TAP similar to DAP adopts a planar adsorption geometry on Au(111), in which the molecular backbone of the adsorbates are oriented parallel with the substrate surface[130]. This conclusion also applies to the adsorption geometry of both molecules at their sub-monolayer coverages (see Figure B.2 (b) and (e)). This indicates that introduction of two additional nitrogen atoms to the backbone of TAP at 7 - and 12 - positions does not results in a change in the adsorption geometry of the molecule in comparison to DAP or PEN on Au(111) surface.

30

Table 3.1.: Assigned vibrations (in cm^{-1}) of DAP and TAP adsorbed on Au(111) for different coverages. Additionally, the corresponding DFT calculated frequencies of the molecules in the gas-phase at the B3LYP level and the 6-311G basis set are given. Dipole active modes are labelled with *da*. The identified modes for each vibration are described with the following abbreviations; γ – out-of-plane; δ – scissoring; ν – stretching; τ – twisting; ω – wagging. Representation (Repr.) of the associated point groups and the orientation of the calculated dipole derivative vector with respect to the molecular geometry, x, perpendicular to the molecular plane; y, short axis and z, long axis of molecular backbone for each mode are listed. Adapted from Ref. [129;130].

DAP

#	Subm.	1 ML	4 ML	DFT	Mode	Repr.
1	367 *da*	368 *da*	369 *da*	399	γ(C-C-C), γ(C-N-C)	B$_{3u}$(x)
2	470 *da*	472 *da*	482 *da*	512	γ(C-C-C), γ(C-N-C)	B$_{3u}$(x)
3	729 *da*	736 *da*	731 *da*	772	γ(C-H)	B$_{3u}$(x)
4	851 *da*	849 *da*	863 *da*	928	γ(C-H)	B$_{3u}$(x)
5	3034	3035	3043	3198	ν(C-H)	B$_{2u}$(z)

TAP

#	Subm.	1 ML	4 ML	DFT	Mode	Repr.
1	473 *da*	472 *da*	498 *da*	524	γ_τ(N-C-N), γ_ω(C-H)	B$_1$(x)
2	761 *da*	753 *da*	740 *da*	798	γ_ω(C-H)	B$_1$(x)
3	874 *da*	844 *da*	888 *da*	935	γ_ω(C-H)	B$_1$(x)
4	1145	1131	-	1206	δ(C-H)	A$_1$(z)
5	1287	1283	1263	1333	ν(C-H), δ(C-H)	A$_1$(z)
6	1471	1470	1453	1449	ν(C-N), ν(C-C), δ(C-H)	A$_1$(z)
7	–	3056	3049	3172	ν(C-H)	A$_1$(z)
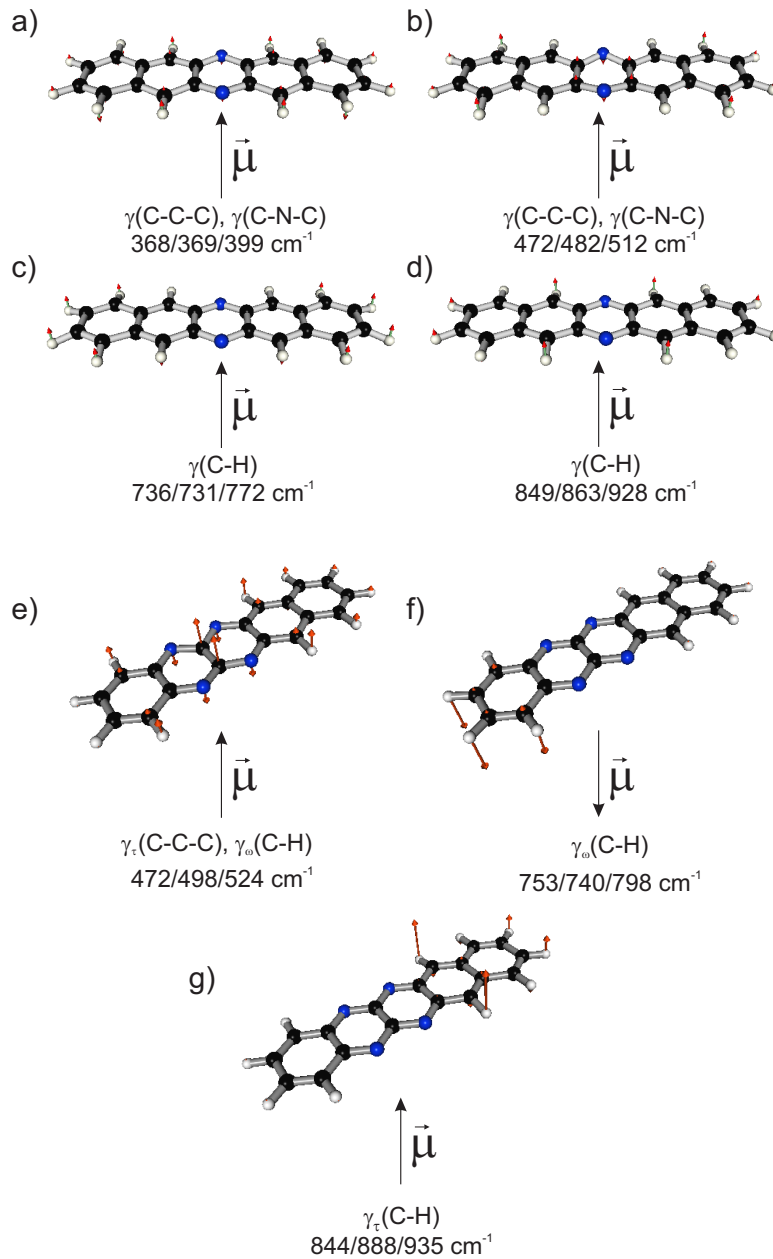
Figure 3.5.: Visualisation of the assigned dipole-active vibrational modes obtained from the DFT calculations (B3LYP/6-311G) for DAP (a-d) and TAP (e-g). The corresponding energies (HREELS monolayer/HREELS multilayer/DFT) are given in wavenumbers (cm^{-1}). The direction of the calculated dipole derivative unit vector ($\vec{\mu}$) is depicted with a black arrow that lies in the plane of the paper. The atomic displacements in each visualization are shown with red arrows. The vibrational modes are visualized by the Facio software [139]. Adapted from Ref. [129;130].

3.1. Influence of N-introduction on the Properties of Pentacene Derivatives

Finally, the electronic HREELS is utilized to investigate the influence of N-introduction in DAP and TAP on the electronic properties of the molecules in comparison to PEN, at the interface with Au(111) and within their thin film. Figure 3.6 shows the electronic HREELS spectra of DAP (left) and TAP (right), for mono - (a and c) and multilayer (b and d) coverages measured with the primary electron energy of 15 eV, together with the corresponding UV/Vis spectra of the molecules measured in chloroform ($CHCl_3$) solution (orange spectra).
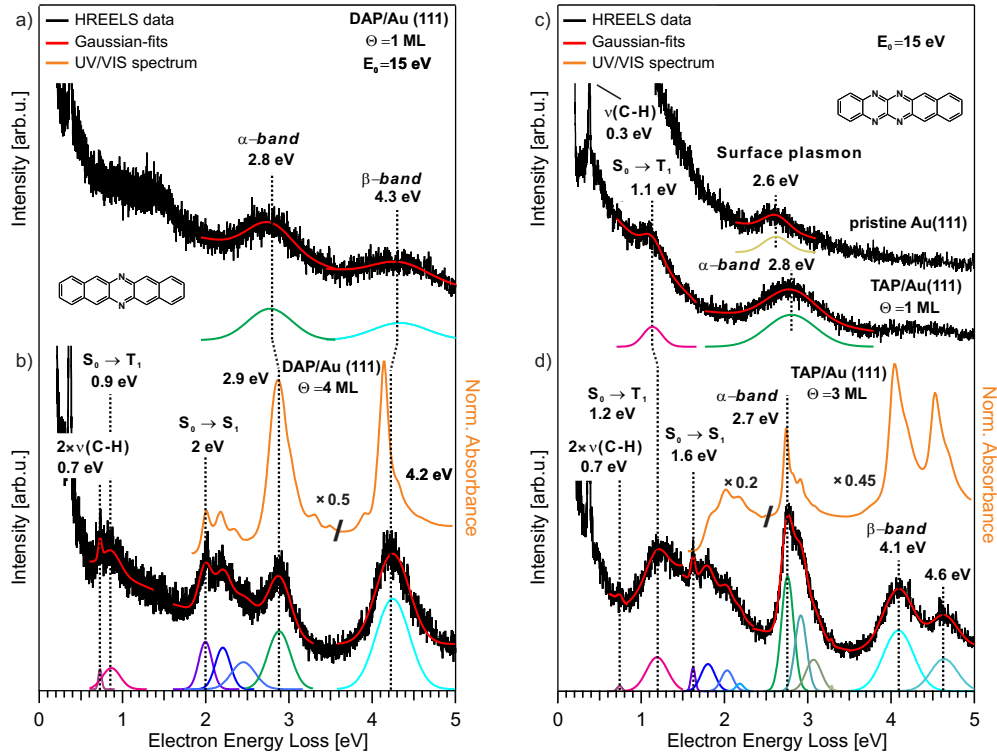
Figure 3.6.: Electronic HREELS spectra of adsorbed DAP (Left) and TAP (right) on Au(111), measured for mono - (a and c) and multilayer (b and d) coverages (black spectra). The electronic loss features were fitted using Gaussian functions (red curves). The corresponding UV/Vis spectra of the molecules are measured in chloroform ($CHCl_3$) (orange spectra). E_0 is the primary energy of the incident electrons. Θ is the coverage in monolayer (ML). Adapted from Ref.[129;130].

The monolayer spectrum of DAP consists of two broad electronic energy loss features at 2.8 and 4.3 eV as shown in figure 3.6 (a). Noticeably, the detected energy of these transitions differ from the expected contribution from the conventional Au(111) surface plasmon (at 2.5 eV) at a monolayer cover-

Results and Discussion

age[140] (see Figures 3.6 (c) and A.1). Therefore, it can be assumed that the loss features originate from the electronic transitions of DAP.

At the coverage of 4 ML, DAP is decoupled from the metallic substrate, which leads to detection of other loss features associated with the molecular electronic transitions in the corresponding spectrum as shown in figure 3.6 (b). This spectrum includes a contribution from an overtone of the in-plane ν(C-H) stretching mode vibration at approximately 0.7 eV (at around 3000 cm^{-1} in Figure 3.4 (b)), which is followed by a weak loss feature at 0.9 eV. At higher energies, the loss feature at 2 eV is accompanied by the so-called acene fingers, that correspond to the vibronic excitations. The contributing vibrations to these excitations are the breathing modes of the molecular backbone, namely the symmetric ν(C-C) and ν(C-N) stretching modes of DAP with a frequency of around 1500 cm^{-1} (186 meV). The loss feature at 2 eV is assigned to the transition of a ground state (S_0) to the first singlet excited state (S_1) and as such the optical gap of DAP[129]. The size of the optical gap is in good agreement with the one obtained from the 2PPE measurements (1.93 eV) on a multilayer coverage (3 ML) of the molecule[129]. The difference of 70 meV between the two values lies within the estimated error of the measurements. Moreover, by utilizing the excited-state calculations in the gas phase, the other loss features at 2.9 and 4.2 eV are assigned to the transition of S_0 to other singlet excited states, S_4 (α - band) and S_9 (β - band)[129]. The energetic positions of the detected broad loss features (at 2.8 and 4.3 eV) at the monolayer coverage are close to the ones assigned to the α - and β - band at the multilayer coverage and as such they are also assigned to the same transitions. Similarly, the detected broad loss feature (at 2.7 eV) in the sub-monolayer coverage of the molecule is assigned to the α - band (see Figure B.4 (a)).

The remaining unassigned loss feature at 0.9 eV is located beneath the assigned $S_0 \rightarrow S_1$ transition of the molecule (at 2 eV) and is in good agreement with the known transition energy of the first triplet excited state (T_1) of parent pentacene at 0.86 eV[141] and coincides with the assigned $S_0 \rightarrow T_1$ transition of PEN at 0.9 eV as measured by electronic HREELS (see Figure 3.7 (c)). Therefore, the detected loss feature at 0.9 eV is assigned to $S_0 \rightarrow T_1$ transition of DAP[129]. It should also be noted that further excited-state calculations on DAP predict a higher value of 1.22 eV for the vertical excitation energy of T_1[129]. The obtained experimental value of 0.9 eV for the transition energy of T_1 satisfies the energetic criteria for an efficient singlet fission process, i.e.

$2E(T_1) < E(S_1)$, when compared to the value of S_1 (2.0 eV)[129]. Therefore, in DAP one singlet exciton can theoretically split into two triplet excitons[142;143].

A comparison between the multilayer HREELS spectra of DAP and PEN revels that introduction of nitrogen atoms into the backbone of DAP results in a negligible narrowing of the optical gap by 100 meV from 2.1 eV for PEN to 2 eV for DAP (See Figure 3.7 (b) and (c)). This effect is attributed to the stabilization of the valence molecular orbitals by nitrogen atoms with high electronegativity[129]. Similar observations have also been made for a variety of N-heteroacenes and their derivatives[24;51;144]. Additionally, the β - band as detected in the spectrum of DAP is shifted by 100 meV to a higher energy. Most noticeably, the spectrum of DAP exhibits a pronounced rise in the intensity of the α - band.

In case of TAP, the monolayer spectrum of the molecule consists of a contribution from the in-plane ν(C-H) stretching mode vibration at approximately 0.3 eV (at around 3000 cm^{-1} in Figure 3.4 (d)), a weak loss feature at 1.1 eV and a broad loss feature at 2.8 eV as shown in figure 3.6 (c). By increasing the coverage of TAP to 4 ML, thus decoupling the molecule from the metallic substrate, the previously detected loss features in the monolayer spectrum, become even more pronounced in the spectrum of the multilayer coverage and shift to 1.2 eV and 2.7 eV (see Figure 3.6 (d)). Other contributions to the spectrum include an overtone of the in-plane ν(C-H) stretching mode vibration at approximately 0.7 eV (at around 3000 cm^{-1} in Figure 3.4 (e)) and other loss features associated with the molecular electronic states, which appear at 1.6 eV, 4.1 eV and 4.6 eV. The loss feature at 1.6 eV, which is accompanied by a vibrational contribution is assigned to the $S_0 \rightarrow S_1$ transition and accordingly, the optical gap of TAP[130]. The vibrational contribution associated with $S_0 \rightarrow S_1$ transition can be attributed to the symmetric ν(C-C) and ν(C-N) stretching modes with a frequency of around 1500 cm^{-1} (186 meV)[130]. The loss feature at 1.1 eV in the monolayer and 1.2 eV at the multilayer coverage are both located beneath the assigned $S_0 \rightarrow S_1$ transition of the molecule (at 1.6 eV) and are energetically close to the previously assigned transition energy of T_1 for PEN and DAP at 0.9 eV. Therefore, the loss feature in question is assigned to the $S_0 \rightarrow T_1$ transition of TAP[130]. The results from further excited-state calculations on TAP also suggests that the excitation energy of T_1 is 1.32 eV, which is in good agreement with the experimental result, when the error and limitations associated with the calculations are considered[130].
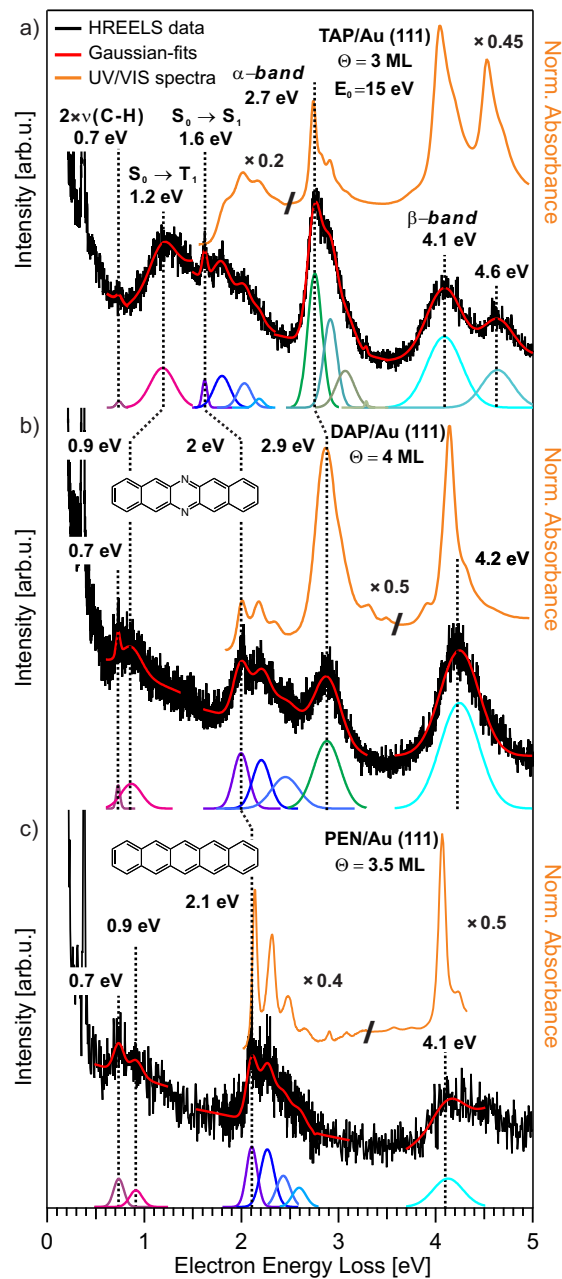
Figure 3.7.: Electronic HREELS spectra of adsorbed (a) TAP, (b) DAP and (c) PEN on Au(111) measured for the multilayer coverage (black spectra). The electronic loss features were fitted using Gaussian functions (red curves). The corresponding UV/Vis spectra are measured in chloroform ($CHCl_3$) solution (orange spectra). E_0 is the primary energy of the incident electrons. Θ is the coverage in monolayer (ML). Adapted from Ref.[129;130].
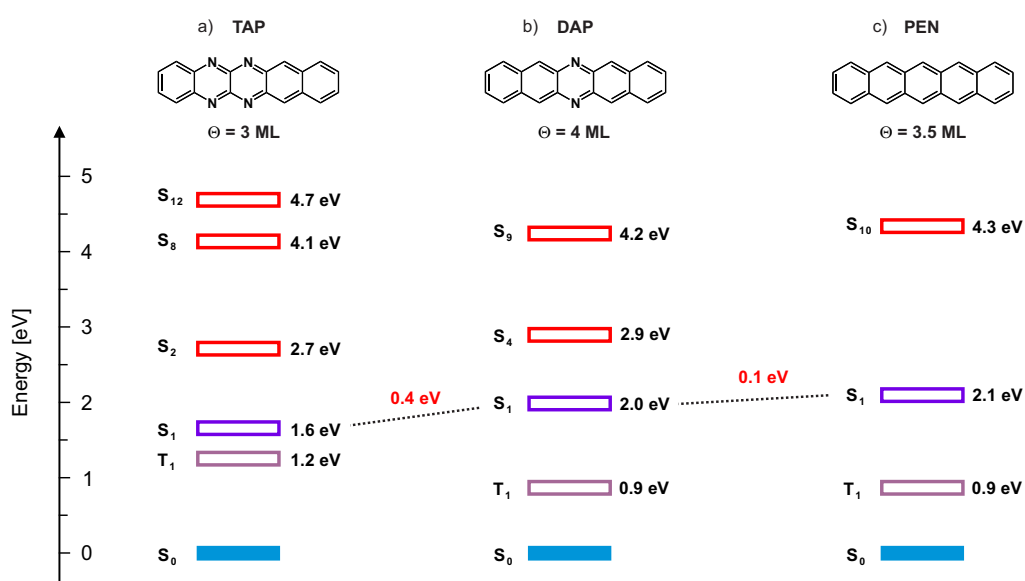
Figure 3.8.: The identified and assigned energies of electronic transitions of the singlet (S) and the first triplet (T_1) states via electronic HREELS for (a) 3 ML of TAP,(b) 4 ML of DAP, and (c) 3.5 ML of PEN adsorbed on Au(111). Adapted from Ref. [130].

Results and Discussion

The obtained experimental values for T_1 (1.2 eV) and S_1 (1.6 eV) indicates that, $2E(T_1) > E(S_1)$. Therefore, in contrast to DAP, in TAP it is not energetically possible to split one singlet exciton into two triplet excitons and as such an efficient singlet fission process for this molecule is not achievable[130]. Moreover, with the help of the DFT calculations, other loss features at 2.7, 4.1 and 4.6 eV are assigned to the transition of S_0 to the excited states at S_2 (α - band), S_8 (β - band) and S_{12}, accordingly[130]. Considering these assignments, the detected broad loss feature at 2.7 eV in the sub-monolayer coverage of the molecule is assigned to the α - band (see Figure B.4 (b))

A comparison between the measured spectrum of DAP and TAP at the multilayer coverage reveals that introduction of four nitrogen atoms into the backbone of TAP significantly alters the electronic structure of the molecule (see Figure 3.7 (a)). The N-introduction results in a narrowing of the optical gap by 400 meV from 2 eV for DAP to 1.6 eV for TAP. A similar shift to a lower energy can also be observed for the α - band by about 200 meV from 2.7 eV for TAP to 2.9 eV for DAP. In contrast, the excitation energies of the β - band does not change significantly (about 100 meV) going from 4.2 eV for DAP to 4.1 eV for TAP. Additionally, the assigned $S_0 \rightarrow T_1$ transition is shifted to a higher energy by 300 eV from 0.9 eV for DAP to 1.2 eV for TAP.

Interestingly, the assigned $S_0 \rightarrow S_{12}$ transition of TAP at 4.6 eV is absent in the measured spectra of DAP and PEN. A similar transition has also been observed in the measured electronic spectra of other linear N-heteroacenes with C_{2v} symmetry including benzo[g]quinoxaline, benzo[b]phenazine and naphtho[2,3-b]phenazine. In contrast, molecules with D_{2h} symmetry such as DAP, phenazine and quinoxalino[2,3-b]quinoxaline do not exhibit such transition in their spectra. Considering that the transition in question also does not appear in the spectra of the corresponding acenes, it is hypothesised[117] that asymmetric introduction of nitrogen atoms in the backbone of the N-heteroacenes reduces the symmetry of the given molecules, which results in formation of an electronic band, that in case of TAP is assigned to the $S_0 \rightarrow S_{12}$ transition.

All of the assigned transitions in the multilayer spectrum of TAP, DAP and PEN, except the assigned $S_0 \rightarrow T_1$ transitions are also present in the corresponding UV/Vis spectrum of the molecules in solution. Among these transitions, the ones assigned to the α - band, the β - band and $S_0 \rightarrow S_{12}$ are in good agreement with the detected transitions in the corresponding UV/Vis

spectra. A similar trend can also be observed for the detected $S_0 \rightarrow S_1$ transitions and their accompanied vibrational contributions in the multilayer spectrum of DAP and PEN. Therefore, it can be concluded that the influence of the metal substrate (adsorbate/substrate-interactions) and intermolecular forces (adsorbate/adsorbate-interactions) on the electronic states of DAP and PEN in the thin film compared to the solution is negligible. In contrast, the $S_0 \rightarrow S_1$ transition as detected in the HREELS spectrum of TAP, does not resemble its counterpart in the UV/Vis spectrum. This is evident from the shift of the $S_0 \rightarrow S_1$ transition from approximately 1.8 eV as measured from the first vibronic transition of the UV/Vis spectrum to 1.6 eV as determined via HREELS measurements. This deviation can be attributed to the influence of metal substrate and intermolecular forces on the electronic states of the molecule in the thin film in comparison to its solution.

The identified and assigned electronic transitions of TAP, DAP and PEN at multilayer coverage are summarized in figure 3.7 (d). The conducted 2PPE measurements on DAP provide further insight into the electronic structure of the molecule by determining the unoccupied and occupied single-electron states or the so called transport states (electron affinities and ionization potentials) of DAP as presented in Ref.[129].

Overall, the most striking deference between TAP, DAP and PEN is the observed pronounce rise of the α - band intensity in the spectra of the investigated N-heteropentacene molecules in comparison to the parent pentacene. This phenomena is attributed to an increase in the oscillator strength of a strongly correlated state (L_s) upon introduction of nitrogen atoms into the backbone of DAP and TAP[129;130]. This finding is the result of the quantum chemical calculations, which were conducted by Dr. Marvin Hoffmann of the Prof. Dr. Andreas Dreuw group of the Interdisziplinäres Zentrum für Wissenschaftliches Rechnen at the Universität Heidelberg. In the following, a summary of the results from the quantum chemical calculations is presented.

It has been reported that the two lowest optically allowed singlet excited states of DAP, S_1 and S_4, exhibit a typical $\pi\pi^*$ character[129;130] . The only conserved physical property of these states that can be determined by exciton analyses is the electron (e) and hole (h) correlation for the associated excitons. Depending on the strength of the e - h correlation, the given singlet excited states may correspond to a so called weakly (L_w) or strongly correlated states (L_s). The calculated correlation coefficients of S_1 and S_4, are 0.068 and 0.205.

Results and Discussion

Therefore, the exciton of S_1 exhibits a weaker e - h correlation and as such corresponds to a L_w state, while S_4 has a stronger correlated exciton and corresponds to a L_s state. By this definition, S_1 and S_4 of DAP correspond to the L_w (S_1) and L_s (S_2) states of TAP and PEN. Thus, the α - bands in DAP (S_4), TAP (S_2) and PEN (S_2) correspond to a strongly correlated state (L_s). As determined by quantum chemical calculations, upon N-introduction, the oscillator strength of the molecules increases from 0 for PEN to 0.2 for DAP and 0.45 for TAP. Interestingly, the intensity of the α - band for each molecule also increases parallel with the associated oscillator strength. Considering that other exciton properties of the L_s states for the given molecules remains approximately the same, it can be concluded that the increase in the oscillator strength leads to the rise in the intensity of the α - band. This trend is also evident from the simulated electronic absorption spectra of PEN, DAP and TAP (see Figure 3.9 (a)) and the results from the electronic HREELS measurement on the corresponding molecules (see Figure 3.7).
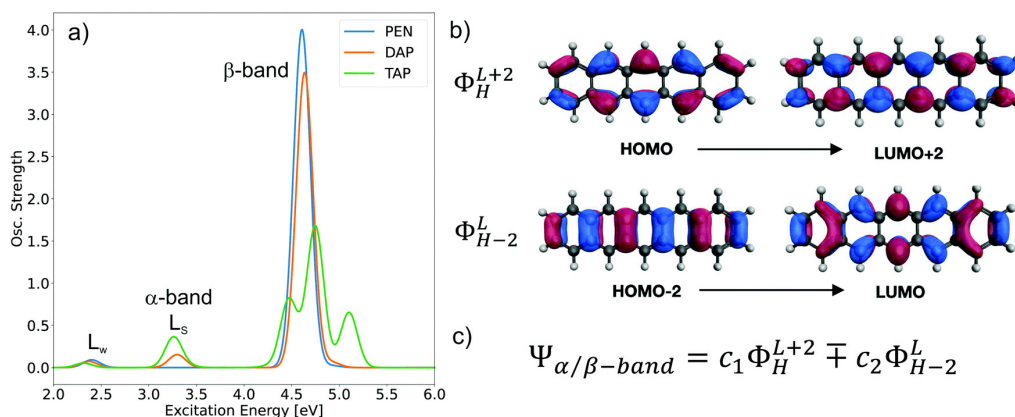
Figure 3.9.: (a) Electronic absorption spectra of PEN, DAP, and TAP, simulated at the ADC(2)/def2-SVP level of theory (FWHM=0.294 eV). (b) Molecular orbitals and the corresponding Slater-determinants ϕ. (c) The wave functions of the electronic states assigned to α - and β - bands, formed from linear combination of the associated Slater-determinants. Taken from Ref.[130].

As can be seen from the same electronic spectra, the pronounced rise in the intensity of the α - band upon nitrogen introduction is followed by a decrease in the β - band intensity. This trend is explained by further quantum chemical calculations, which indicates that the increase in the oscillator strength is also accompanied by an increase in the mixing ratio between the two particle–hole (p - h) basis states of the α - band (L_s). The p - h basis states are defined as the

linear combination of slater-determinants (Φ), which consists of the molecular orbitals associated with electronic transitions. The molecular orbitals involved in the slater-determinants, include a linear combination of HOMO - 2 to LUMO and HOMO to LUMO + 2 for PEN and DAP (see Figure 3.9 (b)) as well as a linear combination of HOMO - 1 to LUMO and HOMO to LUMO + 2 for TAP. The wavefunctions of the electronic states corresponding to α - (L_s) and β - band are given in figure 3.9 (c). For α - band (L_s), the wavefunction is equal to a negative and for β - band to a positive linear combination of the slater-determinants. Therefore, for an almost equal superposition of the given determinants, such as the case of PEN, their negative linear combination results in no oscillator strength for the α - band, while their positive linear combination gives all the oscillator strength to the β - band. In contrast, when the energies of the determinants are not equal, the same linear combinations results in a gain in oscillator strength for both α - and β - band. In case of DAP and TAP, this energy difference is mainly attributed to the effect of nitrogen atoms on the molecular orbital (MO) energies of the α - band (L_s state). Therefore, by increasing the energy difference between the determinants constituting the α - band upon nitrogen introduction, the intensity of the α - band increases with number of substituted nitrogen atoms, going from DAP to TAP, while simultaneously the intensity of the β - band decreases. These observations indicates that altering the MO energies by N-introduction can be used as a method for tuning the electronic structure of organic semiconductors. A detailed description of the carried out quantum chemical calculations on DAP, TAP and PEN and its findings is given in Ref. [129;130;145].

To summarize, in this subsection it has been demonstrated that thin films of two N-heteropentacene, DAP and TAP can be prepared through deposition of the corresponding molecules at 460 K (DAP) and 490 K (TAP) into the ultra-high vacuum chamber and onto Au(111) substrate held at room temperature (300 K). The prepared samples were then characterized by TPD, vibrational and electronic HREELS in combination with DFT calculations. Based on the results from the fragment-mass-resolved TPD measurements it was determined that during annealing of the samples, the DAP and TAP molecules remain intact. The results from the coverage dependent TPD measurements on both molecules indicate that N-introduction in DAP and TAP results in an increase in adsorbate/substrate-interaction for the given molecules in comparison to parent pentacene (PEN), while introduction of two additional nitrogen atoms

into the backbone of TAP does not lead to stronger interaction of the adsobates with the metallic substrate, when compared to DAP. Moreover, as shown via vibrational HREELS measurements, both DAP and TAP, at all coverages adopt a planar adsorption geometry on the Au(111) surface, in which the backbone of the molecule is oriented parallel with the substrate. Finally, through electronic HREELS measurements, it was determined that N-introduction in DAP and TAP affects the electronic structure of the molecules in three ways. First, the narrowing of the optical gap by 100 meV from 2.1 eV for PEN to 2 eV for DAP and by 500 meV to 1.6 eV for TAP, which is attributed to the stabilizes of the valence molecular orbitals by nitrogen atoms with high electronegativity. Second, the pronounced rise in the intensity of the α - band $(S_0 \rightarrow S_2)$ going form PEN to DAP and then TAP, while at the same time the intensity of the β - band $(S_0 \rightarrow S_9$ for DAP and $S_0 \rightarrow S_8$ for TAP) is reduced by going in reverse order and third, shift of the assigned $S_0 \rightarrow T_1$ transition to a higher energy by 300 meV from 0.9 eV for DAP and PEN to 1.2 eV for TAP as the result of altering the energies of the molecular orbitals by the introduced nitrogen atoms in the backbone of the N-heteropentacenes. Moreover, it is found that the asymmetric introduction of nitrogen atoms in TAP give rise to a new electronic transition at 4.6 eV $(S_0 \rightarrow S_{12})$, which is absent in the measured spectra of DAP and PEN.

3.1.2. Arrow-Shaped N-Heteropentacene Derivative

As demonstrated in the previous subsection, DAP and TAP are excellent prototype organic semiconductors for studying the adsorption and electronic properties of N-heteropentacenes. In this subsection, a derivative of this class of compounds, namely TIPS-BAP, is investigated in order to elucidate the influence of N-introduction on the adsorption and electronic properties of arrow-shaped silylethynylated pentacene.

The only other study concerning TIPS-BAP is published by Hoff *et al.*[20]. They were first to synthesized and study this molecule. Their study indicates that TIPS-BAP possess an optical gap of 1.92 eV in CH_2Cl_2 solution. The HOMO and LUMO energy levels of the molecule are estimated to be -5.56 eV and -3.64 eV. As such, it is argued that TIPS-BAP should function as an ambipolar semiconductor. Moreover, it has been reported that the molecules in a single crystal of TIPS-BAP from a brick-wall-like motif (see Figure 3.10), in which the molecules are arranged head-to-tail with a short distance between their planes. This suggests that TIPS-BAP could be a suitable semiconductor for use as active material in organic based (opto)electronic applications.
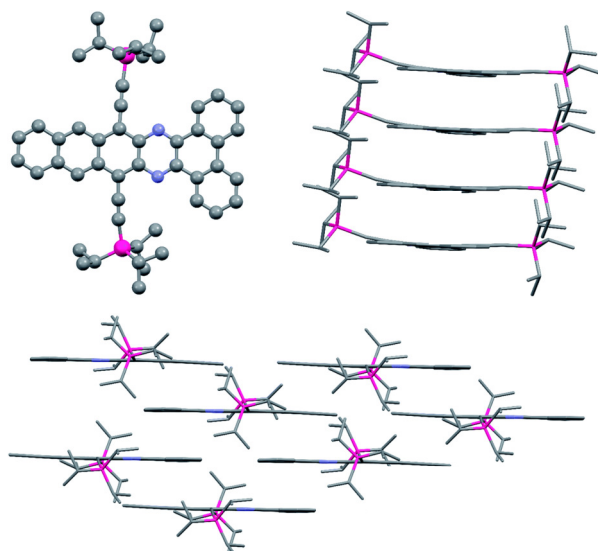
Figure 3.10.: Single crystal structure and packing of TIPS-BAP. Adapted from Ref.[20].

Even though the study by Hoff *et al.*[20] provides valuable information on different properties of TIPS-BAP, absence of a comparison between the molecule and its PAH counterpart, TIPS-BP, prevents us from understanding the influence of N-introduction on reported properties of the molecule. This study,

tries to fill this gap in the knowledge surrounding this set of N-heteropentacene derivatives by drawing such comparison. Some of the results presented in this subsection are published in Ref.[146].

The molecules were synthesized by Dr. Matthias Müller (TIPS-BP and TIPS-BAP) of the Prof. Dr. Uwe H. F. Bunz group of the Organisch-Chemisches Institut at the Universität Heidelberg.

For this study, TIPS-BAP and TIPS-BP samples were prepared *in situ* by deposition of the molecules at 533 K into the ultra-high vacuum chamber and onto Au(111) substrate held at room temperature (300 K). To characterize the prepared samples, in the first step, coverage dependent and fragment-mass-resolved TPD were utilized to demonstrate the possibility of preparing well-defined monolayers and thin films of the adsorbed molecules on Au(111) surface and elucidate the influence of N-introduction on the adsorption properties of the TIPS-BAP in comparison to TIPS-BP.

Figure 3.11 (a) shows the coverage dependent TPD spectra of TIPS-BAP, with different initial coverages of 2, 2.3 and 5 ML for the selected mass-to-charge ratio (m/z) of 73, which corresponds to a silicon-containing ionic fragment of the TIPS group (the structure is depicted in Figure 3.11 (a)). The spectrum consist of two desorption regions. The first region includes two desorption features with peaks at around 470 K (α_1) and 480 K (α_2), both of which exhibit zero-order desorption kinetics and do not saturates with increasing coverage. The α_2 feature is located at the approximate desorption temperature of the 2nd-layer (476 K in red spectrum) and by increasing the coverage it merges to the α_1 feature. Therefore, α_2 can be assigned to the 2nd-layer desorption, while α_1 is assigned to the desorption of higher layers[146]. The second desorption region with a peak at around 580 K (α_3) is clearly separated from the multi- and 2nd-layer desorption features, which hints at formation of a complete adsorbate layer at the interface with the Au (111) surface, before adsorption of higher layers takes place. Therefore, α_3 can be attributed to the desorption of a monolayer coverage[146]. In the following measurements, by integrating the measured spectra and comparing the area of the monolayer desorption feature (α_3) with the total integral, the coverage of the adsorbed molecules on the substrate is determined[110].

A comparison of the corresponding TPD spectra of TIPS-BAP and TIPS-BP, for coverages of 5 and 4.5 ML is shown in figure 3.11 (b). Similar to TIPS-BAP, the spectrum of TIPS-BP also includes two desorption regions with three des-
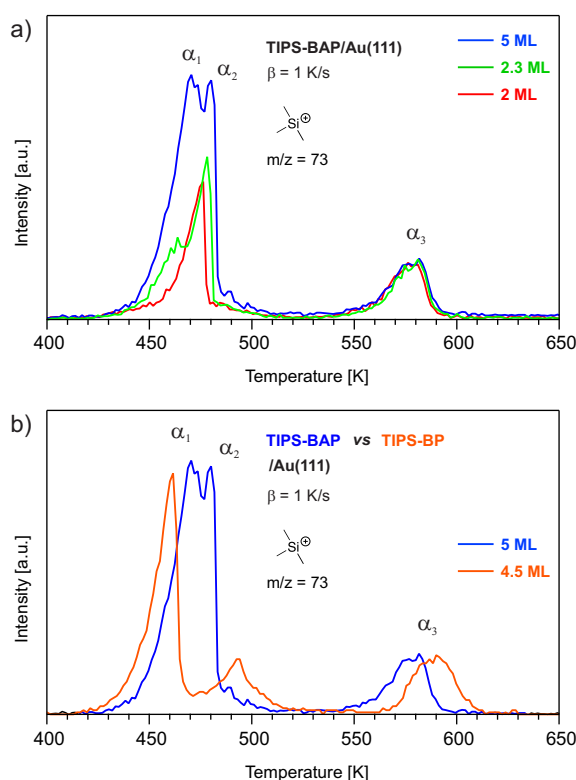
Figure 3.11.: Coverage dependent TPD spectra of (a) TIPS-BAP for the selected mass-to-charge ratio (m/z) of 73 for different initial coverages adsorbed on Au(111), measured with a heating rate of $\beta = 1\ K/s$. Adapted from Ref.[146]. (b) Shows an overlay of the TPD spectra of TIPS-BAP and TIPS-BP. The desorption features are labelled with α_1, α_2 and α_3. The structural formula of the the selected ionic fragment ($m/z = 73$) of the TIPS-group is depicted in the figures.

orption features labelled with α_1, α_2 and α_3. The multilayer desorption feature of both molecules, assigned with α_1, are located at 460 K (TIPS-BP) and 470 K (TIPS-BAP). Shift of the α_1 feature to higher temperatures in TIPS-BAP indicates that N-introduction does influence the adsorbate/adsorbate-interaction in the thin film. Noticeably, the α_2 feature in the TIPS-BP spectrum at 494 K is separated from the multilayer desorption feature (α_1), when compared to the α_2 feature in the spectra of TIPS-BAP. This suggests that the two feature labelled with α_2 in their corresponding desorption spectrum have different origins. Interestingly, it appears that introduction of nitrogen atoms to the backbone of TIPS-BAP reverses the influence of the added phenyl rings on the adsorption property of the molecule, since the spectrum of TIPS-BAP closely resembles the measured spectrum of TIPS-PEN[95]. This reversal trend is also

apparent from the shift of the monolayer desorption feature (α_3) of TIPS-BAP to a lower temperature (at 580 K) in comparison to the assigned desorption feature (α_3) of the same coverage for TIPS-BAP with a peak at approximately 590 K. This observation suggests that N-introduction in TIPS-BAP does not results in an increase in adsorbate/substrate-interactions, which is normally accompanied by an increase in desorption temperature of the adsorbates from the substrate in comparison to their PAH counterparts.

The fragment-mass-resolved TPD spectra of TIPS-BAP and TIPS-BP measured for different fragments of the TIPS group are shown in figure C.1. In case of TIPS-BAP, the spectra shows that the desorption feature of the 2nd-layer (α_2) coincide at the same temperature for all of the selected fragments (see Figure C.1 (a)). This is also the case for the monolayer desorption feature (α_3) except for the measured spectrum of the iso-propyl fragment (43 m/z), which is shifted by 10 K to a lower desorption temperature (570 K) in comparison to other fragments. This suggests that the monolayer coverage of TIPS-BAP degrades before it can be desorbed intact as previously reported for another TIPS substituted molecule, TIPS-PEN[95]. Indeed, as revealed by vibrational HREELS measurement, a subsequent heating of TIPS-BAP sample up to 750 K, results in an incomplete desorption of the molecule from the substrate. The recorded HREELS spectra of the annealed samples include vibrational peaks, which originates from the adsorbates (see Figure C.2 (a)). However, duo to purposed degradation of the iso-propyl fragment, the observed vibrations can not be assigned to any vibrational modes associated with TIPS-BAP with any certainty. In contrast, it can be assumed that the adsorbed TIPS-BAP molecules at higher layers including the 2nd-layer (α_2), which desorb at lower temperatures ($T_S < 570$ K), remains intact. A similar trend has also been observed in the fragment-mass-resolved TPD spectra of TIPS-BP (see Figure C.1 (b)), in which the measured spectrum of 43 m/z fragment is shifted by 10 K to a lower desorption temperature (580 K) at the monolayer coverage in comparison to other fragments. Moreover, the deposition temperature of TIPS-BAP and TIPS-BP at 533 K is much lower than the detected desorption temperature of the iso-propyl fragment at 570 K (TIPS-BAP) and 580 K (TIPS-BP). Therefore, it can be concluded that both molecules were deposited intact on the Au(111) substrate. Based on these observations, a well-defined monolayer coverage can be achieved by deposition of larger amounts of either molecule adding up to a multilayer or

2nd-layer coverage and subsequently heating the sample up to 520 K beneath the observed desorption temperatures of iso-propyl fragment, thus desorbing the higher laying layers, while preserving an intact monolayer coverage. This approach is used in this study to prepare well-defined monolayers of TIPS-BAP and TIPS-BP for further measurements. The preparation parameters for the samples involving both molecules are given in table H.1.

After gaining an insight into the adsorption properties of TIPS-BAP and TIPS-BP on Au(111), in the next step, angle-resolved vibrational HREELS is utilized to investigate the adsorption geometry of TIPS-BAP on Au(111). The initial goal of this study, was to investigate the influence of N-introduction in TIPS-BAP on its adsorption geometry, by comparing the vibrational spectra of TIPS-BAP and its PAH counterpart, TIPS-BP. However, this goal could not be achieved due to poor quality of the obtained results for TIPS-BP. Therefore, in the following, only the results from the conducted vibrational HREELS measurements on TIPS-BAP is presented. Figure 3.12 shows the vibrational HREELS spectra of TIPS-BAP adsorbed on Au(111), for mono - (a) and multilayer (b) coverages, measured in specular (black spectra) and off-specular (red spectra) electron scattering geometry along with the calculated intensities and frequencies of vibrational modes possessing a dynamic dipole moment perpendicular to the molecular backbone (c). The spectrum of TIPS-BAP at the mono - and multilayer coverage include multiple vibrations with high intensity ratio between the specular and off-specular scattered electrons, some of which can be considered as dipole-active vibrations with dipole scattering being their main excitation mechanism. By comparing the results from the obtained vibrational spectra with the calculated intensities and frequencies of B_1 vibrational modes of the corresponding C_{2v} molecular point group in the gas phase (see Figure 3.12 (c)), the dipole-active vibrations are assigned to out-of-plane $\gamma(\text{C-H})_A$ (at 460, 754, 883 and 1042 cm^{-1}) and $\gamma(\text{C-C-C})_A$ modes (at 670 cm^{-1})[146]. These vibrations originate from the arrow-shaped backbone (A) of the molecule. Additionally, the spectra of the molecule include vibrations with low specular to off-specular intensity ratios at 209, 263, 580, 1368, 1461, 2853, 2942, and 3060 cm^{-1}, which are non-dipole-active and as such their main excitation mechanism is impact scattering[146].
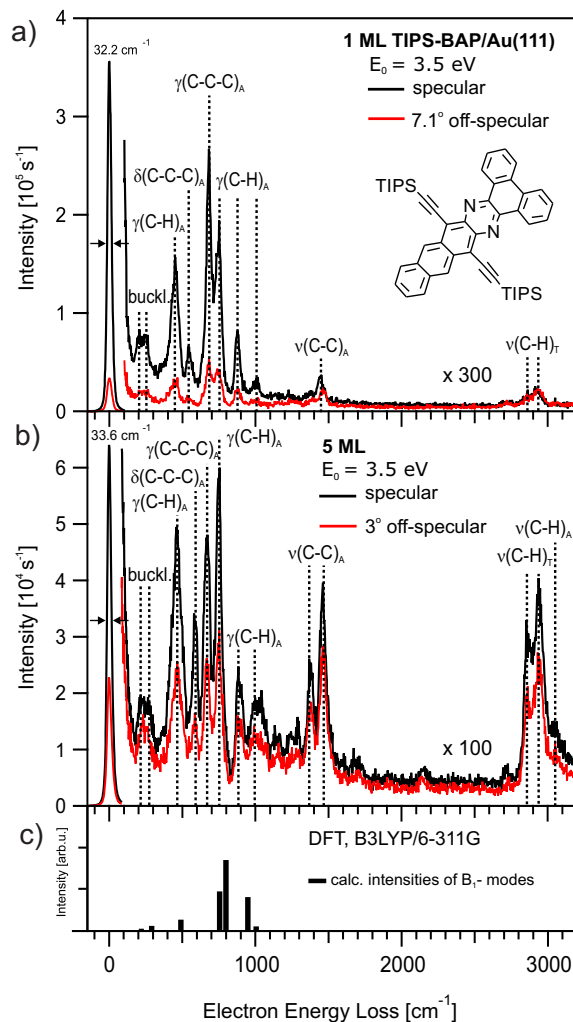
Figure 3.12.: Vibrational HREELS spectra of TIPS-BAP measured in specular (black spectra) and off-specular (red spectra) scattering geometry for mono - (a) and multilayer (b) coverages on Au(111) with the associated DFT-calculations (B3LYP/6-311G) for intensities and frequencies of B_1 symmetric vibrational modes with a dynamic dipole moment perpendicular to the molecular plane (c). E_0 is the primary energy of the incident electrons. The energy resolution of the specular spectra is measured as the full width at half maximum (FWHM) of the elastic peak (zero energy loss peak) and is given in wavenumbers (cm^{-1}). The assigned vibrations are listed in table 3.2. Adapted from Ref.[146].

3.1. Influence of N-introduction on the Properties of Pentacene Derivatives

Once again, by comparing these values with the results from the DFT calculations, some of the corresponding vibrations are assigned to the buckling, in-plane ν(C-C)$_A$ and ν(C-H)$_A$ stretching modes as well as δ(C-C-C)$_A$ scissoring mode[146]. The other vibrations located at 2853 and 2942 cm^{-1} originate primarily from the aliphatic ν(C-H)$_T$ vibrations of the C-H bonds at the TIPS-groups (T)[146]. Detection of these vibrations next to ν(C-H)$_A$ mode at 3060 cm^{-1} in the multilayer spectrum, confirms the conclusion made based on the results from the TPD measurements that the prepared coverage of TIPS-BAP on the Au(111) surface is intact[146].

The results from DFT calculations also indicates that the assigned dipole-active vibrations posses a dynamic dipole moment perpendicular to the molecular plane (x-direction) (see figure 3.13), while the dynamic dipole moment of the assigned non-dipole-active vibration is parallel to the molecular plane along the long axis (z-direction)[146]. At the monolayer coverage, the dipole-active vibrations, particularly the one assigned to the γ(C-C-C) mode at 680 cm^{-1} have higher intensity relative to the non-dipole-active vibrations, e.g. the ν(C-H) stretching modes at around 3000 cm^{-1}. This indicates that at the monolayer coverage, TIPS-BAP adapts a planar adsorption geometry on Au(111) surface, in which the plane of the arrow-shaped molecular backbone is parallel with the surface[146].

At the multilayer spectrum, increasing the coverage of TIPS-BAP to 3 ML results in a decrease in the relative intensities of the dipole-active vibrations, while the overall intensities of the non-dipole-active vibrations is increased. Additionally, the intensity ratio between the specular and off-specular scattered electrons of the dipole-active vibrations are also significantly reduced. This observation can be attributed to the larger distance of the adsorbates at higher layers from the metal surface, which reduces the dipole scattering efficiency at the multilayer coverage. Moreover, in comparison to the monolayer, the multilayer spectra also include additional non-dipole-active vibrations, two of which are assigned to ν(C-C)$_A$ (at 1461 cm^{-1}) and ν(C-H)$_A$ stretching modes (at 3060 cm^{-1}) of the molecular backbone. It can be assumed that at the multilayer coverage, the adsorbed molecules at higher layers slightly tilt out of the plane parallel with the substrate surface. Consequently, the dynamic dipole moments parallel to the molecular plane rotates towards an out-of-plane direction, which results in an increase in the intensity of the corresponding vibrations or detection of additional in-plane vibrations in the

spectrum of the multilayer coverage. This trend is accompanied with a significant increase in the intensity of the vibrations associated with the TIPS group (ν(C-H)$_T$ mode). Considering the low specular to off-specular intensity ratio of these vibrations, the proposed tilt does not induce an excitation via dipole scattering and the impact scattering remains the main excitation mechanism for the corresponding vibrations. Therefore, it can be assumed that in a thin film, the adsorption geometry of TIPS-BAP remains mostly planar with respect to Au(111) surface[146]. The assigned vibrations for TIPS-BAP are listed in table 3.2.

Table 3.2.: Assigned vibrations (in cm^{-1}) of TIPS-BAP adsorbed on Au(111) for different coverages. Additionally, the corresponding DFT calculated frequencies of the molecules in the gas-phase at the B3LYP level and the 6-311G basis set are given. Dipole active modes are labelled with *da*. The identified modes for each vibration are described with the following abbreviations; γ – out-of-plane; δ – scissoring; ν – stretching; A, arrow-shaped backbone; T, TIPS-group. Representation (Repr.) of the associated point groups and the orientation of the calculated dipole derivative vector with respect to the molecular geometry, x, perpendicular to the molecular plane; y, short axis and z, long axis of molecular backbone for each mode are listed. Adapted from Ref.[146].

<div align="center">

TIPS-BAP

#	1 ML	4 ML	DFT	Mode	Repr.
1	205	209	218	buckling	B$_1$(x)
2	237	263	290	buckling	B$_1$(x)
3	451 *da*	460 *da*	489	γ(C-H)$_A$	B$_1$(x)
4	538	580	616	δ(C-C-C)$_A$	A$_1$(z)
5	680 *da*	670 *da*	755	γ(C-C-C)$_A$	B$_1$(x)
6	751 *da*	754 *da*	797	γ(C-H)$_A$	B$_1$(x)
7	877 *da*	883 *da*	947	γ(C-H)$_A$	B$_1$(x)
8	1006 *da*	1042 *da*	1004	γ(C-H)$_A$	B$_1$(x)
9	-	1368	1388	ν(C-C)$_A$	A$_1$(z)
10	1439	1461	1466	ν(C-C)$_A$	A$_1$(z)
11	-	2853	3000	ν(C-H)$_T$	-
12	2914	2942	3005	ν(C-H)$_T$	-
13	-	3060	3196	ν(C-H)$_A$	A$_1$(z)

</div>

a)

γ(C-H)$_A$
451/460/489 cm^{-1}

b)

γ(C-C-C)$_A$
680/670/755 cm^{-1}

c)

γ(C-H)$_A$
751/754/797 cm^{-1}

d)

γ(C-H)$_A$
877/883/948 cm^{-1}

e)

γ(C-H)$_A$
1006/1042/1004 cm^{-1}
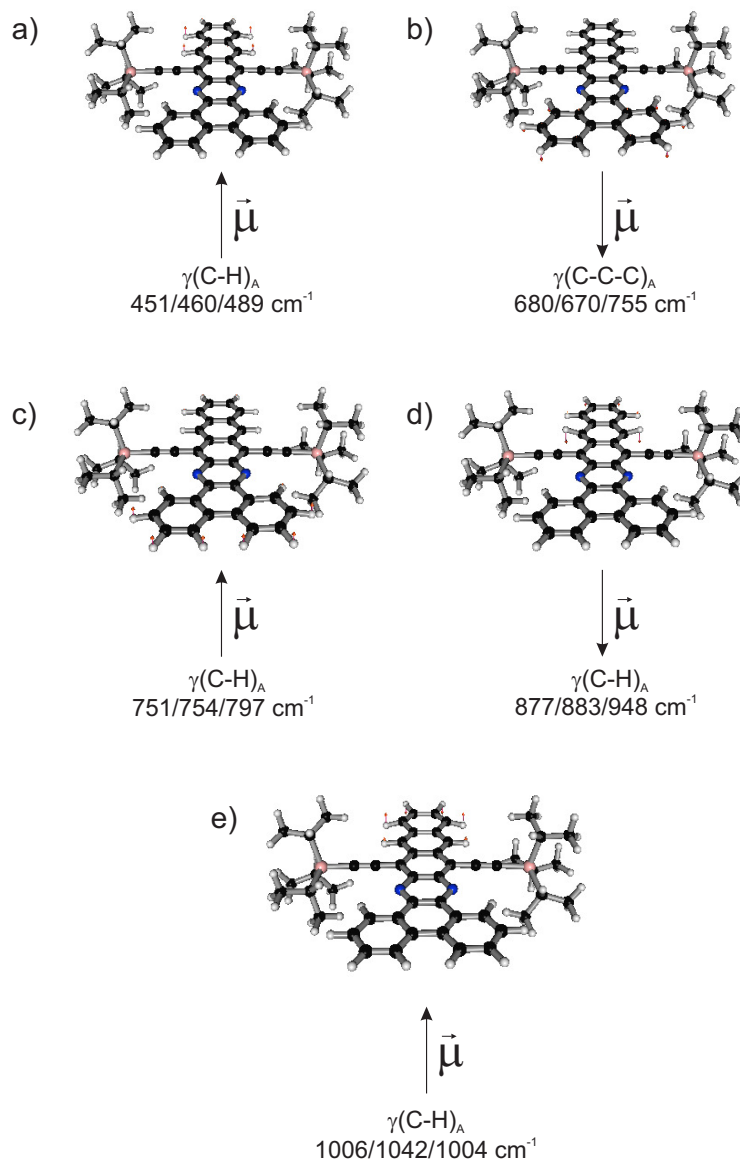
Figure 3.13.: Visualisation of the assigned dipole-active vibrational modes obtained from the DFT calculations (B3LYP/6-311G) for TIPS-BAP. The corresponding energies (HREELS monolayer/HREELS multilayer/DFT) are given in wavenumbers (cm^{-1}). The direction of the calculated dipole derivative unit vector ($\vec{\mu}$) is depicted with a black arrow that lies in the plane of the paper. The atomic displacements in each visualization are shown with red arrows. The vibrational modes are visualized by the Facio software[139].

Results and Discussion

In the final step, the electronic HREELS is utilized to elucidate the influence of N-introduction in TIPS-BAP on its electronic structure in comparison to TIPS-BP, at the interface with Au(111) and within thin films. Figure 3.14 shows the electronic HREELS spectra of TIPS-BP (Left) and TIPS-BAP (right), for mono- (a and c) and multilayer (b and d) coverages measured with the primary electron energy of 15 eV together with the corresponding UV/Vis spectra of the molecules measured in n-hexane (C_6H_{14}) solution (orange spectra). The spectrum of TIPS-BP at the monolayer coverage consists of a contribution from an overtone of the in-plane ν(C-H) stretching mode vibration at approximately 0.7 eV (at around 3000 cm^{-1} in Figure 3.12 (a)), as well as the conventional Au(111) surface plasmon at 2.6 eV[140] as shown in figure 3.14 (a). Absence of any adsorbate-induced loss feature in the monolayer spectrum, aside from the assigned vibrational contribution, indicates that electronic transitions of the molecule are screened by Au(111) substrate. This indicates that the substituted bulky TIPS-groups in the molecule does not create enough or any vertical distance between the adsorbed molecules and Au(111) surface to electronically decouple the aromatic backbone of TIPS-BP from the metallic substrate. A similar observation has also been made for the monolayer coverage of TIPS-PEN[95], which suggests that the added phenyl rings in the backbone of TIPS-BP does not change the electronic properties of the molecule at its monolayer coverage.

By increasing the coverage of TIPS-BP to 4 ML, the molecular thin film is decoupled from the metallic substrate. This results in detection of a loss features at 2.1 eV and its accompanied vibrational contributions as well as a broad loss feature at 3.6 eV as shown in figure 3.14 (b). The loss feature at 2.1 eV is assigned to the transition of the ground state (S_0) to the first singlet excited state (S_1), i.e. the optical gap of the molecule[146]. The accompanied vibrational contributions of $S_0 \rightarrow S_1$ transition corresponds to the excitations of the ν(C-C) breathing mode of the molecular backbone with a frequency of 1461 cm^{-1} (181 meV). Moreover, the broad loss feature at 3.6 eV can also be assigned to $S_0 \rightarrow S_3$ or β - band.

The multilayer spectrum of TIPS-BP closely resembles the measured spectrum of TIPS-PEN at its multilayer coverage (4.4 ML), which also include two main electronic transitions at 1.9 eV ($S_0 \rightarrow S_1$, optical gap) and 4.1 eV ($S_0 \rightarrow S_3$, β-band) with similar loss feature profiles[147]. This indicates that addition of two phenyl rings to the backbone of TIPS-BP results in a widen-
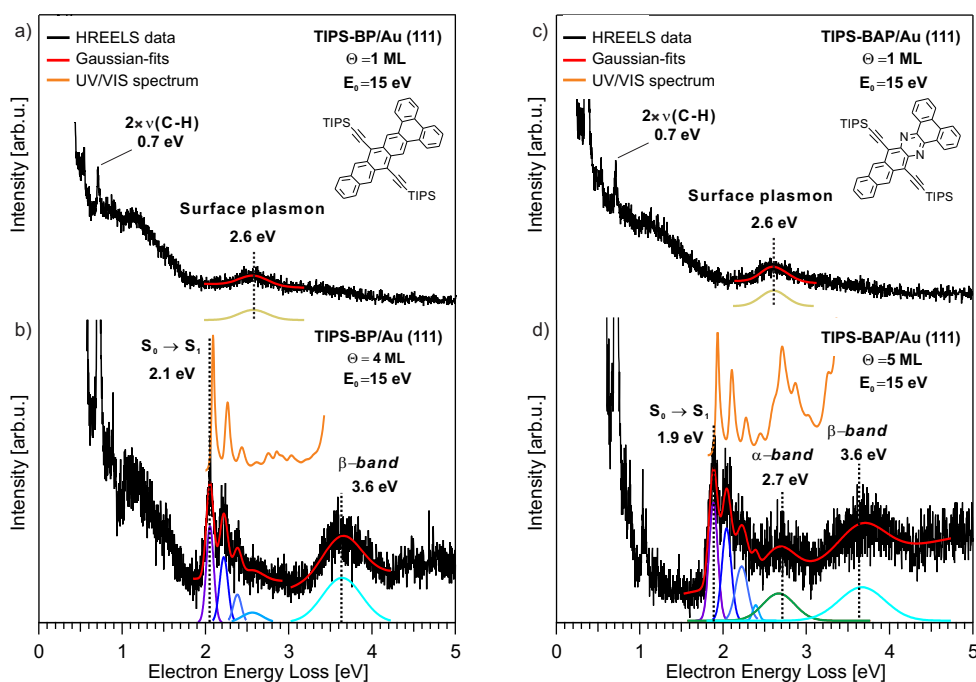
Figure 3.14.: Electronic HREELS spectra of adsorbed TIPS-BP (Left) and TIPS-BAP (right) on Au(111), measured for mono - (a and c) and multilayer (b and d) coverages (black spectra). The electronic loss features were fitted using Gaussian functions (red curves). The corresponding UV/Vis spectra of the molecules are measured in *n*-hexane (C_6H_{14}) solution (orange spectra). E_0 is the primary energy of the incident electrons. Θ is the coverage in monolayer (ML). Adapted from Ref.[146].

ing of the optical gap by 200 meV from 1.9 eV for TIPS-PEN to 2.1 eV for TIPS-BP. Additionally, the β - band as detected in the spectrum of TIPS-BP is shifted by 500 meV to lower energies (3.6 eV) in comparison to the detected β - band (4.1 eV) of TIPS-PEN.

In case of TIPS-BAP, the spectrum of the monolayer coverage consists of similar contributions as detected for the monolayer coverage of TIPS-BP (see Figure 3.14 (c)). At the coverage of 5 ML, by decoupling the adsorbates from the metallic substrate, additional contributions from the molecular electronic states are detected in the spectrum of the multilayer coverage, which includes three electron energy loss feature at 1.9, 2.7 and 3.6 eV as shown in figure 3.14 (d). The loss feature at 1.9 eV is assigned to the $S_0 \rightarrow S_1$ transition or the optical gap of molecule[146]. This transition is accompanied by the so-called acene fingers, that correspond to the vibronic excitations of the ν(C-C) breathing mode of the molecular backbone with a frequency of 1461

cm^{-1} (181 meV)[146]. The measured gap size of 1.9 eV for TIPS-BAP is in good agreement with the one obtained from UV/Vis measurement (1.93 eV) in solution. In contrast, the determined optical gap of the molecule at the monolayer coverage with the 2PPE measurement (1.74 eV) is about 260 meV smaller than the one determined by the electronic HREELS at the multilayer coverage. This deviation is expected, since the adsorbate at the monolayer coverage is electronically coupled to the Au(111) substrate, which leads to a substrate-induced narrowing of the optical gap[146]. Furthermore, by utilizing the excited-state calculations in the gas phase, the loss features at 2.7 and 3.6 eV are assigned to $S_0 \rightarrow S_2$ (α - band) and $S_0 \rightarrow S_3$ (β - band) transitions[146].

The assigned $S_0 \rightarrow S_1$ transitions of TIPS-BP and TIPS-BAP and their accompanied vibrational contributions in the measured electronic spectra of the molecules at their multilayer coverage are in good agreements with the corresponding transitions in the UV/Vis spectra of the molecules in solution. In contrast, the assigned α - band transition of TIPS-BAP, as detected in the electronic spectrum of the molecule, is broad and does not include the associated vibrational contributions as seen in the corresponding UV/Vis spectrum. Regardless, by only considering the good agreements of the detected $S_0 \rightarrow S_1$ transitions of the two molecules in the measured spectra of their thin films with the ones in the spectra of their solutions it can be concluded that the influence of the metal substrate (adsorbate/substrate-interactions) and the intermolecular forces (adsorbate/adsorbate-interactions) on the electronic states of the adsorbed molecules are negligible[146].

A comparison between the multilayer HREELS spectra of TIPS-BP and TIPS-BAP reveals that introduction of nitrogen atoms into the backbone of TIPS-BAP results in a narrowing of the optical gap ($S_0 \rightarrow S_1$ transition) by 100 meV from 2.1 eV for TIPS-BP to 2 eV for TIPS-BAP as shown in figure 3.14 (a) and (b). In comparison, the recorded UV/Vis spectra of both molecules in solution also shows a narrowing of the optical gap by approximately 160 meV. This effect is attributed to the stabilization of the polar first excited singlet state (S_1) of TIPS-BAP in a polar environment[146]. Based on the results from the carried out quantum chemical calculations on both TIPS-BP and TIPS-BAP, it is determined that this polar environment is formed by the N-introduction in TIPS-BAP, which causes the molecule to gain a pronounce static charge-transfer character in comparison to its PAH counterpaart,TIPS-BP, by increasing the electron-hole (e - h) distance of S_1 state from 0.10 A for TIPS-BP to
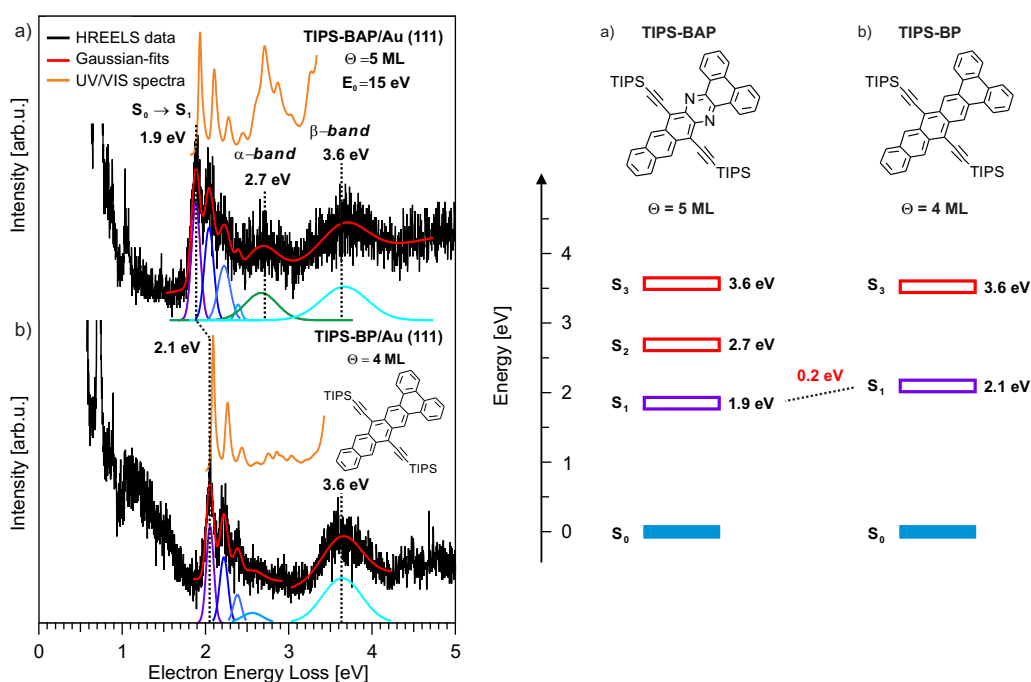
Figure 3.15.: Electronic HREELS spectra (left) of adsorbed (a) TIPS-BAP and (b) TIPS-BP on Au(111), measured for the multilayer coverage (black spectra), adapted from Ref.[146]. The electronic loss features were fitted using Gaussian functions (red curves). The corresponding UV/Vis spectra are measured in *n*-hexane (C_6H_{14}) solution (orange spectra). E_0 is the primary energy of the incident electrons. Θ is the coverage in monolayers (ML). The identified and assigned electronic transitions of the molecules are summarized in an energy level diagram (right).

1.62 A for TIPS-BAP[146].

Aside from the narrowing of the optical gap, the N-introduction in TIPS-BAP leads to a pronounced rise in the intensity of α-band ($S_0 \rightarrow S_2$ transition) in comparison to TIPS-BP. This trend has also been observed for the PEN, DAP and TAP series as presented in the previous subsection, where it has been concluded that an increase in the oscillator strength of a strongly correlated state (L_s) as the result of nitrogen introduction into the backbone of the molecules leads to the intensity rise of the α-band, associated with the L_s state[129;130]. Similarly, the observed pronounced intensity of the α-band in the spectrum of TIPS-BAP is attributed to an increase in the oscillator strength of the L_s state[146]. This finding is the result of the quantum chemical calculations, which were conducted by Dr. Marvin Hoffmann of the Prof. Dr. Andreas Dreuw group of the Interdisziplinäres Zentrum für Wissenschaftliches

Rechnen at the Universität Heidelberg. In the following, a summary of the results from the quantum chemical calculations is presented.

According to the quantum chemical calculations, the two lowest optically allowed singlet excited states of TIPS-BP and TIPS-BAP, S_1 and S_2, exhibit a $\pi\pi^*$ character. For both molecules, the exciton of S_1 posses a weak e - h correlation and therefore corresponds to a weakly correlated state (L_w), while S_2 has a stronger correlation by factors of 2.5 (TIPS-BP) and 2 (TIPS-BAP), and as such corresponds to a strongly correlated state (L_s). Introduction of nitrogen atoms along the long axis of the arrow-shaped aromatic backbone of TIPS-BAP, introduces a static ground state dipole moment in the same direction (see Figure 3.16)[146]. This amplifies the transition dipole moment of the molecule in the direction of long axis, corresponding to a L_s state, rather than in the direction of short axis, that corresponds to a L_w state. As a result, the oscillator strength of L_s state significantly increases from 0.017 for TIPS-BP to 0.382 for TIPS-BAP, which leads to a pronounced intensity increase of the corresponding α-band ($S_0 \rightarrow S_2$ transition)[146]. A detailed description of the carried out quantum chemical calculations on TIPS-BP and TIPS-BAP can be found in Ref.[146].
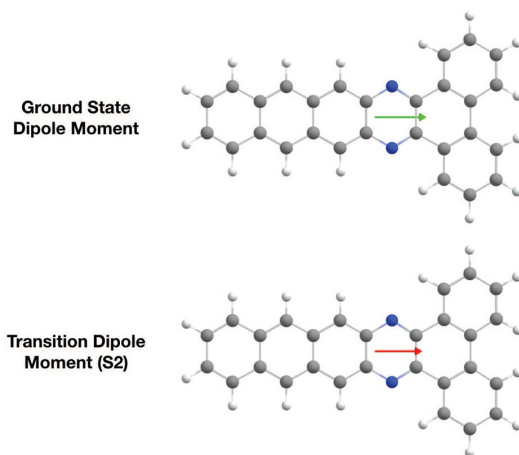
Figure 3.16.: Directions of (top) the ground state dipole moment and (bottom) the transition dipole moment of the second excited singlet state (S_2) of TIPS-BAP. Taken from Ref.[146]

Noticeably, no electron energy loss feature, that can be assigned to the $S_0 \rightarrow T_1$ transition of either TIPS-BP or TIPS-BAP, could be detected. Similarly, the electronic HREELS measurements on TIPS-PEN carried out by

3.1. Influence of N-introduction on the Properties of Pentacene Derivatives

Stein *et al.* also could not identify a possible triplet transition[147]. The identified and assigned electronic transitions of TIPS-BP and TIPS-BAP at their multilayer coverage are summarized in figure 3.15 (c). Other than transitions corresponding to singlet excited states, the conducted 2PPE measurements on TIPS-BAP provide further insight into the electronic structure of the molecule by determining the unoccupied and occupied single-electron states or the so called transport states (electron affinity level) of TIPS-BAP as presented in Ref.[146].

To summarize, in this subsection it has been demonstrated that thin films of an arrow-shaped N-heteropentcene derivative, TIPS-BAP and its PAH counterpart, TIPS-BP, can be prepared through evaporation at 533 K into the ultra-high vacuum chamber and onto Au(111) substrate held at room temperature (300 K). The prepared samples were then characterized by TPD, vibrational and electronic HREELS in combination with DFT calculations. Based on the results from the fragment-mass-resolved TPD measurements, during annealing of the samples, the higher laying layers desorb intact, while the monolayer coverage degrades due to premature desorption of iso-propyl fragment of TIPS group at 570 K (TIPS-BAP) and 580 K (TIPS-BP). Therefore, well-defined monolayers of either molecule were prepared by deposition of larger amounts of molecules adding up to a multi or 2nd-layer coverage and subsequently heating the samples up to 520 K in order to desorb the higher laying layers, while preventing the monolayer degradation. Detection of the aliphatic ν(C-H)$_T$ vibrations of the C-H bonds at the TIPS groups in the measured vibrational HREELS spectra of TIPS-BAP at its mono- and multilayer coverage, further confirms the possibility of preparing intact coverages of both molecules via intact molecular deposition and subsequent annealing. The results from the coverage dependent TPD measurements on both molecules indicates that N-introduction in TIPS-BAP results in an increase in adsorbate/adsorbate-interaction, which is evident from the higher desorption temperature of the multilayer coverage of the molecule in comparison to the desorption temperature of the same coverage of TIPS-BP. Additionally, it has been found that addition of two phenyl rings into the backbone of TIPS-BP may results in a change in the adsorbtion properties of the molecule. A similar change could not be identified for TIPS-BAP, which suggests that N-introduction may reverse the influence of the added phenyl rings in the molecule. Furthermore, as shown via vibrational HREELS measurements, TIPS-BAP at mono- and mul-

tilayer coverage adopt a planar adsorption geometry on the Au(111) surface, in which the arrow shaped N-heteropolycyclc aromatic backbone of the molecule is oriented parallel with the substrate. However a slight tilt of the molecule along its axis, particularly at higher layers, could not be dismissed. Lastly, through electronic HREELS measurements, it has been determined that N-introduction in TIPS-BAP results in the narrowing of the optical gap by 200 meV from 2.1 eV for TIPS-BP to 1.9 eV for TIPS-BAP, which is attributed to the stabilization of the polar first singlet excited state (S_1) of TIPS-BAP in a polar environment as well as the pronounced rise in the intensity of the α - band ($S_0 \rightarrow S_2$) in TIPS-BAP compared to TIPS-BP due to an increased transition dipole moment of the excitation into the second singlet excited state (S_2).

In conclusion, the presented studies in this section provides valuable insights into the influence of N-introduction on the adsorption and electronic properties of two members of N-heteropentcene class of compounds, DAP and TAP, as well as a N-heteropentcene derivative, TIPS-BAP, which can be employed to further develop organic electron transporting (n-channel) semiconductors and subsequently improve and optimize the performance of organic based (opto)electronic devices.

3.2. Influence of Core substitution on the Adsorption and Electronic Properties of Thiadiazole Derivatives

In this section, influence of core substitution via halogens and aromatic groups on the adsorption and electronic properties of thiadiazole derivatives adsorbed on Au(111) is studied by using TPD, vibrational and electronic HREELS. The investigated molecular systems include naphto[2,3-c][1,2,5]thiadiazole (NTD, Figure 3.17 (a.1)) and its chlorine (NTD-Cl, Figure 3.17 (a.2)) and bromine (NTD-Br, Figure 3.17 (a.3)) substituted derivatives as well as phenyl (BBT-Ph, Figure 3.17 (b.1)) and thiophene (BBT-Th, Figure 3.17 (b.2)) substituted benzo[1,2-c;4,5-c']bis[1,2,5]thiadiazole (BBT).

a)

1. X = H; Naphto[2,3-c][1,2,5]thiadiazole (NTD)
2. X = Cl; NTD-Cl
3. X = Br; NTD-Br

b)

1. Ar = ; BBT-Ph
2. Ar = ; BBT-Th

BBT: Benzo[1,2-c;4,5-c']bis[1,2,5]thiadiazole
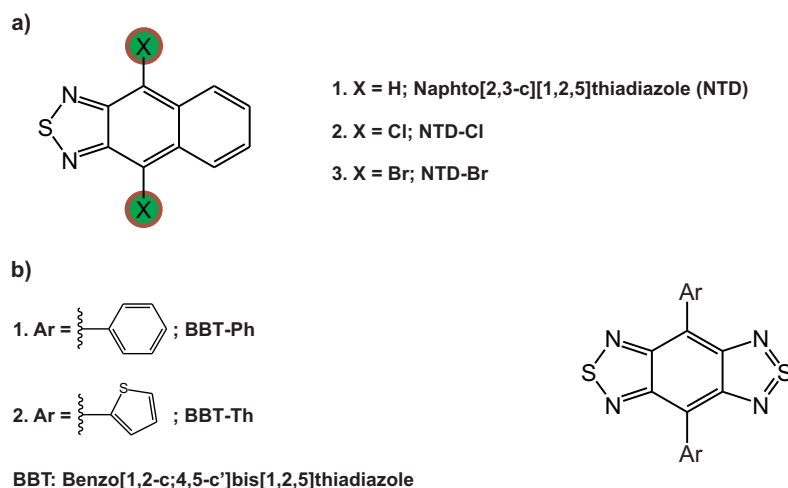
Figure 3.17.: Investigated molecular systems: (a) naphto[2,3-c][1,2,5]thiadiazole (NTD, (1)) and its chlorine (NTD-Cl, (2)) and bromine (NTD-Br, (3)) substituted derivatives as well as (b) phenyl (BBT-Ph, (1)) and thiophene (BBT-Th, (2)) substituted derivatives of benzo[1,2-c;4,5-c']bis[1,2,5]thiadiazole (BBT).

The results from these investigations are presented in two subsections. In the first subsection, by comparing the obtained results for NTD with its halogenated derivatives, effects of the core halogenation on the properties of the corresponding molecules are studied. In the second subsection, by comparing the obtained results for BBT-Ph and BBT-Th, the influence of the substituted aromatic groups in the core of BBT on its derivatives is investigated. Through these studies, it is determined that intact thin films of the given molecules can be prepared via deposition at elevated temperatures into the ultra-high vac-

uum chamber and onto Au(111) substrate. All of the investigated molecules adopt a planar adsorption geometry on the Au(111) surface. Core substitution alters the electronic structure of the corresponding molecules by reducing the assigned energies of the lowest excited electronic singlet states (S) as well as the first triplet states (T_1). This is evident from a narrowing of the optical gap that can be summarized to a reduction of 200 meV from 2.6 eV for NTD to 2.4 eV for NTD-Cl and NTD-Br, as well as a reduction of 400 meV from 2.2 eV for BBT-Ph to 1.8 eV for BBT-Th. Similarly, the assigned $S_0 \rightarrow T_1$ transition of NTD at 1.7 eV is reduced by 100 meV to 1.6 eV for its halogenated derivatives (NTD-Cl and NTD-Br) and BBT-Ph at 1.2 eV by 500 meV to 0.7 eV for BBT-Th.

3.2.1. Naphthothiadiazole Derivatives

NTD was first synthesized by Cava *et al.* in 1964[148] as a S- and N- containing heteropolycyclic molecule with chemical properties analogous to those of anthracene. They found that NTD is highly stable and possesses the characteristics of a highly delocalized aromatic system, in which the sulfur atom exhibits a tetravalent behaviour. A molecular orbital study of NTD indicates that the calculated π-delocalization in the molecule (4.753 β) is comparable to that in antheracene (5.314 β)[149]. Additionally, the calculated value of the first singlet transition of NTD is estimated to be about 455 nm (2.72 eV), which is bathochromically shifted in comparison to the benzo[c][1,2,5]thiadiazole or BTD (308 nm) and thiadiazole (228 nm) as well as naphtho [1,2-e][1,2,5]thiadiazole or angular NTD (343 nm)[150]. Noticeably, it is found that contribution of the heteroatoms such as O, S and Se to the conjugation is lower for the molecule with angular fused ring in comparison to its linear form[150]. Further theoretical and experimental investigations of NTD suggest that in the solid state depending on the used solvents and crystallization conditions, the molecule form three polymorphs with different packing motifs (see Figure 3.18) in its single crystal[151]. In the first polymorph, NTD is packed with a motif of infinite chains of alternating molecules in ...ABAB... sequence, in which molecule A is linked to molecule B trough a weak H-bond between N atom and C-H bond (see Figure 3.18 (a)). In the second polymorph, NTD adapts a sandwich-herringbone packing, in which molecules are arranged in both face-to-edge and faced-to-face geometry (see Figure 3.18 (b)). In the third polymorph, NTD molecules are stacked alternatively in layers that are parallel to one another (see Figure 3.18 (c)). In contrast to the first polymorph, the intermolecular contacts between the molecules in the second and third polymorphs originate from the chalcogen-bond between N and S atoms, which leads to formation of more stable packing motifs for the corresponding polymorphs due to stabilization brought about by chalcogen-bonds.

The halogenated derivatives of NTD were first synthesis by Smith *et al.*[152] in order to compare the bromination and chlorination processes of the molecule with the ones of anthracene. The chlorinated (NTD-Cl) and the brominated (NTD-Br) molecules are utilized as precursors to form donor–acceptor (D–A) molecular systems, in which NTD act as the electron acceptor moiety[68;69]. Given the potentials of NTD, it has been used for applications such as organic semiconductors[81;153;154], OLEDs[155–167], solar cells[81;168;169], fluorescent

imaging[170–172] and luminescent metal – organic frameworks (LMOFs)[173–176].
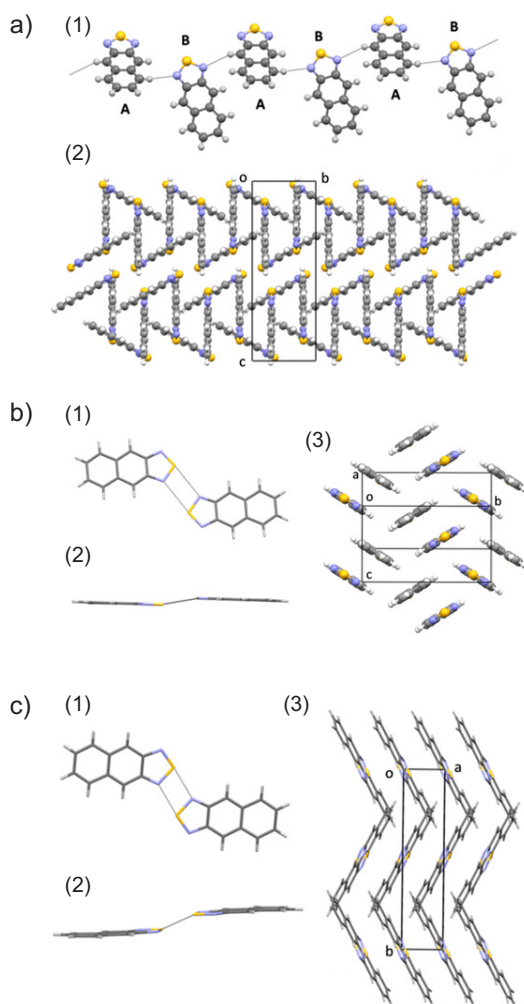
Figure 3.18.: Different polymorphs of NTD in its single crystal: (a) First polymorph,
(b) second polymorph, and (c) third polymorph. Chain of molecules (a.1),
chalcogen-bonded dimer; front view (b.1 and c.1), and edge view (b.2 and
c.2) as well as packing motifs (a.2, b.3 and c.3) of NTD in its polymorphs.
Adapted form Ref.[151].

In the context of this study, it was chosen to investigate NTD as well as
its halogenated derivatives (NTD-Cl and NTD-Br) in order to gain necessary
insights into their adsorption and electronic properties at their thin films and
interfaces with Au(111) substrate, which will be required for forming potential
donor–acceptor (D–A) molecular systems in solid state, via *in situ* deposition
of donor and acceptor molecules on a metallic substrate. Some of the results
presented in this subsection are previously published in Ref.[177].

3.2. Influence of Core substitution on the Properties of Thiadiazole Derivatives

The NTD, NTD-Cl and NTD-Br molecules were synthesized by Dr. Hendrik Hoffmann of the Prof. Dr. Uwe H. F. Bunz group of the Organisch-Chemisches Institut at the Universität Heidelberg.

For this study, samples of NTD and its derivatives were prepared, *in situ* by deposition of the corresponding molecules at 300 K (NTD), 368 K (NTD-Cl) and 388 K (NTD-Br) into the UHV chamber and onto Au(111) substrate held at 200 K. First, through coverage dependent and fragment-mass-resolved TPD measurements, the possibility of preparing thin films and well-defined monolayers of the molecules on Au(111) surface is investigated and subsequently, the influence of core substitution of the parent NTD molecule via halogens (Cl and Br) on its adsorption properties within the thin film and at the interface with Au(111) substrate are explored.

Figure 3.19 (a) shows the coverage dependent TPD spectra of NTD, with different initial coverages of 1.6, 3, 4 and 8 ML for the mass-to-charge ratio (m/z) of 186, which corresponds to the mass of the parent molecular ion (186 amu). The spectra consist of two desorption regions. The first region, includes two desorption peaks (α_1 and α_2) at 263 K, while the second region includes a broad desorption feature extending from 330 K to 450 K (α_3, see inset in Figure 3.19 (a)). The α_1 peak does not saturates with increasing coverage. Therefore, it is assigned to the desorption of a multilayer coverage. The α_2 peak first appears as a shoulder structure at 3 ML and by increasing the coverage merges to the multilayer desorption peak (α_1). This characteristic desorption behaviour is similar to that of the 2nd-layer desorption of TIPS-BAP as observed in the coverage dependent TPD spectra of the molecule in the previous section (see Figure 3.11 (a) in Subsection 3.1.2). Thus, the α_2 peak can be attributed to the desorption of the 2nd-layer. The α_3 feature, as shown in the inset, is separated from the second and multilayer desorption peaks, which suggests that a complete adsorbate layer is formed at the interface with the Au (111) before adsorption of higher layers takes place. Therefore, α_3 is assigned to the desorption of a monolayer coverage.

Furthermore, no distinct vibration, which can be associated with adsorbates could be detected in the vibrational spectrum of BBT-Ph (see Figure D.3 (a)), that is measured after heating the samples up to 750 K. This suggests that the monolayer coverage of NTD desorbs intact from the Au(111) substrate.
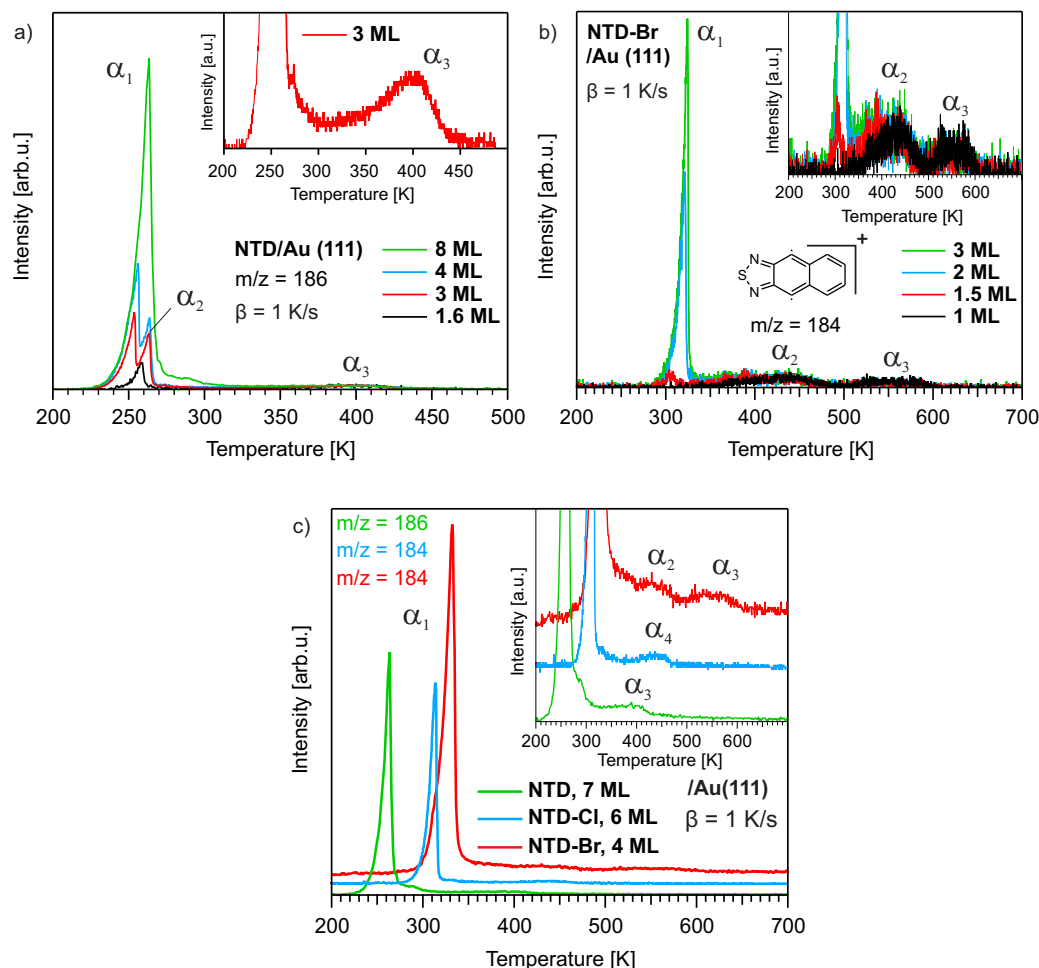
Figure 3.19.: Coverage dependent TPD spectra of (a) NTD with the selected mass-to-charge ratio (m/z) of 186 (adapted from Ref. [177]) and (b) NTD-Br for the biradical fragment with the m/z of 184 with different initial coverages adsorbed on Au(111), measured with a heating rate of $\beta = 1\ K/s$. (c) Shows an overlay of the TPD spectra of NTD, NTD-Br and NTD-Cl. The desorption features are labelled with α_1, α_2, α_3 and α_4. The insets show the monolayer (α_3 in NTD), compressed phase (α_2 in NTD-Br) and the sub-monolayer desorption feature (α_3 in NTD-Br and α_4 in NTD-Cl). The structural formula of the ionic fragment of NTD-Br is depicted in the corresponding figure. The coverage dependent TPD spectra of NTD-Cl is presented in appendix D (see Figure D.1 (a)).

3.2. Influence of Core substitution on the Properties of Thiadiazole Derivatives

In case of NTD-Br (m = 342 amu), the coverage dependent TPD spectra of the fully dehalogenated biradical fragment of the molecule (m/z = 184, the structure formula is depicted in Figure 3.19 (b)) also consist of two desorption regions for different initial coverages of 1, 1.5, 2 and 3 ML as shown in figure 3.19 (b). The first region includes a desorption peak at 321 K (α_1), which exhibits zero-order desorption behaviour and does not saturate with increasing coverage. Therefore, α_1 is assigned to the desorption of a multilayer coverage. The second region includes two broad desorption features, one extending from 350 K to 500 K (α_2) and the other extending from 500 K to 600 K (α_3) (see inset in figure 3.19 (b)). Both α_2 and α_3 saturate at the monolayer coverage. Therefore, it can be assumed that α_2 originates from a more densely packed compressed phase as observed for PEN, DAP and TAP as well as benzene[110;131] and other aromatic organic molecules adsorbed on coinage metal surfaces[132–138]. As such, α_3 can be attributed to a desorption from a submonolayer coverage. Thus, the desorption spectrum of a monolayer coverage can be defined as a spectrum, in which both α_2 and α_3 are saturated. The inset shows the enlarged monolayer desorption region of the measured spectra. The coverage dependent TPD spectra of NTD-Cl share similar trends as the ones observed for NTD-Br, which are discussed in appendix D (see Figure D.1).

Figure 3.19 (c) shows an overlay of the corresponding TPD spectra of NTD (7 ML), NTD-Cl (6 ML) and NTD-Br (4 ML). A comparison between these spectra reveals that upon core halogenation of NTD, the multilayer desorption peak (α_1) of the parent molecule shifts from 263 K to higher temperatures at 313 K for NTD-Cl and 332 K for NTD-Br. Similarly, the assigned monolayer desorption features of the halogenated molecules (α_2 and α_3 in NTD-Br and α_4 in NTD-Cl) are located at higher temperatures in comparison to that of NTD (α_3) at 330 K - 450 K temperature range. These temperature shifts indicate that halogenation leads to increased adsorbate/adsorbate and adsorbate/substrate-interactions within NTD-Cl and NTD-Br thin films and at their interfaces with Au(111) surface.

Considering the clear separation of the monolayer desorption features of NTD and its halogenated derivatives from the desorption features of their multilayer or 2nd - layer coverages, the monolayer coverage of the corresponding molecules can be prepared by deposition of larger amounts of the molecules adding up to a multilayer or 2nd - layer coverage and subsequently heating the sample up to 300 K (NTD), 340 K (NTD-Cl) and 350 K (NTD-Br), in order

to desorb the higher laying layers, while preserving the monolayer coverage. This approach is used to prepare well-defined monolayers of the mentioned molecules for further measurements. The used parameters for preparing the samples are given in table H.1.

As for the multilayer coverage, up to this point, the number of layers formed by the deposited molecules for each sample were determined by integrating a measured TPD spectrum and comparing the area of the total integral with the area of the monolayer desorption region [110]. However, it is found that the TPD spectra of NTD-Br and NTD-Cl, which were measured after conducting the intended vibrational and electronic HREELS measurements on the prepared samples during an overnight measurement period, equal to approximately 15 hours, do not include a signal from the fully dehalogenated molecular fragment (m/z = 184). This indicates that the halogenated molecules may have not been desorb intact from the substrate. This observation was unexpected, since the measured TPD spectra of either molecule, which were conducted immediately after the sample preparation ($\simeq$ 10 min), do include a signal from the fragment in question. This suggests that either time or the characterization process via HREELS (electron beam) may have played a role in inducing the observed effect in the TPD spectra of the halogenated molecules. In order to distinguish the potential contributions of the two mentioned factors, it was decided to perform fragment-mass-resolved TPD measurements on NTD-Br and NTD-Cl samples, at different time intervals, without conducting HREELS measurements. Thus, eliminating any possible influence from characterization process (e^- exposure), while time as the only contributing factor is examined.

Figure 3.20 shows the fragment-mass-resolved TPD spectra of NTD-Br measured for different selected fragments, about 10 minutes after sample preparation (3.20 (a)), after approximately 3 h (3.20 (b)) and 15 h (3.20 (c)). The chosen time intervals correspond to the time that is approximately required to complete the vibrational ($\simeq$ 3 h) and a subsequent overnight electronic HREELS measurements ($\simeq$ 15 h). During the time intervals, the samples were kept at temperatures under 100 K in order to simulate the standard characterization condition via HREELS. For this set of measurements, aside from the m/z = 184, it was chosen to monitor the masses of atomic Br (m/z = 79 and 81) and molecular HBr (m/z = 80 and 82) in order to explore the desorption behaviour of Br substituent, according to the established TPD procedure by Bronner et al [178] for monitoring the on-surface synthesis of another

3.2. Influence of Core substitution on the Properties of Thiadiazole Derivatives

Br-substituted molecule, the well known 10,10-dibromo-9-9-bianthryl (DBBA) precursor, during the bottom-up preparation of atomically precise graphene nanoribbons GNRs[178].
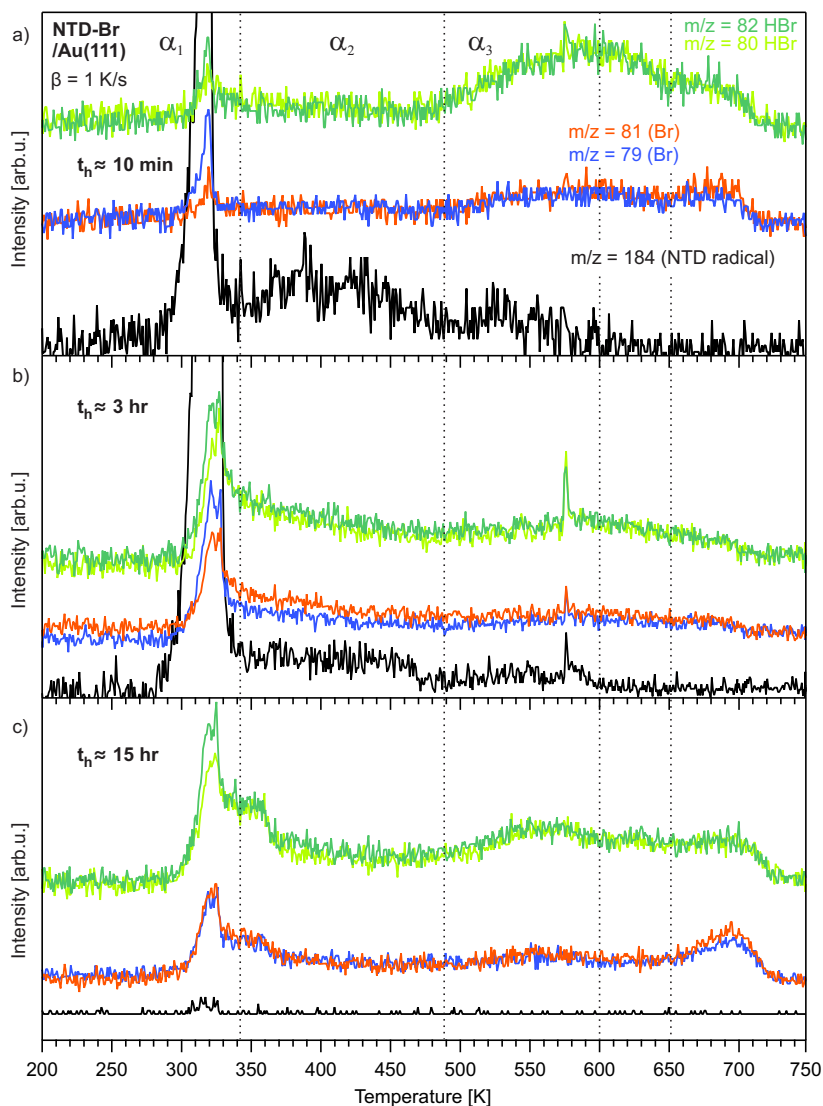
Figure 3.20.: Fragment-mass-resolved TPD spectra of NTD-Br for different selected fragments adsorbed on Au(111). The spectra measured (a) immediately after sample preparation ($\simeq 10$ min), (b) after approximately 3 h and (c) 15 h, with a heating rate of $\beta = 1$ K/s. The dashed lines separates the desorption regions. The desorption features of the biradical fragment (m/z=184) are labelled with α_1, α_2 and α_3 in accordance with the corresponding coverage dependant TPD measurements of the molecule (see Figure 3.19 (b)).

Results and Discussion

The spectrum of the biradical fragment (m/z = 184), recorded immediately after sample preparation (3.20 (a)), exhibits the expected desorption features, i.e. a desorption from the multilayer coverage (α_1), compressed phase (α_2) and sub-monolayer coverage (α_3). The spectra of Br and HBr, also include two desorption features, which coincide at the multilayer desorption feature (α_1) and along the sub-monolayer desorption region extending from approximately 490K to 600K and beyond up to 725K. Noticeably, neither Br nor HBr exhibits a desorption feature at the desorption temperature region associated with the compressed phase (α_2). These observations suggests that at the multilayer coverage, NTD-Br desorbes intact, while at the compressed phase (α_2), the bromine atoms are dissociated from the aromatic backbone of the molecule and most likely remain on the substrate. Consequently, only the signal of the biradical fragment could be detected in the measured TPD spectra.

By further increasing the substrate temperature up to 750 K, other than the sub-monolayer coverage (α_3), the dissociated bromine atoms also desorb from the substrate, in both atomic (Br) and molecular (HBr) form, in what seems to be a two step desorption process. In the first step, extending from 490K to 650K, the intensities of the measured HBr spectra is clearly more pronounced than the one belonging to Br. This indicates that at this temperature range a hydrogen assisted desorption of bromine is the dominant desorption mechanism in comparison to the atomic (Br) desorption.

As proposed by Bronner *et al.*[178], the dissociated bromine atoms, which are adsorbed on the Au(111) substrate, together with the atomic hydrogen can desorb through an associative desorption process in form of HBr. The atomic hydrogen can be released via two reaction pathways, either by formation of H_2 or HBr.

The DFT calculations performed by Bronner *et al.*[178] indicates that formation of HBr is more likely due to higher activation barrier of H_2 formation, even though it is thermodynamically favoured. Therefore, in case of the adsorbed NTD-Br on Au(111), it can be assumed that by increasing the substrate temperature during the TPD measurement, the molecules undergo a dehydrogenation reaction[179], which leads to the release of atomic H and subsequently desorption of Br atoms via molecular HBr formation. This assumption may explain the pronounced rise of the HBr signal at temperatures ranging from 490K to 650K. This step is followed with a second desorption step ranging from 650K to 725K, which can be attributed to desorption from different adsorp-

tion sites. Noticeably, the respective masses of Br_2 and H_2 were also monitored but no trace for either of the masses could be detected in the measured TPD spectra.

By increasing the time interval between the sample preparation and the following TPD measurements to approximately 3 and 15 h, the discussed desorption trends of Br and HBr remains mostly unchanged, while the desorption spectrum of the biradical fragment ($m/z = 184$) disappears after approximately 15 h (see Figure 3.20 (b) and (c)). This observation confirms the assumption that the NTD-Br samples undergo a time dependent process. Given that samples were kept at below 100 K at all time, before performing the TPD measurements, and the absence of a pronounced desorption feature associated with the biradical fragment at the expected multilayer desorption temperature (α_1) as well as the compressed phase (α_2) and the sub-monolayer coverage (α_3), it can be assumed that the time dependent process is not affected by the substrate temperature.

Considering the change in the desorption behaviour of halogenated molecules with the passing of time, the question arises as to weather the adsorption geometry of the corresponding molecules also changes accordingly. To answer this question, it was chosen to perform vibrational HREELS measurements on the mono - and multilayer coverages of NTD-Br after approximately 15 h of preparing the samples and compare the obtained results with the measured vibrational spectra of the sample immediately after preparation (which lasts approximately 3 h). A comparison between the spectra measured at different time intervals reveals that the identified and assigned vibrational modes of NTD-Br after approximately 15 h of sample preparation at both mono - and multilayer coverage (see Figure D.5 (c) and (d)) are similar to ones in the spectra of the molecule, which are measured immediately after the sample preparation (see Figure D.4 (a) and (b)), with little to no change in the energetic positions of the corresponding vibrations. This indicates that the adsoption geometry of the molecule within the thin film and at the interface with Au(111) is not affected with the passing of time up to 15 h. The only significant change that can be found between the compared spectra is an increased in the intensity ratio between the specular and off-specular scattered electrons for the detected vibrations in the spectra of the mono - and multilayer coverages of the sample after 15 h in comparison to the vibrations detected in the spectra of the sample measured immediately after preparation. This

may hints to formation of a more ordered molecular pattern and/or packing of NTD-Br by passing of time.

As for NTD-Cl, similar trends were observed in the obtained spectra from the conducted fragment-mass-resolved TPD (see Figure D.2 (a) and (b)) as well as vibrational HREELS (see Figure D.5 (a) and (b)) measurements on different coverages of the molecule. This suggests that nature of the halogen (either Cl or Br) does not influence the purposed processes occurring to the halogenated molecules.

It should also be noted that a comparison between electronic HREELS spectra of NTD-Br at its multilayer coverage, which were measured over a period of 15 hr showed that by passing of time, the electronic loss features associated with the molecule remain unchanged. This indicates that the time dependant process, does not effect the electronic properties of the molecule.

Overall, based on the results from TPD measurements it can be concluded that NTD-Br and NTD-Cl undergo a temperature as well as a time dependant process on Au(111), which are independent from one another. In case of temperature dependent process further investigation is required, in order to determine the effect of temperature on the adsorption properties as well as final composite of the adsorbates. Similarly, more information is needed to elucidate the mechanism behind time dependent process, which is taking place in the corresponding samples.

In the following, angle-resolved vibrational HREELS measurement is utilized to further investigate the influence of core halogenation of NTD on the adsorption geometry of the molecule on Au(111). Figure 3.21 shows the vibrational spectra of NTD (left) and NTD-Cl (right) adsorbed on Au(111), for mono - (a and d) and multilayer (b and e) coverages, measured in specular (black spectra) and off-specular (red spectra) electron scattering geometry along with the calculated intensities and frequencies of vibrational modes possessing a dynamic dipole moment perpendicular to the molecular backbone (c and f).

The spectra of NTD at the mono - and multilayer coverage (see Figure 3.21 (a) and (b)) include six pronounced vibrations with high intensity ratio between the specular and off-specular scattered electrons, which can be considered as dipole-active vibrations with dipole scattering being their main excitation mechanism.
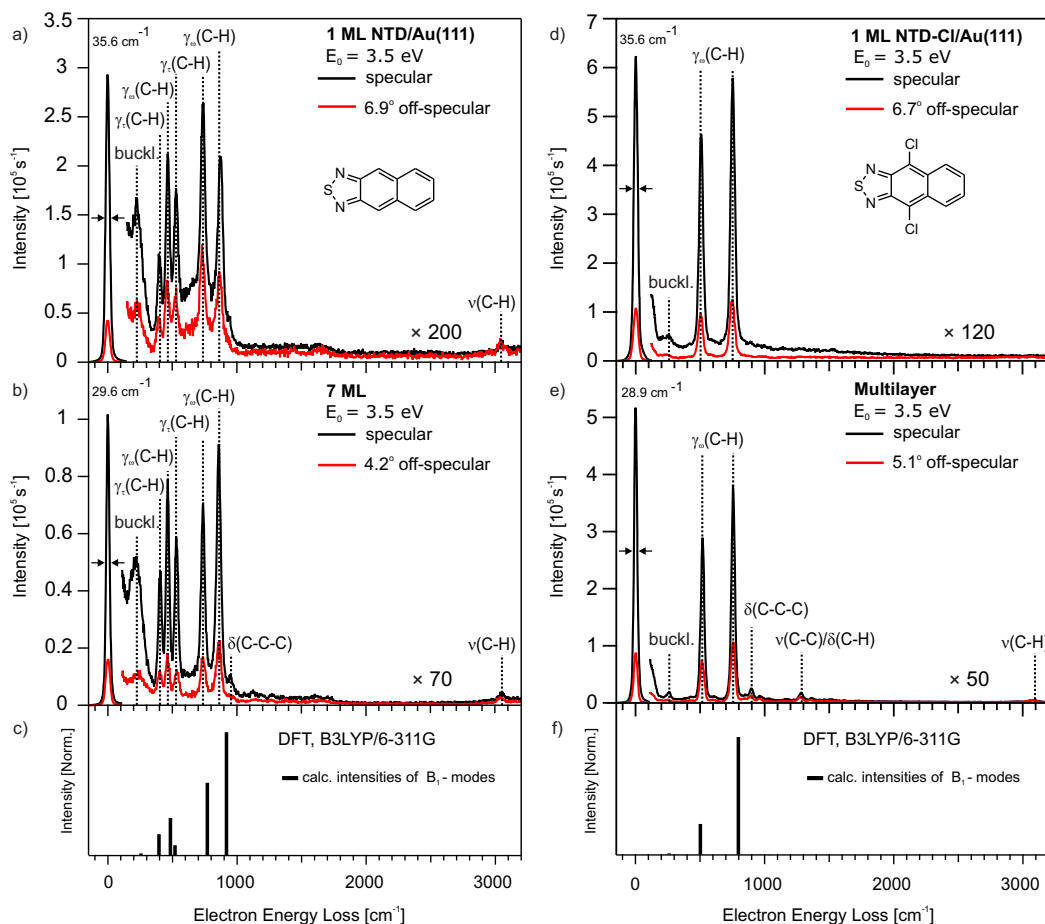
Figure 3.21.: Vibrational HREELS spectra of NTD (Left) and NTD-Cl (right) measured in specular (black spectra) and off-specular (red spectra) scattering geometry for mono - (a and d) and multilayer (b and e) coverages on Au(111) with the associated DFT-calculations (B3LYP/6-311G) for intensities and frequencies of B_1 symmetric vibrational mode with a dynamic dipole moment perpendicular to the molecular plane (c and f). E_0 is the primary energy of the incident electrons. The energy resolution of the specular spectra is measured as the full width at half maximum (FWHM) of the elastic peak (zero energy loss peak) and is given in wavenumbers (cm^{-1}). The assigned vibrations are listed in tables 3.3. Adapted from Ref. [177].

Results and Discussion

By comparing the obtained vibrational spectra with the calculated intensities and frequencies of B_1 vibrational modes of the corresponding D_{2v} molecular point group in the gas phase (see Figure 3.21 (c)), the dipole-active vibrations are assigned to the buckling mode (at 221 cm^{-1}), out-of-plane γ_τ(C-H) twisting mode (at 738 cm^{-1}) and its combination with γ_τ(N-S) twisting modes (at 408 and 528 cm^{-1}) and γ_ω(C-H) wagging modes (at 463 and 857 cm^{-1})[177]. Additionally, the spectra include two vibrations at 951 cm^{-1} (only in the multilayer spectrum) and 3043 cm^{-1} with only small or no difference between the intensities of their specular and off-specular scattered electrons. This indicates that the main excitation mechanism for these vibrations is impact scattering and as such they correspond to non-dipole-active vibrations. With a comparison to the results from the DFT calculations, these vibrations are assigned to the in-plane δ(C-C-C) deformation and ν(C-H) stretching modes[177]. By comparing the measured mono - and multilayer spectra of NTD, it becomes evident that by increasing the coverage to 7 ML, thus increasing the distance of the molecules at higher layers from the metallic substrate, the overall intensity of the dipole-active vibrations decreases relative to the rest of the spectrum. Furthermore, at the multilayer coverage, the intensity of the assigned γ_ω(C-H) vibration at 857 cm^{-1} is increased relative to other dipole - active vibrations.

In case of NTD-Cl, the spectra of the mono - and multilayer coverage are dominated by two high intensity dipole-active vibrations at 519 and 754 cm^{-1} as shown in figure 3.21 (d) and (e). By comparing these results with the calculated intensities and frequencies of B_1 vibrational modes of the corresponding D_{2v} molecular point group in the gas phase (see Figure 3.21 (f)), the given vibrations are assigned to the out-of-plane γ_ω(C-H) wagging modes[177]. Similarly, with another comparison with the results from DFT calculations, other accompanied vibrations are assigned to the non-dipole-active buckling mode (at 260 cm^{-1}) as well as in-plane δ(C-C-C) deformation, ν(C-C) and ν(C-H) stretching modes (at 896, 1284 and 3079 cm^{-1}) in the multilayer spectrum[177].

As for NTD-Br, the identified and assigned vibrations in the measured spectra of the molecule are similar to the ones discussed for NTD-Cl (see Figure D.4). This indicates that halogenation with Br atoms does not change the adsorption geometry of the molecule compared to NTD-Cl. In contrast to NTD, the vibrational spectra of NTD-Cl and NTD-Br exhibit fewer dipole-active vibrations, which is clearly due to halogenation of the corresponding molecules. Table 3.3 provides more details on the assignment of the identified vibrations

of NTD and its halogenated derivatives.

The results from DFT calculations on all three molecules indicate that the assigned dipole-active vibrations posses a dynamic dipole moment perpendicular to the molecular plane (x-direction) (see Figure 3.22), while the dynamic dipole moment of the assigned non-dipole-active vibrations is parallel with the molecular plane along the short axis (y-direction) (see Figure D.6)[177]. Considering that the spectra of NTD, NTD-Cl and NTD-Br at mono - and multilayer coverage consists of predominantly dipole-active vibrations with large components of their dipole moment perpendicular to the Au(111) surface, it can be concluded that at all coverages, NTD and its halogenated derivatives adopt a planar adsorption geometry on Au(111), in which the molecular backbone of the adsorbates are oriented parallel with the substrate surface[177]. This indicates that halogenation with Br and Cl atoms does not change the adsorption geometry of the molecule compared to the parent NTD.

Table 3.3.: Assigned vibrations (in cm^{-1}) of NTD, NTD-Cl and NTD-Br adsorbed on Au(111) for different initial coverages. Additionally, the corresponding DFT calculated frequencies of the molecules in the gas-phase at the B3LYP level and the 6-311G basis set are given. Dipole active modes are labelled with *da*. The identified modes for each vibration are described with the following abbreviations; γ – out-of-plane; δ – deformation; ν – stretching; τ – twisting; ω – wagging. Representation (Repr.) of the associated point groups and the orientation of the calculated dipole derivative vector with respect to the molecular geometry, x, perpendicular to the molecular plane; y, short axis and z, long axis of molecular backbone for each mode are listed. Adapted from Ref. [177].

NTD

#	1 ML	7 ML	DFT	Mode	Repr.
1	221 *da*	221 *da*	257	buckling	B$_1$(x)
2	400 *da*	408 *da*	396	γ_τ(C-H), γ_τ(N-S)	B$_1$(x)
3	465 *da*	463 *da*	484	γ_ω(C-H)	B$_1$(x)
4	530 *da*	528 *da*	520	γ_τ(C-H), γ_τ(N-S)	B$_1$(x)
5	736 *da*	738 *da*	770	γ_τ(C-H)	B$_1$(x)
6	875 *da*	857 *da*	917	γ_ω(C-H)	B$_1$(x)
7	-	951	949	δ(C-C-C)	B$_2$(y)
8	3058	3043	3165	ν(C-H)	B$_2$(y)

NTD-Cl

#	1 ML	Multilayer	DFT	Mode	Repr.
1	250	260	260	buckling	B$_1$(x)
2	508 *da*	519 *da*	502	γ_ω(C-H), γ_τ(N-S)	B$_1$(x)
3	750 *da*	754 *da*	795	γ_ω(C-H)	B$_1$(x)
4	-	896	970	δ(C-C-C)	B$_2$(y)
5	-	1284	1309	ν(C-C), δ(C-H)	B$_2$(y)
6	-	3079	3181	ν(C-H)	B$_2$(y)

NTD-Br

#	1 ML	Multilayer	DFT	Mode	Repr.
1	238	256	263	buckling	B$_1$(x)
2	506 *da*	521 *da*	516	γ_ω(C-H), γ_τ(N-C)	B$_1$(x)
3	745 *da*	760 *da*	811	γ_ω(C-H)	B$_1$(x)
4	-	892	968	δ(C-C-C)	B$_2$(y)
5	-	1260	1308	ν(C-C), δ(C-H)	B$_2$(y)
6	-	3068	3180	ν(C-H)	B$_2$(y)

a)
$\vec{\mu}$
buckling
221/221/257 cm^{-1}

b)
$\vec{\mu}$
γ_τ(C-H), γ_τ(N-S)
400/408/396 cm^{-1}

c)
$\vec{\mu}$
γ_ω(C-H)
465/463/484 cm^{-1}

d)
$\vec{\mu}$
γ_τ(C-H), γ_τ(N-C)
530/528/520 cm^{-1}

e)
$\vec{\mu}$
γ_τ(C-H)
736/738/770 cm^{-1}

f)
$\vec{\mu}$
γ_ω(C-H)
875/857/917 cm^{-1}

g)
$\vec{\mu}$
γ_ω(C-H) ,γ_τ(N-S)
508/519/502 cm^{-1}

h)
$\vec{\mu}$
γ_ω(C-H)
750/754/795 cm^{-1}

Figure 3.22.: Visualisation of the assigned dipole-active vibrational modes obtained from the DFT calculations (B3LYP/6-311G) for NTD (a-f) and NTD-Cl (g and h). The corresponding energies (HREELS monolayer/HREELS multilayer/DFT) are given in wavenumbers (cm^{-1}). The direction of the calculated dipole derivative unit vector ($\vec{\mu}$) is depicted with a black arrow that lies in the plane of the paper. The atomic displacements in each visualization are shown with red arrows. The vibrational modes are visualized by the Avogadro[180] software. Adapted from Ref.[177].

Results and Discussion

Finally, the electronic HREELS is utilized to investigate the influence of core halogenation in NTD-Cl and NTD-Br on their electronic properties in comparison to NTD at the interface with Au(111) and within their thin film. Figure 3.23 shows the electronic HREELS spectra of NTD (Left) and NTD-Cl (right), for mono - (a and c) and multilayer (b and d) coverages measured with the primary electron energy of 15 eV, together with the corresponding UV/Vis spectra of the molecules measured in dichloromethane (CH_2Cl_2) solution (orange spectra).

As shown in figure 3.23 (a), the monolayer spectrum of NTD, includes multiple electron energy loss features at 1.8, 2.7, 3.5, 4.4, 4.9 and 5.8 eV . By increasing the coverage of NTD to 7 ML, the decoupling of molecules from the metallic substrate leads to a significant change in the spectrum of the molecule as can be seen in figure 3.23 (b). At the multilayer coverage, the previously detected loss feature at 2.7 eV in the monolayer spectrum, corresponds to the maximum loss peak (2.8 eV) of the vibrational contributions accompanying the loss feature at 2.6 eV, which is assigned to the transition of the ground state (S_0) to the first singlet excited state (S_1), i.e. the optical gap of NTD[177]. In the molecular orbital picture, the $S_0 \rightarrow S_1$ transition corresponds to the excitation of a single electron from HOMO into the LUMO. The vibrational contribution associated with this transition can be attributed to the so-called breathing modes of the molecular backbone, namely the ν(C-C) stretching mode of NTD with frequencies in rang of 1400-1700 cm^{-1} (174-210 meV)[177]. By utilizing the excited-state calculations in the gas phase, the loss features at 3.5, 4.5, 5 and 5.85 eV are assigned to the transitions of S_0 to the singlet excited states at S_2 (HOMO - 1 $\rightarrow$ LUMO or α - band), S_5 (HOMO - 2 $\rightarrow$ LUMO or β - band), S_8 (HOMO $\rightarrow$ LUMO + 5) and S_{17} (HOMO - 5 $\rightarrow$ LUMO), respectively[177]. The remaining unassigned loss feature at 1.8 eV at the monolayer coverage (1.75 eV at multilayer coverage), is located beneath the assigned $S_0 \rightarrow S_1$ transition of the molecule (at 2.6 eV) and is not present in the corresponding UV/Vis spectrum of NTD in solution. Similar loss features have also been detected in the spectra of PEN, DAP and TAP, which are assigned to $S_0 \rightarrow T_1$ transition of the corresponding molecules (see section 3.1). The calculated value of T_1 for NTD is 1.77 eV[177], which is in good agreement with the obtained experimental value of 1.75 eV from the measured multilayer spectrum. Therefore, this loss feature is assigned to the $S_0 \rightarrow T_1$ transition of NTD[177].
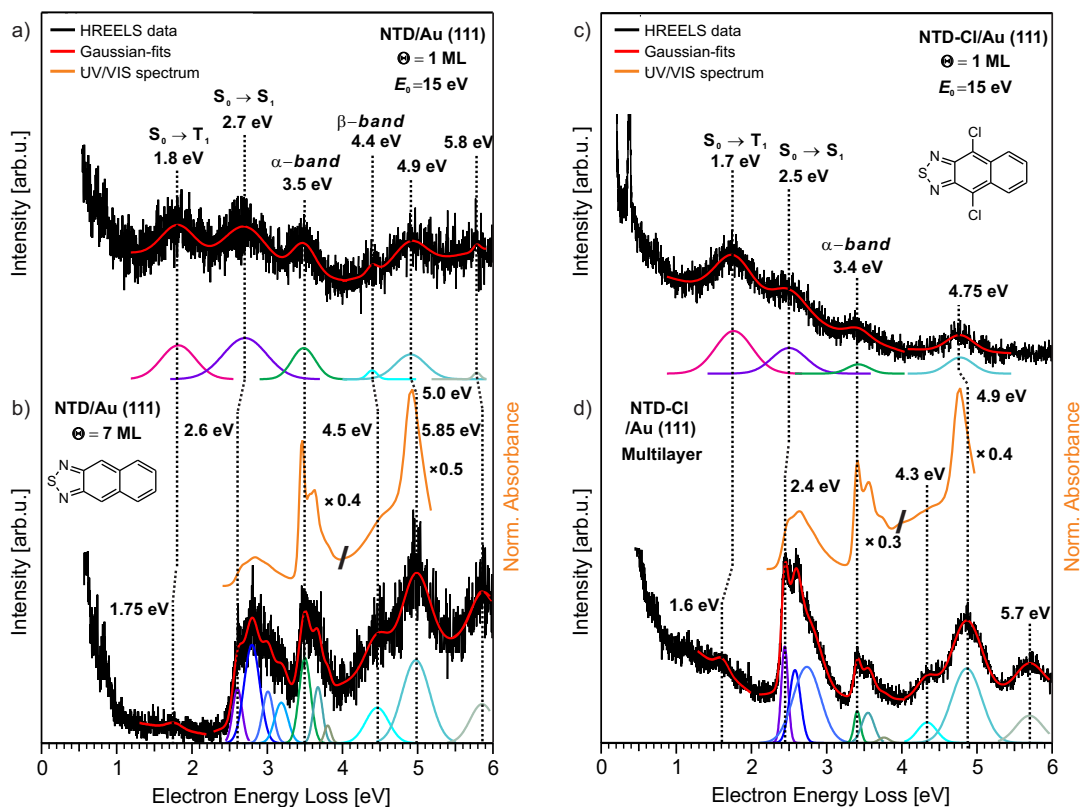
Figure 3.23.: Electronic HREELS spectra of adsorbed NTD (Left) and NTD-Cl (right) on Au(111), measured for mono - (a and c) and multilayer (b and d) coverages (black spectra). The electronic loss features were fitted using Gaussian functions (red curves). The corresponding UV/Vis spectra of the molecules are measured in dichloromethane (CH_2Cl_2) (orange spectra). E_0 is the primary energy of the incident electrons. Θ is the coverage in monolayer (ML). Adapted from Ref.[177].

Similarly, the calculated value of T_1 energy for NTD-Cl (1.62 eV) indicates that the detected loss feature at 1.7 eV in the monolayer spectrum of the molecule originates from the $S_0 \rightarrow T_1$ transition of NTD-Cl[177] (see Figure 3.23 (c)) . At the multilayer coverage, this transition is shifted by 100 meV to a lower energy at 1.6 eV (see Figure 3.23 (d)). In the multilayer spectrum, the previously detected loss features at 2.5 eV, 3.4 eV and 4.75 eV for the monolayer coverage correspond to the loss features at 2.4, 3.4 and 4.9 eV, which together with two other loss features at 4.3 and 5.7 eV are assigned to the transition of S_0 to the singlet excited states at S_1 (optical gap), S_2 (α band), S_5, S_8 and S_{17}, respectively[177].

In case of NTD-Br, the detected and assigned transitions in the spectra of the mono - and multilayer coverages of the molecule resembles the ones assigned in the spectra of NTD-Cl, particularly the $S_0 \rightarrow T_1$ and $S_0 \rightarrow S_1$ transitions, which are located at similar energies of 1.6 and 2.4 eV (see Figure D.7 (a) and (b)). However, for NTD-Br, the energies of the $S_0 \rightarrow S_8$ and $S_0 \rightarrow S_{17}$ transitions are decreased by 100 meV from 4.9 to 4.8 eV for S_8 and by 200 meV from 5.7 to 5.5 eV for S_{17} compared to NTD-Cl.

A comparison between the multilayer HREELS spectra of NTD and its halogenated derivatives revels that chlorination in NTD-Cl and bromination in NTD-Br results in a narrowing of the optical gap by 200 meV from 2.6 eV for NTD to 2.4 eV for NTD-Cl and NTD-Br (see Figure 3.24)[177]. Similarly, other transition energies of the halogenated molecules are also red-shifted compared to NTD (see Figure 3.25). This effect is attributed to the substitution of hydrogen atoms in the halogenated molecules with electron withdrawing chlorine and bromine atoms with much higher electronegativity[177]. A similar trend has also been observed for C_3F_7 (perfluorinated propyl chains) substituted 1,3,8,10-Tetraazaperopyrene (TAPP-H) and its halogenated derivatives, namely TAPP-Cl and TAPP-Br[95].

The assigned transitions of NTD and its halogenated derivatives, particularly $S_0 \rightarrow S_1$, in the measured spectra of the molecules at their multilayer coverage are in good agreements with the corresponding transitions in the UV/Vis spectra of the molecules in solution (see Figure 3.24). This indicates that the influence of the metal substrate (adsorbate/substrate-interactions) and the intermolecular forces (adsorbate/adsorbate-interactions) on the electronic states of the molecules in the thin film are negligible[177].
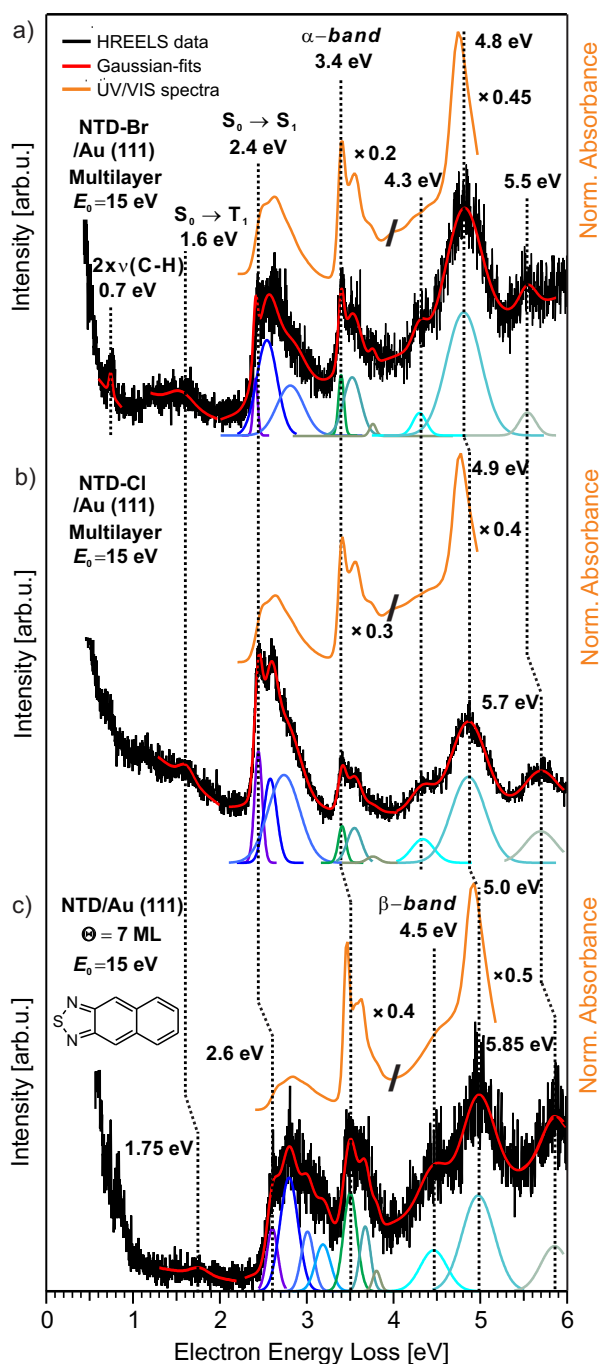
Figure 3.24.: Electronic HREELS spectra of adsorbed (a) NTD-Cl, (b) NTD-Br and (c) NTD on Au(111) measured for the multilayer coverage (black spectra). The electronic loss features were fitted using Gaussian functions (red curves). The corresponding UV/Vis spectra of the molecules are measured in dichloromethane (CH_2Cl_2) (orange spectra). E_0 is the primary energy of the incident electrons. Θ is the coverage in monolayer (ML). Adapted from Ref.[177].
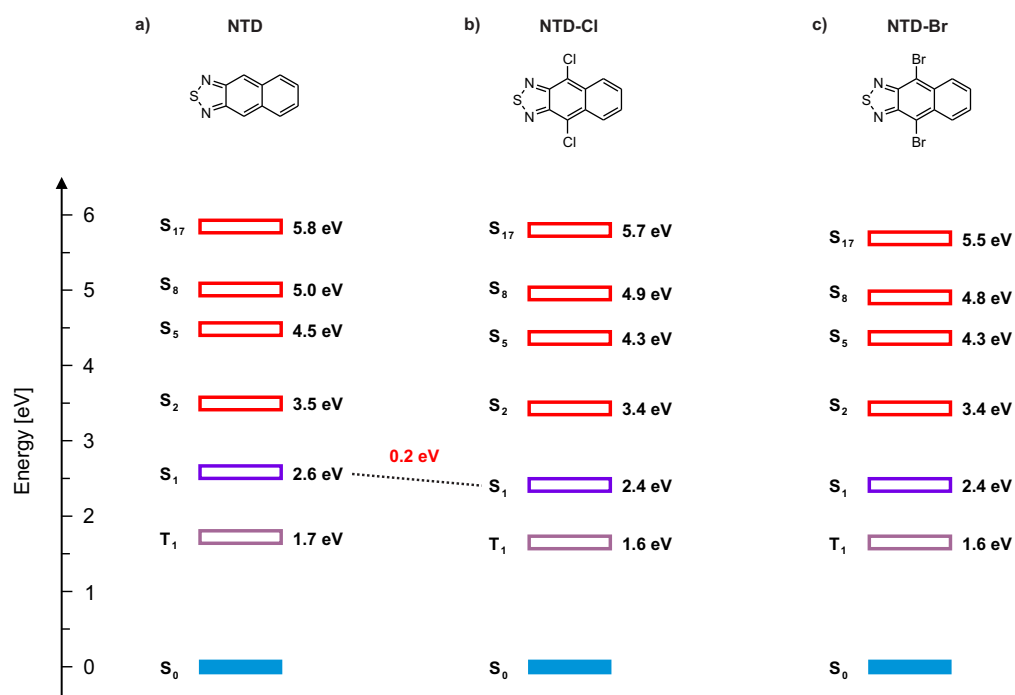
Figure 3.25.: The identified and assigned energies of electronic transitions of the singlet (S) and lowest triplet (T_1) states via electronic HREELS for multilayer coverages of (a) NTD, (b) NTD-Cl, and (c) NTD-Br adsorbed on Au(111). Adapted from Ref. [177].

3.2. Influence of Core substitution on the Properties of Thiadiazole Derivatives

To summarize, in this subsection it has been demonstrated that thin films of NTD and its halogenated derivatives can be prepared through deposition of the corresponding molecules at 300 K (NTD), 368 K (NTD-Cl) and 388 K (NTD-Br) into the ultra-high vacuum chamber and onto Au(111) substrate held at 200 K. The prepared samples were then characterized by TPD, vibrational and electronic HREELS in combination with DFT calculations. Based on the results from the fragment-mass-resolved TPD measurements it was determined that the halogenated molecules undergo a temperature as well as a time dependant process on Au(111). The former seems to takes effect in temperatures ranging from 340K to 650K, while the later is assumed to be temperature independent. Therefore, well-defined monolayers of the molecules were prepared by deposition of a large amounts of molecules adding up to the multilayer or 2nd-layer coverage and subsequently heating the sample up to 300 K (NTD), 340 (NTD-Cl) and 350 K (NTD-Br), just beyond the multilayer desorption temperature of NTD and beneath the desorption temperature of the associated compressed phase of the halogenated molecules, in order to desorb the higher laying layers, while preserving the monolayer coverage. The results from the coverage dependent TPD measurements on the molecules indicates that core halogenation in NTD-Cl and NTD-Br results in an increase in adsorbate/adsorbate and adsorbate/substrate-interaction for the corresponding molecules in comparison to parent NTD. Moreover, as shown via vibrational HREELS measurements, NTD and its halogenated derivatives at their mono- and multilayer coverages adopt a planar adsorption geometry on the Au(111) surface, in which the backbone of the molecule is oriented parallel to the substrate. Finally, through electronic HREELS measurements, it is found that core halogenation in NTD-Cl and NTD-Br results in a reduction of the transition energies of singlet and first triplet states in comparison to NTD. This is evident from the narrowing of the optical gap by 200 meV from 2.6 eV for NTD to 2.4 eV for NTD-Cl and NTD-Br as well as shift of the assigned $S_0 \rightarrow T_1$ transition to the lower energy by 150 meV from 1.75 eV for NTD to 0.6 eV for NTD-Cl and NTD-Br. This effect is attributed to the influence of electron withdrawing halogens with much higher electronegativity than hydrogen atoms on the electronic structure of the halogenated molecules. Noticeably, the influence of the substituted Cl and Br atoms on the transition energies of the S_1 and T_1 states is similar.

3.2.2. Benzobisthiadiazole Derivatives

Similar to NTD, the parent BBT is widely used as an electron acceptor moiety in a variety of donor–acceptor (D–A) molecular systems[71;72;74;77;79;82;181] owing to its high acceptor strength[70]. BBT was first introduced by Ono *et al.*[52] in 1994 as a heterocyclic molecule containing hypervalent sulfur atoms. This molecule is formed by adding two thiadiazole units to the benzene ring, thus increasing the acceptor strength of the molecule from an electronically neutral benzene to the strong electron withdrawing BBT, with benzothiadiazaole (BT) having a weaker electron withdrawing strength[70] (see Figure 3.26 (a)). The calculated energy levels of the frontier orbitals indicates that addition of the second thiadiazole unit in BBT results in reduction of the LUMO energy level of BT from -2.8 eV to -3.853 eV for BBT and consequently the size of the optical gap is reduced from 3.573 eV for BT to 2.252 eV for BBT[182].
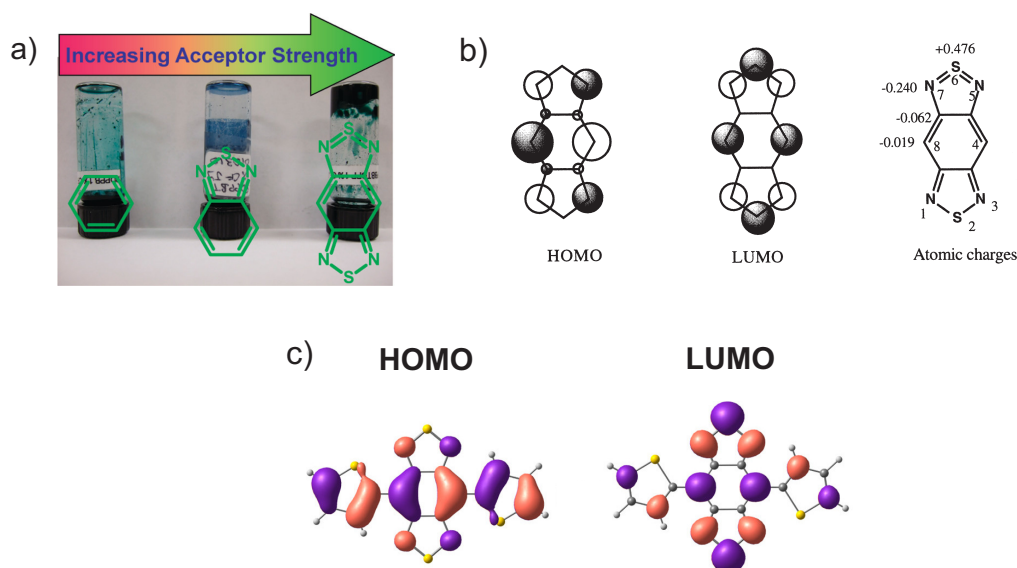
Figure 3.26.: (a) Visual representation of increasing acceptor strength from benzene to benzothiadiazaole and BBT, adapted from Ref.[70]. (b) HOMO and LUMO in BBT and the calculated net atomic charges of the molecule, adapted from Ref.[181]. (c) HOMO and LUMO plots of BBT-Th, adapted from Ref.[183].

Computations conducted on BBT indicates that HOMO and LUMO at the 4- and 8- positions of the central six-ring of the molecule have larger atomic orbital coefficients[52;181] (see Figure 3.26 (b)). As such, introduction of substituents in these positions is used to modify the properties of BBTs[52;181]. For example, substitution of parent BBT (calculated HOMO-LUMO gap = 5.52

eV[181]) by electron-withdrawing bromine atoms leads to a shift of absorption maxima (λ_{max}) of the molecule to 524 nm (2.36 eV) and formation of a network between two ribbon-type columns of the molecule within its crystal structure via short Br-N contacts[52]. Substitution of BBT with other atoms, such as O, in similar fashion has also been reported in literature[184], which further highlights the importance of nature of substituents on the final properties of the corresponding molecules.

Other than atoms, aromatic groups such as phenyl and thiophene were also used as substituents, in order to influence the properties of BBTs[52;53]. Thus, by introduction of phenyl and thiophene groups in the 4- and 8- positions of BBT, two non-classical benzobis(thiadiazole) compounds, namely BBT-Ph and BBT-Th are formed, which have smaller HOMO-LUMO gap (optical gap) in comparison to the corresponding Kekulé-type compounds[181]. The measured λ_{max} of phenyl substituted BBT (BBT-Ph) in solution (CH_2Cl_2) is 558 nm (2.22 eV)[181]. BBT-Ph is reported to be centrosymmetric, with phenyl groups twisted relative to planar BBT moiety with dihedral angle of 45.9° as observed in the in X-ray structure analysis of its single crystal[181]. In contrast to brominated BBT, BBT-Ph have a simpler crystal structure, which consists of tape-like networks of the molecule. This packing motif is the result of S-N interactions between BBT-Ph molecules, which is caused by an electrostatic effect that is induced by positively charged sulfur atoms and negatively charged nitrogen atoms[181]. Substitution of BBT with the thiophene (BBT-Th), which itself is an aromatic donor, narrows the optical gap of the molecule even further to 702 nm (1.77 eV, in $CHCl_3$)[53]. Calculated frontier orbital energies of BBT-Th indicates that LUMO is mostly localized on the BBT moiety (see Figure 3.26 (c)). Karikomi *et al.* reports that with polymerization of BBT-Th, the optical gap of the polymer narrows down to 0.5 eV[53]. In contrast to BBT-Ph, X-ray structure analysis of BBT-Th indicates that the molecule is planar[53]. Therefore, aromatic groups (such as thiophene) can be used as electron donors with the o-quinoid type acceptors (such as BBT) to form D-A molecular systems with favourable electronic and structural properties.

Given the potential of BBT-Th as a prototype D-A molecular system with a narrow optical gap, in the context of this study, it was chosen to investigate this molecule as well as BBT-Ph in order to gain necessary insights into their adsorption and electronic properties at their thin films and interfaces with Au(111) substrate, which will be required for forming potential D–A molecular

systems in solid state.

The BBT-Ph and BBT-Th molecules were synthesized by Dr. Lukas Ahrens of the Prof. Dr. Uwe H. F. Bunz group of the Organisch-Chemisches Institut at the Universität Heidelberg.

For this study, BBT-Ph and BBT-Th samples were prepared, *in situ* by deposition of the corresponding molecules at 443 K (BBT-Ph) and 468 K (BBT-Th) into the UHV chamber and onto Au(111) substrate, held at room temperature (300 K). First, through coverage dependent and fragment-mass-resolved TPD measurements, the possibility of preparing thin films and well-defined monolayers of the molecules on Au(111) surface is investigated and subsequently, the influence of core substitution via aromatic groups (phenyl and thiophene) on the adsorption properties of the molecules within the thin film and at the interface with Au(111) is explored.

Figure 3.27 (a) shows the coverage dependent TPD spectra of BBT-Ph with different initial coverages ranging from 3 to 11 ML for the selected mass-to-charge ratio (m/z) of 173, which corresponds to either the doubly charged parent molecular ion with the molecular mass of 346 *amu* or the ionic fragment of the half of the molecule (the structure formula is depicted in Figure 3.27 (a)). The spectra consist of two desorption regions. The first region includes a desorption peak around 376 K (α_1), while the second region includes a desorption feature at 437 K (α_2), which is followed by a broad desorption feature extending from 470 K to 620 K (α_3) (see inset in Figure 3.27 (a)). The α_1 peak exhibit zero-order desorption behaviour and does not saturates with increasing coverage. Thus, it is assigned to the desorption of a multilayer coverage. The α_2 peak posses the distinct desorption characteristic of a more densely packed compressed phase as observed for NTD-Br and NTD-Cl. Therefore, α_2 is assigned to the desorption of the compressed phase. Consequently, α_3 is attributed to the desorption of a sub-monolayer coverage. Thereby, the desorption spectrum of a monolayer coverage can be defined as a spectrum, in which both α_2 and α_3 are saturated. The inset shows the enlarged mono-layer desorption region of the measured spectrum with the coverage of 3 ML, extending from 400 K to 620 K. In this study, the coverage of the adsorbed BBT-Ph molecules on the substrate is determined by integrating the corresponding TPD spectrum and comparing the total integral with the area of the monolayer desorption region (α_2 and α_3)[110].
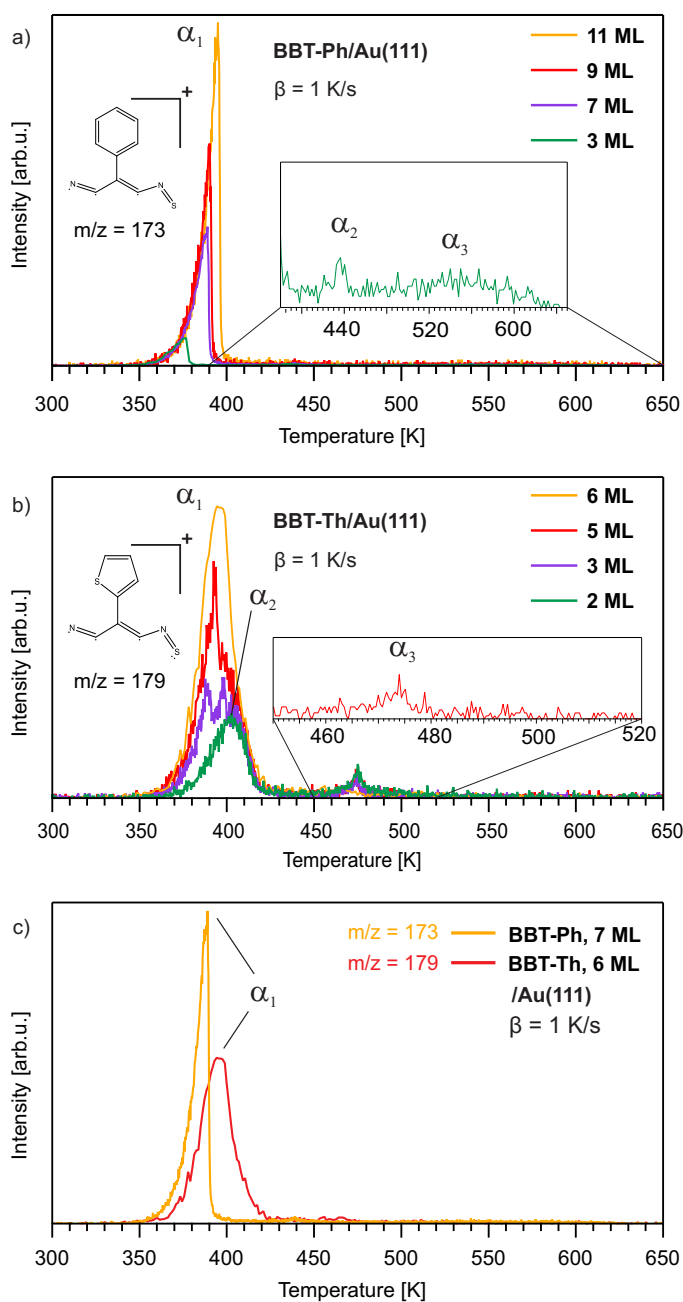
Figure 3.27.: Coverage dependent TPD spectra of (a) BBT-Ph for the selected mass-to-charge ratio (m/z) of 173 and (b) BBT-Th for the selected m/z of 179 adsorbed on Au(111) with different initial coverages, measured with a heating rate of $\beta = 1$ K/s. (c) Shows an overlay of the TPD spectra of BBT-Ph and BBT-Th. The desorption features are labelled with α_1, α_2 and α_3. The insets show the compressed phase (α_2 in BBT-Ph and α_3 in BBT-Th) and the sub-monolayer desorption feature (α_3 in BBT-Ph). The structural formulas of the selected ionic fragments from each molecule are depicted in their corresponding figures.

Results and Discussion

In case of BBT-Th (m = 358 amu), as shown in figure 3.27(b), the measured coverage dependent TPD spectra of the doubly charged molecule (m/z = 179) or the ionic fragment of the half of the molecule (the structure formula is depicted in Figure 3.27 (b)) consist of two desorption regions for different initial coverages ranging from 2 to 6 ML. The first region includes two desorption peaks around 390 K (α_1) and 400 (α_2). The α_1 peak does not saturates with increasing coverage. Therefore, it is assigned to the desorption of a multilayer coverage. The α_2 peak appears to be at its maximum at the 2nd-layer and subsequently merges to the multilayer desorption peak (α_1) at higher coverages. Thus, α_2 can be assigned to the 2nd-layer desorption. A similar trend has also been found in the coverage dependent TPD spectra of NTD (see Figure 3.19 (a)) and TIPS-BAP (see Figure 3.11 (a)). The second region consists of a desorption peak at 470 K (α_3, see inset in Figure 3.27 (b)), which has a similar desorption profile as the assigned α_2 peak in the TPD spectra of BBT-Ph. Similarly, the α_3 peak can be assigned to a more densely packed compressed phase of BBT-Th monolayer coverage. In contrast, the sub-monolayer desorption feature as detected in the spectrum of the BBT-Ph (α_3) is not present in the spectrum of the BBT-Th, which suggests that the sub-monolayer coverage of BBT-Th either does not desorb from the substrate or degrades by increasing temperature during the TPD measurements and as the result does not desorb intact.

This observation is confirmed by the results from the conducted vibrational HREELS measurements on BBT-Th after heating the samples up to 750 K, well beyond the expected desorption temperature of the sub-monolayer coverage. The obtained spectra includes vibrational peaks, which are associated with the adsorbates (see Figure E.3 (c)). The detected vibrations can not be assigned to any of the vibrational modes of BBT-Th, which indicates a possible degradation of the molecule at high substrate temperatures. In contrast, no distinct vibration, which can be associated with adsorbates could be detected in the vibrational spectrum of BBT-Ph (see Figure E.3 (a)), after a similar annealing step (heating the sample up to 750 K), which suggests that the sub-monolayer coverage of BBT-Ph desorbs intact from the Au(111) substrate. Therefore, it can be assumed that substitution of thiophene group in BBT-Th results in a stronger interaction between the molecule and the substrate in comparison to BBT-Ph. This assumption is supported by the shift of the desorption peak associated with the compressed phase (α_3) of BBT-Th by

33 K to a higher temperature at 470 K, when compared to the one assigned for BBT-Ph at 437 K.

Figure 3.27 (C) shows an overlay of the TPD spectra of BBT-Ph (7 ML) and BBT-Th (6 ML). A comparison between the two spectra clearly shows the change in the desorption temperatures of the adsorbates, which highlights the influence of the substituted aromatic group on the adsorption properties of the corresponding molecules and further confirms the effect of the substituted thiophene group in BBT-Th in increasing the adsorbate/adsorbate and adsorbate/substrate-interactions within the thin film and at interface with Au(111). Given the fact that the entirety of the monolayer desorption region of BBT-Th, consisting of the compressed phase (α_3) and the sub-monolayer coverage, could not be detected in the corresponding spectra of the molecule, instead area underneath the second layer desorption peak (α_2) was used as the reference for determining the coverage of the adsorbed BBT-Th molecules on the substrate as described in appendix E.1. Therefore, the given number of layers for each coverage can only be taken as an estimate.

The fragment-mass-resolved TPD spectra of BBT-Ph and BBT-Th measured for selected fragments of the corresponding molecules are shown in figure E.2. For both molecules, the desorption features of the multilayer coverage (α_1), the compressed phase (α_2 in BBT-Ph and α_3 in BBT-Th) and the sub-monolayer coverage (α_3 in BBT-Ph) coincide at the same temperature for all of the selected fragments. Furthermore, the determined coverages of both molecules from each of their fragments are similar to their reference coverage of 3 ML (BBT-Ph) as measured for 173 m/z, with an exception for 141 m/z and 6 ML (BBT-Th) as measured for 179 m/z. These observations suggest that BBT-Ph at all coverages and BBT-Th at coverages higher than sub-monolayer do not degrade during the TPD measurements.

After assigning the desorption features of the adsorbed molecules and identifying their desorption temperatures, for further measurements, it was chosen to prepare the sub - and monolyer coverages of BBT-Ph and BBT-Th samples by direct evaporation of the molecules onto the substrate. The preparation parameters for the samples involving both molecules are given in table H.1.

In the next step, angle-resolved vibrational HREELS is utilized to investigate the influence of core substitution with different aromatic groups in BBT-Ph and BBT-Th on the adsorption geometry of the corresponding molecules on Au(111). Figure 3.28 shows the vibrational HREELS spectra of the molecules

adsorbed on Au(111), measured in specular (black spectrum) and off-specular (red spectrum) electron scattering geometry with the primary electron energy of 3.5 eV along with the calculated intensities and frequencies of vibrational modes possessing a dynamic dipole moment perpendicular to the molecular backbone.

The spectra of BBT-Ph at sub -, mono - and multilayer coverage include three distinct vibrations with high intensity ratio between the specular and off-specular scattered electrons, which are clearly dipole-active with dipole scattering being their main excitation mechanism (see Figure 3.28 (a) ,(b) and (c)). By comparing the results from the vibrational spectra with the calculated intensities and frequencies of B_3 vibrational modes of the corresponding D_2 molecular point group in the gas phase (see Figure 3.28 (d)), the identified dipole-active vibrations are assigned to the out-of-plane γ_ω(C-H) wagging mode (at 694 cm^{-1} and 762 cm^{-1}) and its combination with γ_ω(C-C-C) wagging mode (at 510 cm^{-1}) of the phenyl aromatic groups as visualized in figure 3.29. Similarly, other dipole-active vibrations, are assigned to the out-of-plane buckling mode (at 142 cm^{-1}, in the spectrum of the sub-monolayer coverage) and γ_ω(C-H) wagging mode (at 933 cm^{-1}) of the phenyl aromatic groups. Additionally, the spectra of the molecule include vibrations with low specular to off-specular intensity ratio at 223, 307, 866, 1092, 1192, 1366, 1456 and 3071 cm^{-1}, which are non-dipole-active and as such their main excitation mechanism is impact scattering. Once again, by comparing these values with the results from the DFT calculations, these vibrations are assigned to a series of in-plane modes, including the buckling, δ(C-C-C) scissoring, ω(C-H) wagging, ν_s(C-C-C), ν(C-C-C) and ν(C-N) stretching modes in combination with δ(C-H) scissoring and ν(C-H) stretching modes. A more detailed assignment of the identified vibrations for BBT-Ph is given in table 3.4.

The results from DFT calculations also indicates that the assigned dipole-active vibrations (see figure 3.29) posses dynamic dipole moments that are perpendicular to the molecular plane (x-direction), while the dynamic dipole moments of non-dipole-active vibrations (see figure E.4) are parallel to the molecular plane along the long axis (y-direction) or aromatic group of the molecule (z-direction).

At the sub - and monolayer coverage, the assigned vibrations in the spectra of the molecule are predominately dipole-active. This suggests that at these coverages, BBT-Ph adapts a planar adsorption geometry on Au(111) surface,

in which the molecular backbone of the adsorbates are oriented parallel to the substrate surface. However, the calculated geometry of BBT-Ph in the gas phase is not planar. As can be seen from the visualizations of the assigned vibrations (see Figures 3.29 and E.4), after energy relaxation and geometry optimisation, the phenyl groups in BBT-Ph are twisted by 36.9° with respect to its planar heterocyclic unit. For comparison, The angle of this twist in the crystal structure of BBT-Ph is reported to be 45.9°[181]. Given the fact that the DFT calculations were carried out on a single molecule in the gas phase, without considering the influence of intermolecular forces (adsorbate/adsorbate - interactions) and the metal substrate (adsorbate/substrate - interactions), it is unlikely that phenyl side groups in the adsorbed molecules on Au(111) remains twisted. Additionally, it is known that benzene itself adopt a planar adsorption geometry on Au(111)[185]. Considering these observations, it can be concluded that at sub - and monolayer coverage, phenyl side groups adapt a planar adsorption geometry on Au(111) surface and parallel to the backbone of the molecule. This also results in a change of the point group from D_2 for the molecule with the twisted side group to D_{2h} for the planar molecule.

As for the multilayer coverage, the measured spectrum include additional non-dipole-active vibrations, which are not present in the spectra of the sub - and monolayer coverage. These vibrations originates from both heterocyclic unit and the phenyl groups of the molecule. It is likely that by increasing the coverage of BBT-Ph to 11 ML, the adsorbed molecules at higher layers tilt out of the plane parallel to the substrate surface. Consequently, the dynamic dipole moments parallel to the molecular plane rotates towards an out-of-plane direction, which results in detection of the associated vibrations in the spectrum of the multilayer coverage. Considering the low specular to off-specular intensity ratio of these vibrations, the proposed tilt does not induce an excitation via dipole scattering mechanism for the given vibrations and the impact scattering remains the main excitation mechanism. Therefore, it can be concluded that BBT-Ph in its thin film adapt an adsorption geometry, which is mainly planar.
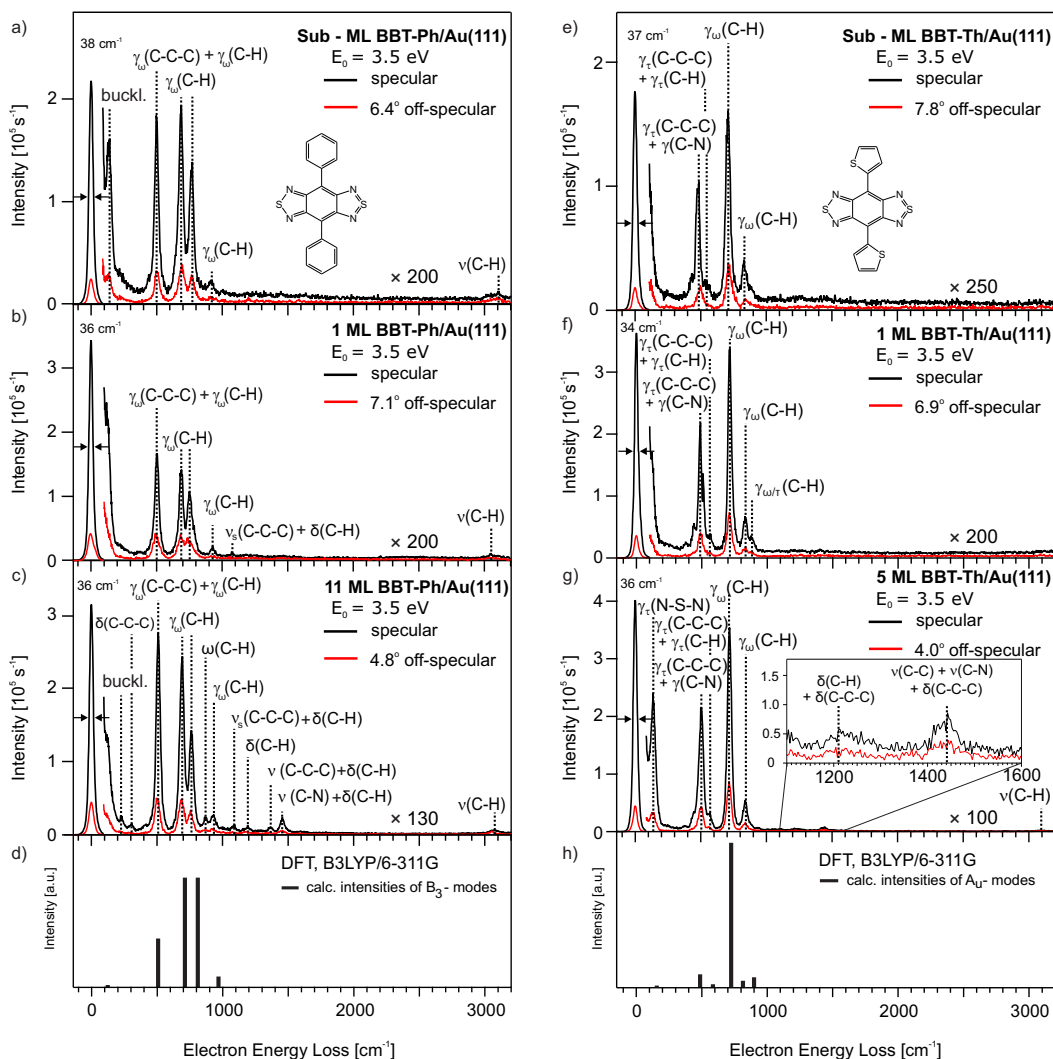
Figure 3.28.: Vibrational HREELS spectra of BBT-Ph (Left) and BBT-Th (right) measured in specular (black spectra) and off-specular (red spectra) scattering geometry for sub - (a and e), mono - (b and f) and multilayer (c and g) coverages adsorbed on Au(111) with the associated DFT-calculations (B3LYP/6-311G) for intensities and frequencies of B_3 and A_u symmetric vibrational modes with a dynamic dipole moment perpendicular to the molecular plane (d and h). E_0 is the primary energy of the incident electrons. The energy resolution of the specular spectra is measured as the full width at half maximum (FWHM) of the elastic peak (zero energy loss peak) and is given in wavenumbers (cm^{-1}). The assigned vibrations are listed in table 3.4.

3.2. Influence of Core substitution on the Properties of Thiadiazole Derivatives

When the vibrational spectra of BBT-Ph at all coverages are compared, the intensities of the three distinct dipole-active vibrations at 510 cm^{-1}, 694 cm^{-1} and 762 cm^{-1}, decreases relative to the rest of the spectrum, by going from the sub - to monolayer coverage and again increases at the multilayer coverage, while their intensities relative to each other remains mostly constant. Considering that these vibrations are assigned to the out-of-plane γ_ω(C-H) and γ_ω(C-C-C) wagging modes with the dynamic dipole moments perpendicular to the molecular plane (x-direction), their higher intensities at sub - and multilayer coverage, suggests that at these coverages, the adsorbed molecules vibrate more freely in an out-of-plane direction. A possible explanation for this trend could be that at sub-monolayer coverage, duo to different polarity of the nitrogen ($\delta-$) and sulphur ($\delta+$) atoms, the adsorbed molecules form islands, in which molecules vibrate more freely. In contrast, at the monolayer coverage, the difference in polarity results in formation of ordered, tape-like network of BBT-Ph, where the molecules are tightly packed[181]. Thus, the out-of-plane vibrations are suppressed by the intermolecular interactions. At the multilayer coverage, the packing of the molecules may differ from the monolayer duo to a different growth mode and/or reduced influence of the Au(111) substrate on the adsorbates at higher layers, which once again induces the out-of-plane vibrations of the molecule.

Noticeably, another pronounce vibration, assigned to the out-of-plane buckling mode (at 142 cm^{-1}) as detected in the spectrum of the sub - monolayer coverage is absent in the measured spectra of the mono - and multilayer coverage. This vibration originates from the phenyl groups, which also includes a breathing motion of the molecular backbone. It can be assumed that at sub-monolayer coverage, duo to the possibility for the molecule to vibrate more freely, this particular vibration can also be detected in the spectrum of the corresponding coverage. However, a similar vibrational mode at a similar wave number could not be detected in the spectrum of the molecule at the multilayer coverage, where molecules can potentially vibrate more feely in comparison to the tightly packed monolayer coverage. This observation suggest that the detected vibration at 142 cm^{-1} may have another origin other than the assigned buckling mode of the molecule. This origin could be the gold-sulphur (Au-S) vibration, which has been observed for alkanethiol self-assembled monolayers on Au(111) at wave numbers around 170 - 320 cm^{-1} [186]. This assignment can account for the absence of the vibration in question in

the multilayer spectrum, where a missing interaction between the adsorbate and the metallic substrate at higher layers prevents a bond between gold and sulphur atoms to form and subsequently vibrates. However the wave number (142 cm^{-1}) at which this vibration is detected is lower than the reported values for alkanethiol self-assembled monolayers (170 - 320 cm^{-1}). This deviation could be explained by the assumption that BBT-Ph at an interface with Au(111) surface form an extended system with a continuous backbone of the molecule, and as such according to the equation of eigenfrequency, $\omega = \sqrt{\frac{k}{\mu}}$, the frequency ω decreases with an increase in the reduced mass μ.

In case of BBT-Th, the vibrational HREELS spectra of sub -, mono - and multilayer coverages of the molecule also include three distinct vibrations with high intensity ratio between the specular and off-specular scattered electrons, which are dipole-active (see Figure 3.28 (d) ,(e) and (f)). By comparing the results from the vibrational spectra with the calculated intensities and frequencies of A_u vibrational modes of the corresponding C_{2h} molecular point group in the gas phase (see Figure 3.28 (H)), the identified dipole-active vibrations are assigned to the combination of γ_τ(C-C-C) twisting and γ_ω(C-N) wagging modes (at 500 cm^{-1}) as well as γ_ω(C-H) wagging modes (at 719 cm^{-1} and 839 cm^{-1}). Other dipole-active vibrations in the spectra of the molecule are assigned to the combination of γ_τ(C-C-C) and γ_ω(C-H) twisting modes (at 585 cm^{-1}), $\gamma_{\omega/\tau}$(C-H) wagging/twisting mode at 874 cm^{-1} (for the monolayer coverage) and γ_τ(N-S-N) twisting mode at 137 cm^{-1} (in the multilayer spectrum). The presence of only dipole-active vibrations in the spectra of the sub - and monolayer coverages of the molecule with the dynamic dipole moments that are perpendicular to the molecular plane (z-direction) as shown in figure 3.29, indicates that at these coverages, BBT-Th adapts a planar adsorption geometry on Au(111) surface.

In contrast, the spectrum of the molecule at the multilayer coverage also include vibrations which are non-dipole-active and posses dynamic dipole moments that are parallel with the molecular plane along the long axis (x-direction) or side group of the molecule (y-direction) as shown in figure E.4. With the help of the DFT calculations, these vibrations are assigned to the combination of in-plane ρ(C-H) and ρ(C-C-C) rocking modes at 1213 cm^{-1} , ν(C-C) and ν(C-N) stretching and ρ(C-C-C) rocking modes at 1443 cm^{-1} as well as ν(C-H) stretching mode at 3089 cm^{-1}. Detection of these vibrations suggests that similar to the case of BBT-Ph, at higher layers, the adsorbed BBT-Th

molecules may have tilted out of the plane parallel to the substrate surface. Consequently, the dynamic dipole moments parallel with the molecular plane rotates towards an out-of-plane direction, which results in detection of the associated vibrations in the spectra of the multilayer coverage. Regardless, it can be assumed that the adsorption geometry of BBT-Th at the multilayer coverage is mainly planar. Table 3.4 provides more details on the assignment of the identified vibrations of BBT-Th.

Noticeably, as can be seen from the visualizations of the assigned vibrations (see figures 3.29 and E.4), after energy relaxation and geometry optimisation, the orientation of thiophene groups in BBT-Th remains planar with respect to the heterocyclic unit of the molecule. This is in contrast to results from the DFT calculated vibrational modes of BBT-Ph, where the phenyl groups are twisted by 36.9° with respect to the heterocyclic unit.

Interestingly, the assigned out-of-plane, dipole-active γ_τ(N-S-N) twisting mode vibration of BBT-Th, as detected in the multilayer spectrum is absent in the measured spectra of the sub - and monolayer coverage. It can be assumed that by increasing the coverage, thus decoupling the molecule from the Au(111) surface, the bonds between the nitrogen and sulphur atoms at the backbone of the molecule can vibrate freely, which leads to an out-of-plane vibration. In contrast, at sub - and monolayer coverages, an increased lateral interaction between the molecules, driven by inter-molecular interaction between the nitrogen atom ($\delta-$) of the molecular backbone and the sulphur atom ($\delta+$) of the thiophene group might suppresses the vibrations of N-S-N bonds. This assumption is supported by the absence of the assigned γ_τ(N-S-N) twisting mode vibration in the spectra of BBT-Ph, despite sharing the same heterocyclic unit (BBT) as BBT-Th, due to the missing sulphur atom in the substituted aromatic group (phenyl group). Same argument can be used to account for the absence of ν(C-H) stretching mode, in the measured spectra of the sub - and monolayer coverages, where due to strong adsorbate/adsorbate - interactions, this particular vibration could be suppressed. In contrast, at the multilayer coverage, due to a potential tilt of the molecules in an out of plane orientation, thus reduced interaction between the adsorbates, the vibration associated with the ν(C-H) stretching mode can be detected.

Table 3.4.: Assigned vibrations (in cm^{-1}) of BBT-Ph and BBT-Th adsorbed on Au(111) for different coverages. Additionally, the corresponding DFT calculated frequencies of the molecules in the gas-phase at the B3LYP level and the 6-311G basis set are given. Dipole active modes are labelled with *da*. The identified modes for each vibration are described with the following abbreviations; γ – out-of-plane; δ – scissoring; ν – stretching; τ – twisting; ω – wagging. Representation (Repr.) of the associated point groups and the orientation of the calculated dipole derivative vector with respect to the molecular geometry, x, perpendicular to the molecular plane of BBT-Ph and along the long axis of BBT-Th; z, short axis of BBT-Ph and perpendicular to the molecular plane of BBT-Th and y, long axis of BBT-Ph and short axis of BBT-Th for the corresponding modes are listed.

BBT-Ph

#	Subm.	1 ML	11 ML	DFT	Mode	Repr.
1	142 *da*	-	-	122	buckling	B$_3$(x)
2	-	-	223	242	buckling	B$_2$(y)
3	-	-	307	294	δ(C-C-C)	B$_2$(y)
4	497 *da*	499 *da*	510 *da*	507	γ_ω(C-C-C), γ_ω(C-H)	B$_3$(x)
5	687 *da*	690 *da*	694 *da*	711	γ_ω(C-H)	B$_3$(x)
6	771 *da*	748 *da*	762 *da*	809	γ_ω(C-H)	B$_3$(x)
7	-	-	866	865	ω(C-H)	B$_1$(z)
8	920 *da*	926 *da*	933 *da*	953	γ_ω(C-H)	B$_3$(x)
9	-	1071	1092	1058	ν_s(C-C-C), δ(C-H)	B$_1$(z)
10	-	-	1192	1214	δ(C-H)	B$_2$(y)
11	-	-	1366	1367	ν(C-C-C), δ(C-H)	B$_2$(y)
12	-	-	1456	1459	ν(CN), δ(C-H)	B$_1$(z)
13	3077	3044	3071	3165	ν(C-H)	B$_1$(z)

BBT-Th

#	Subm.	1 ML	5 ML	DFT	Mode	Repr.
1	-	-	137 *da*	161	γ_τ(N-S-N)	A$_u$(z)
2	487 *da*	490 *da*	500 *da*	488	γ_τ(C-C-C), γ(CN)	A$_u$(z)
3	532 *da*	567 *da*	571 *da*	585	γ_τ(C-C-C), γ_τ(C-H)	A$_u$(z)
4	709 *da*	713 *da*	719 *da*	724	γ_ω(C-H)	A$_u$(z)
5	832 *da*	829 *da*	839 *da*	815	γ_ω(C-H)	A$_u$(z)
6	-	874 *da*	-	899	$\gamma\omega/\tau$(C-H)	A$_u$(z)
7	-	-	1213	1276	δ(C-H), δ(C-C-C)	B$_u$(x, y)
8	-	-	1443	1493	ν(C-C), ν(CN), δ(C-C-C)	B$_u$(x, y)
9	-	-	3089	3204	ν(C-H)	B$_u$(x, y)
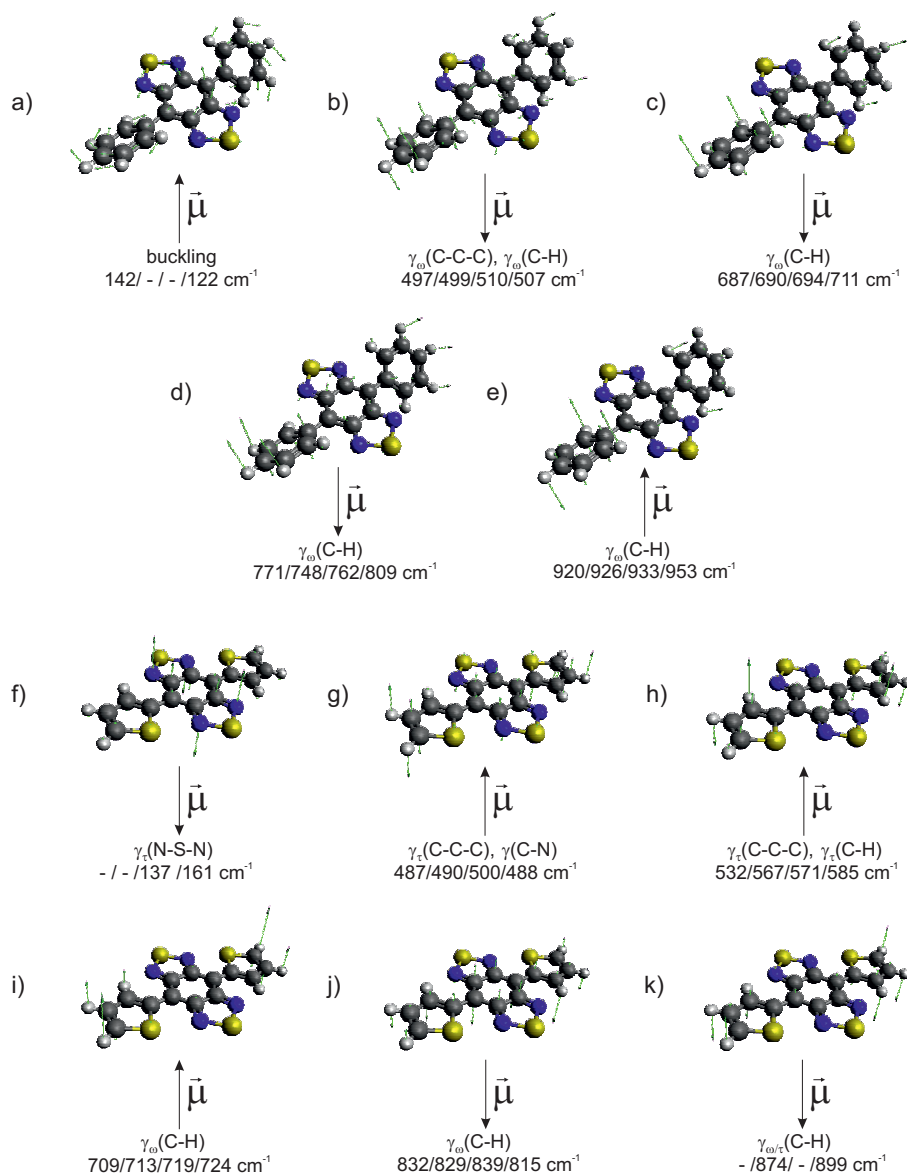
Figure 3.29.: Visualisation of the assigned dipole-active vibrational modes obtained from the DFT calculations (B3LYP/6-311G) for BBT-Ph (a-e) and BBT-Th (f-k). The corresponding energies (HREELS sub-monolayer/HREELS monolayer/HREELS multilayer/DFT) are given in wavenumbers (cm^{-1}). The direction of the calculated dipole derivative unit vector ($\vec{\mu}$) is depicted with a black arrow that lies in the plane of the paper. The atomic displacements in each visualization are shown with green arrows. The vibrational modes are visualized by the Avogadro [180] software.

Results and Discussion

Overall, despite the unique influence of each aromatic substituents on the adsorption properties of the corresponding molecules, it can be concluded that the adsoption geometries of the molecules remain similar, with both BBT-Ph and BBT-Th adopting a planar adsorption geometry in their thin films and at the interface with Au(111) surface.

After gaining a comprehensive understanding of the adsorption properties of BBT-Ph and BBT-Th on Au(111), in the following, the electronic HREELS is utilized to investigate the influence of the different aromatic groups (phenyl and thiophene) on the electronic structure of the corresponding molecules at the interface with Au(111) and within their thin films. Figure 3.30 shows the electronic HREELS spectra of BBT-Ph (Left) and BBT-Th (right), for sub - (a and d), mono - (b and e) and multilayer (c and f) coverages measured with the primary electron energy of 15 eV together with the corresponding UV/Vis spectra of the molecules measured in hexane (C_6H_{14}) solution (orange spectra).

Starting with the monolayer coverage of BBT-Ph, the corresponding spectrum consists of two electron energy loss feature at 1.2 and 2 eV as shown in figure 3.30 (b). By increasing the coverage to 11 ML, thus decoupling the molecular thin film from the metallic substrate, the loss feature at 1.2 eV disappears while the intensity of the previously detected loss features at 2 eV in the monolayer coverage becomes even more pronounced and its energetic position shifts by 200 meV to 2.2 eV (see Figure 3.30 (c)). The loss feature at 2.2 eV is in good agreement with the reported optical gap of BBT-Ph in the literature (2.22 eV)[181]. Therefore, it is assigned to the transition of the ground state (S_0) to the first singlet excited state (S_1), i.e. the optical gap of the molecule. The observed shift of the assigned $S_0 \rightarrow S_1$ transition from 2.2 eV in the multilayer coverage to 2.0 eV in the monolayer coverage can be contributed to the substrate induced narrowing of the optical gap. Accordingly, the loss feature at 1.9 eV as detected in the spectrum of the sub-monolayer coverage can be assigned to $S_0 \rightarrow S_1$ transition (see Figure 3.30 (a)). The other loss feature at 3.5 eV as detected in the multilayer spectrum is also present in the corresponding UV/Vis spectrum of the molecule. Therefore, it can be attributed to the transitions to a higher-lying electronic state of the molecule.
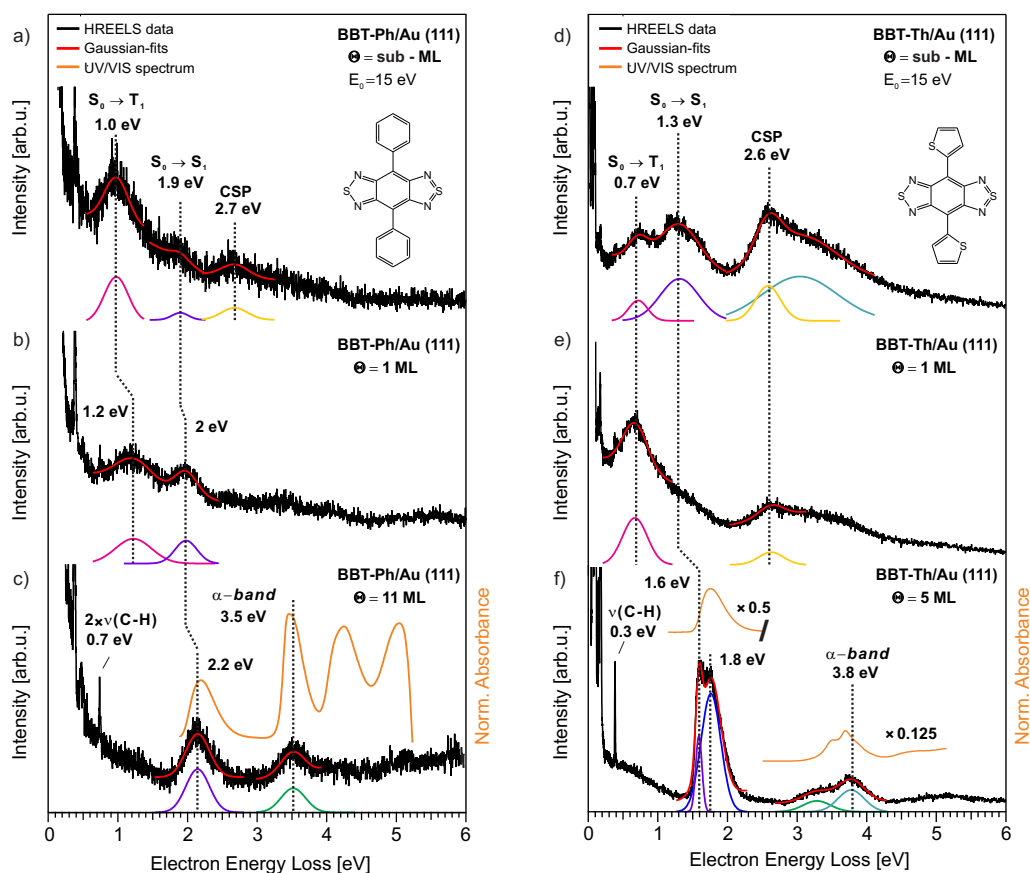
Figure 3.30.: Electronic HREELS spectra of adsorbed BBT-Ph (Left) and BBT-Th (right) on Au(111), measured for sub- monolayer (a and d), mono - (b and e) and multilayer (c and f) coverages (black spectra). The electronic loss features were fitted using Gaussian functions (red curves). The corresponding UV/Vis spectra of the molecules are measured in hexane (C_6H_{14}) (orange spectra). E_0 is the primary energy of the incident electrons. Θ is the coverage in monolayer (ML).

When compared, $S_0 \rightarrow S_1$ and the transition at 3.5, are located at slightly different energetic positions as the corresponding transitions in the UV/Vis spectrum of the molecule. Additionally, the other two higher-lying electronic transitions at approximately 4.3 and 5.1 eV as detected in the UV/Vis spectrum are not present in the spectrum of the thin film. Therefore, it can be assumed that the adsorbate/adsorbate - and adsorbate/substrate - interactions may have influenced the electronic structure of the molecule in its thin film.

The remaining unassigned loss features at 1 eV and 1.2 eV in the sub-monolayer and monolayer spectra of BBT-Ph are located beneath the assigned $S_0 \rightarrow S_1$ transitions (1.9 and 2 eV) of the molecule for the corresponding cover-

ages. Similar loss features have also been detected in the spectra of NTD and its halogenated derivatives, which were assigned to $S_0 \rightarrow T_1$. Therefore, it can be assumed that the loss features at 1 and 1.2 eV in the spectra of BBT-Ph correspond to a transition to the first triplet state (T_1) of the molecule.

Similarly, the spectra of BBT-Th at the sub-monolayer and monolayer coverage also includes two loss features located at the same loss energy of 0.7 eV, which is lower than the known optical gap (1.77 eV) of BBT-Th from the literature[53] (see Figure 3.30 (d) and (e)). Therefore, the loss feature at 0.7 as detected in the spectra of the BBT-Th can potentially be attributed to the $S_0 \rightarrow T_1$ transition of the molecule.

At the monolayer coverage, due to the strong electronic coupling between the adsorbates and the metallic substrate, other than the assigned $S_0 \rightarrow T_1$ transition only the conventional Au(111) surface plasmon at 2.6 eV[140] could be detected in the corresponding spectrum. By reducing the coverage to sub - monolayer, in addition to the $S_0 \rightarrow T_1$ transition and CSP, another loss features at 1.3 eV is detected in the spectrum. As for the multilayer coverage, the spectrum is dominated by a loss feature at 1.6 eV, that is accompanied by a vibrational contribution at 1.8 eV, as well as another loss feature at 3.8 eV. The loss feature at 1.6 eV is in good agreement with the reported optical gap of BBT-Th (1.77 eV)[53] and as such it is assigned to the 0-0 vibrational transition of $S_0 \rightarrow S_1$. The vibrational contribution associated with this transition can be attributed to the ν(C-N) and ν(C-C) stretching modes as well as ρ(C-C-C) deformation mode of the molecular backbone with frequencies in rang of 1430-1450 cm^{-1} (177-180 meV). Noticeably, the corresponding transition in the overlaid UV/Vis spectrum of the molecule does not include a vibrational contribution. This suggests that the intermolecular forces (adsorbate/adsorbate - interactions) in a thin film may have influenced the electronic structure of BBT-Th. This influence is also evident from the energetic shift of the loss feature at 3.8 eV as detected in the spectrum of the thin film in comparison to the corresponding transition in the UV/Vis spectrum at approximately 3.7 eV. This loss feature can be attributed to a transitions to a higher-lying electronic state of the molecule.

When compared to the assigned $S_0 \rightarrow S_1$ transition of BBT-Th at 1.6 eV as determined in the spectrum of its multilayer coverage, the loss feature at 1.3 eV as detected in the sub - monolayer spectrum can also be attributed to the $S_0 \rightarrow S_1$ transition of the molecule. The 0.4 eV energy difference between the

two transitions can be attributed to the substrate induced narrowing of the optical gap. Noticeably, the $S_0 \rightarrow S_1$ transition of the molecule is absent in the spectrum of the monolayer coverage. The most likely explanation for this observation is that this particular transition is overshadowed by the higher background of the $S_0 \rightarrow T_1$ transition in the same spectrum. Similarly, the assigned $S_0 \rightarrow T_1$ transitions of BBT-Ph and BBT-Th are absent in the spectra of the molecules at their multilayer coverages, most likely due to higher background of the $S_0 \rightarrow S_1$ transitions in the corresponding spectra.

A comparison between the determined optical gaps of BBT-Ph and BBT-Th, in the corresponding spectra of their multilayer coverages, shows that substitution of BBT with thiophene instead of phenyl group results in a narrowing of the optical gap of about 600 meV from 2.2 eV for BBT-Ph to 1.6 eV for BBT-Th (see Figure 3.31). Additionally, the transition energies of $S_0 \rightarrow T_1$ are shifted by about 500 eV from 1.2 eV for BBT-Ph to 0.7 eV for BBT-Th at the monolayer coverage and 300 meV from 1 eV for BBT-Ph to 0.7 eV for BBT-Th at the sub - monolayer coverage. The narrowing of the optical gap in BBT-Th in comparison to BBT-Ph, can be attributed to the influence of intramolecular charge transfer between the electron-withdrawing BBT moiety and the electron-donating thiophene group, on the energy levels of HOMO and LUMO in the corresponding molecule[53]. As shown in figure 3.26 (c), the calculated frontier orbital energies of BBT-Th indicates that LUMO is mostly localized on the BBT moiety. Therefore, it can be assumed that by changing the substituents, the change in the HOMO energy level, contribute far more than the change in LUMO energy level to the observed narrowing of the optical gap going from BBT-Ph to BBT-Th[183]. Indeed, further computational studies conducted on the corresponding molecules with non-hypervalent sulfur atoms in their BBT moieties, indicate that substitution of the molecule with thiophene groups reduces the LUMO energy level by 0.14 eV from -3.56 eV for BBT-Ph to -3.7 eV for BBT-Th and increases the HOMO energy level by 0.41 eV from - 5.75 eV for BBT-Ph to -5.34 eV for BBT-Th[54]. Therefore, it can be concluded that substitution of BBT with thiophene groups increases the HOMO energy level much more than it decreases the LUMO energy level and as such thiophene contributes to the narrowing of the optical gap in BBT-Th.
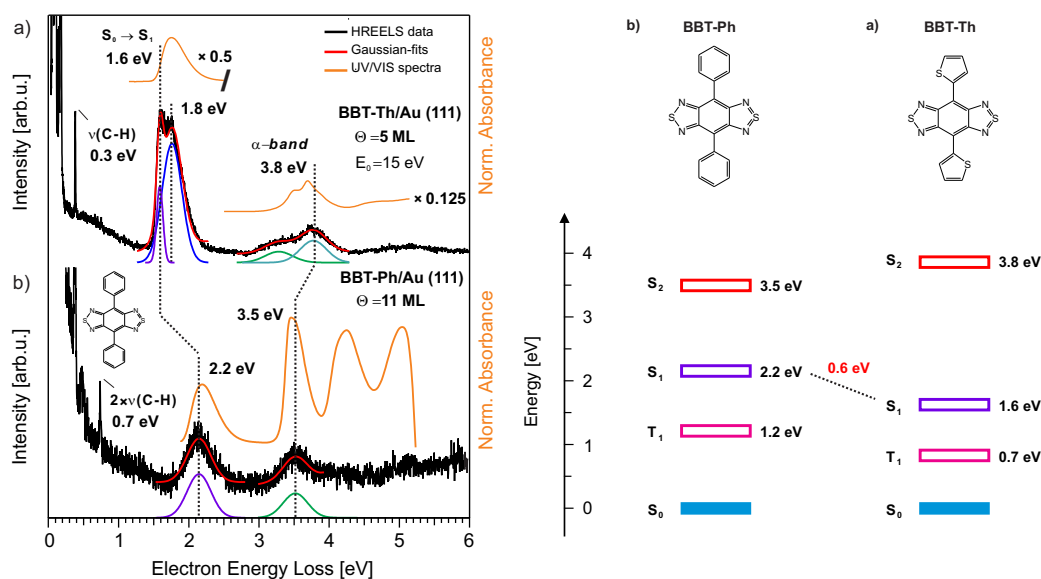
Figure 3.31.: Electronic HREELS spectra (left) of adsorbed (a) BBT-Th and (b) BBT-Ph on Au(111) measured for the multilayer coverage (black spectra). The electronic loss features were fitted using Gaussian functions (red curves). The corresponding UV/Vis spectra of the molecules are measured in hexane (C_6H_{14}) solution (orange spectra). E_0 is the primary energy of the incident electrons. Θ is the coverage in monolayer (ML). The identified and assigned electronic transitions of the molecules as determined from the their mono- (triplet states) and multilayer (singlet states) coverage are summarized in an energy level diagram (right).

3.2. Influence of Core substitution on the Properties of Thiadiazole Derivatives

To summarize, in this subsection it was demonstrated that thin films of BBT-Ph and BBT-Th can be prepared through deposition of the corresponding molecules at 443 K (BBT-Ph) and 468 K (BBT-Th) into the ultra-high vacuum chamber and onto Au(111) substrate held at 300 K. The prepared samples were then characterized by TPD, vibrational and electronic HREELS in combination with DFT calculations. Based on the results from the fragment-mass-resolved TPD measurements it was determined that during annealing of the samples, the BBT-Ph and BBT-Th molecules remain intact. Regardless, it was chosen to prepare the sub - and monolyer coverages of BBT-Ph and BBT-Th samples by direct evaporation of the molecules on the substrate. The results from the coverage dependent TPD measurements on the molecules indicates that core substitution via thiophene group in BBT-Th results in an increase in adsorbate/adsorbate and adsorbate/substrate-interaction for the molecule in comparison to BBT-Ph. Moreover, as shown via vibrational HREELS measurements, BBT-Ph and BBT-Th at their sub-monolayer , mono - and multilayer coverages adopt a planar adsorption geometry on the Au(111) surface. Finally, through electronic HREELS measurements, it is found that core substitution via thiophene in BBT-Th results in a reduction of the transition energies of singlet and first triplet states in comparison to the phenyl substituted BBT-Ph. This is evident from the narrowing of the optical gap by 600 meV from 2.2 eV for BBT-Ph to 1.6 eV for BBT-Th as well as shift of the assigned $S_0 \rightarrow T_1$ transition to the lower energy by 500 meV from 1.2 eV for BBT-Th to 0.7 eV for BBT-Ph. The narrowing of the optical gap is attributed to the stabilization of the frontier orbitals in BBT-Th in comparison to BBT-Ph due to intramolecular charge transfer between the BBT moiety and the substituted thiophene groups.

In conclusion, the presented studies in this section provides new insights into the adsorption and electronic properties of known acceptor molecules, namely NTD and its halogenated derivatives (NTD-Cl and NTD-Br) as well as BBT-Ph and BBT-Th at the interface with Au(111) and within their thin films. The obtained results can be used as a reference for developing potential donor-acceptor heterostructures.

3.3. N-Heterotriangulene Derivatives and Donor/Acceptor-Systems

In this section, first, influence of connectivity via -C=C- bridge on the adsorption and electronic properties of N-heterotriangulene (N-HTA) derivatives adsorbed on Au(111) is studied by utilizing TPD, vibrational and electronic HREELS. Second, electronic HREELS is used to investigate a potential charge transfer (CT) between the studied N-HTA derivatives as donor molecules and two cyano-based acceptor molecules in donor/acceptor (D/A)-systems.
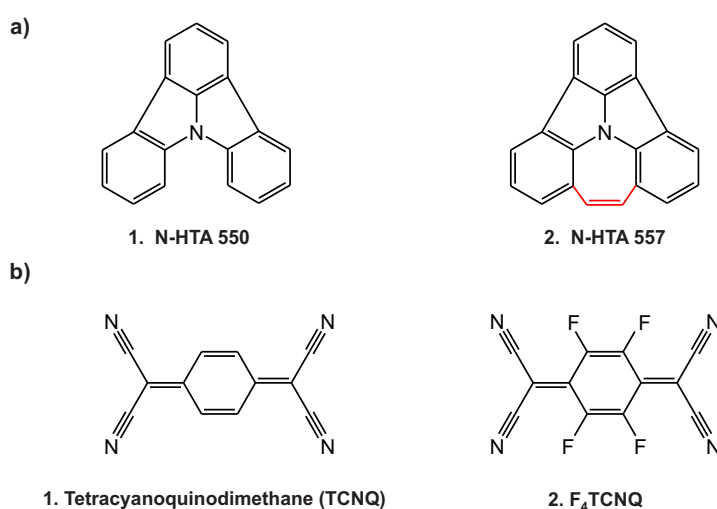
Figure 3.32.: Investigated molecular systems: (a) 5-membered ring N-HTA (N-HTA 550, (1)) and 7-membered ring N-HTA with -C=C- bridge (N-HTA 557, (2)) as well as (b) Tetracyanoquinodimethane (TCNQ, (1)) and its fluorinated derivative (F$_4$TCNQ, (2)).

The investigated molecular systems include indolo[3,2,1-jk]carbazole; 5-membered ring N-HTA (N-HTA 550, Figure 3.32 (a.1)) and 3a^2-azabenzo-[3,4]azuleno[2,1,8,7-jklm]fluorene; 7-membered ring N-HTA (N-HTA 557, Figure 3.32 (a.2)) as well as tetracyanoquinodimethane (TCNQ, Figure 3.32 (b.1)) and 2,3,5,6-tetrafluoro-7,7,8,8- tetracyanoquinodimethane (F$_4$TCNQ, Figure 3.32 (b.2)).

The results from these investigations are presented in two subsections. In the first subsection, by comparing the obtained results for N-HTA 550 and N-HTA 557, effects of the connectivity via -C=C- bridge in N-HTA 557 on the properties of the corresponding molecule are studied. In the second subsection, by comparing the obtained results for the formed D/A-systems, influence of

102

combination of different donors (N-HTA 550 and N-HTA 557) with different acceptors (TCNQ and F_4TCNQ) on the charge transfer in the corresponding D/A-systems are investigated. Through these studies, it is determined that intact thin films of molecules can be prepared via deposition at elevated temperatures into the ultra-high vacuum (UHV) chamber and onto Au(111) substrate. All of the investigated molecules adopt a planar adsorption geometry on the Au(111) surface. Introduction of -C=C- bridge alters the electronic structure of N-HTA 557 by narrowing its optical gap to 2.5 eV from 3.4 eV for N-HTA 550 by 900 meV. Additionally, it is shown that in contrast to N-HTA 550, N-HTA 557 transfer electron to the Au(111) substrate and becomes positively charged. Furthermore, it is found that both N-HTA 550 and N-HTA 557 as donor molecules form CT-states with both of the chosen acceptor molecules (TCNQ and F_4TCNQ) in the D/A-systems. This is evident from detected transitions associated with CT-states at 1.7 and 2.2 eV (TCNQ/N-HTA 550), 1.5 and 1.8 eV (F_4TCNQ/N-HTA 550), 1.3 eV (TCNQ/N-HTA 557) and 0.9 eV (F_4TCNQ/N-HTA 557).

3.3.1. Influence of Connectivity on the Adsorption and Electronic Properties of N-Heterotriangulene Derivatives

N-heterotriangulenes are a class of functional molecules, which are formed by connecting the phenyl rings in triphenylamine via different bridging moieties[87]. The resulting planarized molecules are expected to exhibit improved electronic properties in comparison to propeller-shaped parent triphenylamine, in which the relatively large dihedral angles of the phenyl rings hinders the electronic communication in the molecule[87;88].

In a new approach toward planarization of triphenylamine, Michalsky *et al.*[88] synthesized two novel N-heterotriangulene derivatives, N-HTA 557SB (SB = single bond) and N-HTA 557, by introducing ethylene (-C-C-) and vinylene (-C=C-) bridges to N-HTA 550, respectively. Considering the potentials of N-heterotriangulenes as (opto)electronic materials[187–191], in the context of this study, it was chosen to investigate the properties of N-HTA 557 as a promising electron donating N-heterotriangulene[88], together with its 5-membered ring counterpart (N-HTA 550). Some of the results presented in this subsection are published in Ref.[192].

The N-HTA 550 and N-HTA 557 molecules were synthesized by Ina Michalsky of the Prof. Dr. Milan Kivala group of the Organisch-Chemisches Institut at the Universität Heidelberg[88].

For this study, samples of N-HTA derivatives were prepared, *in situ* by deposition of the corresponding molecules at 373 K (N-HTA 550) and 393 K (N-HTA 557) into the UHV chamber and onto Au(111) substrate held at 200 K. First, through coverage dependent and fragment-mass-resolved TPD measurements, the possibility of preparing thin films and well-defined monolayers of the molecules on Au(111) surface is investigated and subsequently, the influence of the introduced -C=C- bridge in N-HTA 557 on its adsorption properties within the thin film and at the interface with Au(111) is explored.

Figure 3.33 (a) shows the coverage dependent TPD spectra of N-HTA 550, with different initial coverages ranging from sub-monolayer to 5 ML for the selected mass-to-charge ratio (m/z) of 120, which corresponds to the doubly charged parent molecular ion with the molecular mass of 241 *amu*. The spectra consist of two desorption regions. The first region includes a desorption peak at 300 K (α_1), which is followed by a desorption feature at 312 K (α_2), that resembles a shoulder structure.
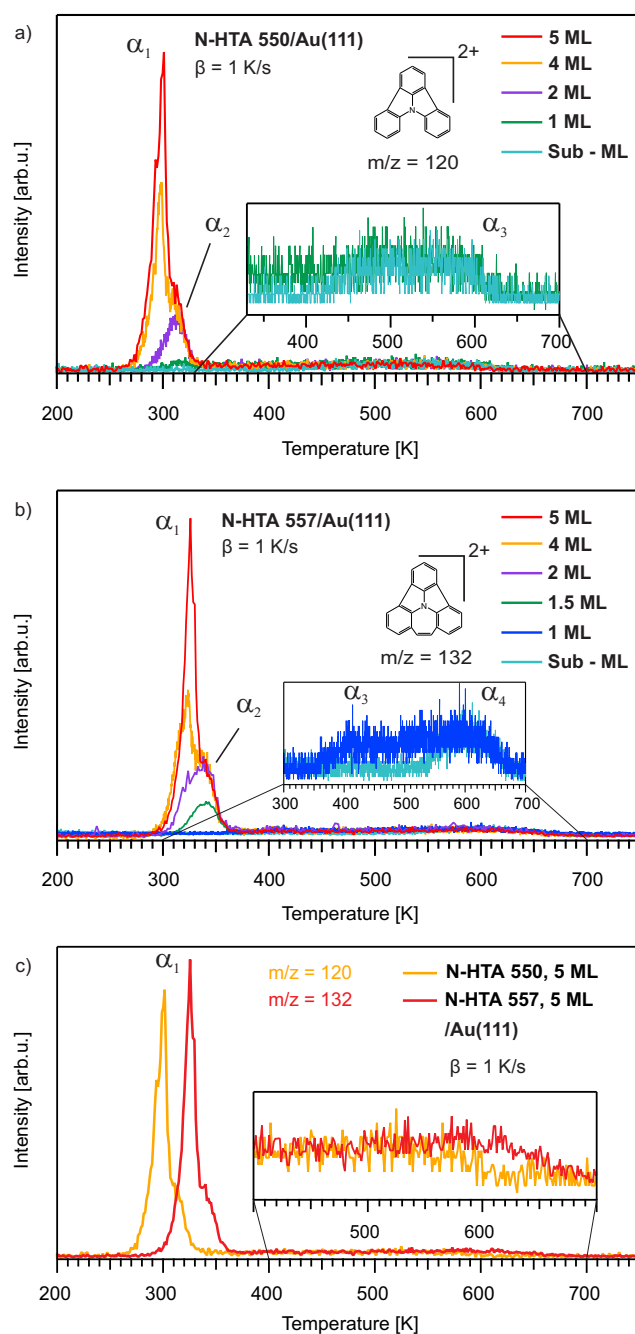
Figure 3.33.: Coverage dependent TPD spectra of (a) N-HTA 550 for the selected mass-to-charge ratio (m/z) of 120 and (b) N-HTA 557 for the selected m/z of 132 adsorbed on Au(111) with different initial coverages, measured with a heating rate of $\beta = 1\ K/s$. (c) Shows an overlay of the TPD spectra of N-HTA 550 and N-HTA 557. The desorption features are labelled with α_1, α_2, α_3 and α_4. The insets show the monolayer (α_3 in N-HTA 550), the compressed phase (α_3 in N-HTA 557) and the sub-monolayer desorption feature (α_4 in N-HTA 557). The structural formulas of the doubly charged parent molecular ions are depicted in their corresponding figures. Adapted from Ref.[192].

Results and Discussion

The α_1 peak does not saturates with increasing coverage and as such it is assigned to the desorption of a multilayer coverage. The α_2 feature first appears as a desorption peak for the 2nd - layer and subsequently merges to the multilayer desorption peak (α_1) at higher coverages. Thus, α_2 is assigned to the 2nd - layer desorption. This characteristic desorption behaviour has also been previously observed in the coverage dependent TPD spectra of TIPS-BAP (see Figure 3.11 (a) in Subsection 3.1.2), NTD (see Figure 3.19 (a) in Subsection 3.2.1) and BBT-Th (see Figure 3.27 (b) in Subsection 3.2.2). Lastly, the second region, extending from 400 K to 610 K (α_3), is assigned to the desorption of a monolayer coverage.

As for N-HTA 557 (m $= 265$ *amu*), the coverage dependent TPD spectra of the doubly charged parent molecular ion (m/z $= 132$) consists of three desorption regions for different initial coverages ranging from sub-monolayer to 5 ML (see Figure 3.33 (b)). The first region includes the same characteristic multilayer desorption peak (at 326 K, α_1) that is accompanied by a 2nd-layer desorption shoulder (at 338 K, α_2). The second desorption region consists of two desorption features, one at 400 K (α_3) and the other extending from 500 K to 670 K (α_4). The α_3 feature saturates with increasing coverage. Therefore, it can be attributed to a desorption from a more densely packed compressed phase. Consequently, α_4 can be assigned to the desorption of a sub-monolayer coverage. As a result, the desorption spectrum of a monolayer coverage can be defined as a spectrum, in which both α_3 and α_4 are saturated (see blue spectrum in the inset of figure 3.33 (b)).

In this study, the coverage of the adsorbed N-HTA 550 and N-HTA 557 molecules on the substrate were determined by integrating a measured TPD spectrum and comparing the area of the total integral with the area of the monolayer desorption region of the corresponding molecules[110].

By comparing the coverage dependent TPD spectra of N-HTA 550 and N-HTA 557, it becomes apparent that formation of the 7-membered ring in N-HTA 557 upon introduction of the -C=C- bridge, affects the adsorption properties of the molecule on Au(111). As can be seen in an overlay of the corresponding TPD spectra of the molecules with the same coverage of 5 ML (see Figure 3.33 (c)), the multilayer desorption peak (at 326 K, α_1) and the monolayer desorption feature (extending to 670 K) of N-HTA 557 are shifted by about 25 K and 60 K to higher temperatures relative to the same desorption features in N-HTA 550 spectrum. Additionally, in contrast to N-HTA 550, the

monolayer desorption spectra of N-HTA 557, also include a compressed phase (at 400 K , α_3). These observations suggest that introduction of -C=C- bridge leads to increased adsorbate/adsorbate and adsorbate/substrate-interactions within N-HTA 557 thin film and at its interface with Au(111).

The assigned desorption features of N-HTA 550 and N-HTA 557 are also present in the corresponding fragment-mass-resolved TPD spectra of the molecules (see Figure F.2). For both molecules, the multilayer (α_1) and 2nd-layer (α_2) desorption peaks, coincide at the same temperature for different selected fragments. The monolayer desorption region (α_3 and α_4) also follows the same trend. Furthermore, the estimated coverages of the measured spectrum for each fragment are mostly similar (5 ML). These observations indicate an intact desorption of higher layers as well as the monolyer coverages of N-HTAs from the substrate. Therefore, the determined coverages of the molecules corresponds to the actual coverage of the molecules on the substrate.

It should also be noted that the results from the subsequent vibrational HREELS measurements on N-HTA 550 and N-HTA 557 reveal that after heating the samples up to 750 K, well beyond the expected desorption temperatures of either molecule from the substrate, vibrational peaks associated with adsorbates can still be detected in the spectra of the corresponding molecules (see Figure F.3 (a) and (c)). Normally, this observation would suggests that by heating the sample up to 750 K, the adsorbed molecules on Au(111) do not desorb completely from the substrate, possibly due to strong bound between adsorbates and the substrate. However, due to high background pressure of both N-HTA 550 and N-HTA 557, as observed during their deposition on and desorption from the substrate, the identified vibrations are attributed to the re-adsorbed molecules on the substrate.

After assigning different desorption features of the adsorbed molecules and identifying the corresponding desorption temperatures, for further measurements, it was chosen to prepare the sub-monolayer and monolyer coverages of N-HTA 550 and N-HTA 557 samples by direct deposition of the molecules on the substrate. The used parameters for preparing the samples are given in table H.1.

In the next step, angle-resolved vibrational HREELS measurements are utilized to further investigate the influence of the introduced -C=C- bridge in N-HTA 557 on the adsorption geometry of the molecule within the thin film and at the interface with Au(111) in comparison to N-HTA 550. Figure 3.34

shows the vibrational spectra of N-HTA 550 (left) and N-HTA 557 (right) adsorbed on Au(111), for mono - (a and d) and multilayer (b and e) coverages, measured in specular (black spectra) and off-specular (red spectra) electron scattering geometry with the primary electron energy of 3.5 eV along with the calculated intensities and frequencies of vibrational modes possessing a dynamic dipole moment perpendicular to the molecular backbone (c and f).
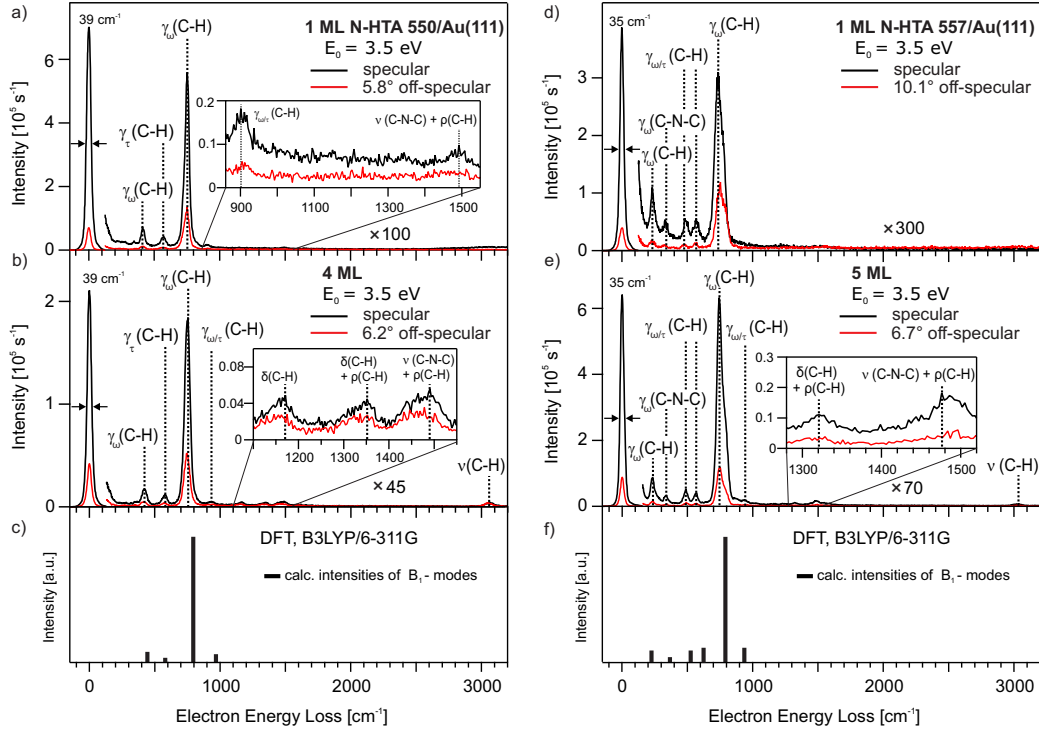
Figure 3.34.: Vibrational HREELS spectra of N-HTA 550 (Left) and N-HTA 557 (right) measured in specular (black spectra) and off-specular (red spectra) scattering geometry for mono - (a and d) and multilayer (b and e) coverages on Au(111) with the associated DFT-calculations (B3LYP/6-311G) for intensities and frequencies of B_1 symmetric vibrational mode with a dynamic dipole moment perpendicular to the molecular plane (c and f). E_0 is the primary energy of the incident electrons. The energy resolution of the specular spectra is measured as the full width at half maximum (FWHM) of the elastic peak (zero energy loss peak) and is given in wavenumbers (cm^{-1}). The assigned vibrations are listed in table 3.5. Adapted from Ref.[192].

The spectra of N-HTA 550 at the mono - and multilayer coverage are dominated by a vibration at approximately 754 cm^{-1} as can be seen in figure 3.34 (a) and (b). This vibration is distinguished by a high intensity ratio between the specular and off-specular scattered electrons, which is in consistent with a

dipole-active vibration with dipole scattering being its main excitation mechanism. By comparing the observed vibrations in the spectra of N-HTA 550 and the calculated intensities and frequencies of B_1 vibrational modes of the corresponding C_{2v} molecular point group in the gas phase (see Figure 3.34 (c)), the 754 cm^{-1} vibration can be assigned to the out-of-plane γ_ω(C-H) wagging mode[192]. Similarly, other dipole-active vibrations are assigned to the out-of-plane γ_ω(C-H) wagging mode (at 422 cm^{-1}), γ_τ(C-H) twisting mode (at 580 cm^{-1}) and $\gamma_{\omega/\tau}$(C-H) wagging/twisting mode (at 932 cm^{-1})[192].

Noticeably, the vibration at 422 cm^{-1} originates from the C-H bonds at the the ring-opening position of N-HTA 550. In addition to the assigned dipole-active vibrations, the spectra also include vibrations with reduced specular to off-specular intensity ratio at 1171 cm^{-1}, 1352 cm^{-1}, 1490 cm^{-1} and 3057 cm^{-1}. This indicates that the main excitation mechanism for these vibrations is impact scattering and as such they correspond to non-dipole-active vibrations. With a comparison to the results from the DFT calculations, these vibrations are assigned to a series of in-plane modes, including δ(C-H) scissoring and ρ(C-H) rocking modes as well as $\nu_{s/as}$(C-N-C) and ν_s(C-H) stretching modes[192].

In case of N-HTA 557, the spectra of the mono - and multilayer coverage are also dominated by a high intensity dipole-active vibration at approximately 743 cm^{-1}. This vibration is assigned to the out-of-plane γ_ω(C-H) wagging mode[192]. Furthermore, the peak associated with this vibration (743 cm^{-1}) has an asymmetric structure, which suggest that it might superimposes another vibrational peak with a lower intensity. The spectra of N-HTA 557 also include other dipole-active vibrations, which are assigned to the out-of-plane γ_ω(C-H) and γ_ω(C-N-C) wagging modes (at 233 cm^{-1} and 339 cm^{-1}) as well as $\gamma_{\omega/\tau}$(C-H) wagging/twisting mode (at 488 cm^{-1}, 569 cm^{-1} and 934 cm^{-1})[192]. The vibrational contribution of the introduced -C=C- bridge to the spectra of N-HTA 557 is recognized by the assigned vibrations at 233 cm^{-1} and 488 cm^{-1}. As expected, these vibrations are not present in the spectra of N-HTA 550. By increasing the coverage of N-HTA 557 to 5 ML, non-dipole-active vibrations appear in the spectrum of the multilayer coverage. These vibrations are assigned to the in-plane ν_s(C-H) scissoring and ρ(C-H) rocking modes (at 1321 cm^{-1}), ν_{as}(C-N-C) stretching and ρ(C-H) rocking modes (at 1486 cm^{-1}) as well as ν_s(C-H) stretching mode (at 3036 cm^{-1}).

Table 3.5.: Assigned vibrations (in cm^{-1}) of N-HTA 550 and N-HTA 557 adsorbed on Au(111) for different coverages. Additionally, the corresponding DFT calculated frequencies of the molecules in the gas-phase at the B3LYP level and the 6-311G basis set are given. Dipole active modes are labelled with *da*. The identified modes for each vibration are described with the following abbreviations; γ – out-of-plane; δ – scissoring; ν – stretching; τ – twisting; ω – wagging; s – symmetric; as – asymmetric. Representation (Repr.) of the associated point groups and the orientation of the calculated dipole derivative vector with respect to the molecular geometry, x, perpendicular to the molecular plane; y, short axis and z, long axis of molecular backbone for each mode are listed. Adapted from Ref.[192].

N-HTA 550

#	Subm.	1 ML	4 ML	DFT	Mode	Repr.
1	415 *da*	410 *da*	422 *da*	443	γ_ω(C-H), γ_ω(C-C-C)	B$_1$(x)
2	570 *da*	572 *da*	580 *da*	581	γ_τ(C-H), γ_ω(C-C-C)	B$_1$(x)
3	750 *da*	753 *da*	754 *da*	794	γ_ω(C-H), γ_ω(C-N-C)	B$_1$(x)
4	922 *da*	901 *da*	932 *da*	969	$\gamma_{\omega/\tau}$(C-H)	B$_1$(x)
5	-	-	1171	1183	δ(C-H), ρ(C-H), ν_s(C-N-C)	A$_1$(z)
6	-	-	1352	1382	δ(C-H), ρ(C-H), ν_{as}(C-C-C)	B$_2$(y)
7	1506	1492	1490	1470	ν_{as}(C-N-C)), ρ(C-H), ν_s(C-C-C)	B$_2$(y)
8	-	-	3057	3192	ν_s(C-H)	A$_1$(z)

N-HTA 557

#	Subm.	1 ML	5 ML	DFT	Mode	Repr.
1	235 *da*	229 *da*	233 *da*	231	γ_ω(C-H)	B$_1$(x)
2	332 *da*	329 *da*	339 *da*	358	γ_ω(C-N-C), $\gamma_{\omega/\tau}$(C-H), γ_ω(C-C-C)	B$_1$(x)
3	493 *da*	481 *da*	488 *da*	518	$\gamma_{\omega/\tau}$(C-H), γ_ω(C-C-C)	B$_1$(x)
4	565 *da*	568 *da*	569 *da*	608	$\gamma_{\omega/\tau}$(C-H), γ_ω(C-N-C)	B$_1$(x)
5	752 *da*	736 *da*	743 *da*	790	γ_ω(C-H), γ_ω(C-N-C)	B$_1$(x)
6	-	-	934 *da*	940	$\gamma_{\omega/\tau}$(C-H)	B$_1$(x)
7	-	-	1321	1363	δ(C-H), ρ(C-H), ν_{as}(C-C-C)	A$_1$(z)
8	-	-	1486	1528	ν_{as}(C-N-C), ρ(C-H), δ(C-H)	B$_2$(y)
9	3051	-	3036	3195	ν_s(C-H)	B$_2$(y)

a)

γ_ω(C-H), γ_ω(C-C-C)
415/410/422/443 cm^{-1}

b)

γ_τ(C-H), γ_ω(C-C-C)
570/572/580/581 cm^{-1}

c)

γ_ω(C-H), γ_ω(C-N-C)
750/753/754/794 cm^{-1}

d)

$\gamma_{\omega/\tau}$(C-H)
922/901/932/969 cm^{-1}

e)

γ_ω(C-H)
235/229/233/231 cm^{-1}

f)

γ_ω(C-N-C), $\gamma_{\omega/\tau}$(C-H), γ_ω(C-C-C)
332/329/339/358 cm^{-1}

g)

$\gamma_{\omega/\tau}$(C-H), γ_ω(C-C-C)
493/481/488/518 cm^{-1}

h)

$\gamma_{\omega/\tau}$(C-H), γ_ω(C-N-C)
565/568/569/608 cm^{-1}

i)

γ_ω(C-H), γ_ω(C-N-C)
752/736/743/790 cm^{-1}

j)

$\gamma_{\omega/\tau}$(C-H)
- / - /934/940 cm^{-1}

Figure 3.35.: Visualisation of the assigned dipole-active vibrational modes obtained from the DFT calculations (B3LYP/6-311G) for N-HTA 550 (a-d) and N-HTA 557 (e-j). The corresponding energies (HREELS sub-monolayer/HREELS monolayer/HREELS multilayer/DFT) are given in wavenumbers (cm^{-1}). The direction of the calculated dipole derivative unit vector ($\vec{\mu}$) is depicted with a black arrow that lies in the plane of the paper. The atomic displacements in each visualization are shown with green arrows. The vibrational modes are visualized by the Avogadro[180] software. Adapted from Ref.[192].

Results and Discussion

All of the assigned dipole-active vibrations posses a dynamic dipole moments that is perpendicular to the molecular plane (x-direction) (see Figure 3.35), while the dynamic dipole moments of the assigned non-dipole-active vibrations are parallel with the molecular backbone (z- and y-directions) (see Figure F.4). Given that the assigned vibrations in the mono - and multilayer spectra of N-HTA 550 and N-HTA 557 are predominately dipole-active, it can be concluded that at the corresponding coverages, both molecules adapts a planar adsorption geometry on Au(111) surface, in which the molecular backbone of the adsorbates are oriented parallel to the substrate surface[192]. Same conclusion can be drawn for the adsorption geometry of the molecules in their sub-monolayer coverage based on the observation made in the corresponding spectra (see Figure F.3 (b) and (e)). This indicates the introduced -C=C-bridge in N-HTA 557 dose not influence the overall adsorption geometry of the molecule on Au(111).

After gaining a comprehensive understanding of the adsorption geometry of N-HTA 550 and N-HTA 557 on Au(111), in the following, the electronic HREELS is utilized to investigate the electronic structure of the molecules at the interface with Au(111) and within their thin film. The purpose of this set of measurements is to elucidate the influence of the introduced -C=C- bridge in N-HTA 557 on the electronic structure of the molecule in comparison to N-HTA 550.

Figure 3.36 shows the electronic HREELS spectra of N-HTA 550 (Left) and N-HTA 557 (right), for mono - (a and c) and multilayer (b and d) coverages measured with the primary electron energy of 15 eV together with the corresponding UV/Vis spectra of the molecules measured in dichloromethane (CH_2Cl_2) solution (orange spectra). The monolayer spectrum of N-HTA 550 consists of only a contribution from the conventional Au (111) surface plasmon (CSP) at 2.6 eV[140] (see Figure 3.36 (a)). By increasing the coverage to 4 ML, thus electronically decoupling the molecular thin film from the metallic substrate, the loss features associated with electronic transitions of the molecule can now be detected in the spectrum of the multilayer coverage (see Figure 3.36 (b)). In this spectrum, the loss feature at 3.4 eV is in good agreement with the reported optical gap of N-HTA 550 in the literature (3.3 eV)[88;193]. Therefore, the loss features at 3.4 eV and 3.5 eV are assigned to the 0-0 and 0-1 vibrational transitions of the ground state (S_0) to the first singlet excited state (S_1)[192]. The vibrational contribution associated with this transition can

be attributed to the out-of-plane γ_ω(C-H) and γ_ω(C-N-C) wagging modes at approximately 754 cm^{-1} (93 meV)[192] as assigned in figure 3.34 (b). In the molecular orbital picture, the $S_0 \rightarrow S_1$ transition corresponds to an excitation of a single electron from HOMO into the LUMO, which represent 90 % of the S_1 state[192]. Furthermore, with the help of excited-state calculations, other loss features at 3.85, 4.5 and 5.4 eV are assigned to the transition of S_0 to the singlet excited states at S_2 (or α - band), S_3 and S_5, accordingly. The $S_0 \rightarrow S_2$ transition also includes a vibrational contribution at 3.95 eV. This transition largely corresponds to an excitation of a single electron from the HOMO-2 into the LUMO[192]. Likewise, $S_0 \rightarrow S_3$ (4.5 eV) and $S_0 \rightarrow S_5$ (5.4 eV) mostly correspond to HOMO-1 $\rightarrow$ LUMO and HOMO $\rightarrow$ LUMO + 1 transitions, accordingly[192].
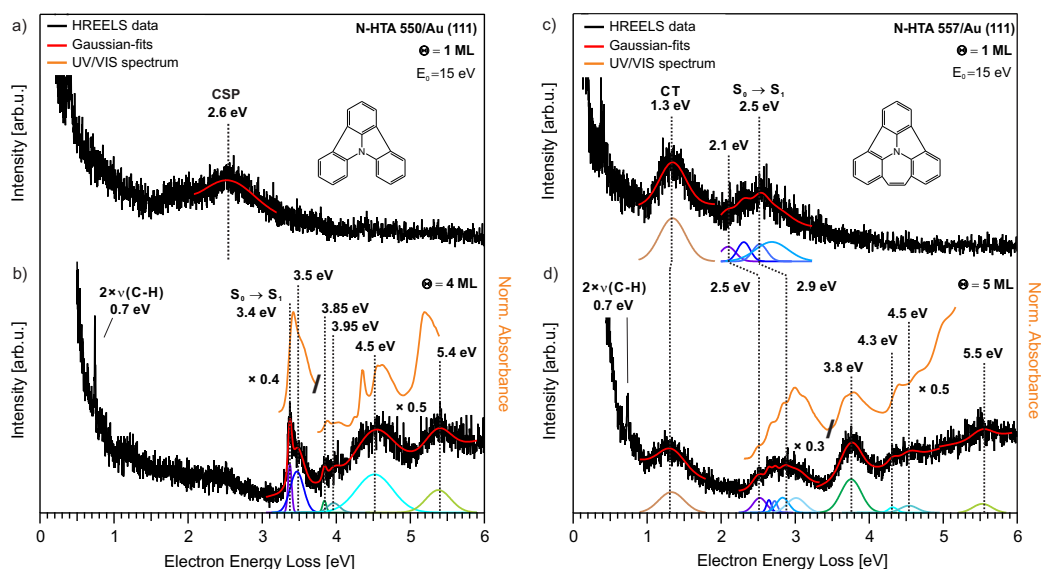
Figure 3.36.: Electronic HREELS spectra of adsorbed N-HTA 550 (Left) and N-HTA 557 (right) on Au(111), measured for mono - (a and c) and multilayer (b and d) coverages (black spectra). The electronic loss features were fitted using Gaussian functions (red curves). The corresponding UV/Vis spectra of the molecules are measured in dichloromethane (CH$_2$Cl$_2$) (orange spectra). E_0 is the primary energy of the incident electrons. Θ is the coverage in monolayer (ML). Adapted from Ref.[192].

In case of N-HTA 557, the monolayer spectrum consists of a pronounced loss feature at 1.3 eV, followed by a broad transition with a peak onset located at 2.1 eV that is accompanied by other vibrational contributions (see Figure 3.36 (c)). The loss feature and the following transitions are also present in

the spectrum of the multilayer coverage, where the peak onset is shifted to a higher energy loss at 2.5 eV, while the loss feature remained at 1.3 eV (see Figure 3.36 (d)). The peak onset at 2.5 eV is in good agreement with the reported optical gap of N-HTA 557 in the literature (2.39 eV)[88]. It is assigned to the 0-0 vibrational transition (the optical gap) of $S_0 \rightarrow S_1$ with maximum absorption at 2.9 eV. The observed reduction of the peak onset energy from 2.5 eV in the multilayer coverage to 2.1 eV in the monolayer by 0.4 eV can be contributed to the substrate induced narrowing of the optical gap. Moreover, the vibrational contribution associated with $S_0 \rightarrow S_1$ transition can be attributed to the out-of-plane $\gamma_{\omega/\tau}$(C-H) vibration at approximately 934 cm^{-1} (116 meV) and the combined ν(C-N-C) stretching and ρ(C-H) rocking vibration at approximately 1486 cm^{-1} (184 meV) as assigned in figure 3.34 (e). Additionally, it is determined that the $S_0 \rightarrow S_1$ transition corresponds mostly to an excitation of a single electron from HOMO into LUMO (78 %) with an admixture of HOMO to LUMO+1 (18 %), which represent the orbital relaxation of the S_1 state[192]. Furthermore, the excited-state calculations were utilized to assign other loss features at higher energies to the transition of S_0 to the singlet excited states at S_2 (3.8 eV), S_3 (4.3 and 4.5 eV) and S_4 (5.5 eV). These transitions are represented by HOMO $\rightarrow$ LUMO + 1 (73 %) with the admixture of HOMO $\rightarrow$ LUMO (13 %) for $S_0 \rightarrow S_2$, HOMO - 1 $\rightarrow$ LUMO for $S_0 \rightarrow S_3$ and HOMO - 2 $\rightarrow$ LUMO for $S_0 \rightarrow S_4$[192]. Furthermore, the spectra of the multilayer coverages of N-HTAs include contributions from overtones of an in-plane ν(C-H) stretching mode vibration (at around 3000 cm^{-1} in Figure 3.34 (b) and (e)) at approximately 0.7 eV.

The remaining unassigned loss feature at 1.3 eV is located beneath the 0-0 vibrational transition of the assigned $S_0 \rightarrow S_1$ of N-HTA 557 in mono - (2.1 eV) and multilayer (2.5 eV) coverage and is not present in the corresponding UV/Vis spectrum of the molecule. This loss feature is also observed in the measured spectrum of the sub-monolayer coverage (see Figure F.5 (c)). Additionally, the relative intensity of this loss feature is at its highest at the monolayer and by increasing the coverage of the adsorbed molecules, its intensity decreases. Thus, it can be assumed that this loss feature originates from the electron transfer from N-HTA 557 to the Au(111) surface, which can be detected by HREELS due to its surface sensitivity. This leads to formation of a positively charged N-HTA 557[192]. Indeed, the results from the quantum chemical calculations of N-HTA 557 cation reveal that the charged molecule

posses an electronic state at 1.35 eV, which is in good agreement with the
energy of the identified loss feature (1.3 eV) in the corresponding electronic
HREELS spectrum of the molecule[192]. Moreover, the calculated ionization
potential (IP) of N-HTA 557 yields a value of 6.28 eV, which supports the
possibility of a charge transfer from the adsorbate to the substrate[192]. This
becomes more evident when considering that N-HTA 550 with a IP value of
about 0.8 eV higher than the one of N-HTA 557, does not exhibit a loss feature
in its electronic spectra that can be associated with such charge transfer[192].
Therefore, the loss feature at 1.3 eV is assigned to a CT-state[192].
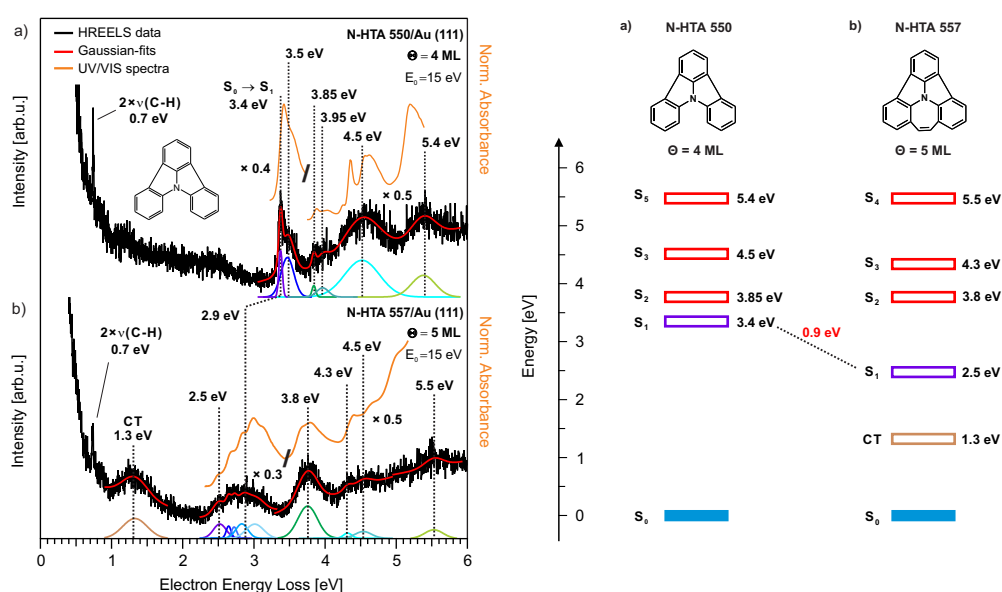
Figure 3.37.: Electronic HREELS spectra (left) of adsorbed (a) N-HTA 550 and (b)
N-HTA 557 on Au(111) measured for the multilayer coverage (black spec-
tra). The electronic loss features were fitted using Gaussian functions (red
curves). The corresponding UV/Vis spectra of the molecules are measured
in dichloromethane (CH_2Cl_2) solution (orange spectra). E_0 is the primary
energy of the incident electrons. Θ is the coverage in monolayer (ML). The
identified and assigned electronic transitions of the molecules are summa-
rized in an energy level diagram (right). Adapted from Ref.[192].

Overall, the excitation energies of the identified and assigned transitions in
the multilayer spectra of N-HTA 550 and N-HTA 557 are reduced by about
100 meV, when compared to the corresponding transitions in the overlaid
UV/Vis spectra of the molecules in solution (see Figure 3.37 (a) and (b)). This
observation indicates that the assigned electronic transitions in the thin films
of N-HTA 550 and N-HTA 557 are most likely influenced by the intermolecular

forces (adsorbate/adsorbate - interactions)[192].

A comparison between the determined optical gap of N-HTA 550 and - N-HTA 557, as assigned to the 0-0 vibrational transition of $S_0 \rightarrow S_1$ in the corresponding multilayer spectra of the molecules, clearly shows that introduction of -C=C- bridge in N-HTA 557 results in a narrowing of the optical gap of about 0.9 eV from 3.4 eV for N-HTA 550 to 2.5 eV for N-HTA 557 (see Figure 3.37). The UV/Vis spectra of the molecules also follow a similar trend. Additionally, the estimated narrowing of the optical gap from the calculated vertical energies of $S_0 \rightarrow S_1$ transition yields a value of 0.83 eV[192], which agrees well with the experimentally determined value of 0.9 eV. This is attributed to the extension of the π-system in N-HTA 557 via -C=C- bridge, which results in a change of the HOMO and LUMO energies, and subsequently the narrowing of the optical gap (HOMO-LUMO gap)[192]. This is evident from the visualization of the frontier molecular orbitals of N-HTA 557 (see Figure 3.38), which shows that HOMO, LUMO and LUMO+1 of the molecule are particularly affected by the extension of the π-system via -C=C- bridge. When the orbital energies are compared, going from N-HTA 550 to N-HTA 557, the HOMO energy increases by 0.6 eV from -6.83 eV to -6.23 eV, while the LUMO energy decreases by 0.43 eV from -0.14 eV to -0.57 eV. Similarly LUMO+1 energy decreases by about 1 eV from 1.01 to 0.03 eV. This trend can be explained with the typical particle-in-a-box picture[192].

Furthermore, the results from quantum chemical calculations performed on N-HTA 557SB, in which the 7-membered ring is formed with a single bond (-C-C- bridge), reveals that the calculated vertical energies of the molecule are very similar to that of N-HTA 550[192]. This result further confirms the effect of π-extension on the excited states of N-HTA 557. Therefore, it can be concluded that changing the molecular structure via suitable connectivity between different moieties of N-HTA can be used to modify the electronic structure of its derivatives. More details regarding the quantum chemical calculations conducted on the investigated N-HTA molecules in this study are presented in Ref.[192]. These calculations were conducted by Dr. Marvin Hoffmann and Christian Walla of the Prof. Dr. Andreas Dreuw group of the Interdisziplinäres Zentrum für Wissenschaftliches Rechnen at the Universität Heidelberg.

LUMO+1

LUMO

HOMO

HOMO-1

HOMO-2

N-HTA 557 SB　　　**N-HTA 550**　　　**N-HTA 557**
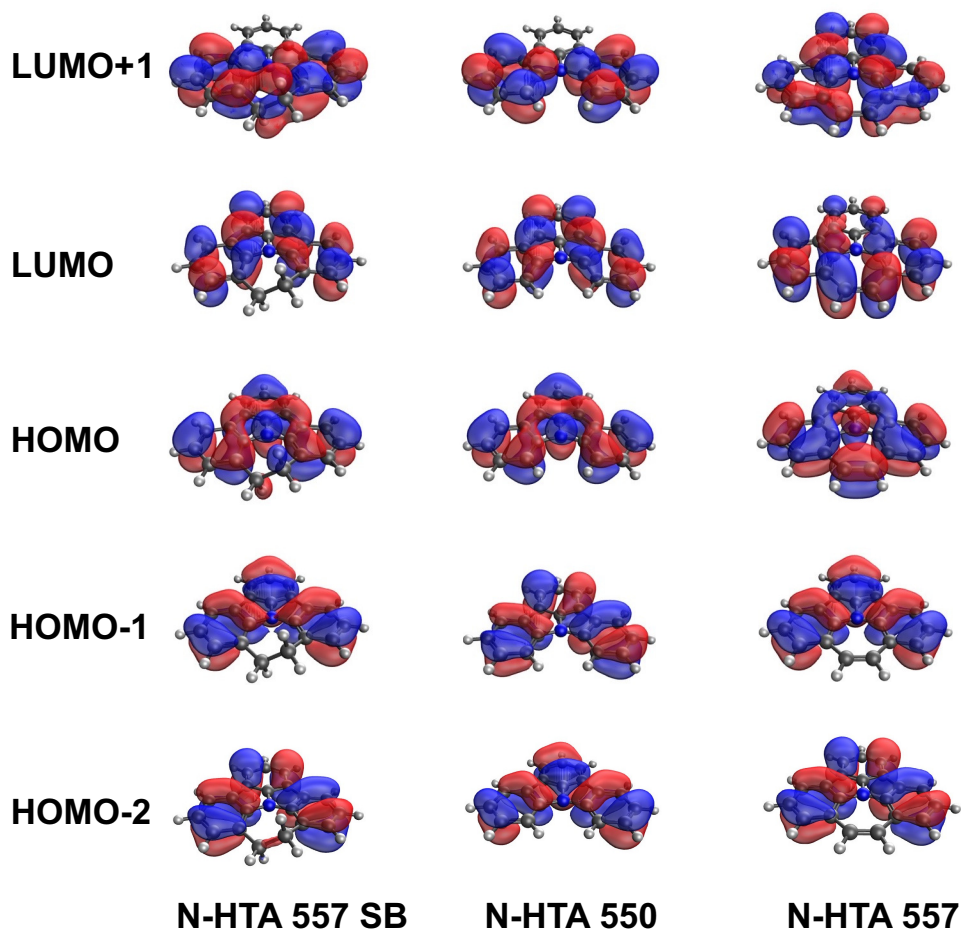
Figure 3.38.: Frontier molecular orbitals of electronic states with low excitation energies of the N-HTA derivatives ; N-HTA 557SB (left), N-HTA 550 (middle), N-HTA 557 (right). Taken from Ref.[192].

Results and Discussion

To summarize, in this subsection it has been demonstrated that thin films of N-HTA 550 and N-HTA 557 can be prepared through deposition of the corresponding molecules at 373 K (N-HTA 550) and 393 K (N-HTA 557) into the ultra-high vacuum chamber and onto Au(111) substrate held at 200 K. The prepared samples were then characterized by TPD, vibrational and electronic HREELS in combination with DFT calculations. Based on the results from the fragment-mass-resolved TPD measurements it was determined that during annealing of the samples, the N-HTA 550 and N-HTA 557 molecules remain intact. Regardless, it was chosen to prepare the sub-monolayer and monolyer coverages of N-HTA 550 and N-HTA 557 samples by direct evaporation of the molecules on the substrate. The results from the coverage dependent TPD measurements on the molecules indicates that introduction of the -C=C- bridge in N-HTA 557 results in an increase in adsorbate/adsorbate and adsorbate/substrate-interaction for the molecule in comparison to N-HTA 550. Moreover, as shown via vibrational HREELS measurements, N-HTA 550 and N-HTA 557 at their sub-monolayer, mono - and multilayer coverages adopt a planar adsorption geometry on the Au(111) surface. Finally, through electronic HREELS measurements, it is found that introduction of the -C=C- bridge in N-HTA 557 results in a narrowing of the optical gap of about 0.9 eV from 3.4 eV for N-HTA 550 to 2.5 eV for N-HTA 557. Additionally, it is shown that in contrast to N-HTA 550, N-HTA 557 transfer electron to the Au(111) substrate and becomes positively charged. These effects are attributed to the influence of -C=C- bridge on the electronic structure of N-HTA 557 by extending the π-system in the molecule in comparison to N-HTA 550.

3.3.2. N-Heterotriangulene based Donor/Acceptor-Systems

After gaining a comprehensive understanding of the adsorption and electronic properties of N-HTA 550 and N-HTA 557 as two N-heterotriangulene-based donor (D) molecule, in the following, these molecules are used in combination with two well-known cyano-based acceptor (A) molecules namely, TCNQ and F$_4$TCNQ, to investigate the possibility of charge transfer in the corresponding D/A-systems. This investigation is inspired by the work of Michalsky *et al.*[88], in which they demonstrated that N-HTA 557 can undergo donor/acceptor interactions with the mentioned acceptors in both solid state and solution. This leaves the possibility of observing such interactions in the formed thin films of the D/A-systems, on Au(111) substrate, which is the focus of this study.

Similar to the presented results for N-HTA derivatives, the adsorption and electronic properties of TCNQ and F$_4$TCNQ molecules on Au(111) substrate were previously investigated by Dr. Friedrich Maaß with the same experimental setup used here and the obtained results are presented in Ref.[95]. These results are consulted in this study together with the observation made for N-HTAs, to interpret the obtained results for the corresponding D/A-systems. The used TCNQ and F$_4$TCNQ molecules for this study were purchased from TCI chemicals.

In order to prepare these systems, first a mono - or multilayer coverage of either one of the donor molecules (N-HTA 550 or N-HTA 557) are deposited on Au(111). This step is then followed by deposition of a monolayer coverage of the acceptor molecule (TCNQ or F$_4$TCNQ) on top of the underlying donor molecule coverage. Thereby, decoupling the acceptor molecules, from the substrate, while inducing a potential charge transfer between the donor and acceptor molecules. The conducted TPD studies (see appendix G.1) clearly shows that preparation of the D/A-systems via direct deposition of donor and subsequently acceptor molecules is possible. Therefore, this method is used to prepare samples for further vibrational and electronic HREELS measurements on the D/A-systems. Results from the vibrational HREELS measurements (see appendix G.2) indicate that TCNQ and F$_4$TCNQ molecules adsorb with a mainly planar geometry on the underlying N-HTA coverages. Such adsorption geometry should facilitate an intermolecular charge transfer between the donor and acceptor molecules at their interface.

The electronic HREELS is utilized to investigate the electronic structure of the formed D/A-systems. In the presented results from this set of mea-

surements, in order to distinguish between the contributions from donor and acceptor molecules to the overall electronic HREELS spectra of each system, the assigned electron energy loss features from donor molecules are labelled with orange and acceptor molecules with blue color.

The electronic HREELS spectra of TCNQ/N-HTA systems are shown in figure 3.39. The spectrum of the TCNQ/N-HTA 550 bilayer consists of the conventional Au(111) surface plasmon (CSP) at 2.5 eV[140], a strong electron energy loss feature with a peak maximum at 3 eV and a broad loss feature at 5.4 eV (see Figure 3.39 (a)). By comparing this spectrum with the measured electronic HREELS spectra of TCNQ on Au(111) (see Figure G.8 (a)), the peak maximum at 3 eV can be assigned to the transition of ground state (S_0) to the first singlet excited state (S_1), i.e. the optical gap of TCNQ as previously reported in Ref.[95]. Similarly, a comparison with the measured electronic HREELS spectrum of N-HTA 550 at its multilayer coverage on Au(111) reveals that the observed broad loss feature at 5.4 eV in the spectrum of the D/A-bilayer corresponds to a higher transition ($S_0 \rightarrow S_5$) of N-HTA 550 (see Figure 3.36(b)).
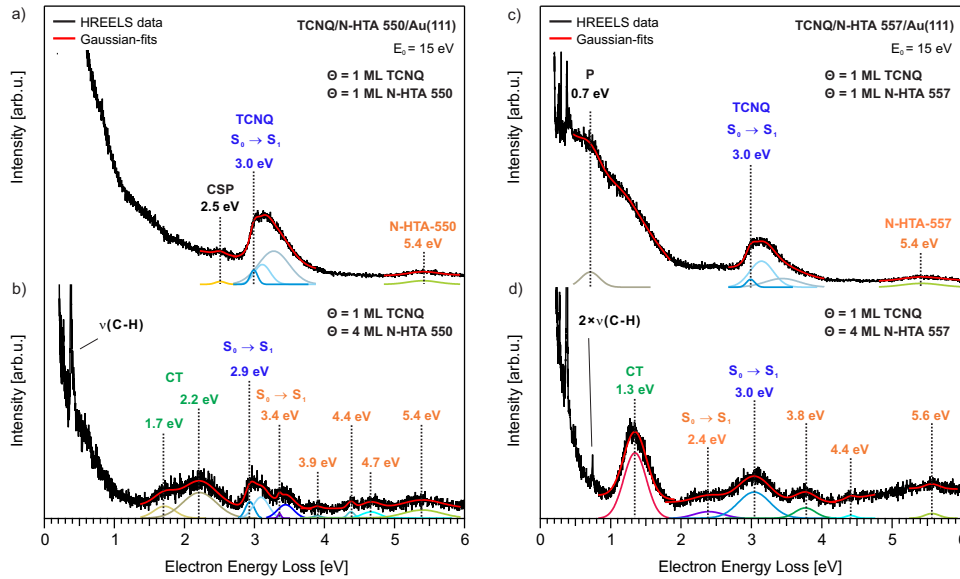
Figure 3.39.: Electronic HREELS spectra of 1 ML of TCNQ deposited on (a) 1 ML and (b) 4 ML of N-HTA 550 as well as (c) 1 ML and (d) 4 ML of N-HTA 557 on Au(111) (black spectra). The electronic loss features were fitted using Gaussian functions (red curves). E_0 is the primary energy of the incident electrons. Θ is the coverage in monolayer (ML). The contributions from TCNQ are marked with blue, N-HTA 550/557 with orange and CT-transitions with green colors.

By increasing the N-HTA 550 coverage to 4 ML, thus electronically decoupling the donor molecules at higher layers in addition to the overlying acceptor molecules from the metallic substrate, further loss features associated with N-HTA 550 can also be detected in the spectrum of the compound (see Figure 3.39 (b)). In this spectrum, aside from the $S_0 \rightarrow S_1$ transition of TCNQ at 2.9 eV, the contribution of N-HTA 550 to the spectrum is evident from the $S_0 \rightarrow S_1$ transition (optical gap) at 3.4 eV as well as other higher transitions associated with the molecule at 3.9 eV (S_2), 4.4 eV (S_3), 4.7 eV (S_4) and 5.4 eV (S_5), which are mostly in good agreement with the assigned transitions of N-HTA 550 in the spectrum of its multilayer coverage on Au(111).

Interestingly, the spectrum of TCNQ/N-HTA 550 system at the multilayer coverage also includes two low-energy loss feature at 1.7 eV and 2.2 eV, which are both located beneath the $S_0 \rightarrow S_1$ transition of both donor and acceptor molecules and are absent in the spectrum of the corresponding D/A-bilayer as well as the measured spectra of individual TCNQ and N-HTA 550 molecules adsorbed on Au(111). These observations suggest that the loss features at 1.7 eV and 2.2 eV are the result of an interaction between the donor and acceptor molecules and originate from possible CT-states of TCNQ/N-HTA 550 system.

However, the question remains as to why the assigned CT-transitions could not be detected in the spectrum of the D/A-bilayer. It can be assumed that at the bilayer, the donor molecule at its monolayer coverage is strongly coupled with Au(111). As a result, no charge transfer between the over laying TCNQ and the under laying N-HTA 550 takes place. This assumption is supported by the fact that increasing the coverages of N-HTA 550 to 4 ML, thus decoupling the donor molecules at higher layers from the metallic substrate leads to detection of the loss features associated with CT-transitions between the two molecules in the multilayer spectrum of the system.

As for TCNQ/N-HTA 557 system, the spectrum of its bilayer (see Figure 3.39 (c)) consist of a contribution at 0.7 eV, the $S_0 \rightarrow S_1$ transition of TCNQ at 3 eV and a broad loss feature at 5.4 eV which can be assigned to the higher transition ($S_0 \rightarrow S_4$) of N-HTA 557, when compared with the measured electronic HREELS spectrum of the molecule at its multilayer coverage on Au (111) (see Figure 3.36 (d)). The contribution at 0.7 eV is located in an energetic position close to the assigned plasmonic excitation (P) of TCNQ on Au(111) (at 0.5 and 0.6 eV in Figure G.8 (a) and (b)). Accordingly, the observed loss feature at 0.7 eV in the spectrum of the TCNQ/N-HTA 557

bilayer is attributed to plasmonic excitation of TCNQ. The origin of this excitation is discussed in details in Ref.[95].

Increasing the N-HTA 557 coverage to 4 ML leads to a complete decoupling of the acceptor molecules from the substrate (see Figure 3.39 (d)). Thus, the spectrum of TCNQ/N-HTA 557 system consists predominately of loss features, which can be assigned to the electronic transitions of either donor or acceptor molecules. These include the $S_0 \rightarrow S_1$ transitions of N-HTA 557 at 2.4 eV (see Figure 3.36 (d)) and TCNQ at 3 eV as well as other higher transitions of N-HTA 557 at 3.8 eV (S_2), 4.4 eV (S_3) and 5.6 eV (S_4), which are all in good agreement with the assigned transitions of the molecules in the measured electronic HREELS spectra of their multilayer coverages on Au(111).

In addition to the already assigned transitions, the spectrum of the D/A-system at the multilayer coverage, also includes a pronounced loss feature at 1.3 eV, which exhibits a similar behaviour as the two CT-transitions in TCNQ/N-HTA 550 compound. This loss feature is located beneath the $S_0 \rightarrow S_1$ transition of both donor and acceptor molecules and is also absent in the spectrum of the D/A-bilayer and only appears by increasing the coverage of donor molecule at the multilayer coverage. This suggests that the detected loss feature at 1.3 eV may also originates from a charge transfer between donor and acceptor molecules in TCNQ/N-HTA 557 system.

However, when the spectrum of the corresponding D/A-system is compared to the spectrum of N-HTA 557 at the multilayer coverage on Au(111) (see Figure 3.36 (d)), it becomes apparent that the loss feature in question is conveniently located at the same electron energy loss (1.3 eV) as previously assigned to CT-state of N-HTA 557 on Au(111). Whether the detected loss feature at 1.3 eV in the D/A-system originates from a charge transfer between TCNQ and N-HTA 557 molecules or is the result of the electron transfer from N-HTA 557 to Au(111) can be clarified by the fact that increasing the N-HTA 557 coverage in the compound induces the loss feature in question, whereas in the case of the adsorbed individual donor molecule on Au(111), a similar increase in coverage results in a decrease in the intensity of the loss feature at the multilayer in comparison to the monolayer coverage (see Figure 3.36 (c) and (d)). This indicates that loss feature results from donor-acceptor interaction and potentially originates from the charge transfer between N-HTA 557 molecules at higher layers with the overlaying TCNQ rather than the charge transfer between N-HTA 557 molecule and Au(111) at the interface with the substrate. As a result, it can be

concluded that both donor molecules, N-HTA 550 and N-HTA 557, undergo a charge transfer with the overlaying TCNQ in TCNQ/N-HTA systems at the multilayer coverage and as such form CT-complexes.

After gaining an insight into the influence of N-HTA derivatives as donor molecules on the overall electronic structure of the TCNQ/N-HTA systems, in the following, another acceptor molecule, F_4TCNQ, is used to form F_4TCNQ /N-HTA systems, in order to investigate the influence of a stronger acceptor molecule on the electronic structure of the corresponding D/A-systems. Figure 3.40 shows the measured electronic HREELS spectra of F_4TCNQ/N-HTA systems on Au(111).
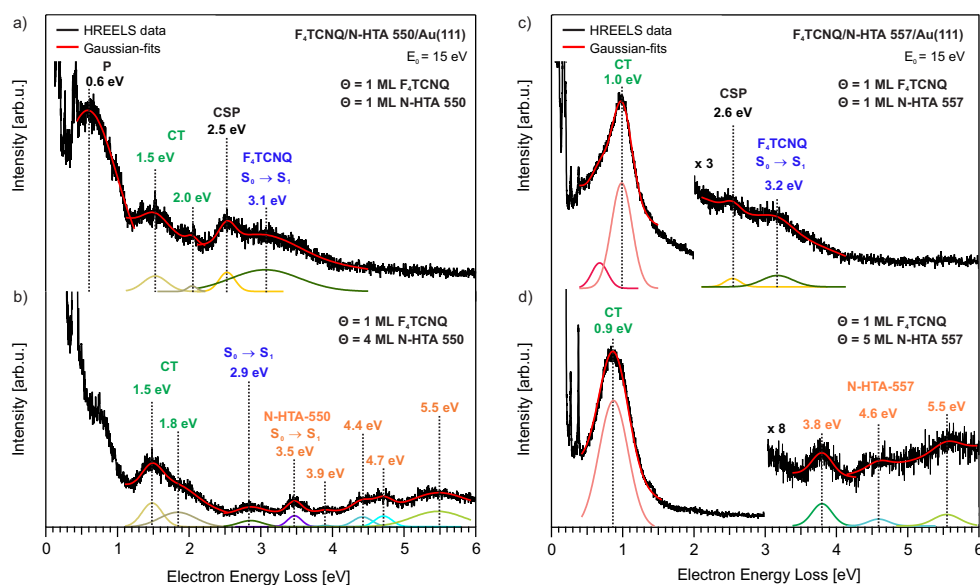
Figure 3.40.: Electronic HREELS spectra of 1 ML of F_4TCNQ deposited on (a) 1 ML and (b) 4 ML of N-HTA 550 as well as (c) 1 ML and (d) 5 ML of N-HTA 557 on Au(111) (black spectra). The electronic loss features were fitted using Gaussian functions (red curves). E_0 is the primary energy of the incident electrons. Θ is the coverage in monolayer (ML). The contributions from F_4TCNQ are marked with blue, N-HTA 550/557 with orange and CT-transitions with green colors.

Starting with the F_4TCNQ /N-HTA 550 bilayer (see Figure 3.40 (a)), the spectrum of the compound consists of a contribution at 0.6 eV, two low-energy loss features at 1.5 eV and 2 eV, the conventional Au(111) surface plasmon at 2.5 eV and a broad loss features at 3.1 eV, which agrees with the $S_0 \rightarrow S_1$ transition, i.e. the optical gap of F_4TCNQ[95] from the measured electronic HREELS spectrum of the molecule at its multilayer coverage on Au(111) (see

Results and Discussion

Figure G.8 (c)). The contribution at 0.6 eV, labelled with letter P, resembles the observed plasmonic excitation of F_4TCNQ on Au(111) as reported in Ref.[95].

As previously seen for the TCNQ/N-HTA 557 system, by increasing the the coverage of the underlying donor molecule, in this case N-HTA 550, to 4 ML, thus completely decoupling the overlaying acceptor molecules from the metallic substrate, the majority of the detected loss features in this spectrum can be assigned to the electronic transitions of either donor or acceptor molecules. These include the $S_0 \rightarrow S_1$ transitions of F_4TCNQ at 2.9 eV and N-HTA 550 at 3.5 eV as well as other higher transitions of N-HTA 550 at 3.9 eV, 4.4 eV, 4.7 eV and 5.5 eV, which are all in good agreement with the assigned transitions of the molecule in the measured electronic HREELS spectrum of its multilayer coverage on Au(111).

The two unassigned low-energy loss feature at 1.5 eV and 2.0 eV as can be seen in the spectrum of the D/A-bilayer are also present in the spectrum of the multilayer coverage at 1.5 eV and 1.8 eV. These loss features are located beneath the $S_0 \rightarrow S_1$ transition of F_4TCNQ and N-HTA 550 and are absent in the measured electronic HREELS spectra of both molecules on Au(111). Interestingly, the double peak structure of these loss features resembles the previously assigned CT-transitions of TCNQ/N-HTA 550 system. However, in case of F_4TCNQ/N-HTA 550 system, the features are shifted to lower energies by 200 meV and 400 meV and exhibit a different profile, where the low energy loss peak (at 1.5 eV) have a higher relative intensity in comparison to the second feature (at 2.0 eV/1.8 eV). These observations indicates that similar to the case of TCNQ/N-HTA 550 system, these two loss features are also the result of a possible charge transfer, this time between F_4TCNQ and N-HTA 550. Therefore, it can be concluded that the F_4TCNQ/N-HTA 550 system forms a CT-complex.

A comparison between the the results from the electronic HREELS measurements on F_4TCNQ/N-HTA 550 and TCNQ/N-HTA 550 systems reveals that by changing the acceptor molecule from TCNQ to F_4TCNQ, thus increasing the acceptor strength of the molecule, in contrast to TCNQ/N-HTA 550 system, a charge transfer between donor and acceptor molecules can also takes place at the F_4TCNQ/N-HTA 550 bilayer. This observation indicates that forming a CT-complex with F_4TCNQ as an acceptor molecule instead of TCNQ changes the behaviour of the charge transfer in a way that the un-

derlying donor molecule interacts with the overlaying acceptor molecule at a monolayer coverage on Au(111). This behaviour can only be interpreted as the result of influence of a stronger acceptor, F_4TCNQ, on the overall electronic structure of the F_4TCNQ/N-HTA 550 system.

The influence of F_4TCNQ on the D/A-systems is also evident from the measured electronic spectra of F_4TCNQ/N-HTA 557 bilayer as shown in figure 3.40 (c). This spectrum consists of a pronounced low-energy loss feature at 1 eV, resembling the previously assigned CT-transition of the TCNQ/N-HTA 557 system (at 1.3 eV), the conventional Au(111) surface plasmon at 2.6 eV and the $S_0 \rightarrow S_1$ transition of F_4TCNQ at 3.2 eV. The loss feature at 1 eV is located beneath the $S_0 \rightarrow S_1$ transition of F_4TCNQ in the same spectrum and the known $S_0 \rightarrow S_1$ transition of N-HTA 557 at 2.1 eV from its measured electronic HREELS spectrum at the monolayer coverage on Au (111) (see Figure 3.36 (c)). Additionally, it is absent in the measured electronic HREELS spectra of both donor and acceptor molecules at their mono- or multilayer coverage on Au(111). These observations suggests that the loss feature at 1 eV, similar to other assigned low-energy loss features in the previously investigated D/A-system, originates from a charge transfer between the donor and acceptor molecules and as such it is assigned to a CT-transition. This indicates that the F_4TCNQ/N-HTA 557 system forms a CT-complex.

By increasing the coverage of N-HTA 557 to 5 ML, the CT-transition of the D/A-system shifts to a lower electron energy loss at 0.9 eV and its relative intensity to the rest of the spectrum increases even more as shown in figure 3.40 (d). Surprisingly, the $S_0 \rightarrow S_1$ transitions of neither F_4TCNQ nor N-HTA 557 can be detected in the measured multilayer spectrum of this D/A-system. This is in contrast to the previously observed behaviour of other D/A-systems, where increasing the coverage of the underlying donor molecule results in detection of its $S_0 \rightarrow S_1$ transition along with the ones of the acceptor molecule at the multilayer coverage. However, other higher transitions associated with N-HTA 557 at 3.8 eV, 4.6 eV and 5.5 eV can still be detected in the multilayer spectra of the D/A-system, which are all in good agreement with the assigned transitions of the molecule at its multilayer coverage on Au(111).
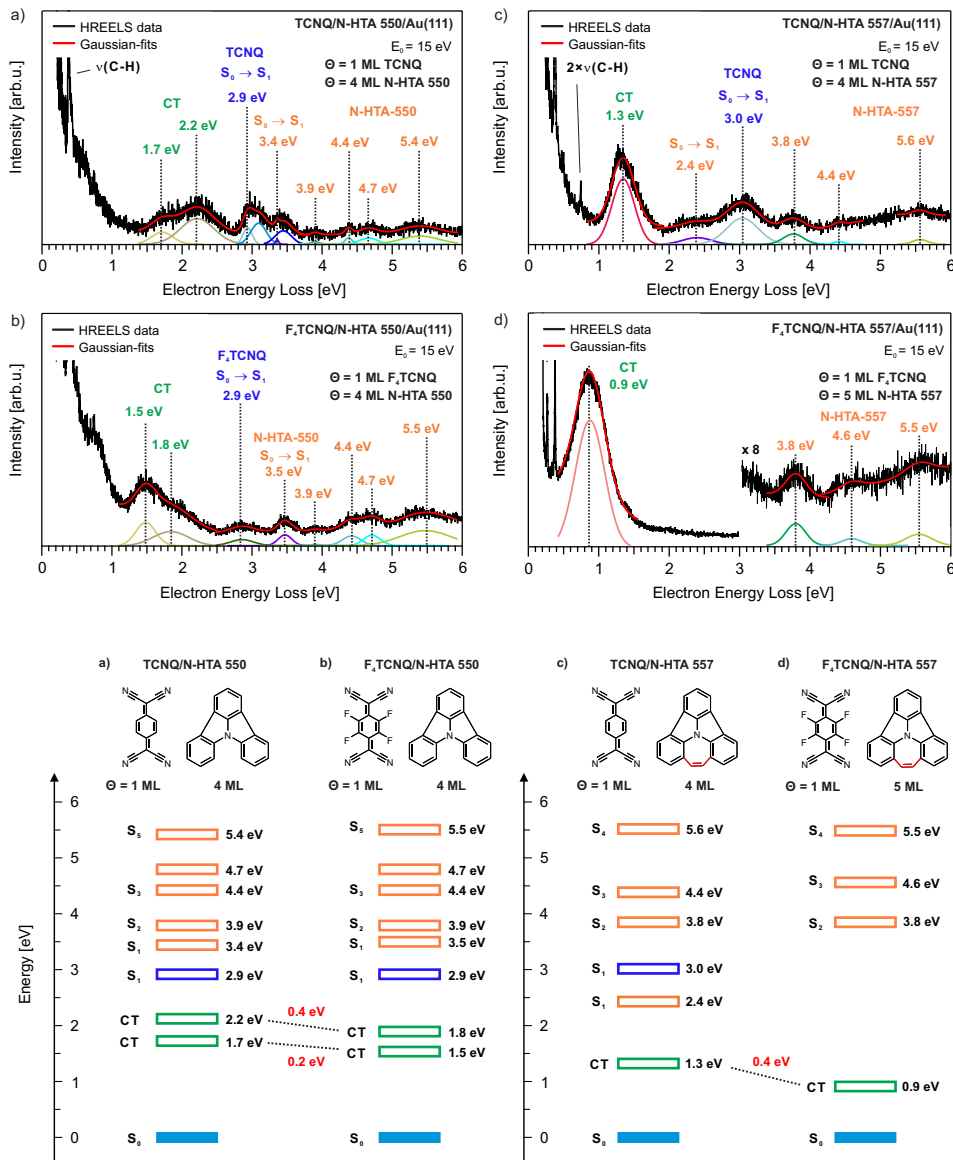
Figure 3.41.: Electronic HREELS spectra (top) of 1 ML of TCNQ deposited on (a) 4 ML of N-HTA 550 and (c) 4 ML of N-HTA 557 as well as 1 ML of F$_4$TCNQ deposited on (b) 4 ML of N-HTA 550 and (d) 5 ML of N-HTA 557 on Au(111) (black spectra). The electronic loss features were fitted using Gaussian functions (red curves). E$_0$ is the primary energy of the incident electrons. Θ is the coverage in monolayer (ML). The contributions from TCNQ and F$_4$TCNQ are marked with blue, N-HTA 550/557 with orange and CT-transitions with green colors. The identified and assigned electronic transitions of the D/A-systems are summarized in an energy level diagram (bottom).

Noticeably, when the obtained spectra of the formed D/A-system are compared (see figure 3.41 top), it becomes clear that regardless of the nature of the used acceptor molecule, the number of identified CT-transition for each of the D/A-systems is determined by the used donor molecule. To be specific, it appears that D/A-systems with N-HTA 550 as donor (see figure 3.41 (a) and (b)) exhibit two CT-transition and the ones formed with N-HTA 557 exhibit only one pronounced CT-transition (see figure 3.41 (c) and (d)). The identified and assigned energies of electronic transitions of the singlet (S) and CT-states in the D/A-systems are summarized in an energy level diagram in figure 3.41 (bottom).

Furthermore, the spectra of the TCNQ/N-HTA and F_4TCNQ/N-HTA systems also include two contributions from the in plane ν_s(C-N) and ν_s(C-H) stretching modes vibrations in their multilayer coverages (see figure 3.42 (e), (f), (g) and (h)). By comparing the low-energy loss region of these spectra with the same region in the spectra of individual molecules, N-HTA 550 and N-HTA 557 as well as TCNQ and F_4TCNQ, at their multilayer coverages on Au(111) (see figure 3.42 (a), (b), (c) and (d)), the observed ν_s(C-N) vibrations are attributed to TCNQ and F_4TCNQ, while the ν_s(C-H) vibrations can originate from either TCNQ or N-HTA derivatives or a combination of both.

The same comparison also shows that going from the adsorbed coverages of individual TCNQ and F_4TCNQ molecules on Au(111) to their corresponding D/A-system with N-HTA derivatives, the energetic positions of the ν_s(C-N) vibrations are shifted from 275 meV (for TCNQ) to 274 and 273 meV (for TCNQ/N-HTA system) and from 277 meV (for F_4TCNQ) to 272 and 270 meV (for F_4TCNQ/N-HTA system). This indicates that N-HTA 557 induces a much larger energy shift (about 7 meV) for the given vibration, toward a lower energy in F_4TCNQ/N-HTA 557, in comparison to N-HTA 550.

This trend agrees well with the findings of Michalsky *et al.*[88], in which they also observed a shift of ν_s(C-N) vibrations of the acceptor molecules toward lower wavenumbers in D/A-systems in comparison to pristine acceptor. They report that in case of TCNQ, ν_s(C-N) vibration of the molecule, shifts from 2224 cm^{-1} (276 meV) for the pristine molecule to 2220 cm^{-1} (275 meV) for the co-crystallized molecule with N-HTA 557, while the same vibrations shifts from 2226 cm^{-1} (276 meV) for pristine F_4TCNQ molecule to 2219 cm^{-1} (275 meV) in its amorphous solid with N-HTA 557[88]. These observations are another sign of donor/acceptor interactions, in which the stronger donor

molecule (N-HTA 557), exhibit larger energy-shift with the stronger acceptor molecule (F$_4$TCNQ).
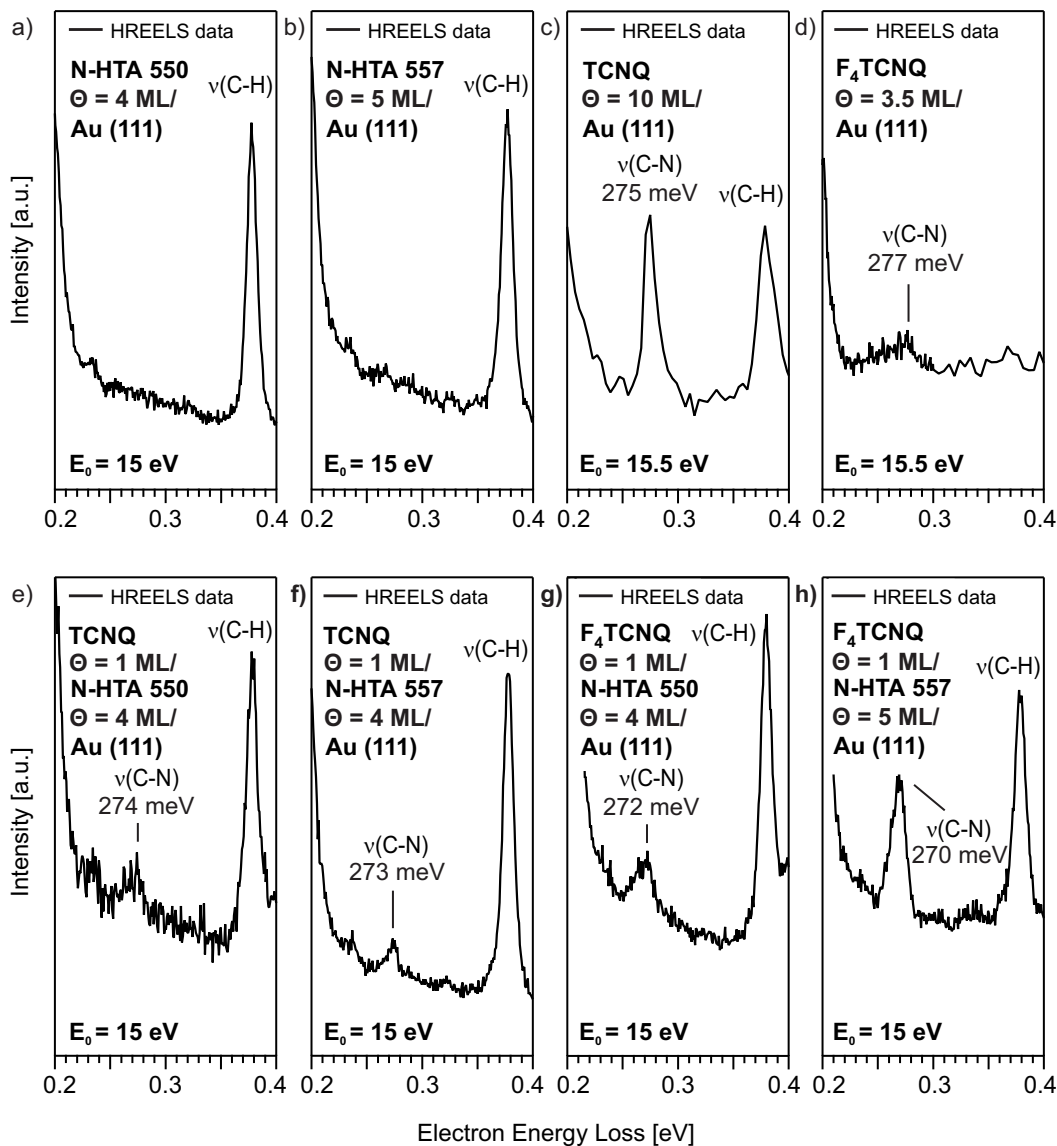
Figure 3.42.: Low electron energy loss region of HREELS spectra of (a) N-HTA 550 (4 ML), (b) N-HTA 557 (5 ML), (c) TCNQ (10 ML) and (d) F$_4$TCNQ (3.5 ML) adsorbed on Au(111) as well as 1 ML of TCNQ deposited on (e) 4 ML of N-HTA 550, (f) 4 ML of N-HTA 557 and 1 ML of F$_4$TCNQ deposited on (g) 4 ML of N-HTA 550, (h) 5 ML of N-HTA 557 on Au(111). E$_0$ is the primary energy of the incident electrons. Θ is the coverage in monolayer (ML).

Finally, in order to investigate the influence of sample preparation on charge transfer between the donor and acceptor molecules, the N-HTA 557/F_4TCNQ system is formed, in which the preparation order is reversed. This means that in the first step a mono- or multilayer coverage of F_4TCNQ is deposited on Au(111) and in the second step a monolayer of N-HTA 557 is deposited on top of the underlying F_4TCNQ coverage to form a potential CT-complex. The results from this study is presented in appendix (see G.3).

To summarize, in this subsection it has been demonstrated that bilayers and thin films of D/A-systems with N-HTA 550 and N-HTA 557 as donor molecules as well as TCNQ and F_4TCNQ as acceptor molecules can be prepared by first depositing a mono - or multilayer coverage of either one of the donor molecules as a decoupling layer onto Au(111) substrate held at 200 K, followed by deposition of a monolayer of one of the acceptor molecules onto the underlying molecular coverage. Through electronic HREELS measurements, it is found that the prepared D/A-systems form CT-states at 1.7 eV and 2.2 eV (TCNQ/N-HTA 550), 1.5 eV and 1.8 eV (F_4TCNQ/N-HTA 550), 1.3 eV (TCNQ/N-HTA 557), and 0.9 eV (F_4TCNQ/N-HTA 557). In case of TCNQ/N-HTA systems, the CT-states are only formed at the multilayer coverage, while in F_4TCNQ/N-HTA systems the corresponding CT-states are also formed at their bilayer. This observation is attributed to the stronger acceptor strengths of F_4TCNQ in comparison to TCNQ.

In conclusion, the presented studies in this section provide valuable insights into the adsorption and electronic properties of two N-heterotriangulene derivatives, namely N-HTA 550 and the newly synthesized N-HTA 557 as potential donor molecules, at the interface with Au(111) and within their thin films. Additionally, the studied charge transfer properties of N-HTA derivatives in their D/A-systems, which are formed in combination with two known acceptor molecules, TCNQ and F_4TCNQ, can be used as a reference for developing other D/A-systems based on small molecule organic semiconductors.

4. Conclusion

In this thesis, high-resolution electron energy-loss spectroscopy (HREELS) and temperature-programmed desorption (TPD) techniques in combination with density functional theory (DFT) calculations have been used to investigate the influence of N-introduction, core substitution and connectivity on the adsorption and electronic properties of various of N-heteropolycycles. The studied molecules included derivatives of linear- (DAP and TAP) and arrow-shaped (TIPS-BAP) N-heteropentacenes, naphto- (NTD, NTD-Cl and NTD-Br) and benzobis- (BBT-Ph and BBT-Th) thiadiazoles as well as N-heterotriangulenes (N-HTA 550 and N-HTA 557).

In the presented studies, results from TPD measurements provided valuable insights into the effects of alteration made to the molecules on the adsorbate/adsorbate and adsorbate/substrate-interactions. It has been found that N-introduction in DAP and TAP results in an increase in adsorbate/substrate-interactions in comparison to parent pentacene (PEN), while introduction of two additional N-atoms into the backbone of TAP does not lead to stronger interaction of the adsorbate with the metallic substrate, when compared to DAP. In case of TIPS-BAP, addition of N-atoms results in an increase in adsorbate/adsorbate-interactions, which is evident from the higher desorption temperature of the multilayer coverage of the molecule in comparison to the desorption temperature of its polycyclic aromatic hydrocarbon (PAH) counterpart, TIPS-BP. In contrast, it has been observed that at the monolayer coverage, TIPS-BAP desorb at a lower temperature relative to TIPS-BP. This desorption behaviour is attributed to the interplay of N-atoms and the phenyl rings in the backbone of TIPS-BAP, which leads to weaker adsorbate/substrate-interactions. As for core substitution in thiadiazole derivatives, it is revealed that halogenation via Cl and Br atoms in NTD-Cl and NTD-Br as well as substitution of thiophene groups in BBT-Th result in an increase in adsorbate/adsorbate and adsorbate/substrate-interaction for the corresponding molecules in comparison to phenyl substituted BBT-Ph. Similarly, in case of N-heterotriangulene derivatives, structural variation through introduction of

-C=C- bridge in N-HTA 557 also results in an increase in adsorbate/adsor
-bate and adsorbate/substrate-interaction for the molecule in comparison to
N-HTA 550. These observations indicate that alteration of molecules can affect
their interactions with neighbouring molecules as well as the substrate.

Furthermore, as shown via vibrational HREELS measurements, all of the
studied molecules, at all coverages adopt a planar adsorption geometry rela-
tive to the substrate surface. This general finding indicates that symmetric
and asymmetric N-introduction in DAP and TAP or TIPS-BAP, core substitu-
tion via large halogen atoms in NTD-Cl and NTD-Br as well as connecting the
moieties of N-HTA 557 via -C=C- bridge, do not change the adsorption geome-
try of the corresponding molecules compared to their planar parent molecules
(PEN, TIPS-BP, NTD and N-HTA 550). Additionally, examination of the
TIPS-BAP and TIPS-BP as well as BBT-Ph and BBT-Th revealed that despite
the presence of bulky (TIPS) and aromatic (phenyl and thiophene) side groups
in these molecules, the adsorption geometry of the molecules remains planer
even at multilayer coverage. These observations are attributed to the strong
interaction of adsorbates with Au(111) substrate, which forces the molecules
to adapt the planer geometry, and possibly the packing of the molecules in
their thin films that favours the planer geometry.

Finally, through electronic HREELS measurements, it was determined that
N-introduction can affect the electronic structure of N-heteropolycycles in
three ways, namely narrowing the optical gap ($S_0 \rightarrow S_1$ transition), shifting
the assigned $S_0 \rightarrow T_1$ transition to a higher energy and inducing a pronounced
rise in the intensity of the α - band ($S_0 \rightarrow S_2$) in comparison to parent PAHs.
As observed for linear N-heteropentacenes, upon N-introduction, the optical
gap is reduced by 100 meV from 2.1 eV for PEN to 2 eV for DAP and by
500 meV to 1.6 eV for TAP, due to stabilization of the valence molecular
orbitals by N-atoms with high electronegativity, while the assigned $S_0 \rightarrow T_1$
transition shifts to a higher energy by 300 meV from 0.9 eV for DAP and
PEN to 1.2 eV for TAP. Similarly, the optical gap of the arrow-shaped N-
heteropentacene is reduced by 200 meV from 2.1 eV for TIPS-BP to 1.9 eV
for TIPS-BAP, as a result of the stabilization of the polar first excited sin-
glet state (S_1) of TIPS-BAP in a polar environment. The pronounced rise in
the intensity of the α - band going form PEN to DAP and then TAP, and
going form TIPS-BP to TIPS-BAP has been attributed to the alteration of
the energies of the molecular orbitals and the change in their transition dipole

moments by the introduced N-atoms in the backbone of the corresponding N-heteropentacene derivatives. The electronic structure of N-heteropolycycles can also be fine-tuned by core substitution. As demonstrated for naphtothiadiazole derivatives, the core halogenation in NTD-Cl and NTD-Br results in a reduction of the transition energies of singlet and lowest triplet states in comparison to NTD. This is evident from the narrowing of the optical gap by 200 meV from 2.6 eV for NTD to 2.4 eV for NTD-Cl and NTD-Br as well as the shift of the assigned $S_0 \rightarrow T_1$ transition to a lower energy by 150 meV from 1.75 eV for NTD to 0.6 eV for NTD-Cl and NTD-Br. These trends are attributed to the influence of electron withdrawing halogens with much higher electronegativity than hydrogen atoms on the electronic structure of the halogenated molecules. Similarly, substitution of benzobisthiadiazole derivatives with thiophene groups in BBT-Th, results in a reduction of the transition energies of singlet and lowest triplet states of the molecule in comparison to the phenyl substituted BBT-Ph due to stabilization of frontier orbitals in BBT-Th as the result of intramolecular charge transfer between the BBT moiety and the substituted thiophene groups. This is evident from the narrowing of the optical gap by 600 meV from 2.2 eV for BBT-Ph to 1.6 eV for BBT-Th as well as shift of the assigned $S_0 \rightarrow T_1$ transition to the lower energy by 500 meV from 1.2 eV for BBT-Th to 0.7 eV for BBT-Ph. Moreover, it has been found that electronic structure of a molecule can also be adjusted by changing its structure through connecting different moieties of the corresponding molecule. This is exhibited by introduction of -C=C- bridge in N-HTA 557, which resulted in a narrowing of the optical gap of about 0.9 eV from 3.4 eV for N-HTA 550 to 2.5 eV for N-HTA 557. This finding is attributed to the influence of -C=C-bridge on the electronic structure of N-HTA 557 by extending the π-system in the molecule in comparison to N-HTA 550. Subsequently, it has been demonstrated that the studied N-heterotriangulenes can be used as donor molecules in D/A-systems in combination with well-known acceptor molecules (TCNQ and F_4TCNQ) to form charge transfer (CT)-complexes.

Ultimately, the findings from the presented studies in this thesis provided new and valuable insights into the adsorption and electronic properties of N-heteropolycycles on a metallic substrate and within their thin films. In future works, further investigation of N-heteropolycyclic molecules in the scope of collaborative research center SFB 1249 can lead to a comprehensive understanding of the properties of this class of aromatic compounds, which can be used

to improve and optimize the performance of organic based (opto)electronic devices.

Bibliography

[1] Heywang, W.; Zaininger, K. H. Silicon: the Semiconductor Material. *Silicon* **2004**, 25–42.

[2] Claeys, C.; Simoen, E. Germanium-Based Technologies: From Materials to Devices. *Germanium-Based Technologies: From Materials to Devices* **2007**, 1–449.

[3] D'Andrade, B. W.; Forrest, S. R. White Organic Light-Emitting Devices for Solid-State Lighting. *Advanced Materials* **2004**, *16*, 1585–1595.

[4] Reineke, S.; Lindner, F.; Schwartz, G.; Seidler, N.; Walzer, K.; Lüssem, B.; Leo, K. White organic light-emitting diodes with fluorescent tube efficiency. *Nature 2009 459:7244* **2009**, *459*, 234–238.

[5] Torsi, L.; Magliulo, M.; Manoli, K.; Palazzo, G. Organic field-effect transistor sensors: a tutorial review. *Chemical Society Reviews* **2013**, *42*, 8612–8628.

[6] Lee, J.; Chen, H. F.; Batagoda, T.; Coburn, C.; Djurovich, P. I.; Thompson, M. E.; Forrest, S. R. Deep blue phosphorescent organic light-emitting diodes with very high brightness and efficiency. *Nature Materials 2015 15:1* **2015**, *15*, 92–98.

[7] Crone, B.; Dodabalapur, A.; Gelperin, A.; Torsi, L.; Katz, H. E.; Lovinger, A. J.; Bao, B. Electronic sensing of vapors with organic transistors. *Applied Physics Letters* **2001**, *78*, 2229–2231.

[8] Ma, L. P.; Liu, J.; Yang, Y. Organic electrical bistable devices and rewritable memory cells. *Applied Physics Letters* **2002**, *80*, 2997–2999.

[9] Möller, S.; Periov, C.; Jackson, W.; Taussig, C.; Forrest, S. R. A polymer/semiconductor write-once read-many-times memory. *Nature 2003 426:6963* **2003**, *426*, 166–169.

Bibliography

[10] Forrest, S. R. The path to ubiquitous and low-cost organic electronic appliances on plastic. *Nature 2004 428:6986* **2004**, *428*, 911–918.

[11] Chih Wei Chu, B.; Ouyang, J.; Tseng, J.-H.; Yang, Y.; Yang, Y.; Chu, C. W.; Tseng, J.-h.; Ouyang, J. Organic Donor–Acceptor System Exhibiting Electrical Bistability for Use in Memory Devices. *Advanced Materials* **2005**, *17*, 1440–1443.

[12] Gather, M. C.; Köhnen, A.; Falcou, A.; Becker, H.; Meerholz, K. Solution-Processed Full-Color Polymer Organic Light-Emitting Diode Displays Fabricated by Direct Photolithography. *Advanced Functional Materials* **2007**, *17*, 191–200.

[13] Sekitani, T.; Yokota, T.; Zschieschang, U.; Klauk, H.; Bauer, S.; Takeuchi, K.; Takamiya, M.; Sakurai, T.; Someya, T. Organic nonvolatile memory transistors for flexible sensor arrays. *Science* **2009**, *326*, 1516–1519.

[14] Sekitani, T.; Zschieschang, U.; Klauk, H.; Someya, T. Flexible organic transistors and circuits with extreme bending stability. *Nature Materials 2010 9:12* **2010**, *9*, 1015–1022.

[15] Yokota, T.; Zalar, P.; Kaltenbrunner, M.; Jinno, H.; Matsuhisa, N.; Kitanosako, H.; Tachibana, Y.; Yukita, W.; Koizumi, M.; Someya, T. Ultraflexible organic photonic skin. *Science Advances* **2016**, *2*.

[16] Müllen, K.; Scherf, U. Organic Light Emitting Devices: Synthesis, Properties and Applications. *Organic Light Emitting Devices: Synthesis, Properties and Applications* **2006**, 1–410.

[17] Bunz, U. H.; Engelhart, J. U.; Lindner, B. D.; Schaffroth, M. Large N-heteroacenes: new tricks for very old dogs? *Angewandte Chemie (International ed. in English)* **2013**, *52*, 3810–3821.

[18] Miao, Q.; Miao, Q. Ten Years of N-Heteropentacenes as Semiconductors for Organic Thin-Film Transistors. *Advanced Materials* **2014**, *26*, 5541–5549.

[19] Bunz, U. H. The Larger Linear N-Heteroacenes. *Accounts of Chemical Research* **2015**, *48*, 1676–1686.

[20] Hoff, J. J.; Zhu, L.; Dong, Y.; Albers, T.; Steel, P. J.; Cui, X.; Wen, Y.; Lebedyeva, I.; Miao, S. Diazapentacene derivatives: synthesis, properties, and structures. *RSC Advances* **2016**, *6*, 86824–86828.

[21] Bunz, U. H.; Freudenberg, J. N-Heteroacenes and N-Heteroarenes as N-Nanocarbon Segments. *Accounts of chemical research* **2019**, *52*, 1575–1587.

[22] Winkler, M.; Houk, K. N. Nitrogen-rich oligoacenes: Candidates for n-channel organic semiconductors. *Journal of the American Chemical Society* **2007**, *129*, 1805–1815.

[23] Tverskoy, O.; Rominger, F.; Peters, A.; Himmel, H. J.; Bunz, U. H. An Efficient Synthesis of Tetraazapentacenes. *Angewandte Chemie International Edition* **2011**, *50*, 3557–3560.

[24] Herz, J.; Buckup, T.; Paulus, F.; Engelhart, J.; Bunz, U. H.; Motzkus, M. Acceleration of singlet fission in an aza-derivative of TIPS-pentacene. *Journal of Physical Chemistry Letters* **2014**, *5*, 2425–2430.

[25] Braun, S.; Salaneck, W. R.; Fahlman, M. Energy-Level Alignment at Organic/Metal and Organic/Organic Interfaces. *Advanced Materials* **2009**, *21*, 1450–1472.

[26] Brédas, J. L.; Norton, J. E.; Cornil, J.; Coropceanu, V. Molecular understanding of organic solar cells: The challenges. *Accounts of Chemical Research* **2009**, *42*, 1691–1699.

[27] May, V.; Kühn, O. *Charge and Energy Transfer Dynamics in Molecular Systems: Third Edition*; Wiley-VCH, 2011.

[28] Beljonne, D.; Cornil, J.; Muccioli, L.; Zannoni, C.; Brédas, J. L.; Castet, F. Electronic Processes at Organic-Organic Interfaces: Insight from Modeling and Implications for Opto-electronic Devices †. *Chemistry of Materials* **2011**, *23*, 591–609.

[29] Koch, N.; Ueno, N.; Wee, A. T. S. The molecule-metal interface. **2013**, 255.

Bibliography

[30] Gruenewald, M.; Wachter, K.; Meissner, M.; Kozlik, M.; Forker, R.; Fritz, T. Optical and electronic interaction at metal–organic and organic–organic interfaces of ultra-thin layers of PTCDA and SnPc on noble metal surfaces. *Organic Electronics* **2013**, *14*, 2177–2183.

[31] Oehzelt, M.; Koch, N.; Heimel, G. Organic semiconductor density of states controls the energy level alignment at electrode interfaces. *Nature Communications 2014 5:1* **2014**, *5*, 1–8.

[32] Köhler, A.; Bässler, H. Electronic processes in organic semiconductors: An introduction. *Electronic Processes in Organic Semiconductors: An Introduction* **2015**, 1–405.

[33] Ibach, H. Electron Energy Loss Spectrometers. **1991**, *63*.

[34] Ibach, H. Physics of surfaces and interfaces. *Physics of Surfaces and Interfaces* **2006**, 1–646.

[35] Jensen Frank Introduction to Computational Chemistry, 3rd Edition — Wiley. *WILEY* **2017**, 660.

[36] Bronner, C.; Leyssner, F.; Stremlau, S.; Utecht, M.; Saalfrank, P.; Klamroth, T.; Tegeder, P. Electronic structure of a subnanometer wide bottom-up fabricated graphene nanoribbon: End states, band gap, and dispersion. *Physical Review B - Condensed Matter and Materials Physics* **2012**, *86*, 085444.

[37] Bronner, C.; Stremlau, S.; Gille, M.; Brauße, F.; Haase, A.; Hecht, S.; Tegeder, P. Aligning the Band Gap of Graphene Nanoribbons by Monomer Doping. *Angewandte Chemie International Edition* **2013**, *52*, 4422–4425.

[38] Hahn, L.; Maaß, F.; Bleith, T.; Zschieschang, U.; Wadepohl, H.; Klauk, H.; Tegeder, P.; Gade, L. H. Core Halogenation as a Construction Principle in Tuning the Material Properties of Tetraazaperopyrenes. *Chemistry – A European Journal* **2015**, *21*, 17691–17700.

[39] Maass, F.; Stein, A.; Kohl, B.; Hahn, L.; Gade, L. H.; Mastalerz, M.; Tegeder, P. Substrate-Directed Growth of N-Heteropolycyclic Molecules on a Metal Surface. *Journal of Physical Chemistry C* **2016**, *120*, 2866–2873.

[40] Maaß, F.; Utecht, M.; Stremlau, S.; Gille, M.; Schwarz, J.; Hecht, S.; Klamroth, T.; Tegeder, P. Electronic structure changes during the on-surface synthesis of nitrogen-doped chevron-shaped graphene nanoribbons. *Physical Review B* **2017**, *96*, 045434.

[41] Swiderek, P.; Michaud, M.; Hohlneicher, G.; Sanche, L. Electron energy loss spectroscopy of solid naphthalene and acenaphthene: search for the low-lying triplet states. *Chemical Physics Letters* **1990**, *175*, 667–673.

[42] Swiderek, P.; Fraser, M. J.; Michaud, M.; Sanche, L. Electron-energy-loss spectroscopy of the low-lying triplet states of styrene. *The Journal of Chemical Physics* **1994**, *100*, 70–77.

[43] Dimitrakopoulos, C. D.; Purushothaman, S.; Kymissis, J.; Callegari, A.; Shaw, J. M. Low-voltage organic transistors on plastic comprising high-dielectric constant gate insulators. *Science* **1999**, *283*, 822–824.

[44] Appleton, A. L.; Brombosz, S. M.; Barlow, S.; Sears, J. S.; Bredas, J. L.; Marder, S. R.; Bunz, U. H. Effects of electronegative substitution on the optical and electronic properties of acenes and diazaacenes. *Nature Communications 2010 1:1* **2010**, *1*, 1–7.

[45] Witte, G.; Wöll, C. Growth of aromatic molecules on solid substrates for applications in organic electronics. *Journal of Materials Research* **2004**, *19*, 1889–1916.

[46] Coropceanu, V.; Li, H.; Winget, P.; Zhu, L.; Brédas, J. L. Electronic-Structure Theory of Organic Semiconductors: Charge-Transport Parameters and Metal/Organic Interfaces. *https://doi.org/10.1146/annurev-matsci-071312-121630* **2013**, *43*, 63–87.

[47] Lu, M. C.; Wang, R. B.; Yang, A.; Duhm, S. Pentacene on Au(1 1 1), Ag(1 1 1) and Cu(1 1 1): From physisorption to chemisorption. *Journal of Physics: Condensed Matter* **2016**, *28*, 094005.

[48] Yang, X.; Egger, L.; Fuchsberger, J.; Unzog, M.; Lüftner, D.; Hajek, F.; Hurdax, P.; Jugovac, M.; Zamborlini, G.; Feyer, V.; Koller, G.; Puschnig, P.; Tautz, F. S.; Ramsey, M. G.; Soubatch, S. Coexisting charge states in a unary organic monolayer film on a metal. *Journal of Physical Chemistry Letters* **2019**, *10*, 6438–6445.

Bibliography

[49] Maass, F.; Ajdari, M.; Kabeer, F. C.; Vogtland, M.; Tkatchenko, A.; Tegeder, P. Nonadditivity of the Adsorption Energies of Linear Acenes on Au(111): Molecular Anisotropy and Many-Body Effects. *Journal of Physical Chemistry Letters* **2019**, *10*, 1000–1004.

[50] Anthony, J. E.; Brooks, J. S.; Eaton, D. L.; Parkin, S. R. Functionalized pentacene: Improved electronic properties from control of solid-state order [20]. *Journal of the American Chemical Society* **2001**, *123*, 9482–9483.

[51] Müller, M.; Rüdiger, E. C.; Koser, S.; Tverskoy, O.; Rominger, F.; Hinkel, F.; Freudenberg, J.; Bunz, U. H. "Butterfly Wings" Stabilize Heptacene. *Chemistry – A European Journal* **2018**, *24*, 8087–8091.

[52] Bissell A P de Silva H Q N Gunaratne P L M Lynch, R. A.; M Maguire C P McCoy, G. E.; A S Sandanayake T, K. R.; Blssell A P de Silva H Q N Gunaratne, R. A.; M Lynch G E M Maguire K R A S Sandanayake, P. L.; Sot, C.; Ono, K.; Tanaka, S.; Yamashita, Y.; Yamashita K Ono S Tanaka, I. Y. Benzobis(thiadiazole)s Containing Hypervalent Sulfur Atoms: Novel Heterocycles with High Electron Affinity and Short Intermolecular Contacts between Heteroatoms. *Angewandte Chemie International Edition in English* **1994**, *33*, 1977–1979.

[53] Karikomi, M.; Kitamura, C.; Tanaka, S.; Yamashita, Y. New Narrow-Bandgap Polymer Composed of Benzobis(1,2,5-thiadiazole) and Thiophenes. *Journal of the American Chemical Society* **1995**, *117*, 6791–6792.

[54] Thomas, A.; Bhanuprakash, K.; Prasad, K. M. Near infrared absorbing benzobis(thiadiazole) derivatives: computational studies point to biradical nature of the ground states. *Journal of Physical Organic Chemistry* **2011**, *24*, 821–832.

[55] Mishra, A.; Uhrich, C.; Reinold, E.; Pfeiffer, M.; Bäuerle, P. Synthesis and Characterization of Acceptor-Substituted Oligothiophenes for Solar Cell Applications. *Advanced Energy Materials* **2011**, *1*, 265–273.

[56] Fitzner, R.; Reinold, E.; Mishra, A.; Mena-Osteritz, E.; Bäuerle, P.; Ziehlke, H.; Körner, C.; Leo, K.; Riede, M.; Weil, M.; Tsaryova, O.;

Weiß, A.; Uhrich, C.; Pfeiffer, M. Dicyanovinyl–Substituted Oligothiophenes: Structure-Property Relationships and Application in Vacuum-Processed Small Molecule Organic Solar Cells. *Advanced Functional Materials* **2011**, *21*, 897–910.

[57] Fitzner, R.; Mena-Osteritz, E.; Mishra, A.; Schulz, G.; Reinold, E.; Weil, M.; Körner, C.; Ziehlke, H.; Elschner, C.; Leo, K.; Riede, M.; Pfeiffer, M.; Uhrich, C.; Bäuerle, P. Correlation of π-conjugated oligomer structure with film morphology and organic solar cell performance. *Journal of the American Chemical Society* **2012**, *134*, 11064–11067.

[58] Meerheim, R.; Körner, C.; Leo, K. Highly efficient organic multi-junction solar cells with a thiophene based donor material. *Applied Physics Letters* **2014**, *105*, 63306.

[59] Koch, N.; Heimel, G.; Wu, J.; Zojer, E.; Johnson, R. L.; Brédas, J. L.; Müllen, K.; Rabe, J. P. Influence of molecular conformation on organic/metal interface energetics. *Chemical Physics Letters* **2005**, *413*, 390–395.

[60] Yokoyama, T.; Kurata, S.; Tanaka, S. Direct identification of conformational isomers of adsorbed oligothiophene on Cu(100). *Journal of Physical Chemistry B* **2006**, *110*, 18130–18133.

[61] Kiel, M.; Duncker, K.; Hagendorf, C.; Widdra, W. Molecular structure and chiral separation in α -sexithiophene ultrathin films on Au(111): Low-energy electron diffraction and scanning tunneling microscopy. *Physical Review B - Condensed Matter and Materials Physics* **2007**, *75*, 195439.

[62] Varene, E.; Martin, I.; Tegeder, P. Optically induced inter- and intrafacial electron transfer probed by two-photon photoemission: Electronic states of sexithiophene on Au(111). *Journal of Physical Chemistry Letters* **2011**, *2*, 252–256.

[63] Kakudate, T.; Tsukamoto, S.; Nakaya, M.; Nakayama, T. Initial stage of adsorption of octithiophene molecules on Cu(111). *Surface Science* **2011**, *605*, 1021–1026.

Bibliography

[64] Varene, E.; Bogner, L.; Meyer, S.; Pennec, Y.; Tegeder, P. Coverage-dependent adsorption geometry of octithiophene on Au(111). *Physical Chemistry Chemical Physics* **2011**, *14*, 691–696.

[65] Varene, E.; Bogner, L.; Bronner, C.; Tegeder, P. Ultrafast exciton population, relaxation, and decay dynamics in thin oligothiophene films. *Physical Review Letters* **2012**, *109*, 207601.

[66] Bogner, L.; Yang, Z.; Baum, S.; Corso, M.; Fitzner, R.; Bauerle, P.; Franke, K. J.; Pascual, J. I.; Tegeder, P. Electronic states and exciton dynamics in dicyanovinyl-sexithiophene on Au(111). *Journal of Physical Chemistry C* **2016**, *120*, 27268–27275.

[67] Bronsch, W.; Wagner, T.; Baum, S.; Wansleben, M.; Zielke, K.; Ghanbari, E.; Györök, M.; Navarro-Quezada, A.; Zeppenfeld, P.; Weinelt, M.; Gahl, C. Interplay between Morphology and Electronic Structure in α-Sexithiophene Films on Au(111). *Journal of Physical Chemistry C* **2019**, *123*, 7931–7939.

[68] Li, W.; Pan, Y.; Xiao, R.; Peng, Q.; Zhang, S.; Ma, D.; Li, F.; Shen, F.; Wang, Y.; Yang, B.; Ma, Y. Employing -100Fluorescent Molecule with Hybridized Local and Charge-Transfer Excited State. *Advanced Functional Materials* **2014**, *24*, 1609–1614.

[69] Qiu, Y.; Wei, P.; Zhang, D.; Qiao, J.; Duan, L.; Li, Y.; Gao, Y.; Wang, L. Novel Naphtho[2,3-c][1,2,5]thiadiazole Derivative for Non-doped Small Molecular Organic Red-Light-Emitting Diodes. *Advanced Materials* **2006**, *18*, 1607–1611.

[70] Yuen, J. D.; Fan, J.; Seifter, J.; Lim, B.; Hufschmid, R.; Heeger, A. J.; Wudl, F. High performance weak donor-acceptor polymers in thin film transistors: Effect of the acceptor on electronic properties, ambipolar conductivity, mobility, and thermal stability. *Journal of the American Chemical Society* **2011**, *133*, 20799–20807.

[71] Qian, G.; Dai, B.; Luo, M.; Yu, D.; Zhan, J.; Zhang, Z.; Dongge, M.; Wang, Z. Y. Band gap tunable, donor-acceptor-donor charge-transfer heteroquinoid-based chromophores: Near infrared photoluminescence and electroluminescence. *Chemistry of Materials* **2008**, *20*, 6208–6216.

142

[72] Qian, G.; Zhong, Z.; Luo, M.; Yu, D.; Zhang, Z.; Wang, Z. Y.; Ma, D. Simple and Efficient Near-Infrared Organic Chromophores for Light-Emitting Diodes with Single Electroluminescent Emission above 1000 nm. *Advanced Materials* **2009**, *21*, 111–116.

[73] Sun, Y.; Duan, L.; Wei, P.; Qiao, J.; Dong, G.; Wang, L.; Qiu, Y. An ambipolar transporting naphtho[2,3-c][1,2,5]thiadiazole derivative with high electron and hole mobilities. *Organic Letters* **2009**, *11*, 2069–2072.

[74] Kono, T.; Kumaki, D.; Nishida, J. I.; Tokito, S.; Yamashita, Y. Dithienylbenzobis(thiadiazole) based organic semiconductors with low LUMO levels and narrow energy gaps. *Chemical Communications* **2010**, *46*, 3265–3267.

[75] Wang, M.; Hu, X.; Liu, P.; Li, W.; Gong, X.; Huang, F.; Cao, Y. Donor-acceptor conjugated polymer based on naphtho[1,2- c:5,6- c]bis[1,2,5]thiadiazole for high-performance polymer solar cells. *Journal of the American Chemical Society* **2011**, *133*, 9638–9641.

[76] Chen, X. K.; Guo, J. F.; Zou, L. Y.; Ren, A. M.; Fan, J. X. A promising approach to obtain excellent n -type organic field-effect transistors: Introducing pyrazine ring. *Journal of Physical Chemistry C* **2011**, *115*, 21416–21428.

[77] Fan, J.; Yuen, J. D.; Wang, M.; Seifter, J.; Seo, J. H.; Mohebbi, A. R.; Zakhidov, D.; Heeger, A.; Wudl, F. High-Performance Ambipolar Transistors and Inverters from an Ultralow Bandgap Polymer. *Advanced Materials* **2012**, *24*, 2186–2190.

[78] Zhang, L.; Pei, K.; Yu, M.; Huang, Y.; Zhao, H.; Zeng, M.; Wang, Y.; Gao, J. Theoretical investigations on donor-acceptor conjugated copolymers based on naphtho[1,2-c:5,6-c]bis[1,2,5]thiadiazole for organic solar cell applications. *Journal of Physical Chemistry C* **2012**, *116*, 26154–26161.

[79] Mamada, M.; Shima, H.; Yoneda, Y.; Shimano, T.; Yamada, N.; Kakita, K.; Machida, T.; Tanaka, Y.; Aotsuka, S.; Kumaki, D.; Tokito, S. A Unique Solution-Processable n-Type Semiconductor Material Design for High-Performance Organic Field-Effect Transistors. *Chemistry of Materials* **2015**, *27*, 141–147.

Bibliography

[80] Chatterjee, S.; Ie, Y.; Karakawa, M.; Aso, Y. Naphtho[1,2-c:5,6-c′]bis[1,2,5]thiadiazole-Containing π-Conjugated Compound: Non-fullerene Electron Acceptor for Organic Photovoltaics. *Advanced Functional Materials* **2016**, *26*, 1161–1168.

[81] Yen, Y. S.; Ni, J. S.; Hung, W. I.; Hsu, C. Y.; Chou, H. H.; Lin, J. T. Naphtho[2,3-c][1,2,5]thiadiazole and 2H-Naphtho[2,3-d][1,2,3]triazole-Containing D-A-π-A Conjugated Organic Dyes for Dye-Sensitized Solar Cells. *ACS Applied Materials and Interfaces* **2016**, *8*, 6117–6126.

[82] Brymora, K.; Ducasse, L.; Delaure, A.; Hirsch, L.; Jarrosson, T.; Niebel, C.; Serein-Spirau, F.; Peresutti, R.; Dautel, O.; Castet, F. Computational design of quadrupolar donor-acceptor-donor molecules with near-infrared light-harvesting capabilities. *Dyes and Pigments* **2018**, *149*, 882–892.

[83] Fan, J.; Zhang, Y.; Zhang, K.; Liu, J.; Jiang, G.; Li, F.; Lin, L.; Wang, C. K. Towards boosting the exciton lifetime and efficiency of near-infrared aggregation induced emitters with hybridized local and charge transfer excited states: a multiscale study. *Journal of Materials Chemistry C* **2019**, *7*, 8874–8887.

[84] Hosseini, S. M.; Roland, S.; Kurpiers, J.; Chen, Z.; Zhang, K.; Huang, F.; Armin, A.; Neher, D.; Shoaee, S. Impact of Bimolecular Recombination on the Fill Factor of Fullerene and Nonfullerene-Based Solar Cells: A Comparative Study of Charge Generation and Extraction. *Journal of Physical Chemistry C* **2019**, *123*, 6823–6830.

[85] Lo, Y. C.; Yeh, T. H.; Wang, C. K.; Peng, B. J.; Hsieh, J. L.; Lee, C. C.; Liu, S. W.; Wong, K. T. High-efficiency red and near-infrared organic light-emitting diodes enabled by pure organic fluorescent emitters and an exciplex-forming cohost. *ACS Applied Materials and Interfaces* **2019**, *11*, 23417–23427.

[86] Jia, A.; Liu, H.; Yun, Y.; Agbolaghi, S. Bottlebrush compatibilizers with polythiophene backbones and dielectric/conductive side brushes in naphthothiadiazole solar systems. *Solar Energy* **2019**, *194*, 311–320.

144

[87] Hammer, N.; Schaub, T. A.; Meinhardt, U.; Kivala, M. N-Heterotriangulenes: Fascinating Relatives of Triphenylamine. *Chemical record (New York, N.Y.)* **2015**, *15*, 1119–1131.

[88] Michalsky, I.; Gensch, V.; Walla, C.; Hoffmann, M.; Rominger, F.; Oeser, T.; Tegeder, P.; Dreuw, A.; Kivala, M. Fully Bridged Triphenylamines Comprising Five- and Seven-Membered Rings. *Chemistry – A European Journal* **2022**, *28*, e202200326.

[89] Lüssem, B.; Tietze, M. L.; Kleemann, H.; Hoßbach, C.; Bartha, J. W.; Zakhidov, A.; Leo, K. Doped organic transistors operating in the inversion and depletion regime. *Nature communications* **2013**, *4*.

[90] Salzmann, I.; Heimel, G. Toward a comprehensive understanding of molecular doping organic semiconductors (review). *Journal of Electron Spectroscopy and Related Phenomena* **2015**, *204*, 208–222.

[91] Vandewal, K. Interfacial Charge Transfer States in Condensed Phase Systems. *https://doi.org/10.1146/annurev-physchem-040215-112144* **2016**, *67*, 113–133.

[92] Zhang, J.; Xu, W.; Sheng, P.; Zhao, G.; Zhu, D. Organic Donor-Acceptor Complexes as Novel Organic Semiconductors. *Accounts of Chemical Research* **2017**, *50*, 1654–1662.

[93] Siegmund, B.; Mischok, A.; Benduhn, J.; Zeika, O.; Ullbrich, S.; Nehm, F.; Böhm, M.; Spoltore, D.; Fröb, H.; Körner, C.; Leo, K.; Vandewal, K. Organic narrowband near-infrared photodetectors based on intermolecular charge-transfer absorption. *Nature communications* **2017**, *8*.

[94] Lüth, H. *Solid Surfaces, Interfaces and Thin Films*; Graduate Texts in Physics; Springer International Publishing: Cham, 2015.

[95] Maaß, F. The Metal/Organic Interface - Binding, Adsorption Geometry, and Electronic Structure. Ph.D. thesis, 2018.

[96] Miller, J. B.; Siddiqui, H. R.; Gates, S. M.; Russell, J. N.; Yates, J. T.; Tully, J. C.; Cardillo, M. J. Extraction of kinetic parameters in temperature programmed desorption: A comparison of methods. *The Journal of Chemical Physics* **1987**, *87*, 6725–6732.

Bibliography

[97] King, D. A. Thermal desorption from metal surfaces: A review. *Surface Science* **1975**, *47*, 384–402.

[98] Redhead, P. A. Thermal desorption of gases. *Vacuum* **1962**, *12*, 203–211.

[99] Ibach, H.; Mills, D. L. Electron energy loss spectroscopy and surface vibrations. **1982**, 366.

[100] Rocca, M. Low-energy EELS investigation of surface electronic excitations on metals. *Surface Science Reports* **1995**, *22*, 1–71.

[101] Physik, I. F.; Leyßner, F. Analysis of functional organic molecules at noble metal surfaces by means of vibrational spectroscopies. Ph.D. thesis, 2011.

[102] Pischel, J. Über die schwingungsspektroskopische Untersuchung von Anregungen im mittleren und fernen Infrarot an Oberflächen metallischer Einkristalle. Ph.D. thesis, 2014.

[103] Hohenberg, P.; Kohn, W. Inhomogeneous electron gas. *Physical Review* **1964**, *136*, B864.

[104] Kohn, W.; Sham, L. J. Self-consistent equations including exchange and correlation effects. *Physical Review* **1965**, *140*, A1133.

[105] Stephens, P. J.; Devlin, F. J.; Chabalowski, C. F.; Frisch, M. J. Ab Initio calculation of vibrational absorption and circular dichroism spectra using density functional force fields. *Journal of Physical Chemistry®* **1994**, *98*, 11623–11627.

[106] Becke, A. D. Density-functional thermochemistry. III. The role of exact exchange. *The Journal of Chemical Physics* **1993**, *98*, 5648–5652.

[107] Lee, C.; Yang, W.; Parr, R. G. Development of the Colle-Salvetti correlation-energy formula into a functional of the electron density. *Physical Review B* **1988**, *37*, 785.

[108] M. J. Frisch, G. W. Trucks, H. B. Schlegel, G. E. Scuseria, M. A. Robb, J. R. Cheeseman, G. Scalmani, V. Barone, G. A. Petersson, H. Nakatsuji, X. Li, M. Caricato, A. Marenich, J. Bloino, B. G. Janesko, R. Gomperts, B. Mennucci, H. P. Hratchian, J. V. Ort, . Gaussian 09, Revision B.01. 2009.

[109] Stremlau, S. High Resolution Vibrational Spectroscopy of Functional Organic Molecules at Surfaces. Ph.D. thesis, 2015.

[110] Maaß, F.; Jiang, Y.; Liu, W.; Tkatchenko, A.; Tegeder, P. Binding energies of benzene on coinage metal surfaces: Equal stability on different metals. *Journal of Chemical Physics* **2018**, *148*.

[111] Russell, R. F. Gold in hybrid microelectronics - The complementary use of thin and thick film integrated circuits. *Gold Bulletin* **1974**, *7*, 30–34.

[112] Li, P.; Ding, F. Origin of the herringbone reconstruction of Au(111) surface at the atomic scale. *Science Advances* **2022**, *8*, 2900.

[113] Pappenberger, R. High Resolution Electron Energy Loss Spectroscopy Studies on Organic Molecule-Metal Interfaces and Thin Molecular Films. M.Sc. thesis, 2021.

[114] Tumino, F.; Casari, C. S.; Passoni, M.; Russo, V.; Li Bassi, A. Pulsed laser deposition of single-layer MoS2 on Au(111): from nanosized crystals to large-area films. *Nanoscale Advances* **2019**, *1*, 643–655.

[115] Wang, Y.; Hush, N. S.; Reimers, J. R. Simulation of the Au(111)-(22X 3) surface reconstruction. *Physical Review B - Condensed Matter and Materials Physics* **2007**, *75*, 233416.

[116] VanAllan, J. A.; Adel, R. E.; Reynolds, G. A. Polynuclear Heterocycles. II. Addition Reactions of Benzophenazines. *Journal of Organic Chemistry* **1962**, *27*, 2873–2878.

[117] Ege, G.; Vogler, H. Über die Berechnung der 1H-NMR-Spektren linearer Di-aza-acene. *Zeitschrift fur Naturforschung - Section B Journal of Chemical Sciences* **1972**, *27*, 1164–1165.

[118] Wang, X.; Lau, K. C. Theoretical investigations on charge-transfer properties of novel high mobility n-channel organic semiconductors- Diazapentacene derivatives. *Journal of Physical Chemistry C* **2012**, *116*, 22749–22758.

[119] Sutton, C.; Risko, C.; Brédas, J. L. Noncovalent Intermolecular Interactions in Organic Electronic Materials: Implications for the Molecular Packing vs Electronic Properties of Acenes. *Chemistry of Materials* **2016**, *28*, 3–16.

Bibliography

[120] Bogatko, S.; Haynes, P. D.; Sathian, J.; Wade, J.; Kim, J. S.; Tan, K. J.; Breeze, J.; Salvadori, E.; Horsfield, A.; Oxborrow, M. Molecular Design of a Room-Temperature Maser. *Journal of Physical Chemistry C* **2016**, *120*, 8251–8260.

[121] Klues, M.; Witte, G. Crystalline packing in pentacene-like organic semiconductors. *CrystEngComm* **2017**, *20*, 63–74.

[122] Charlton, R. J.; Fogarty, R. M.; Bogatko, S.; Zuehlsdorff, T. J.; Hine, N. D.; Heeney, M.; Horsfield, A. P.; Haynes, P. D. Implicit and explicit host effects on excitons in pentacene derivatives. *The Journal of Chemical Physics* **2018**, *148*, 104108.

[123] Kouno, H.; Kawashima, Y.; Tateishi, K.; Uesaka, T.; Kimizuka, N.; Yanai, N. Nonpentacene Polarizing Agents with Improved Air Stability for Triplet Dynamic Nuclear Polarization at Room Temperature. *Journal of Physical Chemistry Letters* **2019**, *10*, 2208–2213.

[124] Sosorev, A.; Dominskiy, D.; Chernyshov, I.; Efremov, R. Tuning of Molecular Electrostatic Potential Enables Efficient Charge Transport in Crystalline Azaacenes: A Computational Study. *International Journal of Molecular Sciences 2020, Vol. 21, Page 5654* **2020**, *21*, 5654.

[125] Kummer, F.; Zimmermann, H. Über die Elektronenspektren linearer Diaza- und Tetraaza-Acene. *Berichte der Bunsengesellschaft für physikalische Chemie* **1967**, *71*, 1119–1126.

[126] Liu, D.; Li, Z.; He, Z.; Xu, J.; Miao, Q. Induced crystallization of rubrene with diazapentacene as the template. *Journal of Materials Chemistry* **2012**, *22*, 4396–4400.

[127] Isoda, K.; Nakamura, M.; Tatenuma, T.; Ogata, H.; Sugaya, T.; Tadokoro, M. Synthesis and Characterization of Electron-accepting Nonsubstituted Tetraazaacene Derivatives. *https://doi.org/10.1246/cl.2012.937* **2012**, *41*, 937–939.

[128] Naibi Lakshminarayana, A.; Ong, A.; Chi, C. Modification of acenes for n-channel OFET materials. *Journal of Materials Chemistry C* **2018**, *6*, 3551–3563.

148

[129] Ajdari, M.; Schmitt, T.; Hoffmann, M.; Maass, F.; Reiss, H.; Bunz, U. H.; Dreuw, A.; Tegeder, P. Electronic Properties of 6,13-Diazapentacene Adsorbed on Au(111): A Quantitative Determination of Transport, Singlet and Triplet States, and Electronic Spectra. *Journal of Physical Chemistry C* **2020**, *124*, 13196–13205.

[130] Hoffmann, M.; Ajdari, M.; Landwehr, F.; Tverskoy, O.; Bunz, U. H.; Dreuw, A.; Tegeder, P. Influence of N-introduction in pentacene on the electronic structure and excited electronic states. *Physical Chemistry Chemical Physics* **2022**, *24*, 3924–3932.

[131] Rockey, T. J.; Yang, M.; Dai, H. L. Adsorption energies, inter-adsorbate interactions, and the two binding sites within monolayer benzene on Ag(111). *Journal of Physical Chemistry B* **2006**, *110*, 19973–19978.

[132] Schulze, M.; Bronner, C.; Tegeder, P. Adsorption energetics of azobenzenes on noble metal surfaces. *Journal of Physics Condensed Matter* **2014**, *26*.

[133] Hagen, S.; Leyssner, F.; Nandi, D.; Wolf, M.; Tegeder, P. Reversible switching of tetra-tert-butyl-azobenzene on a Au(1 1 1) surface induced by light and thermal activation. *Chemical Physics Letters* **2007**, *444*, 85–90.

[134] Tegeder, P.; Hagen, S.; Leyssner, F.; Peters, M. V.; Hecht, S.; Klamroth, T.; Saalfrank, P.; Wolf, M. Electronic structure of the molecular switch tetra-tert-butyl-azobenzene adsorbed on Ag(111). *Applied Physics A: Materials Science and Processing* **2007**, *88*, 465–472.

[135] McNellis, E. R.; Bronner, C.; Meyer, J.; Weinelt, M.; Tegeder, P.; Reuter, K. Azobenzene versus 3,3',5,5'-tetra-tert-butyl-azobenzene (TBA) at Au(111): Characterizing the role of spacer groups. *Physical Chemistry Chemical Physics* **2010**, *12*, 6404–6412.

[136] Bronner, C.; Priewisch, B.; Rück-Braun, K.; Tegeder, P. Photoisomerization of an azobenzene on the Bi(111) surface. *Journal of Physical Chemistry C* **2013**, *117*, 27031–27038.

[137] Óvári, L.; Luo, Y.; Leyssner, F.; Haag, R.; Wolf, M.; Tegeder, P. Adsorption and switching properties of a N -benzylideneaniline based molecular switch on a Au(111) surface. *Journal of Chemical Physics* **2010**, *133*.

Bibliography

[138] Bronner, C.; Tegeder, P. Photo-induced and thermal reactions in thin films of an azobenzene derivative on Bi(111). *New Journal of Physics* **2014**, *16*.

[139] Suenaga, M. Facio 19.1.4. 2016.

[140] Park, S. J.; Palmer, R. E. Plasmon dispersion of the Au(111) surface with and without self-assembled monolayers. *Physical Review Letters* **2009**, *102*.

[141] Rao, A.; Wilson, M. W.; Albert-Seifried, S.; Di Pietro, R.; Friend, R. H. Photophysics of pentacene thin films: The role of exciton fission and heating effects. *Physical Review B - Condensed Matter and Materials Physics* **2011**, *84*, 195411.

[142] Smith, M. B.; Michl, J. Singlet fission. *Chemical Reviews* **2010**, *110*, 6891–6936.

[143] Smith, M. B.; Michl, J. Recent Advances in Singlet Fission. *https://doi.org/10.1146/annurev-physchem-040412-110130* **2013**, *64*, 361–386.

[144] Miao, S.; Appleton, A. L.; Berger, N.; Barlow, S.; Marder, S. R.; Hardcastle, K. I.; Bunz, U. H. 6,13-Diethynyl-5,7,12,14-tetraazapentacene. *Chemistry – A European Journal* **2009**, *15*, 4990–4993.

[145] Dreuw, A.; Tegeder, P. Influence of N-introduction on the electronic structure and properties of polyacenes: experiment and quantum chemistry in concert. *Physical Chemistry Chemical Physics* **2023**, *25*, 17079–17091.

[146] Ajdari, M.; Stein, A.; Hoffmann, M.; Müller, M.; Bunz, U. H.; Dreuw, A.; Tegeder, P. Lightening up a Dark State of a Pentacene Derivative via N-Introduction. *Journal of Physical Chemistry C* **2020**, *124*, 7196–7204.

[147] Stein, A.; Maaß, F.; Tegeder, P. Triisopropylsilylethynyl-Pentacene on Au(111): Adsorption Properties, Electronic Structure, and Singlet Fission Dynamics. *Journal of Physical Chemistry C* **2017**, *121*, 18075–18083.

[148] Cava, M. P.; Schlessinger, R. H. 2,3-Naphthoquinonoid heterocycles. II. A highly stabilized thiadiazole analog of anthracene. *Tetrahedron Letters* **1964**, *5*, 3815–3818.

[149] Ray, N. K.; Narasimhan, P. T. Molecular orbital study of some heterocycles containing nitrogen and sulphur. *Theoretica Chimica Acta* **1966**, *5*, 401–405.

[150] Gyul'maliev, A. M.; Stankevich, I. V.; Todres, Z. V. An investigation in the field of aromatic heterocycles. *Chemistry of Heterocyclic Compounds 1975 9:11* **1973**, *9*, 1331–1336.

[151] Centore, R.; Borbone, F.; Carella, A.; Causà, M.; Fusco, S.; Gentile, F. S.; Parisi, E. Hierarchy of Intermolecular Interactions and Selective Topochemical Reactivity in Different Polymorphs of Fused-Ring Heteroaromatics. *Crystal Growth and Design* **2020**, *20*, 1229–1236.

[152] Smith, W. T.; Kovelsky, A. C.; Patterson, J. M. Halogenation of naphtho[2,3-c]-1,2,5-thiadiazole. *Journal of Heterocyclic Chemistry* **1968**, *5*, 295–297.

[153] Kim, J.; Yun, M. H.; Kim, G. H.; Kim, J. Y.; Yang, C. Replacing 2,1,3-benzothiadiazole with 2,1,3-naphthothiadiazole in PCDTBT: towards a low bandgap polymer with deep HOMO energy level. *Polymer Chemistry* **2012**, *3*, 3276–3281.

[154] Pachariyangkun, A.; Suda, M.; Hadsadee, S.; Jungsuttiwong, S.; Nalaoh, P.; Pattanasattayavong, P.; Sudyoadsuk, T.; Yamamoto, H. M.; Promarak, V. Effect of thiophene/furan substitution on organic field effect transistor properties of arylthiadiazole based organic semiconductors. *Journal of Materials Chemistry C* **2020**, *8*, 17297–17306.

[155] Wei, P.; Duan, L.; Zhang, D.; Qiao, J.; Wang, L.; Wang, R.; Dong, G.; Qiu, Y. A new type of light-emitting naphtho[2,3-c][1,2,5]thiadiazole derivatives: synthesis, photophysical characterization and transporting properties. *Journal of Materials Chemistry* **2008**, *18*, 806–818.

[156] Chen, L.; Wang, L.; Jing, X.; Wang, F. Color tuning of Novel 2,1,3-Naphthothiadiazole and 2,1,3-Benzoselenadiazole based D-A-D´ Type dopants to realize highly efficient saturated red emission in non-polar solvents. *Journal of Materials Chemistry* **2011**, *21*, 10265–10267.

Bibliography

[157] Liu, T.; Xie, G.; Zhong, C.; Gong, S.; Yang, C.; Liu, T.; Xie, G.; Zhong, C.; Gong, S.; Yang, C. Boosting the Efficiency of Near-Infrared Fluorescent OLEDs with an Electroluminescent Peak of Nearly 800 nm by Sensitizer-Based Cascade Energy Transfer. *Advanced Functional Materials* **2018**, *28*, 1706088.

[158] Tang, X.; Li, X. L.; Liu, H.; Gao, Y.; Shen, Y.; Zhang, S.; Lu, P.; Yang, B.; Su, S. J.; Ma, Y. Efficient near-infrared emission based on donor-acceptor molecular architecture: The role of ancillary acceptor of cyanophenyl. *Dyes and Pigments* **2018**, *149*, 430–436.

[159] Funchien, P.; Chasing, P.; Sudyoadsuk, T.; Promarak, V.; Li, R.; Chemcomm, .; Communication, C. A highly efficient near infrared organic solid fluorophore based on naphthothiadiazole derivatives with aggregation-induced emission enhancement for a non-doped electroluminescent device. *Chemical Communications* **2020**, *56*, 6305–6308.

[160] Wan, Q.; Tong, J.; Zhang, B.; Li, Y.; Wang, Z.; Tang, B. Z. Exploration of High Efficiency AIE-Active Deep/Near-Infrared Red Emitters in OLEDs with High-Radiance. *Advanced Optical Materials* **2020**, *8*, 1901520.

[161] Wan, Q.; Zhang, R.; Zhuang, Z.; Li, Y.; Huang, Y.; Wang, Z.; Zhang, W.; Hou, J.; Tang, B. Z. Molecular Engineering to Boost AIE-Active Free Radical Photogenerators and Enable High-Performance Photodynamic Therapy under Hypoxia. *Advanced Functional Materials* **2020**, *30*, 2002057.

[162] Chen, L.; He, X.; Zhao, Y. Purely organic and saturated red emitters for a non-doped electroluminescent device with an EQE of 6.3roll-off. *Materials Advances* **2021**, *2*, 6068–6074.

[163] He, X.; Gao, L.; Liu, H.; Liu, F.; Jiang, D.; Du, C.; Sun, C.; Lu, P. Highly efficient red fluorescent OLEDs based on diphenylacridine-naphthothiadiazole derivatives with upper level intersystem crossing. *Chemical Engineering Journal* **2021**, *404*, 127055.

[164] Therdkatanyuphong, P.; Kaiyasuan, C.; Chasing, P.; Kaewpuang, T.; Chawanpunyawat, T.; Sudyoadsuk, T.; Promarak, V. Efficient Solution-Processable Non-Doped Emissive Materials Based on Oligocarbazole

152

End-Capped Molecules for Simple Structured Red, Green, Blue, and White Electroluminescent Devices. *ACS Applied Electronic Materials* **2021**, *3*, 1311–1322.

[165] Tang, X.; Liu, H.; Liu, F.; He, X.; Xu, X.; Chen, J.; Peng, Q.; Lu, P. Efficient Red Electroluminescence From Phenanthro[9,10-d]imidazole-Naphtho[2,3-c][1,2,5]thiadiazole Donor-Acceptor Derivatives. *Chemistry – An Asian Journal* **2021**, *16*, 1942–1948.

[166] Li, Y.; Yao, J.; Wang, C.; Zhou, X.; Xu, Y.; Hanif, M.; Qiu, X.; Hu, D.; Ma, D.; Ma, Y. Highly efficient deep-red/near-infrared D-A chromophores based on naphthothiadiazole for OLEDs applications. *Dyes and Pigments* **2020**, *173*, 107960.

[167] Kongsabay, S.; Funchien, P.; Chasing, P.; Sudyodsuk, T.; Promarak, V. An efficient solution-processable hybridized local and charge-transfer (HLCT)-based deep-red fluorescent emitter for simple structured non-doped OLED. *Journal of Luminescence* **2022**, *248*, 118921.

[168] Shen, P.; Bin, H.; Chen, L.; Zhang, Z. G.; Li, Y. Synthesis and photovoltaic properties of 4,9-dithien-2'-yl-2,1,3-naphthothiadiazole-based D-A copolymers. *Polymer* **2015**, *79*, 119–127.

[169] Wang, C. K.; Che, X.; Lo, Y. C.; Li, Y. Z.; Wang, Y. H.; Forrest, S. R.; Liu, S. W.; Wong, K. T. New D-A-A'-Configured Small Molecule Donors Employing Conjugation to Red-shift the Absorption for Photovoltaics. *Chemistry – An Asian Journal* **2020**, *15*, 2520–2531.

[170] Zhang, Z.; Fang, X.; Liu, Z.; Liu, H.; Chen, D.; He, S.; Zheng, J.; Yang, B.; Qin, W.; Zhang, X.; Wu, C. Semiconducting Polymer Dots with Dual-Enhanced NIR-IIa Fluorescence for Through-Skull Mouse-Brain Imaging. *Angewandte Chemie International Edition* **2020**, *59*, 3691–3698.

[171] Li, J.; Zhang, Z.; Deng, X.; Xu, Z.; Wang, L.; Xu, G.; Wang, K.; Wang, D.; Tang, B. Z. A potent luminogen with NIR-IIb excitable AIE features for ultradeep brain vascular and hemodynamic three-photon imaging. *Biomaterials* **2022**, *287*, 121612.

[172] Xu, Z.; Zhang, Z.; Deng, X.; Li, J.; Jiang, Y.; Law, W. C.; Yang, C.; Zhang, W.; Chen, X.; Wang, K.; Wang, D.; Xu, G. Deep-Brain Three-Photon Imaging Enabled by Aggregation-Induced Emission Luminogens with Near-Infrared-III Excitation. *ACS Nano* **2022**, *16*, 6712–6724.

[173] Liu, X. Y.; Li, Y.; Tsung, C. K.; Li, J. Encapsulation of yellow phosphors into nanocrystalline metal–organic frameworks for blue-excitable white light emission. *Chemical Communications* **2019**, *55*, 10669–10672.

[174] Liu, X. Y.; Lustig, W. P.; Li, J. Functionalizing Luminescent Metal-Organic Frameworks for Enhanced Photoluminescence. *ACS Energy Letters* **2020**, *5*, 2671–2680.

[175] Wu, S.; Ren, D.; Zhou, K.; Xia, H. L.; Liu, X. Y.; Wang, X.; Li, J. Linker Engineering toward Full-Color Emission of UiO-68 Type Metal-Organic Frameworks. *Journal of the American Chemical Society* **2021**, *143*, 10547–10552.

[176] Ren, D.; Xia, H. L.; Zhou, K.; Wu, S.; Liu, X. Y.; Wang, X.; Li, J. Tuning and Directing Energy Transfer in the Whole Visible Spectrum through Linker Installation in Metal–Organic Frameworks. *Angewandte Chemie International Edition* **2021**, *60*, 25048–25054.

[177] Ajdari, M.; Landwehr, F.; Hoffmann, M.; Hoffmann, H.; Bunz, U. H.; Dreuw, A.; Tegeder, P. Influence of Core Halogenation on the Electronic Structure of Naphthothiadiazole Derivatives. *Journal of Physical Chemistry C* **2021**, *125*, 6359–6366.

[178] Bronner, C.; Björk, J.; Tegeder, P. Tracking and removing br during the on-surface synthesis of a graphene nanoribbon. *Journal of Physical Chemistry C* **2015**, *119*, 486–493.

[179] Clair, S.; De Oteyza, D. G. Controlling a Chemical Coupling Reaction on a Surface: Tools and Strategies for On-Surface Synthesis. *Chemical Reviews* **2019**, *119*, 4717–4776.

[180] Hanwell, M. D.; Curtis, D. E.; Lonie, D. C.; Vandermeerschd, T.; Zurek, E.; Hutchison, G. R. Avogadro: An advanced semantic chemical editor, visualization, and analysis platform. *Journal of Cheminformatics* **2012**, *4*, 1–17.

[181] Yamashita, Y.; Ono, K.; Tomura, M.; Tanaka, S. Synthesis and Properties of Benzobis(thiadiazole)s with Nonclassical π-Electron Ring Systems. *Tetrahedron* **1997**, *53*, 10169–10178.

[182] Chmovzh, T. N.; Knyazeva, E. A.; Mikhalchenko, L. V.; Golovanov, I. S.; Amelichev, S. A.; Rakitin, O. A. Synthesis of the 4,7-Dibromo Derivative of Highly Electron-Deficient [1,2,5]Thiadiazolo[3,4-d]pyridazine and Its Cross-Coupling Reactions. *European Journal of Organic Chemistry* **2018**, *2018*, 5668–5677.

[183] Köse, M. E. Evaluation of acceptor strength in thiophene coupled donor-acceptor chromophores for optimal design of organic photovoltaic materials. *Journal of Physical Chemistry A* **2012**, *116*, 12503–12509.

[184] Berionni, G.; Wu, J. I.; Schleyer, P. V. Aromaticity evaluations of planar [6]Radialenes. *Organic Letters* **2014**, *16*, 6116–6119.

[185] Syomin, D.; Kim, J.; Koel, B. E.; Elison, G. B. Identification of adsorbed phenyl (C6H5) groups on metal surfaces: Electron-induced dissociation of benzene on Au(111). *Journal of Physical Chemistry B* **2001**, *105*, 8387–8394.

[186] Kato, H. S.; Noh, J.; Hara, M.; Kawai, M. An HREELS study of alkanethiol self-assembled monolayers on Au(111). *Journal of Physical Chemistry B* **2002**, *106*, 9655–9658.

[187] Fang, Z.; Su, W.; Zhang, W.; Xu, Y.; Xiong, Y.; Luo, M.; Fan, J.; Yin, X. Chiral discrimination and interaction mechanism between enantiomers and serum albumins. *Journal of molecular recognition : JMR* **2013**, *26*, 161–164.

[188] Meinhardt, U.; Lodermeyer, F.; Schaub, T. A.; Kunzmann, A.; Dral, P. O.; Sale, A. C.; Hampel, F.; Guldi, D. M.; Costa, R. D.; Kivala, M. N-Heterotriangulene chromophores with 4-pyridyl anchors for dye-sensitized solar cells. *RSC Advances* **2016**, *6*, 67372–67377.

[189] Hirai, M.; Tanaka, N.; Sakai, M.; Yamaguchi, S. Structurally Constrained Boron-, Nitrogen-, Silicon-, and Phosphorus-Centered Polycyclic π-Conjugated Systems. *Chemical reviews* **2019**, *119*, 8291–8331.

Bibliography

[190] Schaub, T. A.; Padberg, K.; Kivala, M. Bridged triarylboranes, -silanes, -amines, and -phosphines as minimalistic heteroatom-containing polycyclic aromatic hydrocarbons: Progress and challenges. *Journal of Physical Organic Chemistry* **2020**, *33*, e4022.

[191] Wagner, J.; Zimmermann Crocomo, P.; Kochman, M. A.; Kubas, A.; Data, P.; Lindner, M. Modular Nitrogen-Doped Concave Polycyclic Aromatic Hydrocarbons for High-Performance Organic Light-Emitting Diodes with Tunable Emission Mechanisms**. *Angewandte Chemie International Edition* **2022**, *61*, e202202232.

[192] Ajdari, M.; Pappenberger, R.; Walla, C.; Hoffmann, M.; Michalsky, I.; Kivala, M.; Dreuw, A.; Tegeder, P. Impact of Connectivity on the Electronic Structure of N-Heterotriangulenes. *Journal of Physical Chemistry C* **2023**, *127*, 542–549.

[193] Kader, T.; Stöger, B.; Fröhlich, J.; Kautny, P. Azaindolo[3,2,1-jk]carbazoles: New Building Blocks for Functional Organic Materials. *Chemistry – A European Journal* **2019**, *25*, 4412–4425.

List of Publications and Award

Publications Related to this Thesis

Impact of Connectivity on the Electronic Structure of N-Hetero-triangulenes
Mohsen Ajdari, Ronja Pappenberger, Christian Walla, Marvin Hoffmann, Ina Michalsky, Milan Kivala, Andreas Dreuw, and Petra Tegeder
J. Phys. Chem. C, **127** (2023) 542-549.

Influence of N-Introduction in Pentacene on the Electronic Structure and Excited Electronic States
Marvin T. Hoffmann, Mohsen Ajdari, Felix Landwehr, Olena Tverskoy, Uwe H. F. Bunz, Andreas Dreuw, and Petra Tegeder
Phys. Chem. Chem. Phys., **24** (2022) 3924-3932.

Influence of Core Halogenation on the Electronic Structure of Naphthothiadiazole Derivatives
Mohsen Ajdari, Felix Landwehr, Marvin Hoffmann, Hendrik Hoffmann, Uwe H. F. Bunz, Andreas Dreuw, and Petra Tegeder
J. Phys. Chem. C, **125** (2021) 6359-6366.

Electronic Properties of 6,13-Diazapentacene Adsorbed on Au(111): A Quantitative Determination of Transport, Singlet and Triplet States and Electronic Spectra
Mohsen Ajdari, Tanja Schmitt, Marvin Hoffmann, Friedrich Maaß, Hilmar Reiss, Uwe H. F. Bunz, Andreas Dreuw, and Petra Tegeder
J. Phys. Chem. C, **124** (2020) 13196-13205.

Lightening up a Dark State of a Pentacene Derivative via N-Introduction
Mohsen Ajdari, Arnulf Stein, Marvin Hoffmann, Matthias Müller, Uwe H. F. Bunz, Andreas Dreuw, and Petra Tegeder
J. Phys. Chem. C, **124** (2020) 7196-7204.

Publication not Related to this Thesis

Nonadditivity of the Adsorption Energies of Linear Acenes on Au(111): Molecular Anisotropy and Many-Body Effects
Friedrich Maass, Mohsen Ajdari, Fairoja Cheenicode Kabeer, Maximilian Vogtland, Alexandre Tkatchenko, and Petra Tegeder
J. Phys. Chem. Lett., **10** (2019) 1000-1004.

Publications in Preparation

Electronic Properties of Charge Transfer Complexes Formed by N-Heterotriangulenes and Strong Acceptors
Mohsen Ajdari, Ronja Pappenberger, Ina Michalsky, Leonie Pap, Christian Huck, Marvin Hoffmann, Friedrich Maass, Milan Kivala, Andreas Dreuw, and Petra Tegeder.
in preparation

Influence of Core Substitutions on the Electronic Structure of Benzobisthiadiazoles
Mohsen Ajdari, Ronja Pappenberger, Larissa Winkelmann, Lukas Ahrens, Uwe H. F. Bunz, Andreas Dreuw, and Petra Tegeder.
in preparation

Award

Heidelberg (2021)   Dr.-Sophie-Bernthsen Award
Faculty of Chemistry and Earth Sciences
Ruprecht-Karls-Universität Heidelberg

Acknowledgements

Acknowledgements

In our working group, I had the privilege to work with Christian Huck, Martin Richter, Gabriel Sauter, Tanja Schmitt, Vipilan Sivanesan, Jakob Steidel, Arnulf Stein, Michael Tzschoppe and Nadine von Coelln. I am grateful for the company and support of my current and former colleagues.

My sincere gratitude goes to my predecessor and mentor, Dr. Friedrich Maaß, whose mentorship paved the way for me to continue with HREELS experiments.

I am specially thankful to Klaus Schmitt and his team in the precision engineering workshop and Günter Meinusch of the electronic workshop for providing me with the needed technical support.

I would like to extend my thanks to Angelika Neuner, Marina Sommer and Anja Ihli for their administrative support.

Finally, I am forever thankful to my mother, Farahnaz Kolahchi, for her unconditional support throughout my academic studies.

Thank you !

Appendix

Appendix

A. Au(111)

A.1. Vibrational and Electronic HREELS Measurements

Reference vibrational and electronic HREELS spectra of pristine Au(111) substrate, after cleaning with standard sputtering and annealing cycles.
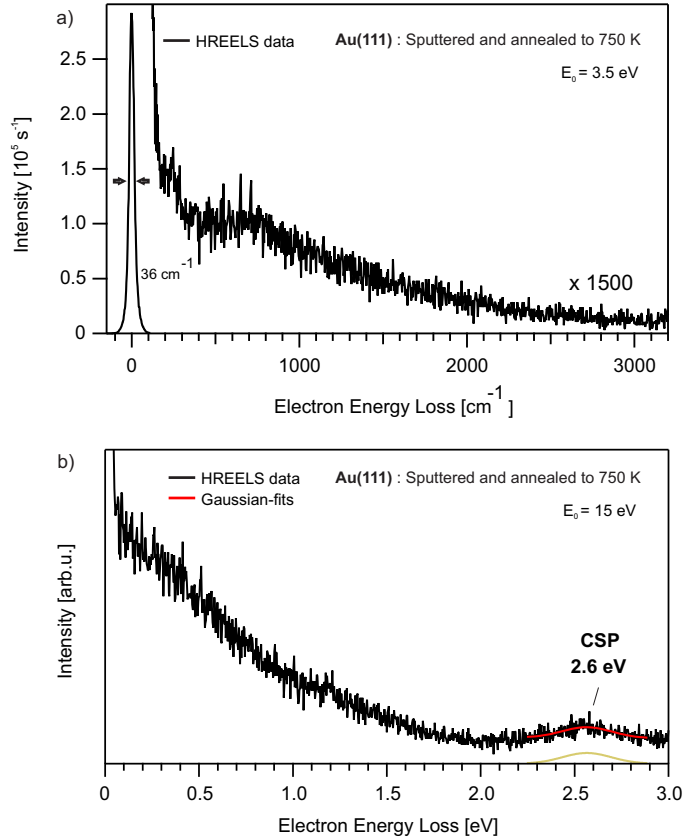

Figure A.1.: Sputtered and annealed Au(111): Vibrational (a) and electronic (b) HREELS spectra measured in specular (black spectra) scattering geometry. E_0 is the primary energy of the incident electrons. The energy resolution of the specular spectra is measured as the full width at half maximum (FWHM) of the elastic peak (zero energy loss peak) and is given in wavenumbers (cm^{-1}).

B. Linear N-Heteropentacene Derivatives

B.1. TPD Measurements

In order to compare the desorption behaviour of different selected ionic fragments of the adsorbed DAP and TAP on Au(111), fragment-mass-resolved TPD measurements were carried out on the multilayer coverages of DAP and TAP as shown in figure B.1. Different desorption features of the spectra are assigned with α_1, α_2 and α_3 in accordance with the corresponding TPD measurements of each molecule in subsection 3.1.1 (see Figure 3.3).
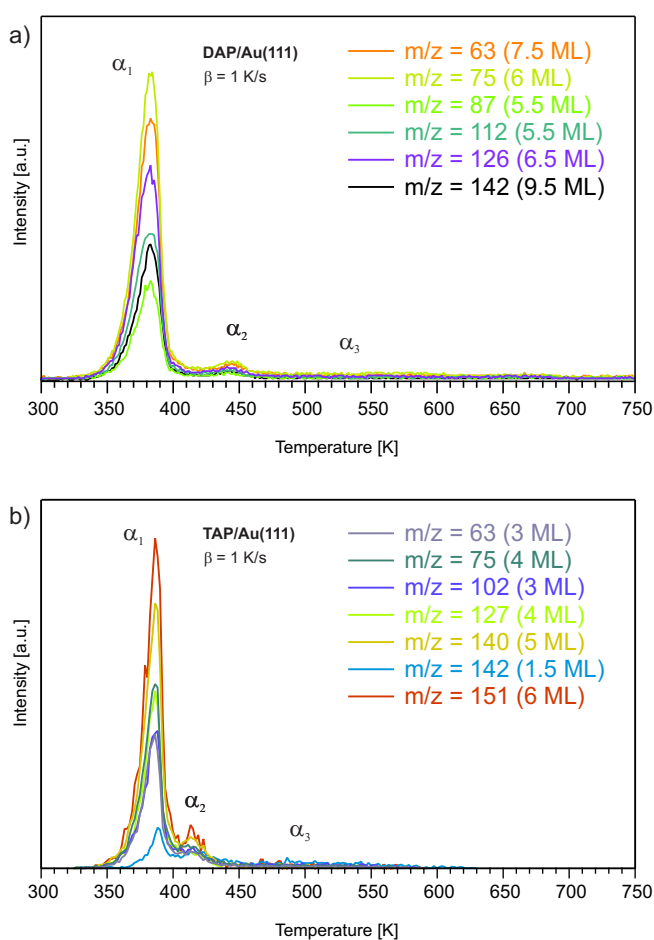
Figure B.1.: Fragment-mass-resolved TPD spectra of (a) DAP and (b) TAP for different selected ionic fragments adsorbed on Au(111), measured with a heating rate of $\beta = 1\ K/s$. The desorption features are labelled with α_1, α_2 and α_3.
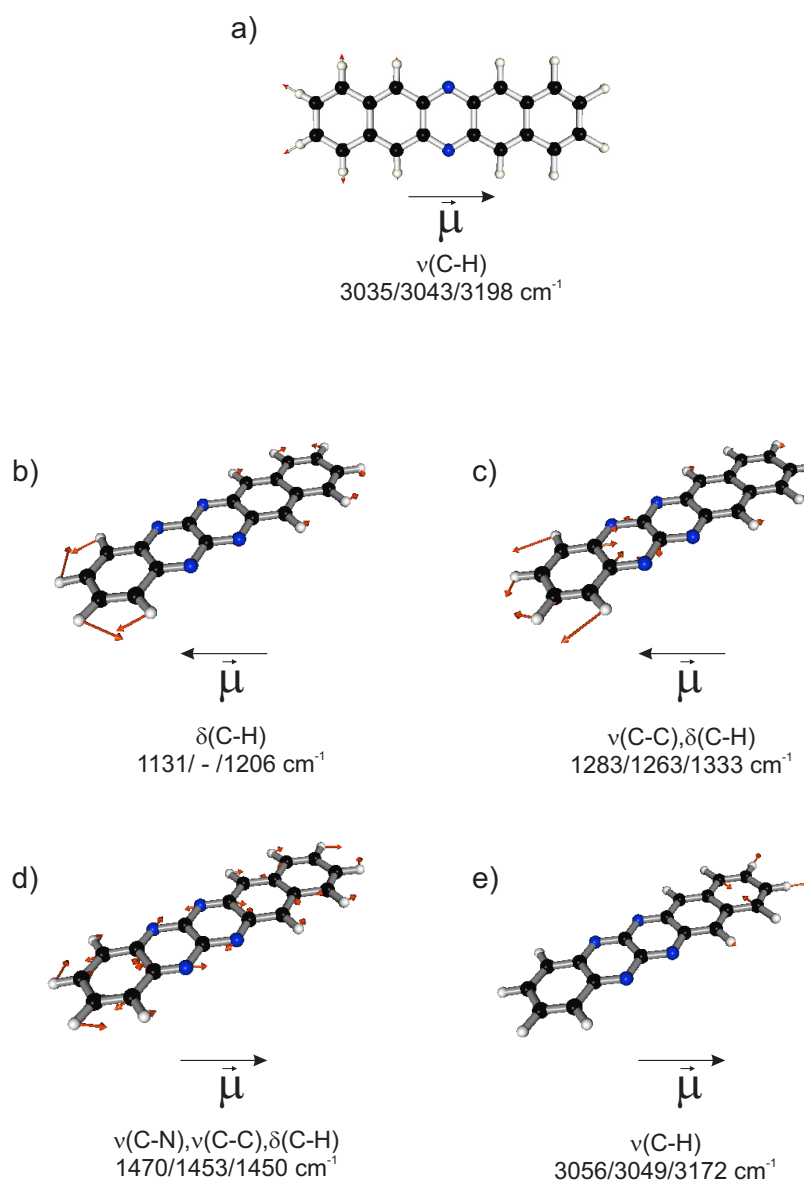
Appendix

B.2. Vibrational HREELS Measurements

The measured vibrational HREELS spectra of the annealed DAP and TAP samples as well as their sub-monolayer coverage adsorbed on Au(111) are shown in figure B.2. The assigned vibrations of sub-monolayer, mono - and multilayer coverage are listed in tables 3.1. The assigned non-dipole-active vibrations are visualized in figure B.3.
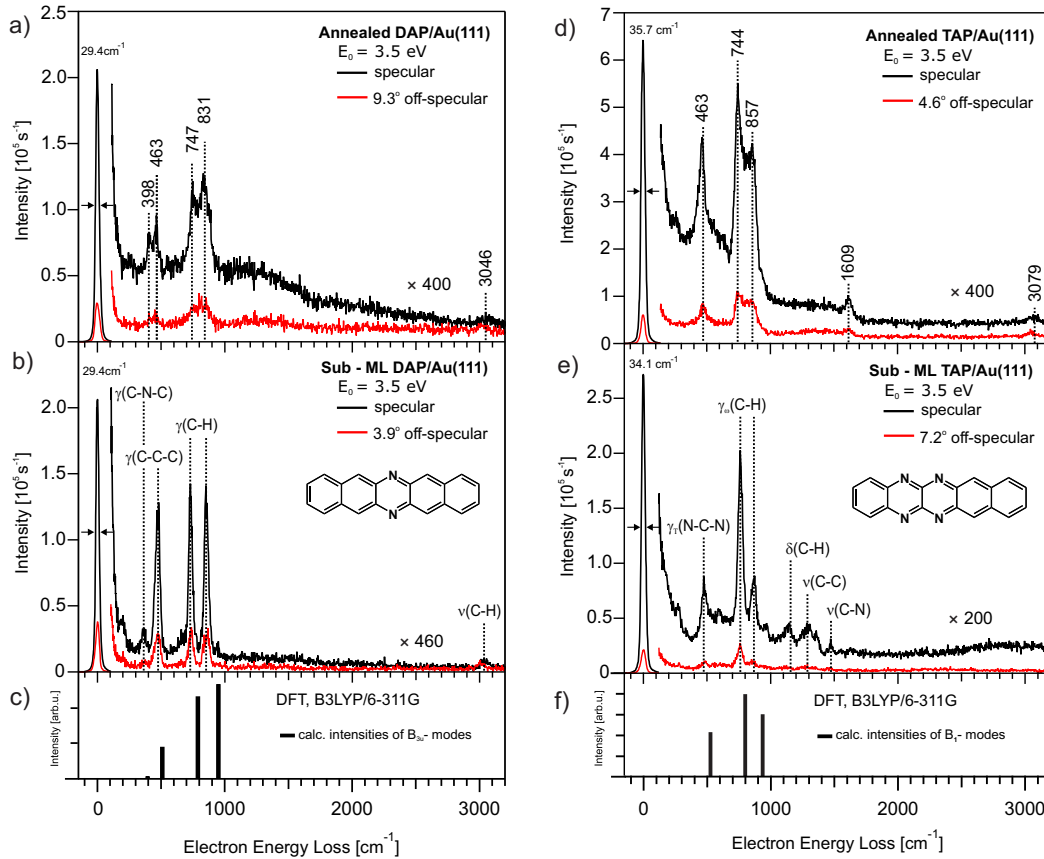
Figure B.2.: Vibrational HREELS spectra of DAP (Left) and TAP (right) measured in specular (black spectra) and off-specular (red spectra) scattering geometry for post annealed samples (a and d) and sub-monolayer (b and e) coverage on Au(111) with the associated DFT-calculations (B3LYP/6-311G) for intensities and frequencies of B_{3u} and B_1 symmetric vibrational modes with a dynamic dipole moment perpendicular to the molecular plane (c and f). E_0 is the primary energy of the incident electrons. The energy resolution of the specular spectra is measured as the full width at half maximum (FWHM) of the elastic peak (zero energy loss peak) and is given in wavenumbers (cm^{-1}).

a)

$\vec{\mu}$

ν(C-H)
3035/3043/3198 cm^{-1}

b)

$\vec{\mu}$

δ(C-H)
1131/ - /1206 cm^{-1}

c)

$\vec{\mu}$

ν(C-C),δ(C-H)
1283/1263/1333 cm^{-1}

d)

$\vec{\mu}$

ν(C-N),ν(C-C),δ(C-H)
1470/1453/1450 cm^{-1}

e)

$\vec{\mu}$

ν(C-H)
3056/3049/3172 cm^{-1}

Figure B.3.: Visualisation of the assigned non-dipole-active vibrational modes obtained from the DFT calculations (B3LYP/6-311G) for DAP (a) and TAP(b-e). The corresponding energies (HREELS monolayer/HREELS multilayer/DFT) are given in wavenumbers (cm^{-1}). The direction of the calculated dipole derivative unit vector ($\vec{\mu}$) is depicted with a black arrow that lies in the plane of the paper. The atomic displacements in each visualization are shown with red arrows. The vibrational modes are visualized by the Facio software[139]. Adapted from Ref.[129].

B.3. Electronic HREELS Measurements

The measured electronic HREELS spectra of sub-monolayer and monolayer coverages of DAP and TAP adsorbed on Au(111) are shown in figure B.4.
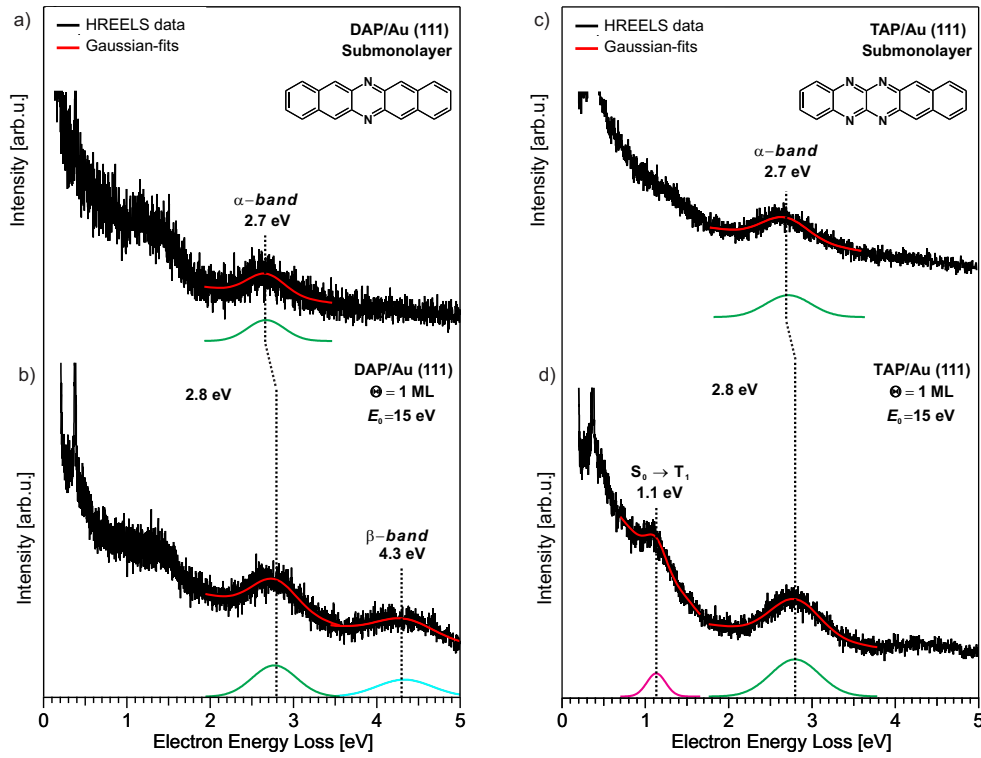

Figure B.4.: Electronic HREELS spectra of adsorbed DAP (Left) and TAP (right) on Au(111), measured for sub-monolayer (a and c) and monolayer (b and d) coverages. E_0 is the primary energy of the incident electrons. Θ is the coverage in monolayer (ML). Adapted from Ref. [130].

C. Arrow-Shaped N-Heteropentacene Derivative

C.1. TPD Measurements

In order to compare the desorption behaviour of different selected ionic fragments of TIPS group in the adsorbed TIPS-BP and TIPS-BAP on Au(111), fragment-mass-resolved TPD measurements were carried out on the multilayer coverages of both molecules as shown in figure C.1. Different desorption features of the spectra are assigned with α_1, α_2 and α_3 in accordance with the corresponding TPD measurements of each molecule in subsection 3.1.2 (see Figure 3.11).
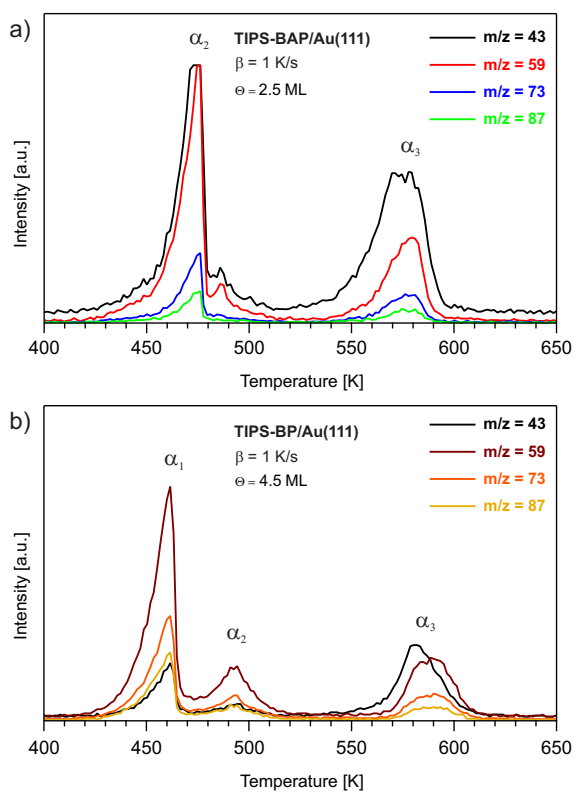
Figure C.1.: Fragment-mass-resolved TPD spectra of (a) TIPS-BAP and (b) TIPS-BP for different selected ionic fragments of TIPS group adsorbed on Au(111), measured with a heating rate of $\beta = 1$ *K/s*. The desorption features are labelled with α_1, α_2 and α_3.

C.2. Vibrational HREELS Measurements

The measured vibrational HREELS spectra of the annealed TIPS-BAP sample as well as its monolayer coverage adsorbed on Au(111) are shown in figure C.2. The assigned vibrations of mono - and multilayer coverage are listed in table 3.2.
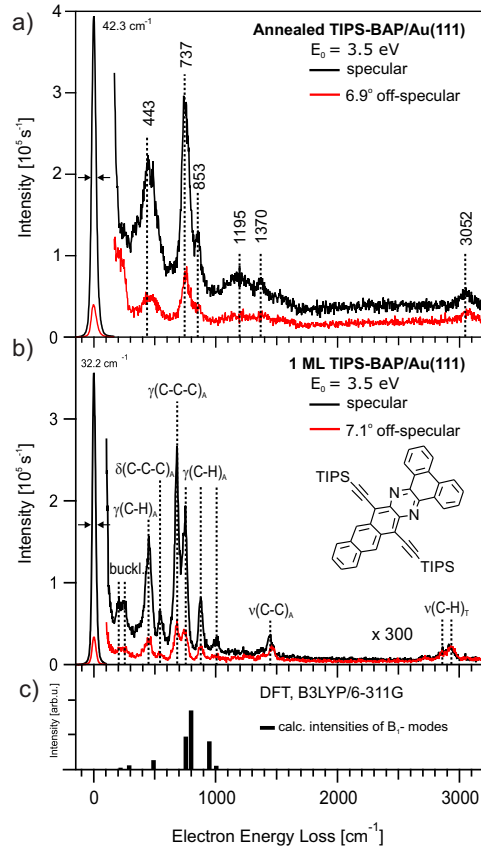

Figure C.2.: Vibrational HREELS spectra of TIPS-BAP measured in specular (black spectra) and off-specular (red spectra) scattering geometry for post annealed sample (a) and monolayer coverage (b) adsorbed on Au(111) with the associated DFT-calculations (B3LYP/6-311G) for intensities and frequencies of B_1 symmetric vibrational modes with a dynamic dipole moment perpendicular to the molecular plane (c). E_0 is the primary energy of the incident electrons. The energy resolution of the specular spectra is measured as the full width at half maximum (FWHM) of the elastic peak (zero energy loss peak) and is given in wavenumbers (cm^{-1}). Adapted from Ref. [146].

D. Naphthothiadiazole Derivatives

D.1. TPD Measurements

Figure D.1 shows the coverage dependent TPD spectra of NTD-Cl (m = 254 amu), with different initial coverages of 5, 6 and 10 ML for the fully dehalogenated biradical fragment of the molecule (m/z = 184).
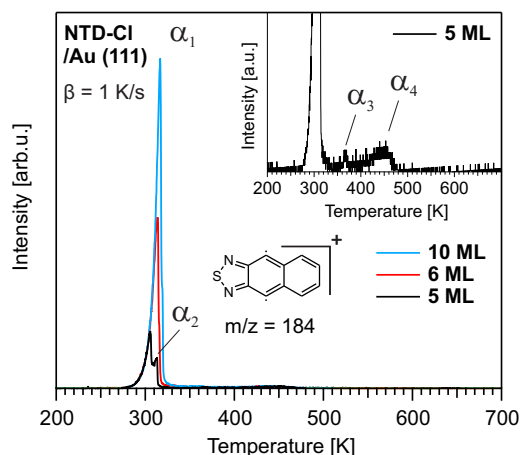

Figure D.1.: Coverage dependent TPD spectra of NTD-Cl for the biradical fragment with the mass-to-charge ratio (m/z) of 184 with different initial coverages adsorbed on Au(111), measured with a heating rate of $\beta = 1$ K/s. The desorption features are labelled with α_1, α_2, α_3 and α_4. The inset shows the monolayer desorption features (α_3 and α_4). The structural formula of the ionic fragment of NTD-Cl is depicted in the figure.

The spectra consist of two desorption regions. The first region includes two desorption peaks at 318 K (α_1) and 313 K (α_2). The α_1 peak does not saturates with increasing coverage. Therefore, α_1 is assigned to the desorption of a multilayer coverage. The α_2 peak appears as a shoulder structure at 5 ML and by increasing the coverage merges to the multilayer desorption peak (α_1). This characteristic desorption behaviour is similar to that of the 2nd-layer desorption of NTD as observed in the coverage dependent TPD spectra of the molecule (see Figure 3.19 (a)). Thus, the α_2 peak can be attributed to the desorption of the 2nd-layer. The second region includes a desorption peak at 365 K (α_3) and a broad desorption feature extending from 398 K to 483 K (α_4). Both α_3 and α_4 saturate with increasing coverage. Therefore, it can be assumed that α_3 originates from a more densely packed compressed phase, while α_4 can be attributed to a desorption from a sub-monolayer coverage.

Thus, the desorption spectrum of a monolayer coverage can be defined as a spectrum, in which both α_3 and α_4 are saturated. The inset shows the enlarged monolayer desorption region of the measured spectra.

Additionally, in order to compare the desorption behaviour of different selected fragments of the adsorbed NTD-Cl on Au(111), fragment-mass-resolved TPD measurements were carried out on the multilayer coverages of NTD-Cl, after different time intervals as shown in figure D.2.
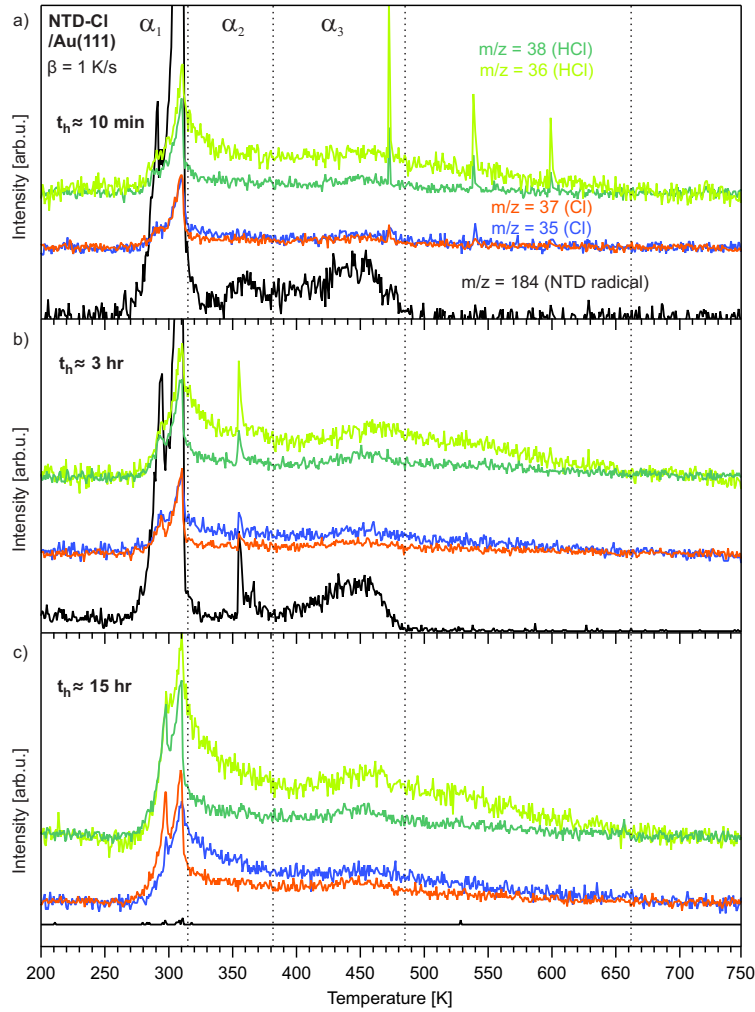
Figure D.2.: Fragment-mass-resolved TPD spectra of NTD-Cl for different selected fragments adsorbed on Au(111). The spectra measured (a) immediately after sample preparation ($\simeq$ 10 min), (b) after approximately 3 h and (c) 15 h, with a heating rate of $\beta = 1$ K/s. The dashed lines separates the desorption regions. The desorption features of the biradical fragment (m/z=184) are labelled with α_1, α_3 and α_4 in accordance with the corresponding coverage dependant TPD measurements of the molecule (see Figure D.1).

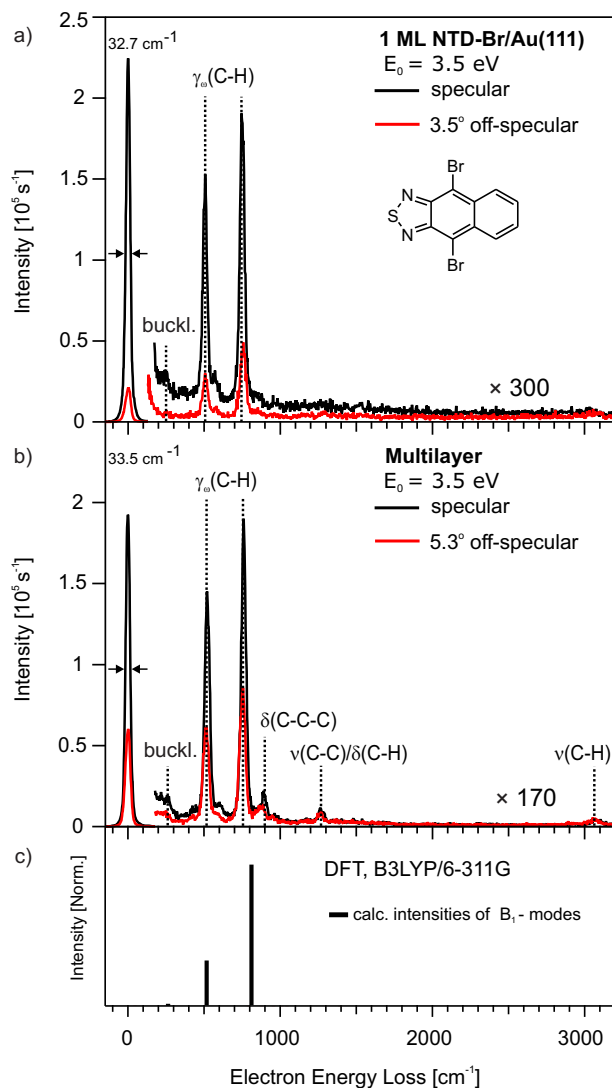## D.2. Vibrational HREELS Measurements

The measured vibrational HREELS spectra of the annealed NTD as well as its monolayer coverage adsorbed on Au(111) are shown in figure D.3.
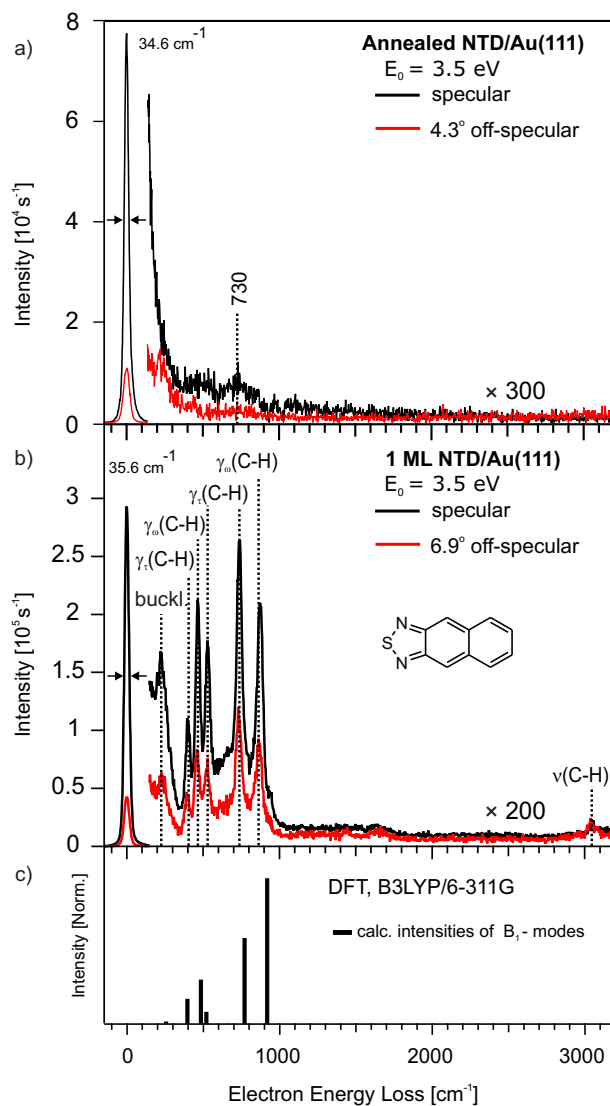
Figure D.3.: Vibrational HREELS spectra of NTD, measured in specular (black spectra) and off-specular (red spectra) scattering geometry for post annealed sample (a) and monolayer (b) coverage on Au(111) with the associated DFT-calculations (B3LYP/6-311G) for intensities and frequencies of B_1 symmetric vibrational mode with a dynamic dipole moment perpendicular to the molecular plane (c). E_0 is the primary energy of the incident electrons. The energy resolution of the specular spectra is measured as the full width at half maximum (FWHM) of the elastic peak (zero energy loss peak) and is given in wavenumbers (cm^{-1}). Adapted from Ref.[177].
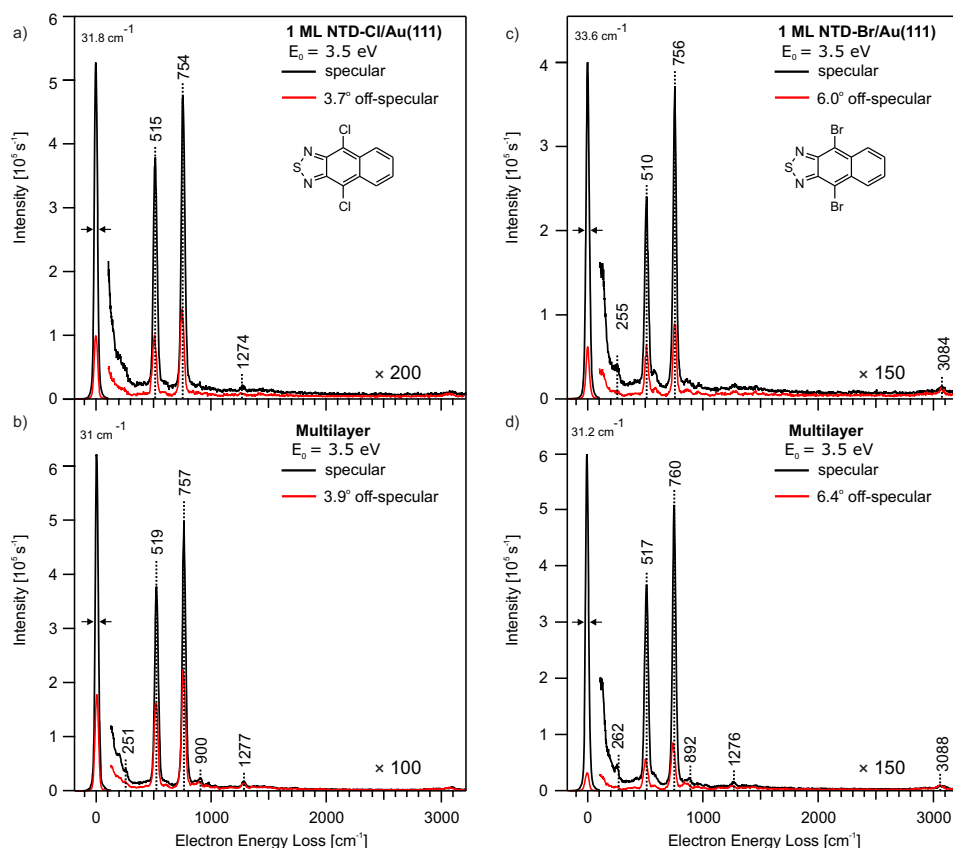
The measured vibrational HREELS spectra of mono - and multilayer coverages of NTD-Br adsorbed on Au(111) are shown in figure D.4. The assigned vibrations of mono - and multilayer coverage are listed in tables 3.3.


Figure D.4.: Vibrational HREELS spectra of NTD-Br measured in specular (black spectra) and off-specular (red spectra) scattering geometry for mono - (a) and multilayer (b) coverages on Au(111) with the associated DFT-calculations (B3LYP/6-311G) for intensities and frequencies of B_1 symmetric vibrational mode with a dynamic dipole moment perpendicular to the molecular plane (c). E_0 is the primary energy of the incident electrons. The energy resolution of the specular spectra is measured as the full width at half maximum (FWHM) of the elastic peak (zero energy loss peak) and is given in wavenumbers (cm^{-1}). Adapted from Ref.[177].

Figure D.5 shows the measured vibrational HREELS spectra of mono - and multilayer coverages of NTD-Cl and NTD-Br after approximately 15 hr of preparing the samples. The identified and assigned vibrational modes of the molecules from these spectra are similar to the ones located in the spectra of the molecule, which are measured immediately after the sample preparation (see Figure 3.21 for NTD-Cl and Figure D.4 for NTD-Br), with little to no change in the energetic positions of the corresponding vibrations.


Figure D.5.: Vibrational HREELS spectra of NTD-Cl (Left) and NTD-Br (right) measured after approximately 15 h of sample preparation in specular (black spectra) and off-specular (red spectra) scattering geometry for mono - (a and b) and multilayer (c and d) coverages on Au(111). E_0 is the primary energy of the incident electrons. The energy resolution of the specular spectra is measured as the full width at half maximum (FWHM) of the elastic peak (zero energy loss peak) and is given in wavenumbers (cm^{-1}).
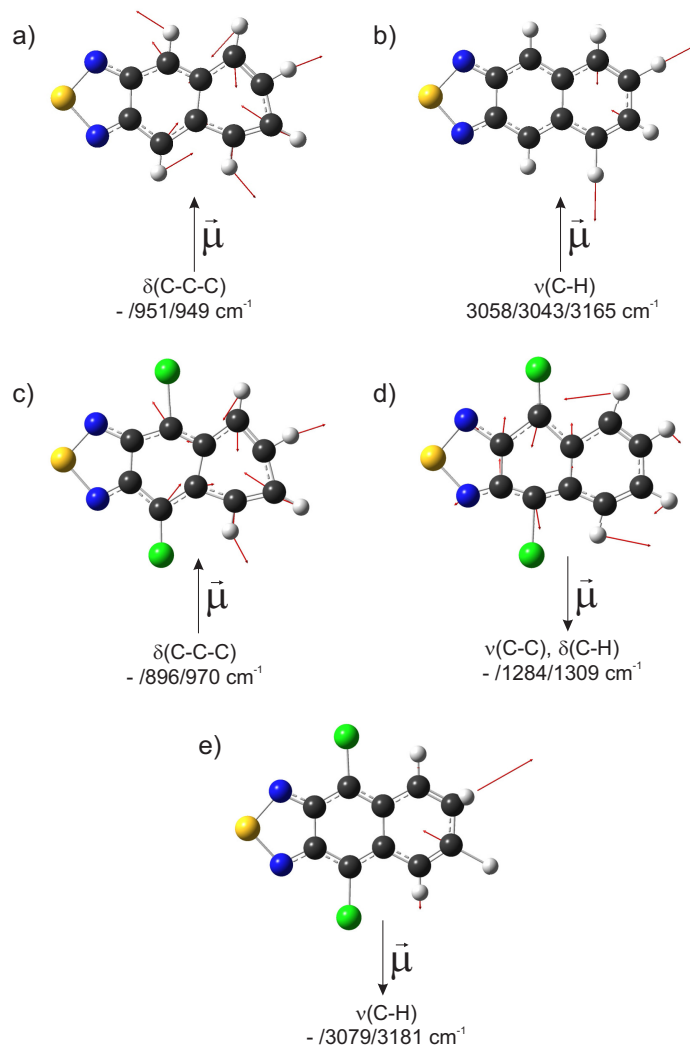
Figure D.6.: Visualisation of the assigned non-dipole-active vibrational modes obtained from the DFT calculations (B3LYP/6-311G) for NTD (a and b) and NTD-Cl (c-e). The corresponding energies (HREELS monolayer/HREELS multilayer/DFT) are given in wavenumbers (cm^{-1}). The direction of the calculated dipole derivative unit vector ($\overrightarrow{\mu}$) is depicted with a black arrow that lies in the plane of the paper. The atomic displacements in each visualization are shown with red arrows. The vibrational modes are visualized by the Avogadro[180] software. Adapted from Ref.[177].

D.3. Electronic HREELS Measurements

The measured electronic HREELS spectra of mono - and multilayer coverage of NTD-Br adsorbed on Au(111) are shown in figure D.7.
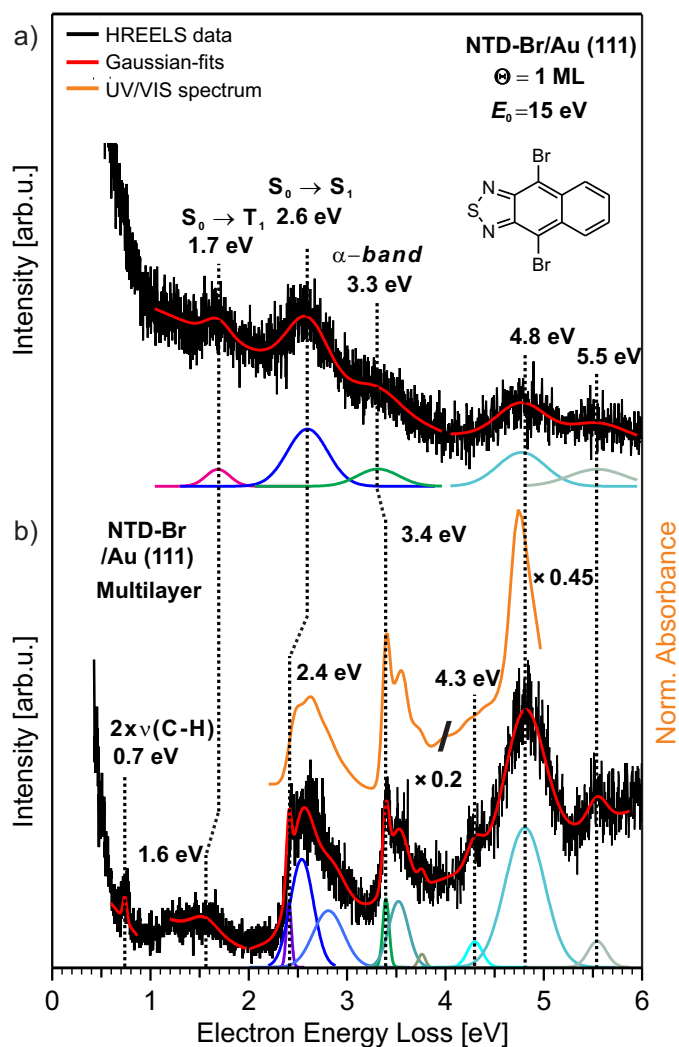

Figure D.7.: Electronic HREELS spectra of adsorbed NTD-Br on Au(111), measured for mono - (a) and multilayer (b) coverages (black spectra). The electronic loss features were fitted using Gaussian functions (red curves). The corresponding UV/Vis spectrum of the molecule is measured in dichloromethane (CH_2Cl_2) (orange spectrum). E_0 is the primary energy of the incident electrons. Θ is the coverage in monolayer (ML). Adapted from Ref. [177].

# E. Benzobisthiadiazole Derivatives

E.1. TPD Measurements

Given the fact that the entirety of the monolayer desorption region of BBT-Th, which consists of the compressed phase (α_3) and the sub-monolayer coverage, could not be detected in the corresponding spectra of the molecule (see Figure 3.27 (b)), instead area underneath the second layer desorption peak (α_2) was used as the reference for determining the coverage of the adsorbed BBT-Th molecules on the substrate. Therefore, the given number of layers for each coverage can only be taken as an estimate.
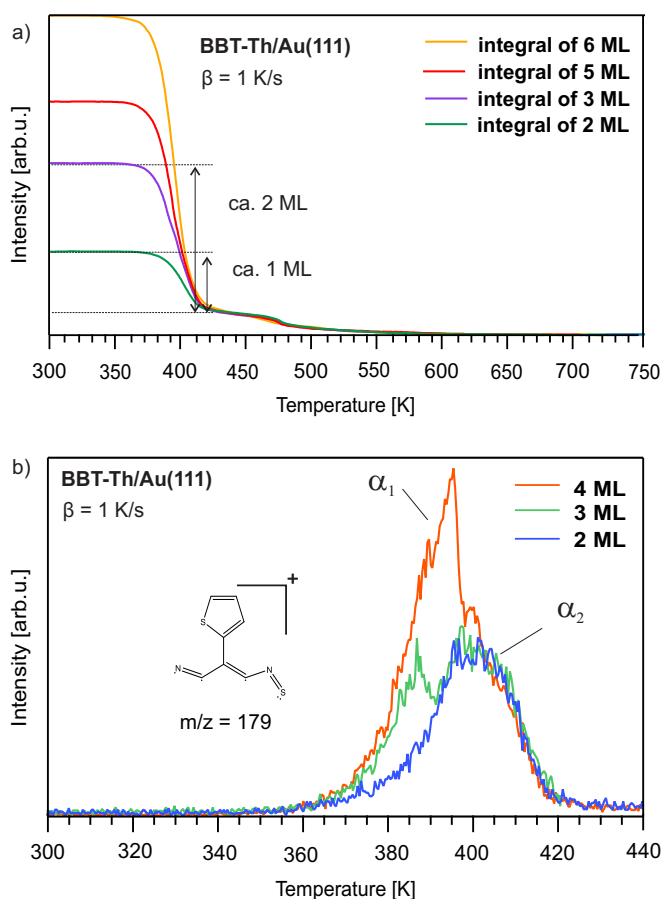
Figure E.1.: (a) Integral of the coverage dependent TPD spectra of BBT-Th for (b) the selected mass-to-charge ration (m/z) of 179 adsorbed on Au(111) with different initial coverages, measured with a heating rate of $\beta = 1\ K/s$.

In order to compare the desorption behaviour of different selected fragments of the adsorbed BBT-Ph and BBT-Th on Au(111), fragment-mass-resolved TPD measurements were carried out on the multilayer coverages of both molecules as shown in figure E.2. Different desorption features of the spectra are assigned with α_1, α_2 and α_3 in accordance with the corresponding TPD measurements of each molecule in subsection 3.2.2 (see Figure 3.27).
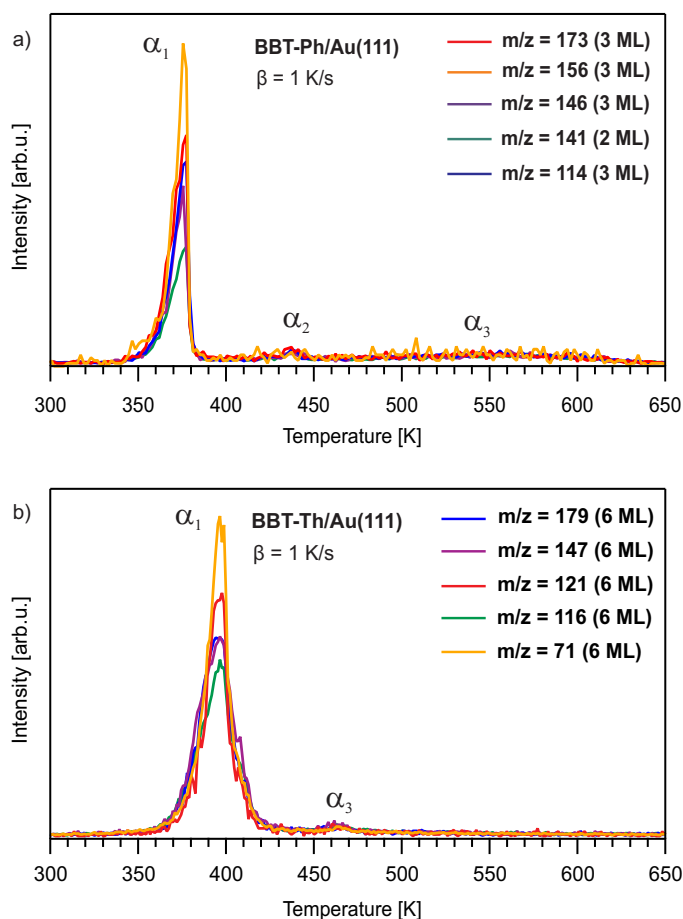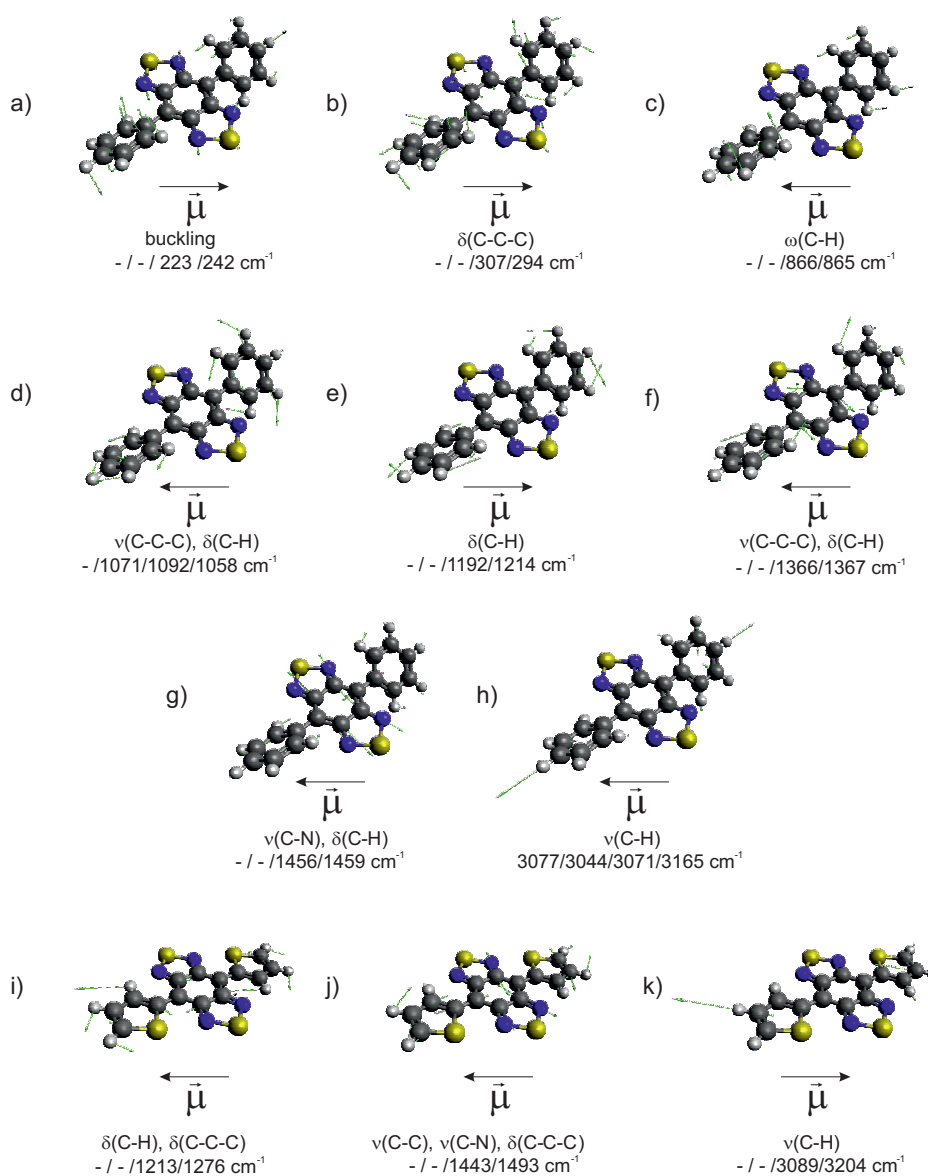

Figure E.2.: Fragment-mass-resolved TPD spectra of (a) BBT-Ph and (b) BBT-Th for different selected fragments adsorbed on Au(111), measured with a heating rate of $\beta = 1\ K/s$. The desorption features are labelled with α_1, α_2 and α_3.

E.2. Vibrational HREELS Measurements

The measured vibrational HREELS spectra of the annealed BBT-Ph and BBT-Th samples as well as their sub-monolayer coverage adsorbed on Au(111) are shown in figure E.3. The assigned vibrations of sub - monolayer coverage are listed in table 3.4.
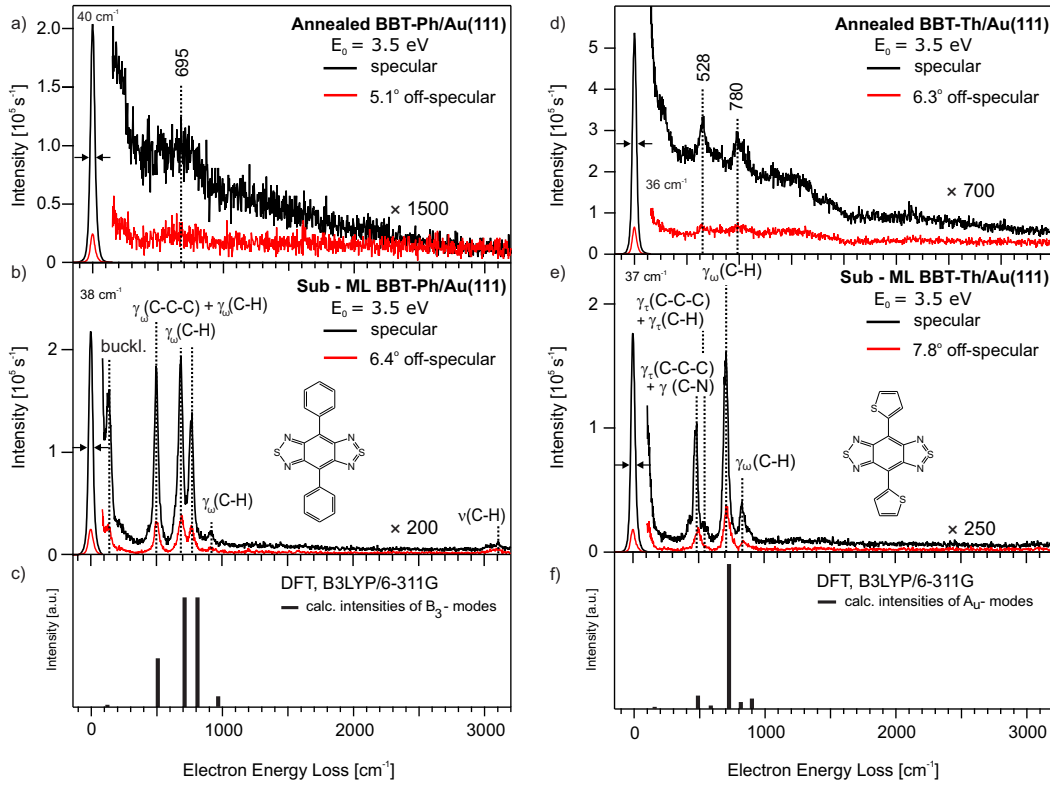

Figure E.3.: Vibrational HREELS spectra of BBT-Ph (Left) and BBT-Th (right) measured in specular (black spectra) and off-specular (red spectra) scattering geometry for post annealed samples (a and d) and sub-monolayer (b and e) coverage on Au(111) with the associated DFT-calculations (B3LYP/6-311G) for intensities and frequencies of B_3 and A_u symmetric vibrational modes with a dynamic dipole moment perpendicular to the molecular plane (c and f). E_0 is the primary energy of the incident electrons. The energy resolution of the specular spectra is measured as the full width at half maximum (FWHM) of the elastic peak (zero energy loss peak) and is given in wavenumbers (cm^{-1}).

Figure E.4.: Visualisation of the assigned non-dipole-active vibrational modes obtained from the DFT calculations (B3LYP/6-311G) for BBT-Ph (a-h) and BBT-Th (i-k). The corresponding energies (HREELS sub-monolayer/HREELS monolayer/HREELS multilayer/DFT) are given in wavenumbers (cm^{-1}). The direction of the calculated dipole derivative unit vector ($\overrightarrow{\mu}$) is depicted with a black arrow that lies in the plane of the paper. The atomic displacements in each visualization are shown with green arrows. The vibrational modes are visualized by the Avogadro[180] software.

Appendix

F. N-Heterotriangulene Derivatives

F.1. Mass Spectra
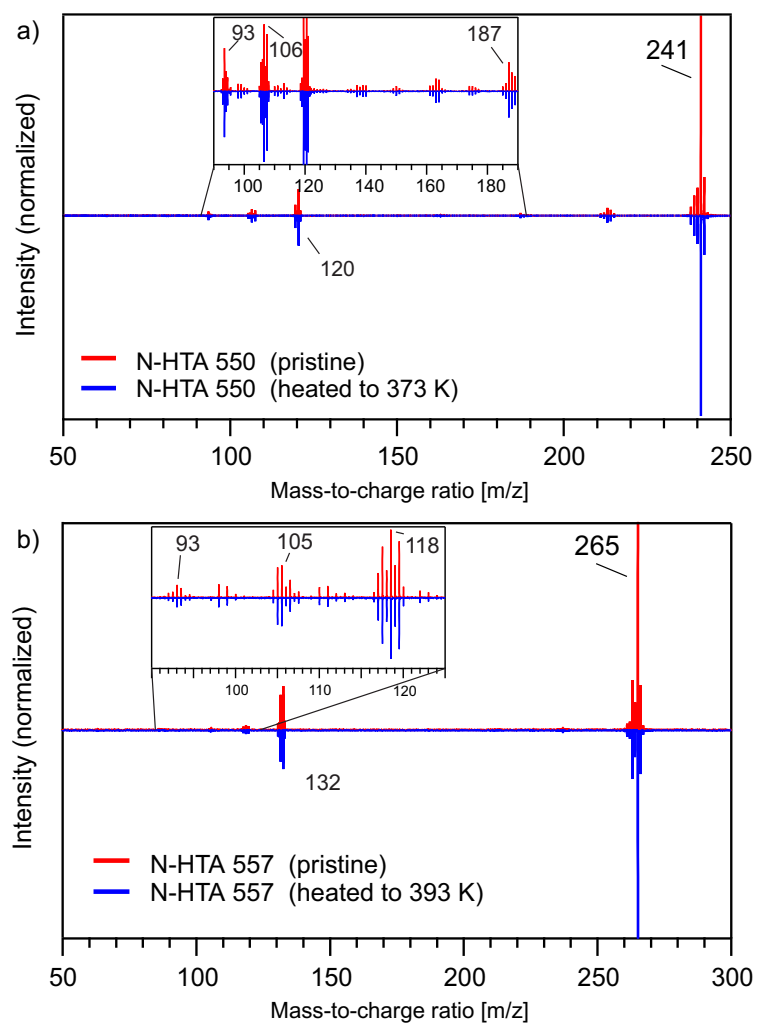
Figure F.1.: Electron ionisation mass spectra (EI-MS) of (a) N-HTA 550 and (b) N-HTA 557 for pristine molecules (red spectra) and heated molecules (blue spectra) up to 373 K (N-HTA 550) and 393 K (N-HTA 557). The fragments used during the TPD measurements are labelled.

F.2. TPD Measurements

In order to compare the desorption behaviour of different selected fragments of the adsorbed N-HTA 550 and N-HTA 557 on Au(111), fragment-mass-resolved TPD measurements were carried out on the multilayer coverages of both molecules (see Figure F.2). Different desorption features of the spectra are assigned with α_1, α_2, α_3 and α_4 in accordance with the corresponding coverage dependent TPD measurements of each molecule in subsection 3.3.1 (see Figure 3.33).
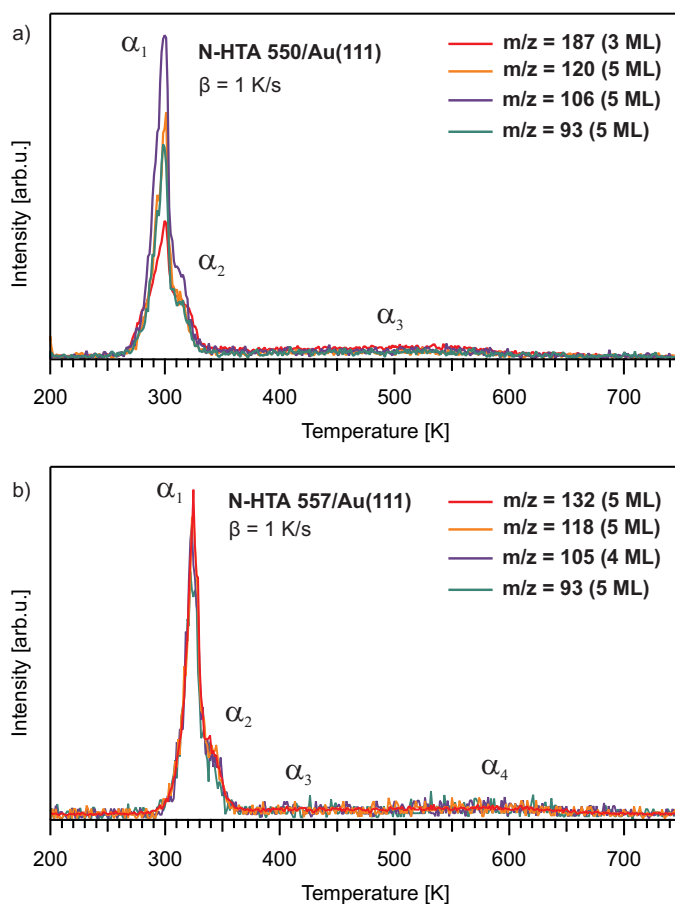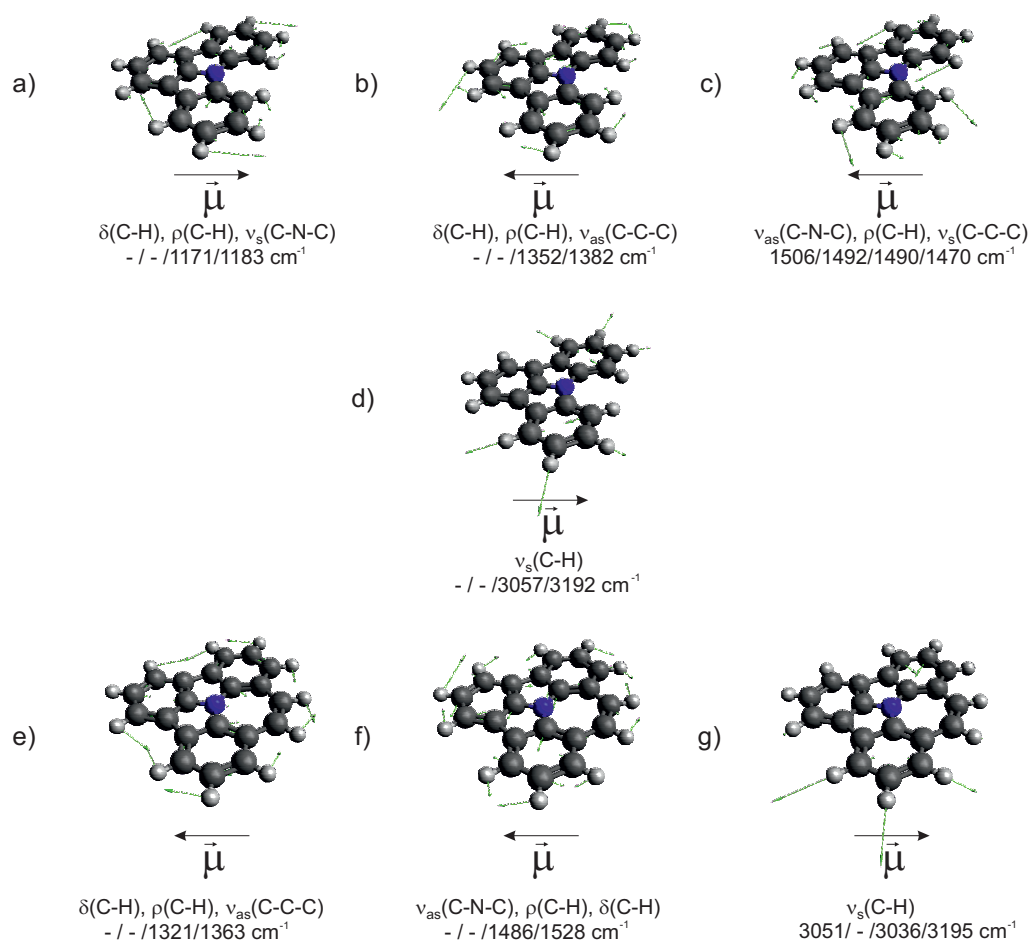

Figure F.2.: Fragment-mass-resolved TPD spectra of (a) N-HTA 550 and (b) N-HTA 557 for different selected fragments adsorbed on Au(111), measured with a heating rate of $\beta = 1$ *K/s*. The desorption features are labelled with α_1, α_2, α_3 and α_4. Adapted from Ref.[192].

F.3. Vibrational HREELS Measurements

The measured vibrational HREELS spectra of the annealed N-HTA 550 and N-HTA 557 samples as well as their sub-monolayer coverages adsorbed on Au(111) are shown in figure F.3. The assigned vibrations of the sub-monolayer coverages are listed in table 3.5.
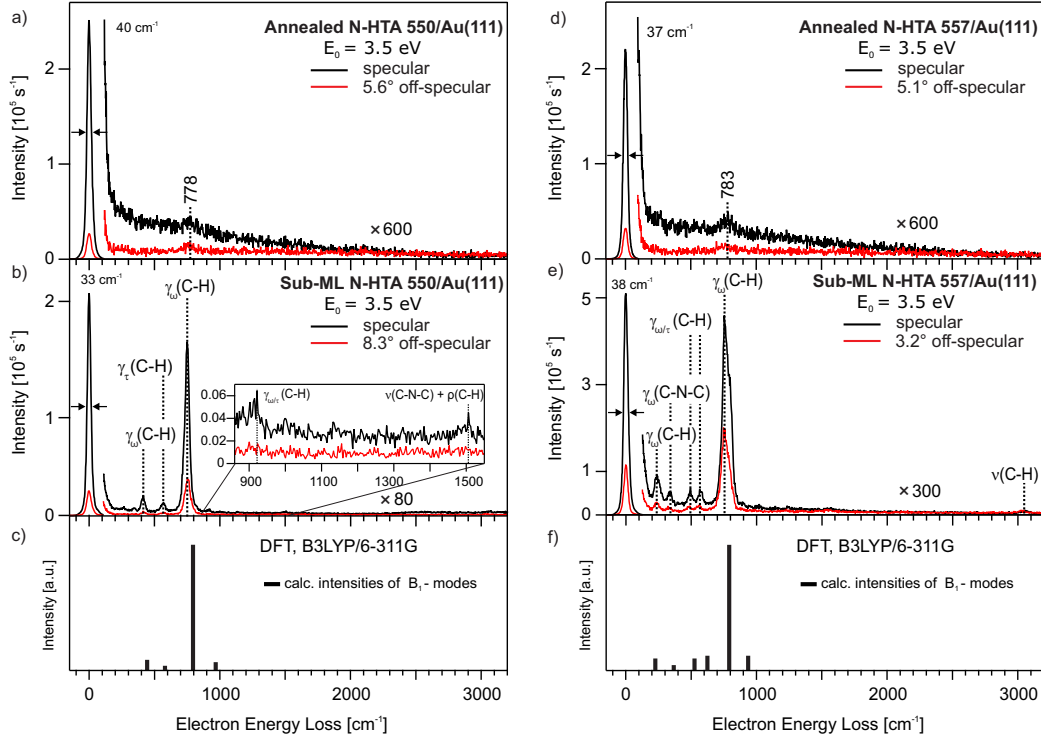
Figure F.3.: Vibrational HREELS spectra of N-HTA 550 (Left) and N-HTA 557 (right) measured in specular (black spectra) and off-specular (red spectra) scattering geometry for post annealed samples (a and d) and sub-monolayer (b and e) coverage on Au(111) with the associated DFT-calculations (B3LYP/6-311G) for intensities and frequencies of B_1 symmetric vibrational mode with a dynamic dipole moment perpendicular to the molecular plane (c and f). E_0 is the primary energy of the incident electrons. The energy resolution of the specular spectra is measured as the full width at half maximum (FWHM) of the elastic peak (zero energy loss peak) and is given in wavenumbers (cm^{-1}). Adapted from Ref. [192].

a) δ(C-H), ρ(C-H), ν$_s$(C-N-C)
- / - /1171/1183 cm^{-1}

b) δ(C-H), ρ(C-H), ν$_{as}$(C-C-C)
- / - /1352/1382 cm^{-1}

c) ν$_{as}$(C-N-C), ρ(C-H), ν$_s$(C-C-C)
1506/1492/1490/1470 cm^{-1}

d) ν$_s$(C-H)
- / - /3057/3192 cm^{-1}

e) δ(C-H), ρ(C-H), ν$_{as}$(C-C-C)
- / - /1321/1363 cm^{-1}

f) ν$_{as}$(C-N-C), ρ(C-H), δ(C-H)
- / - /1486/1528 cm^{-1}

g) ν$_s$(C-H)
3051/ - /3036/3195 cm^{-1}

Figure F.4.: Visualisation of the assigned non-dipole-active vibrational modes obtained from the DFT calculations (B3LYP/6-311G) for N-HTA 550 (a-d) and N-HTA 557 (e-g). The corresponding energies (HREELS sub-monolayer/HREELS monolayer/HREELS multilayer/DFT) are given in wavenumbers (cm^{-1}). The direction of the calculated dipole derivative unit vector ($\vec{\mu}$) is depicted with a black arrow that lies in the plane of the paper. The atomic displacements in each visualization are shown with green arrows. The vibrational modes are visualized by the Avogadro[180] software. Adapted from Ref.[192].

F.4. Electronic HREELS Measurements

The measured electronic HREELS spectra of sub-monolayer and monolayer coverage of N-HTA 550 and N-HTA 557 adsorbed on Au(111) are shown in figure F.5.
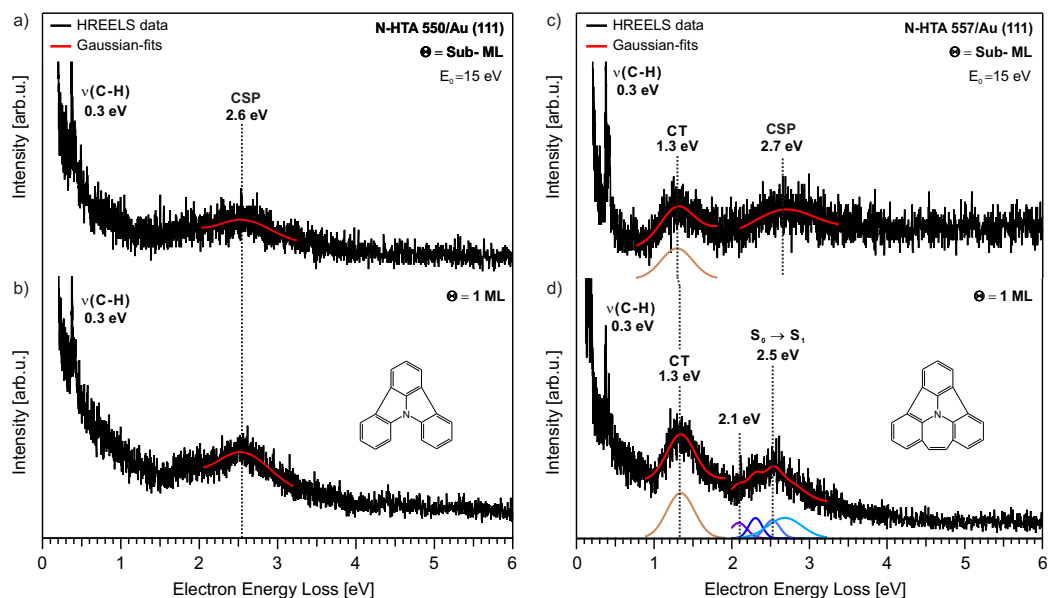
Figure F.5.: Electronic HREELS spectra of adsorbed N-HTA 550 (Left) and N-HTA 557 (right) on Au(111), measured for sub-monolayer (a and c) and monolayer (b and d) coverages (black spectra). The electronic loss features were fitted using Gaussian functions (red curves). E_0 is the primary energy of the incident electrons. Θ is the coverage in monolayer (ML). Adapted from Ref. [192].

G. N-Heterotriangulene based Donor/Acceptor-Systems

G.1. TPD Measurements

After preparing the samples, through coverage dependent TPD measurements, the adsorption properties of the D/A-systems on Au(111) are investigated. Figure G.1 (a) shows the TPD spectra of TCNQ/N-HTA 550 bilayer with the selected mass-to-charge ratio (m/z) of 102, which corresponding to the half of the parent molecular ion of TCNQ (204 *amu*). The spectra consist of two desorption regions. The first region includes two overlaid desorption peaks corresponding to TCNQ (orange spectra) and N-HTA 550 (red spectra), at approximately 327 K (α_1). The second region includes a broad desorption feature originating from N-HTA 550 coverage, which extends from 416 K to 642 K (α_2).

By increasing the coverage of N-HTA 550 to 4 ML, the desorption peaks of each molecule assigned with α_1 can be distinguished from one another with the desorption peak associated with N-HTA 550 having a higher intensity relative to the one attributed to TCNQ as shown in figure G.1 (b). Moreover, at the multilayer coverage, the broad desorption feature of N-HTA 550 can still be detected in the same temperature range as previously identified (α_2) for the bilayer. With a comparison between the spectra of TCNQ/N-HTA 550 system and the measured TPD spectra of each of its components on Au(111) (see Figures G.3 (a) and 3.33 (a)), it can be concluded that α_1 originates from the desorption of TCNQ together with higher coverages of N-HTA 550, while α_2 can be assigned to the monolayer desorption feature of N-HTA 550. Absence of any desorption feature which can be attributed to the TCNQ monolayer desorption peak (α_2) in the spectra of the system, suggests that the TCNQ molecules are adsorbed entirely on top of the N-HTA 550 layer, thus by desorbing the underlying N-HTA 550 coverage, the overlaying TCNQ monolayer desorbs as well.

Similar arguments can be used to describe the spectra of TCNQ/N-HTA 557 system as shown in G.1 (c) and G.1 (d). In these spectra, the monolayer coverage of the acceptor molecule (TCNQ) desorbs at a lower temperature (α_1) together with a higher coverage ($\theta > 1$ ML) of N-HTA 557. Subsequently, the monolayer of donor molecule (N-HTA 557), desorbs across a broad tempera-

ture range extending from 380 K to 660 K (α_2). Therefore, it can be concluded that the nature of the underlying molecules (N-HTA 550 or N-HTA 557) or its coverage does not change the desorption behaviour of the overlaying acceptor molecule in TCNQ/N-HTA systems.
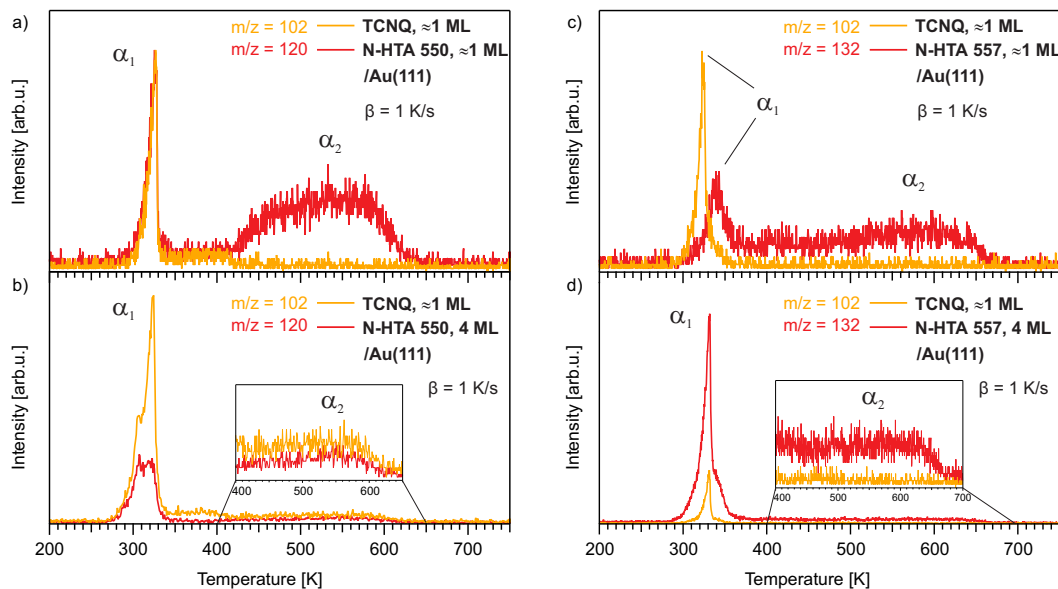
Figure G.1.: TPD spectra of approximately 1 ML of TCNQ deposited on (a) approximately 1 ML and (b) 4 ML of N-HTA 550 as well as (c) approximately 1 ML and (d) 4 ML of N-HTA 557 adsorbed on Au(111). The spectra are measured with a heating rate of $\beta = 1$ K/s for the selected m/z of 102 (TCNQ), 120 (N-HTA 550) and 132 (N-HTA 557).

In case of F_4TCNQ/N-HTA systems, the TPD spectra of F_4TCNQ is measured for the selected m/z of 138, which corresponding to the half of the parent molecular ion of the molecule (276 *amu*). Overall, the spectra of these D/A-systems, similar to the spectra of TCNQ/N-HTA systems, consisting of two desorption regions. In the first region, α_1 is located at approximately the same temperature as the identified multilayer desorption temperatures of the individual molecules (see Figure 3.33 and Figure G.3 (b)) on Au (111), since the acceptor molecules (F_4TCNQ) are decoupled from the substrate and desorb together with the multilayers of the N-HTAs. Thus, α_1 can be assigned to the desorption from a higher coverage in the spectra of F_4TCNQ/N-HTA systems. Likewise, in the second region, α_2 is assigned to the desorption region of N-HTA 550 or N-HTA 557 monolayer coverages. Noticeably, F_4TCNQ also exhibit desorption features in the assigned α_2 des-

orption region in F_4TCNQ/N-HTA systems. This is in contrast to the observed desorption behaviour of TCNQ as the acceptor molecule in the measured spectra of TCNQ/N-HTA systems, where the overlaying monolayer coverage of the acceptor molecules is desorbed together with the underlying donor molecules at the multilayer desorption temperatures (α_1). At first glance this may suggests that the identified desorption features of F_4TCNQ at higher temperature regions (α_2) originate from the monolayer coverage of the molecule adsorbed on Au(111) substrate. However, upon a closer comparison of the F_4TCNQ/N-HTA desorption spectra with one of the adsorbed F_4TCNQ on Au(111), it becomes clear that the desorption features in question are located in temperature regions higher that of the adsorbed monolayer of F_4TCNQ on Au(111).
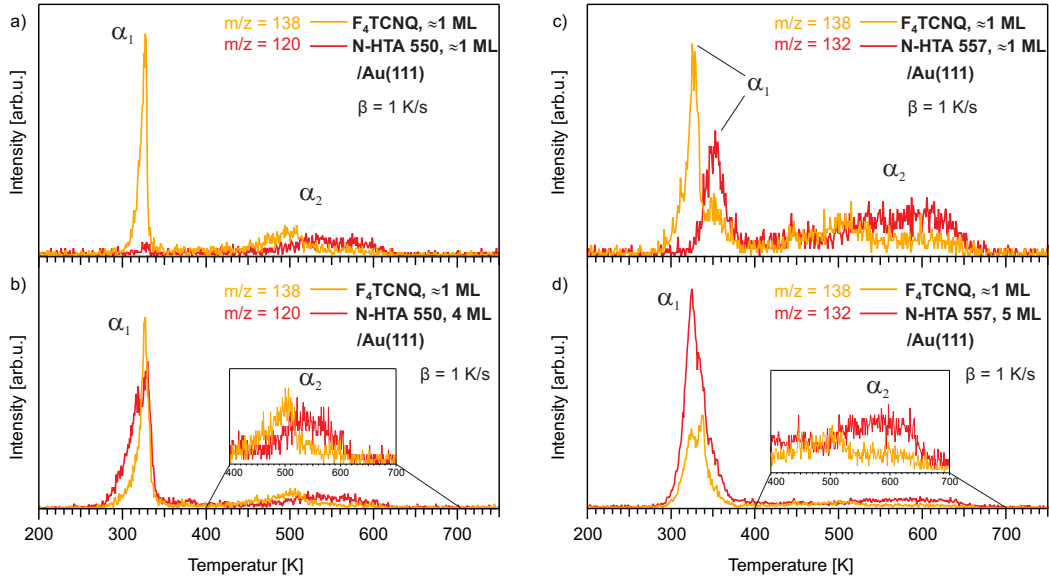

Figure G.2.: TPD spectra of approximately 1 ML of F_4TCNQ deposited on (a) approximately 1 ML and (b) 4 ML of N-HTA 550 as well as (c) approximately 1 ML and (d) 5 ML of N-HTA 557 adsorbed on Au(111). The spectra are measured with a heating rate of $\beta = 1$ K/s for the selected m/z of 138 (F_4TCNQ), 120 (N-HTA 550) and 132 (N-HTA 557).

Additionally, the fact that the overlaying F_4TCNQ monolayer coverage exhibits a desorption feature along with the monolayer desorption region of the adsorbed donor molecules on Au (111), regardless of the nature of the underlying molecules (N-HTA 550 or N-HTA 557) or their coverage, suggests that observed desorption feature of F_4TCNQ at higher temperatures may have originated from the co-desorption of the acceptor and the donor molecules. This can

be attributed to a stronger adsorbate/adsorbate interaction between F_4TCNQ and N-HTA derivatives in comparison to TCNQ. It should also be noted that the presence of the α_1 peak in the given desorption spectra of N-HTA 550 and N-HTA 557 for the corresponding TCNQ/ N-HTA and F_4TCNQ/N-HTA bilayers suggests that the actual coverages achieved on the substrate after direct deposition of N-HTA molecules are slightly more than the intended monolayer. This deviation from the the intended coverage after a direct deposition of molecules is expected and is an unintended consequence of this method of sample preparation. The corresponding preparation parameters used for these samples are given in table H.1.
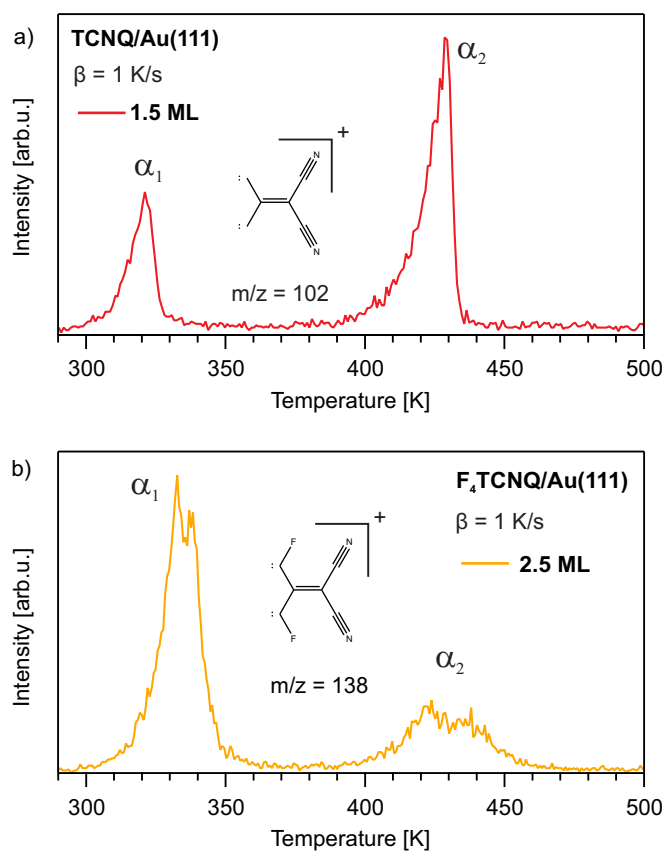
Figure G.3.: TPD spectra of (a) TCNQ for the selected m/z of 102 and (b) F_4TCNQ for the selected m/z of 138 adsorbed on Au(111), measured with a heating rate of $\beta = 1$ K/s. The desorption features are labelled with α_1 and α_2. The structural formulas of the selected ionic fragments from each molecule are depicted in their corresponding figures.

Appendix

G.2. Vibrational HREELS Measurements

The angle-resolved vibrational HREELS measurement is utilized to investigate the adsorption geometry of the deposited TCNQ and F_4TCNQ molecules on the N-HTA derivatives adsorbed on Au(111). In this set of measurements, the identified vibrations in the spectra of each system are assigned by comparing the corresponding results with the results obtained from the spectra of individual molecules adsorbed on Au(111). In order to distinguish between the contributions of the donor and acceptor molecules to the overall spectra of the systems, the assigned vibrations of the acceptor molecules, either TCNQ or F_4TCNQ, are labelled with blue color.

The spectra of TCNQ/N-HTA 550 system consist of vibrations associated with both donor and acceptor molecules (see Figure G.4 (a) and (b)). In the TCNQ/N-HTA 550 bilayer, the contribution of TCNQ to the spectrum includes three dipole-active vibrations with a high intensity ratio between specular and off-specular scattered electrons, which are assigned to the buckling mode (at 209 cm^{-1}) as well as γ_ω(C-C-C) and γ_ω(C-H) wagging modes (at 464 cm^{-1} and 858 cm^{-1}) (see Figure G.4 (a)). These vibrations are joined by six non-dipole-active vibrations, with reduced specular to off-specular ratios, that are assigned to δ(C-N) scissoring mode (at 133 cm^{-1}), a combination of δ(C-H) scissoring and ν(C-C-C) stretching modes (at 1339 cm^{-1} and 1549 cm^{-1}) as well as ν_s(C-H) stretching mode (at 3057 cm^{-1}). As for N-HTA 550, the contribution of the molecule to the spectrum of the bilayer includes three dipole-active vibrations, assigned to γ_ω(C-H) wagging modes (at 406 cm^{-1} and 745 cm^{-1}) and γ_τ(C-H) twisting modes (at 561 cm^{-1}) as well as a single non-dipole-active vibration assigned to δ(C-H) scissoring mode (at 1162 cm^{-1}).

A comparison between the vibrational HREELS spectra of the deposited monolayer of TCNQ on N-HTA 550 and directly on Au (111) (see Figure G.6 (b)) reveals that some of the assigned non-dipole-active vibrations in the spectra of the bilayer, namely δ(C-N) scissoring, combination of δ(C-H) scissoring and ν(C-C-C) stretching as well as ν(C-N) stretching modes, are missing in the measured monolayer spectrum of TCNQ adsorbed on Au (111). Given that the assigned vibrations in this spectrum are predominately dipole-active with a dynamic dipole moment that is perpendicular to the molecular plane, it can be concluded that at a monolayer coverage, TCNQ adapts a planar adsorption geometry on Au(111)[95]. In contrast, presence of non-dipole-active vibrations with a dynamic dipole moment that is parallel with the molecular backbone

of TCNQ in the spectra of the TCNQ/N-HTA 550 bilayer suggest that adsorption geometry of the adsorbed TCNQ monolayer on top of the underlying N-HTA 550 monolayer is not strictly planar.
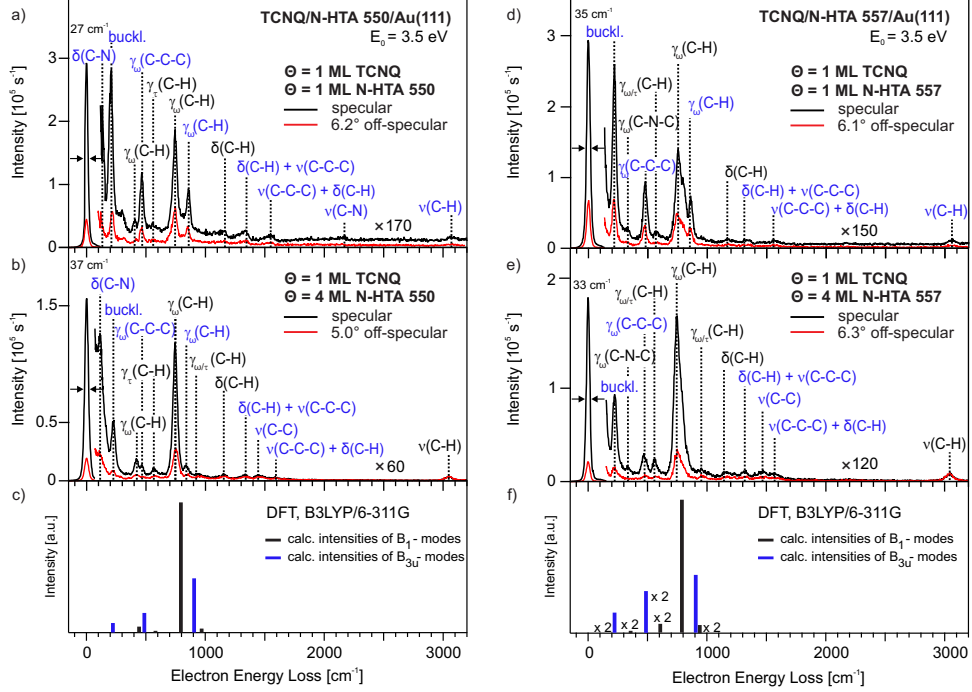
Figure G.4.: Vibrational HREELS spectra of 1 ML of TCNQ deposited on (a) 1 ML and (b) 4 ML of N-HTA 550 as well as (d) 1 ML and (e) 4 ML of N-HTA 557 adsorbed on Au(111), measured in specular (black spectra) and off-specular (red spectra) scattering geometry, with the associated DFT-calculations (B3LYP/6-311G) for intensities and frequencies of B_{3u} (TCNQ) and B_1 (N-HTA 550/557) symmetric vibrational modes with a dynamic dipole moment perpendicular to the molecular plane (c and f). E_0 is the primary energy of the incident electrons. The energy resolution of the specular spectra is measured as the full width at half maximum (FWHM) of the elastic peak (zero energy loss peak) and is given in wavenumbers (cm^{-1}). The assigned vibrations of TCNQ (in blue) and N-HTA 550/557 (in black) are listed in table G.1.

By increasing the coverage of underlying N-HTA 550 to 4 ML, the intensity of detected vibrations associated with TCNQ decreases relative to the ones assigned to N-HTA 550. As a result, the previously assigned ν(C-N) stretching mode vibration of TCNQ can no longer be detected in the spectrum of the multilayer coverage, while a new dipole-active vibration at 919 cm^{-1} can now be identified in the same spectrum, which is assigned to the $\gamma_{\omega/\tau}$(C-H)

vibrational mode of N-HTA 550. An exception is the presence of the ν(C-C) stretching mode vibration of TCNQ in the spectrum of the multilayer at 1439 cm^{-1}, which could not be detected in spectrum of the bilayer. Despite these observations, no significant change in the spectra of TCNQ/N-HTA 550 multilayer can be seen, which suggest that increasing the coverage of N-HTA 550 does affect the adsorption geometry of the overlaying TCNQ coverage. Therefore, it can be concluded that TCNQ adsorb with a mostly planer geometry on the multilayer coverage of N-HTA 550.

As for the TCNQ/N-HTA 557 system, the contributions of TCNQ to the spectra of the system at bi- and multilayer coverages consist of mostly similar vibrations associated with the molecule as detected and assigned in the spectra of the TCNQ/N-HTA 550 system (see Figure G.4 (c) and (d)). The only exception to this observation is the absence of the previously assigned δ(C-N) scissoring mode (at 133 cm^{-1}) and ν(C-N) stretching mode (at 2172 cm^{-1}) vibrations in the spectra of the TCNQ/N-HTA 557 system. Additionally, the contribution of N-HTA 557 to the spectra of the system includes four dipole-active vibrations, which are assigned to γ_ω(C-N-C) and γ_ω(C-H) wagging modes (at 329 cm^{-1} and 743 cm^{-1}) as well as $\gamma_{\omega/\tau}$(C-H) wagging/twisting modes (at 329 cm^{-1} and 743 cm^{-1}), along with two non-dipole-active vibration assigned to δ(C-H) scissoring (at 1166 cm^{-1}) and ν(C-H) stretching modes (at 3042 cm^{-1}). By increasing the N-HTA 557 coverage to 4 ML, the assigned vibrations in the spectra of the bilayer, follows a similar trend as observed in the spectra of the TCNQ/N-HTA 550 system, where increasing the coverage of the underlying donor molecule results in a decreased intensity of the dipole active vibrations of the acceptor relative to its non-dipole active vibrations in the spectrum of the multilayer coverage in comparison to the bilayer. These observations suggests that TCNQ at a monolayer coverage adsorb with a relatively planer geometry on the underlying coverages of N-HTA 557. This indicates that the nature of the underlying molecules (N-HTA 550 or N-HTA 557) or its coverage does not induce a significant change in the adsorption geometry of the overlaying TCNQ molecules.

In case of F_4TCNQ/N-HTA systems, the contributions of F_4TCNQ to the spectra of the systems include vibrations, which are assigned to the buckling, γ_ω(C-C-C) wagging modes as well as ν(C-C) stretching mode and its combination with δ(C-F) scissoring mode (see Figure G.5). These vibrations are similar to the ones previously assigned in the measured spectrum of the ad-

sorbed monolayer coverage of F_4TCNQ on the $Au(111)$ with the exception of the ν(C-C-C) stretching mode vibration, which is absent in the spectra of the systems. It is likely that this particular vibration is overlayed by γ_ω(C-H) wagging mode vibrations of N-HTA 550 at 746 cm^{-1} and N-HTA 557 at 753 cm^{-1}. Additionally, the assigned ν(C-N) stretching mode vibration of F_4TCNQ can only be detected in the F_4TCNQ/ N-HTA 557 multilayer spectrum. As for N-HTA 550 and N-HTA 557, the contributions of molecules to the spectra of the systems consists of vibrations, which are already assigned in the spectra of TCNQ/N-HTA systems.

However, some of the previously assigned vibrations, including the γ_τ(C-H) twisting mode vibration of N-HTA 550 at 561 cm^{-1} as well as the γ_ω(C-N-C) and γ_ω(C-H) wagging modes and δ(C-H) scissoring mode vibrations of N-HTA 557 at 329 cm^{-1}, 743 cm^{-1} and 1166 cm^{-1} are absent in the in the spectra of F_4TCNQ/N-HTA systems. These vibrations are either overlayed by the vibrations associated with F_4TCNQ or simply could not be detected in the measured spectra of the systems.When compared, the assigned non-dipole-active vibrations of F_4TCNQ more pronounced in the spectra of the F_4TCNQ/N-HTA 557 system. Considering that these vibrations posses a dynamic dipole moment that is parallel with the molecular backbone, it can be assumed that the underlying N-HTA 557 coverage induces a tilt in the overlying F_4TCNQ molecules out of the plane paralleled to the substrate. Regardless, due to presence of the dominant buckling mode vibrations of F_4TCNQ in the spectra of F_4TCNQ/N-HTA systems at both bi- and multilayer coverages and the fact that this vibration posses a dynamic dipole moments that is perpendicular to the molecular plane, it can be concluded that similar to TCNQ, F_4TCNQ molecules adsorb with a mainly planer geometry on the underlying N-HTA coverages.
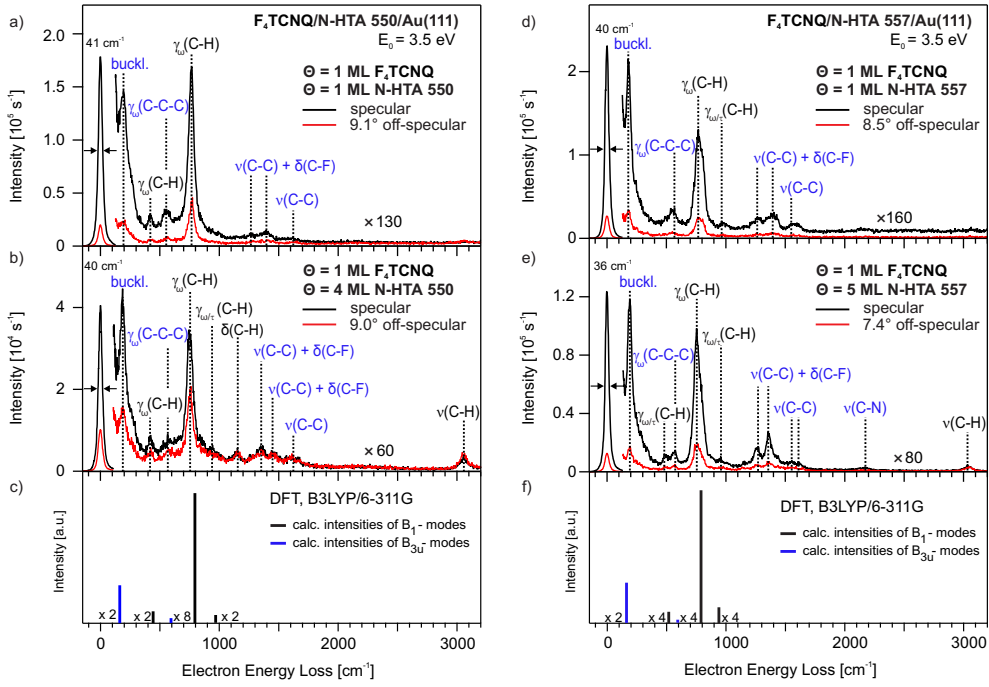
Figure G.5.: Vibrational HREELS spectra of 1 ML of F_4TCNQ deposited on (a) 1 ML and (b) 4 ML of N-HTA 550 as well as (d) 1 ML and (e) 5 ML of N-HTA 557 adsorbed on Au(111), measured in specular (black spectra) and off-specular (red spectra) scattering geometry, with the associated DFT-calculations (B3LYP/6-311G) for intensities and frequencies of B_{3u} (F_4TCNQ) and B_1 (N-HTA 550/557) symmetric vibrational modes with a dynamic dipole moment perpendicular to the molecular plane (c and f). E_0 is the primary energy of the incident electrons. The energy resolution of the specular spectra is measured as the full width at half maximum (FWHM) of the elastic peak (zero energy loss peak) and is given in wavenumbers (cm^{-1}). The assigned vibrations of F_4TCNQ (in blue) and N-HTA 550/557 (in black) are listed in table G.1.
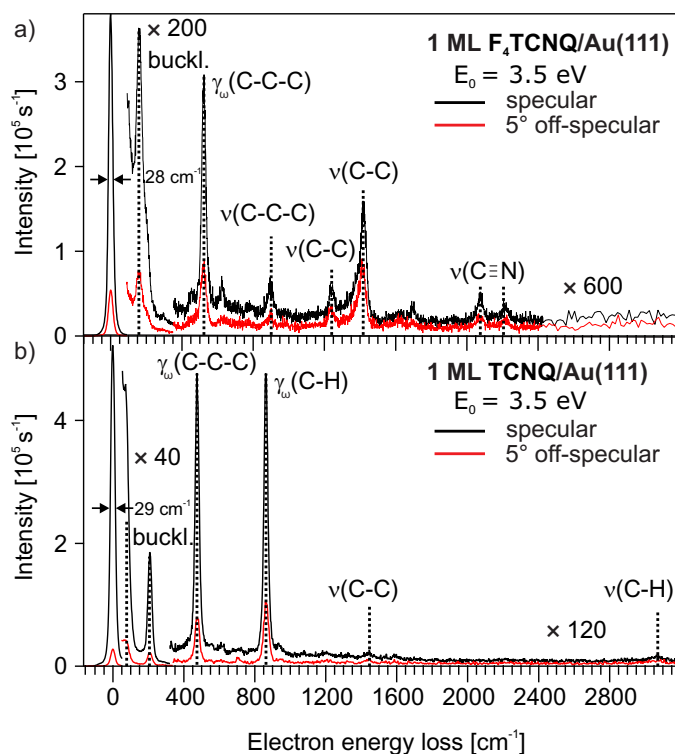
Figure G.6.: Vibrational HREELS spectra of (a) F$_4$TCNQ and (b) TCNQ measured in specular (black spectra) and off-specular (red spectra) scattering geometry for the monolayer coverage adsorbed on Au(111). E$_0$ is the primary energy of the incident electrons. The energy resolution of the specular spectra is measured as the full width at half maximum (FWHM) of the elastic peak (zero energy loss peak) and is given in wavenumbers (cm^{-1}). Adapted from Ref. [95].

Table G.1.: Assigned vibrations (in cm^{-1}) of 1 ML of TCNQ deposited on 1 and 4 ML of N-HTA 550 (first table) as well as 1 and 4 ML of N-HTA 557 (second table) and 1 ML of F$_4$TCNQ deposited on 1 and 4 ML of N-HTA 550 (third table) as well as 1 and 5 ML of N-HTA 557 (forth table), adsorbed on Au(111). Dipole active modes are labelled with *da*. The identified modes for each vibration are described with the following abbreviations; γ – out-of-plane; ρ – rocking; δ – scissoring; ν – stretching; τ – twisting; ω – wagging; s – symmetric; as – asymmetric. Representation (Repr.) of the associated point groups and the orientation of the calculated dipole derivative vector with respect to the molecular geometry, x, perpendicular to the molecular plane; y, short axis and z, long axis of molecular backbone for each mode are listed. For the assignment of the vibrations associated with TCNQ and F$_4$TCNQ, Ref.[95] was consulted. As for N-HTA 550 and N-HTA 557, the assignments of the vibrations are made based on Table 3.5.

<div align="center">

TCNQ/N-HTA 550 system

</div>

			Mode		
#	1 ML	4 ML	TCNQ	N-HTA 550	Repr.
1	133	112	δ(CN)	-	B$_{1u}$(z)
2	209 *da*	228 *da*	buckl.	-	B$_{3u}$(x)
3	406 *da*	419 *da*	-	γ_ω(C-H), γ_ω(C-C-C)	B$_1$(x)
4	464 *da*	467 *da*	γ_ω(C-C-C)	-	B$_{3u}$(x)
5	561 *da*	561 *da*	-	γ_τ(C-H), γ_ω(C-C-C)	B$_1$(x)
6	745 *da*	745 *da*	-	γ_ω(C-H), γ_ω(C-N-C)	B$_1$(x)
7	858 *da*	838 *da*	γ_ω(C-H)	-	B$_{3u}$(x)
8	-	919 *da*	-	$\gamma_{\omega/\tau}$(C-H)	B$_1$(x)
9	1162	1155	-	δ(C-H), ρ(C-H), ν_s(C-N-C)	A$_1$(z)
10	1339	1336	δ(C-H), ν(C-C-C)	-	B$_{2u}$(y)
11	-	1439	ν(C-C)	-	B$_{2u}$(y)
12	1549	1588	ν(C-C-C), δ(C-H)	-	B$_{2u}$(y)
13	2172	-	ν(CN)	-	B$_{2u}$(y)
14	3057	3041	ν(C-H)	ν(C-H)	A$_1$(z)

TCNQ/N-HTA 557 system

#	1 ML	4 ML	Mode TCNQ	Mode N-HTA 557	Repr.
1	219 *da*	223 *da*	buckl.	-	B$_{3u}$(x)
2	329 *da*	329 *da*	-	γ_ω(C-N-C), $\gamma_{\omega/\tau}$(C-H), γ_ω(C-C-C)	B$_1$(x)
3	481 *da*	471 *da*	γ_ω(C-C-C)	-	B$_{3u}$(x)
4	575 *da*	562 *da*	-	$\gamma_{\omega/\tau}$(C-H), γ_ω(C-N-C)	B$_1$(x)
5	755 *da*	743 *da*	-	γ_ω(C-H), γ_ω(C-N-C)	B$_1$(x)
6	859 *da*	-	γ_ω(C-H)	-	B$_{3u}$(x)
7	-	952 *da*	-	$\gamma_{\omega/\tau}$(C-H)	B$_1$(x)
8	1169	1166	-	δ(C-H), ρ(C-H)	A$_1$(z)
9	1327	1327	δ(C-H), ν(C-C-C)	-	B$_{2u}$(y)
10	-	1469	ν(C-C)	-	B$_{2u}$(y)
11	1562	1550	ν(C-C), δ(C-H)	-	B$_{2u}$(y)
12	3054	3042	ν(C-H)	ν(C-H)	B$_2$(y)

F$_4$TCNQ/N-HTA 550 system

#	1 ML	4 ML	Mode		Repr.
			F$_4$TCNQ	**N-HTA 550**	
1	193 *da*	187 *da*	buckl.	-	B$_{3u}$(x)
2	420 *da*	423 *da*	-	γ_ω(C-H), γ_ω(C-C-C)	B$_1$(x)
3	555 *da*	565 *da*	γ_ω(C-C-C)	-	B$_{3u}$(x)
4	768 *da*	746 *da*	-	γ_ω(C-H), γ_ω(C-N-C)	B$_1$(x)
5	-	943 *da*	-	$\gamma_{\omega/\tau}$(C-H)	B$_1$(x)
6	-	1153	-	δ(C-H), ρ(C-H), ν_s(C-N-C)	A$_1$(z)
7	1266	-	ν(C-C), δ(C-F)	-	B$_{1u}$(z)
8	-	1366	ν(C-C), δ(C-F)	-	B$_{2u}$(y)
9	1411	1440	ν(C-C), δ(C-F)	-	A$_g$
10	1621	1615	ν(C-C)	-	B$_{2u}$(y)
11	-	3055	-	ν(C-H)	A$_1$(z)

F$_4$TCNQ/N-HTA 557 system

| #	1 ML	5 ML	Mode F$_4$TCNQ	Mode N-HTA 557	Repr.
1	177 *da*	191 *da*	buckl.	-	B$_{3u}$(x)
2	-	482 *da*	-	$\gamma_{\omega/\tau}$(C-H), γ_ω(C-C-C)	B$_1$(x)
3	568 *da*	572 *da*	γ_ω(C-C-C)	-	B$_{3u}$(x)
4	768 *da*	753 *da*	-	γ_ω(C-H), γ_ω(C-N-C)	B$_1$(x)
5	965 *da*	956 *da*	-	$\gamma_{\omega/\tau}$(C-H)	B$_1$(x)
6	1266	1273	ν(C-C), δ(C-F)	-	B$_{1u}$(z)
7	-	1354	ν(C-C), δ(C-F)	-	B$_{2u}$(y)
8	1404	-	ν(C-C), δ(C-F)	-	A$_g$
9	-	1554	ν(C-C)	-	B$_{3u}$(x)
10	1598	1609	ν(C-C)	-	B$_{2u}$(y)
11	-	2167	ν(CN)	-	B$_{2u}$(y)
12	-	3033	-	ν(C-H)	B$_2$(y)

G.3. Electronic HREELS Measurements

All of the investigated D/A-systems presented in the main text were prepared by first depositing a mono - or multilayer coverage of the donor molecules, N-HTA 550 or N-HTA 557, on Au(111) to form a decoupling layer for the over-laying acceptor molecules, TCNQ or F_4TCNQ. Thereby, inducing a charge transfer between the donor and acceptor molecules. The results from electronic HREELS measurements on TCNQ/N-HTA and F_4TCNQ/N-HTA systems have proved this concept to be true. Here, in order to investigate the influence of sample preparation on charge transfer between the donor and acceptor molecules, the N-HTA 557/F_4TCNQ system is formed, in which the preparation order is reversed. This means that in the first step a mono- or multilayer coverage of F_4TCNQ is deposited on Au(111) and in the second step a monolayer of N-HTA 557 is deposited on top of the underlying F_4TCNQ coverage to form a potential CT-complex.

Figure G.7 (a) shows the electronic HREELS spectrum of N-HTA 557 /F_4TCNQ bilayer. This spectrum is dominated by the plasmonic excitation of F_4TCNQ at 0.7 eV, which is followed by the conventional Au (111) surface plasmon at 2.6 eV, a weak loss feature at 3 eV, which probably originates from $S_0 \rightarrow S_1$ transition of F_4TCNQ. Absence of any transition in this spectrum, which can be assigned to a CT-state indicates that at such D/A-bilayer, the F_4TCNQ monolayer can not act as a decoupling layer and as predicted it couples strongly with Au(111), which hinders a charge transfer between the donor and acceptor molecules. In comparison, a transition at 1 eV in the spectrum of F_4TCNQ/N-HTA 557 bilayer, in which the N-HTA 557 monolayer act as the decoupling layer, were assigned to the CT-transition of the corresponding D/A-system.

By increasing the F_4TCNQ coverage to 5 ML, the dominating feature of the spectrum is replaced by a loss peak at 1 eV, which resembles the CT-transition of the F_4TCNQ/N-HTA 557 system and accordingly is assigned as such (see Figure G.7 (b)). This spectrum also includes a broad loss feature at higher energies, in which the features at 3.1 is assigned to $S_0 \rightarrow S_1$ transition of F_4TCNQ. Interestingly, no loss feature, which can be assigned to any of N-HTA 557 transitions could be detected in the spectrum of either bilayer or multilayer coverage. Detection of the CT-transition at 1 eV in this spectrum indicates that regardless of the nature of the underlying layer, a charge transfer between the donor and acceptor molecules at higher layers is expected.
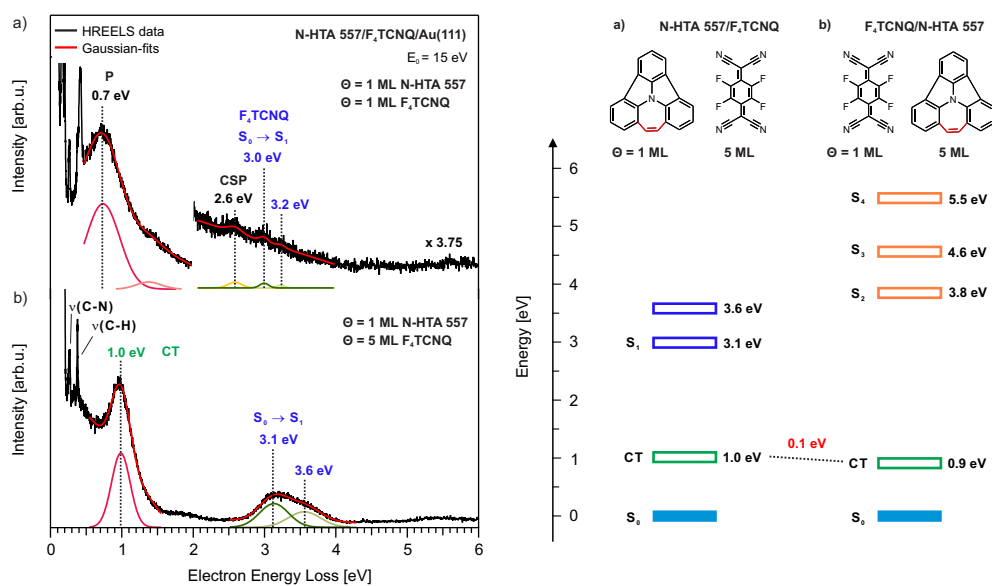
Figure G.7.: Electronic HREELS spectra (left) of 1 ML of N-HTA 557 deposited on (a) 1 ML and (b) 5 ML of F_4TCNQ on Au(111) (black spectra). The electronic loss features were fitted using Gaussian functions (red curves). E_0 is the primary energy of the incident electrons. Θ is the coverage in monolayer (ML). The contributions from F_4TCNQ are marked with blue and CT-transition with green colors. The identified and assigned electronic transitions of N-HTA 557/F_4TCNQ versus F_4TCNQ/N-HTA 557 systems at the multilayer coverage are summarized in an energy level diagram (right).

The measured electronic HREELS spectra of multi - and monolayer coverages of TCNQ and F$_4$TCNQ adsorbed on Au(111) (T$_S$=300 K) are shown in figure G.8.
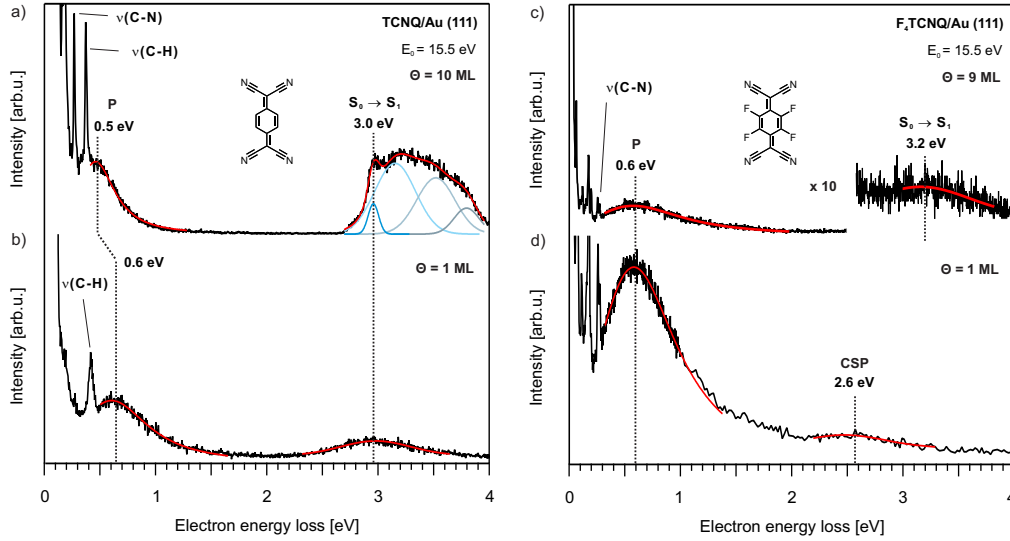
Figure G.8.: Electronic HREELS spectra of adsorbed TCNQ (Left) and F$_4$TCNQ (right) on Au(111), measured for mono - (a and c) and multilayer (b and d) coverages (black spectra). The electronic loss features were fitted using Gaussian functions (red curves). E$_0$ is the primary energy of the incident electrons. Θ is the coverage in monolayer (ML). Adapted from Ref.[95].

H. Sample Preparation Parameters

Table H.1.: Preparation parameters of all the measured samples in this thesis: Used molecules and substrate, determined coverage in monolayer (Θ), dosing temperature (T_D), dosing time (t_D), and substrate temperature (T_S).

Molecule	Substrate	Θ [ML]	T_D [K]	t_D [s]	T_S [K]
DAP	Au(111)	4	460	800	300
TAP	Au(111)	3	490	900	300
TIPS-BP	Au(111)	4	533	900	300
TIPS-BAP	Au(111)	5	533	2000	300
NTD	Au(111)	7	300	800	200
NTD-Cl	Au(111)	-	368	450	200
NTD-Br	Au(111)	-	388	700	200
BBT-Ph	Au(111)	11	443	2000	300
BBT-Ph	Au(111)	1	443	100	300
BBT-Ph	Au(111)	Subm.	443	50	300
BBT-Th	Au(111)	6	468	340	300
BBT-Th	Au(111)	1	468	80	300
BBT-Th	Au(111)	Subm.	468	150	300
N-HTA 550	Au(111)	4	373	200	200
N-HTA 550	Au(111)	1	373	80	200
N-HTA 550	Au(111)	Subm.	373	55	200
N-HTA 557	Au(111)	5	393	750	200
N-HTA 557	Au(111)	1	393	150	200
N-HTA 557	Au(111)	Subm.	393	75	200
TCNQ	Au(111)	1	383	200	200
F_4TCNQ	Au(111)	1	403	150	200

**GESAMTFAKULTÄT FÜR MATHEMATIK, INGENIEUR-
UND NATURWISSENSCHAFTEN**

**COMBINED FACULTY OF MATHEMATICS, ENGINEERING
AND NATURAL SCIENCES**

RUPRECHT-KARLS-
UNIVERSITÄT
HEIDELBERG

**Eidesstattliche Versicherung gemäß § 8 der Promotionsordnung für die Gesamtfakultät
für Mathematik, Ingenieur- und Naturwissenschaften der Universität Heidelberg /
Sworn Affidavit according to § 8 of the doctoral degree regulations of the Combined
Faculty of Mathematics, Engineering and Natural Sciences at Heidelberg University**

1. Bei der eingereichten Dissertation zu dem Thema / The thesis I have submitted entitled

   …………………………………………………………………………………………………….

   …………………………………………………………………………………………………….

   handelt es sich um meine eigenständig erbrachte Leistung / is my own work.

2. Ich habe nur die angegebenen Quellen und Hilfsmittel benutzt und mich keiner unzulässigen Hilfe
   Dritter bedient. Insbesondere habe ich wörtlich oder sinngemäß aus anderen Werken übernommene
   Inhalte als solche kenntlich gemacht. / I have only used the sources indicated and have not made
   unauthorised use of services of a third party. Where the work of others has been quoted or
   reproduced, the source is always given.

3. Die Arbeit oder Teile davon habe ich wie folgt/bislang nicht[1] an einer Hochschule des In- oder
   Auslands als Bestandteil einer Prüfungs- oder Qualifikationsleistung vorgelegt. / I have not yet/have
   already[1] presented this thesis or parts thereof to a university as part of an examination or degree.

   Titel der Arbeit / Title of the thesis: …………………………………………………………………….

   Hochschule und Jahr / University and year: …………………...………………………………………......

   Art der Prüfungs- oder Qualifikationsleistung / Type of examination or degree: …………………………

4. Die Richtigkeit der vorstehenden Erklärungen bestätige ich. / I confirm that the declarations made
   above are correct.

5. Die Bedeutung der eidesstattlichen Versicherung und die strafrechtlichen Folgen einer unrichtigen oder
   unvollständigen eidesstattlichen Versicherung sind mir bekannt. / I am aware of the importance of
   a sworn affidavit and the criminal prosecution in case of a false or incomplete affidavit.

Ich versichere an Eides statt, dass ich nach bestem Wissen die reine Wahrheit erklärt und nichts
verschwiegen habe. / I affirm that the above is the absolute truth to the best of my knowledge and that
I have not concealed anything.

…………………………………………..   …………………………..………………………..
Ort und Datum / Place and date   Unterschrift / Signature

[1] Nicht Zutreffendes streichen. Bei Bejahung sind anzugeben: der Titel der andernorts vorgelegten Arbeit, die
Hochschule, das Jahr der Vorlage und die Art der Prüfungs- oder Qualifikationsleistung. / Please cross out what is
not applicable. If applicable, please provide: the title of the thesis that was presented elsewhere, the name of the
university, the year of presentation and the type of examination or degree.

The German text is legally binding.